Universidad
Carlos III de Madrid

TESIS DOCTORAL

Vapour Condensation in Boundary Layer Flows

Autor:
Mario Durán Camejo

Director:
Luis López Bonilla

Gregorio Millán Institute of Fluid Dynamics,
Nanoscience and Industrial Mathematics

Leganés, septiembre de 2013

TESIS DOCTORAL

Vapour Condensation in Boundary Layer Flows

Autor: Mario Durán Camejo

Director: Luis López Bonilla

Firma del tribunal calificador:

(Nombre y Apellidos) Firma

Presidente:

Vocal:

Secretario:

Calificación:

Leganés, de de

To my mother, who has known to wait.
To Luis, who trusted me

Acknowledgement

"Your common man has no conception of the zeal that animates a scientific investigator..."

The Moth, by H. G. Wells

Ohne Furcht vor dem Odium der Peinlichkeit, neigen wir vielmehr der Ansicht zu, dass nur das Gründliche wahrhaft unterhaltend sei.

"We do not fear being called meticulous, inclining as we do to the view that only the exhaustive can be truly interesting"

Der Zauberberg (The Magic Mountain), by Thomas Mann

I have to thank in first place Dr. Luis López Bonilla for having provided the theme of my thesis as a continuation of his previous research labour, for contributing with his guidance and advices to make it possible and, very important too, for having given me the opportunity for a full dedication to this work (*), a work that has been like a long journey. A long journey produces, of course, a long list of interconnected people and events that have contributed to a safe and sound arrival to the final destination. In this long list I have to remark all my fellows in the Group of Modelization, Numerical Simulation and Industrial Mathematics for their sympathy and support. That list is formed by people that still remain in the group and by people that are not any longer, people that have shared the whole journey and people that only shared a part of it, but this is a natural consequence of a long journey and it doesn't change any essential. From other institutions I wish to be thankful also to Dr. Ana Carpio, Dr. Manuel Arias Zugasti and Dr. José Luis Castillo that have offered their assistance and guidance, and to Dr. Pedro García-Ybarra who have assesed part of the work detailed in Appendix A. Special mention deserve Dr. David Rodríguez Espeso for whose enthusiastic collaboration in the agglomeration stochastic simulation and other aspects of the work, I feel in debt. I have to add that this collaboration was possible thanks to my advisor Dr. Luis López Bonilla.

Finally, I wish also to thank Dr. Amable Liñán, Dr. Manuel Kindelán, Dr. Pedro García-Ybarra and Dr. Ana Carpio for having accepted to join the thesis examination committee.

In a different context, but not in a lower level, I have to mention my mother, naturally, my family, my friends MariCarmen, Heriberto and Fernando (they know why), Rosi, Jose, and particularly Orencito (who arrived in the right moment).

(*)Supported by the Spanish Ministerio de Economía y Competitividad grants FIS2011-28838-C02-01, by the Autonomous Region of Madrid grants P2009/ENE-1597 (HYSYCOMB) and S-0505/ENE/0229 (COMLIMAMS) and by own funds of the Group of Modelization, Numerical Simulation and Industrial Mathematics.

Abstract

This thesis has two purposes. Metaphorically we can say that it works in two different scales -which, makes sense, nevertheless-.

First, it deals with homogeneous vapour condensation in boundary layer flows. Boundary layer flows, as it is very well known, has the property of ubiquity. Every flow in contact with solid surfaces or even flows in mutual contact become boundary layer flows at some scale. The vapour condensation, and many other phase transition phenomena, develops intensively in that boundary layers. However, the description and modeling of homogeneous condensation has been less treated in the literature if compared with the case of heterogeneous condensation (that is, the condensation in presence of particles). A model of homogeneous vapour condensation in a boundary layer flow has been developed for the special case of stagnation-point incompressible flow near a cold wall with self-similar solution and a monodisperse distribution of resulting droplets. Complete model has been solved numerically and in addition a very good approximation to the model has been obtained by applying perturbative methods. We have extended this model in several directions: other flows admitting self-similar solutions, polydisperse distribution of droplets, mixed homogeneous and heterogeneous condensation and homogeneous condensation in counterflow boundary layers in compressible flows. In the case of mixed condensation we have showed that it is possible to tackle homogeneous and heterogenous condensation independently, in an iterative scheme. Of course, all these new directions have been treated in a less detailed form and keep open to future work.

Second, the thesis has intended to bring together closely related themes that has been, however, studied separately. Then, we have widened the initial scope to other aspects a, for instance, coagulation and agglomeration of nanometric particles, thermophoresis and ice formation. Specifically, agglomeration and thermophoresis become essential in the understanding of condensation processes in combustion chambers where a very rich chemical activity is taking place, and ice formation is important if we want to extend the condensation process to atmospheric environments.

The essential theme of this thesis is important in many aspects:

1. It deals with phenomena present in a wide variety of natural and industrial situations whose understanding may result in improvements of known processes or in the better

forecast of some desirable or not desirable behaviors.

2. We have been forced to gather a lot of normally disperse or not directly connected information and methods that have an effect in the comprehension and description of those phenomena.

The mathematical treatment of some aspects of the problem has been undertaken in parallel with numerical simulation of some others. Therefore, a lot of work is waiting for completion or full develop. This is mainly the case of the stochastic-thermophoretic simulation of the agglomeration process of nanometric particles, that is described in appendix A, or the proposed model for the description of wedge flows near the leading edge, that ends the chapter 2.

We have adopted the terms 'boundary layer flow' and 'counterflow boundary layers' for denoting the boundary layers when ocurring close to solid walls and those ocurring at the interface of two flows away from any solid surfaces, respectively.

Resumen

Este trabajo de tesis tiene dos propósitos. Metáfóricamente podemos decir que funciona en dos escalas diferentes -lo cual no deja de tener sentido-.

En primer lugar, trata sobre la condensación de vapores en flujos de capa límite. Los flujos de capa límite, como es bien conocido, tienen el don de la ubicuidad. Cualquier flujo en contacto con superficies sólidas o, incluso en contacto mutuo, deviene un flujo de capa límite en alguna escala. La condensación de vapores, y muchos otros fenómenos de transición de fase, se desarrollan intensamente en esas capas límite. Sin embargo, la descripción y modelización de la condensación homogénea ha sido menos tratada en la literatura si la comparamos con la condensación heterogénea (aquella que ocurre sobre partículas presentes en el flujo). Hemos desarrollado un modelo para la condensación homogénea de vapor en un flujo de capa límite particular, el llamado flujo de remanso, cerca de una pared fría, para un fluido incompresible y asumiendo una distribución monodispersa de gotas resultantes. Este problema admite una solución de semejanza. El modelo completo ha sido resuelto numéricamente y además se ha obtenido una buena aproximación del mismo mediante la aplicación de métodos perturbativos. Ese modelo se ha extendido en varias direcciones: Otros tipos de flujo que admitan también soluciones auto-semejantes, la condensación mixta u homogénea y heterogénea simultáneas, y la condensación homogénea en el caso de capas límite en contraflujos con fluidos compresibles. En el caso de la condensación mixta hemos demostrado que es posible abordar las condensaciones homogénea y heterogénea independientemente, con un esquema iterativo. Por supuesto, todas estas nuevas direcciones han sido tratadas de forma menos detallada y está pendientes de trabajo futuro.

En segundo lugar, el trabajo ha intentado acercarse a otros temas muy relacionados con él pero que han sido normalmente estudiados de forma separada. Así, hemos ampliado el objetivo inicial para abarcar otros aspectos como pueden ser la coagulación y la aglomeración de partículas nanométricas, la termoforesis o la formación de hielo. Específicamente, la aglomeración y la termoforesis son esenciales para entender los procesos de condensación en cámaras de combustión donde se está produciendo una muy rica actividad química. La formación de hielo es importante si queremos extender los procesos de condensación al ámbito atmosférico.

El tema esencial de este trabajo de tesis es importante en varios aspectos:

1. Se ocupa de fenómenos presentes en una amplia variedad de situaciones tanto naturales como de los procesos industriales, cuya comprensión puede resultar en el perfeccionamiento de procesos conocidos o en un mejor pronóstico de algunas conductas tanto deseables como indeseables.

2. Nos hemos visto obligados a recopilar mucha información normalmente dispersa o no directamente conectada con el tema esencial, sobre métodos que tienen un gran efecto en la comprensión y descripción de los fenómenos más arriba señalados.

El tratamiento matemático de algunos aspectos del problema ha sido llevado a cabo en paralelo con simulaciones numéricas de algunos otros. Por lo tanto, una gran cantidad de trabajo queda todavía por hacer o por completar. Este es principalmente el caso de la simulación estocástico-termoforética de la aglomeración de partículas nanométricas, que es descrita en el apéndice A, o el modelo propuesto para la descripción de flujos de cu'na muy cerca del vórtice, que cierra el capítulo 2.

Hemos adoptado los términos 'boundary layer flow' y 'conterflow boundary layers' para referirnos a las capas límite que ocurren cerca de una pared sólida y las que ocurren en la interfaz de dos flujos, lejos de cualquier superficie sólida, respectivamente.

Contents

Chapter 1

Introduction

1.1 Fixing the goals

Nowadays research work is very often performed not in an isolated space but rather well on a very known previous network whether by continuing the layout of unfinished roads or by completing small unpaved portions of them far from their point of continuation. Our work should be classified into the last group for we resort once more to Boundary Layer Theory. Boundary Layer Theory has been since it was proposed by L. Prandtl in 1904 a source of research and applications on the study of fluid motion. Local viscous effects allow to discriminate small regions inside a fluid that can be treated separately from the whole. One kind of these situations is given in the zone of contact of fluids with solid objects or between fluids with different features as well. Inside these regions, where velocity and physical properties of the fluid experienced drastic changes if compared with the outside, some phenomena are enhanced, for instance, causing changes in the physical state of substances present in the fluid. In this work we are focusing on nucleation from the gaseous state and condensation followed by the transport process of resulting droplets. We have had an immediate precedent in a series of papers dealing with the subject [9, 78, 79]. With that in mind, new different situations have been developed in the present thesis dealing with steady condensation in boundary layer flows and counterflow boundary layers. The thesis is structured into three parts, reminding in some way the alternating classical sonata scheme with a central part more intimate than the other two. While the extreme parts are focused in boundary layer problems, the central one is occupied by the theme of agglomeration. It is a justified drift from the main path to which we finally return. All this work is described in the following sections.

1.2 Boundary layer incompressible flows: the combustion chamber

The combustion chamber is a scenario where condensation and subsequent deposition play a very important and practical role. Combustion chemistry is briefly described paying attention to the dimensional scale of solid and gaseous byproducts and the time scale of their appearance. This problem is treated in chapters 2, 3 and 4, whose specific contents are detailed in the following subsections.

1.2.1 homogeneous condensation

Since heterogeneous condensation in a combustion chamber has been already treated in the references, we start developing a theory for homogeneous condensation and deposition from boundary layers, that includes also an asymptotic approach. For we are moving in a wall temperature range above 800 K flow has been always considered to be incompressible. A first and very complete attempt is made for an stagnation-point flow in the vicinity of the chamber walls. The procedure has been also extended to the more general case of wedge flows by introducing some scaling functions that have to be obtained analytically. Besides, the obliquely impinging flow is also treated as a particular subcase of a wedge flow.

In principle, calculations have been made for a single condensible vapour species but the case of multi-species vapours is straightforward. Otherwise, our model has considered a monodisperse size distribution of clusters but an iterative procedure for taking in account polydisperse distributions, is elaborated.

All that is the theme of chapter 2.

1.2.2 mixed condensation

Mixed condensation means for us the simultaneous homogeneous and heterogeneous condensation. We had to deal with two limit cases: condensation on spherical particles and on fractal-like agglomerates of nanometric particles. The reason for that rests on the chemical processes that are occurring in the chamber. Models of both cases have been solved exactly and by using an iterative method based on splitting the solution in an homogeneous and an heterogeneous part. Due to the complexity of obtaining the condensation rate on fractal-like structures, a first approach is done with a chain-like agglomerate.

This part is treated in chapter 3.

1.2.3 the agglomeration process

Considering the importance of fractal-like agglomerates for the vapor condensation we drift apart a little to the subject of agglomerate formation. The agglomerate formation has been simulated by the Monte Carlo method for gathering direct information about the structure of the agglomerates in the early stages of the combustion process. In addition to the fractal exponent and the radius of gyration, two new parameters are proposed for characterizing the structure of the agglomerates: the tree-ness and the eccentricity indexes. A method for calculating the condensation rate on fractal-like structures, based on exploratory rays thrown from every particle, is also proposed.

Some experimental work is mentioned for emphasizing the importance of thermophoresis in the agglomerate mobility (mobility is taken here in its most common sense) which suggests that a stochastic simulation is not perhaps the best one.

This part is treated in chapter 4.

1.2.4 something else about the agglomeration process

As an improvement to the previous one, a simulation of a stochastically and thermophoretically driven agglomeration process is proposed. Calculation of forces on the particles is performed by an approximate rule based on the "cast shadow" on particle surface. Those forces have to take in account not only direct incidence from the surrounding gas but successive specular and diffuse reflections from the neighbor particles, for which a strict geometric analysis of that problem has been undertaken.

This part is treated in the appendix A.

1.3 Counterflow boundary layers in compressible flows: atmospheric scenarios

In this part we go back to the conducting thread but tackling now with a counterflow boundary problem as it can be expected to occur in the atmosphere. There is a very wide range of flow interactions to be expected in an atmospheric scenario. We have chosen amongst them the case of two impinging jets. Depending on jet characteristics that case could lead to potential solutions that can be found in the theoretical hydrodynamics literature. In addition, some other solutions are only possible considering vorticity in the flow. It is the case of unequal impinging jets. Since temperatures in the atmosphere reaches minimum values below 273 K flow is considered to be compressible and the condensation process have been extended to attain solidification of the droplets for which a model of freezing based on the critical size of solid nuclei is developed. We have devoted the last chapter (5) to this problem.

Chapter 2

Theory of homogeneous vapour condensation and solid surface deposition from boundary layer flows

Homogeneous condensation of single-species vapours mixed with a carrier gas in the stagnation-point boundary layer flow near a cold wall is considered (Stagnation-point flow is the most simple potential flow in two dimensions and leads to self-similar solutions for the velocity and temperature fields from one side and for the vapour concentration and the droplet's size and density, from the other). There is a condensation region near the wall with supersaturated vapour. Assuming that the surface tension times the molecular area is much larger than the thermal energy far from the wall, droplets are nucleated exclusively in a narrow nucleation layer where the Zeldovich flux of clusters surpassing the critical nucleus size is maximum. The vapour condenses in the free molecular regime on the droplets, which are thermophoretically attracted to the wall. Unlike the narrow condensation region for heterogeneous condensation on solid particles, in the case of homogeneous condensation the condensation region is wide even when the rate of vapour scavenging by droplets is large. A singular perturbation theory of homogeneous vapour condensation in boundary layer flow approximates very well the vapour and droplet density profiles, the nucleation layer and the deposition rates at the wall for wide ranges of the wall temperature and the scavenging parameter B. A key point in the theory is to select a trial vapour number density profile among a one parameter family of profiles between an upper and a lower bound. The maximum of the Zeldovich flux for supercritical nucleii provides the approximate location of the nucleation layer and an approximate droplet density profile. Then the condensate number of molecules and the vapour density profile are calculated by matched asymptotic expansions that also yield the deposition rates. For sufficiently large wall temperatures, a more precise corrected asymptotic theory is given.

The model is also arranged for dealing with polydisperse cluster size distributions, for which a stepped procedure is implemented in order to obtain the different nucleation layers.

Finally, model is extended to the more general case of wedge boundary layer flows (the stagnation-point flow is a particular case of). Self-similar solutions can also be obtained by introducing some scaling functions for the vapour concentration, the equilibrium vapour concentration and the droplet'size and density.

2.1 Single-species vapour in a planar stagnation-point flow

2.1.1 introduction

The effects of condensation in fluid flows have been studied in many situations of interest ranging from condensation trail formation in aircraft wakes [83], shock-tube experiments [63], steam turbines [22] and combustion chambers [92]. When there are solid particles in the carrier gas, the supersaturated vapours condense on them and they are carried to cold walls thermophoretically [15, 16, 38, 79]. This heterogeneous condensation is important in aerosol formation [21, 33, 85], fouling and corrosion in biofuel plants [88], outside vapour deposition processes used for making optical fibres [31, 103], chemical vapour deposition, vapour condensation and aerosol capture by cold plates or rejection by hot ones [92].

In this section, we consider homogeneous condensation of single-species vapours mixed with a carrier gas in the stagnation point boundary layer flow near a cold wall. [38], [15, 16], [31] and [79] considered heterogeneous condensation in the case of diluted vapours in a carrier gas and a diluted suspension of solid particles upon which the vapour may condense. [15, 16] study a simple thermophysical model in which the carrier gas is considered to be incompressible, the Soret and Dufour effects are ignored and the particles and droplets move towards the wall by thermophoresis [21, 119]. [38] and [31] deal with more complicated thermophysical models in which the carrier gas is compressible, its viscosity has an algebraic dependence with temperature and the Soret effect is included. In all cases, the presence of vapours and suspended solid particles does not affect the laminar boundary layer flow of the carrier gas, which is described by coupled ordinary differential equations in a similarity variable. In this paper, we adapt the thermophysical model by [15, 16] to the case of homogeneous condensation. The carrier gas does not contain solid particles and therefore droplets form as clusters of condensate molecules surpass the critical nucleus size. These droplets are created at the Zeldovich flux as described in [115] and grow in the free molecular regime. Under different experimental conditions, there are other nucleation rates that improve the classical nucleation theory [81, 96] and there are other growth laws that hold for any droplet size [96]. It is straightforward to extend our analysis using these nucleation and growth rates instead of the Zeldovich flux and the free-molecular-regime growth law.

The numerical solutions of the model equations for the Hiemenz stagnation point flow are interpreted using a singular perturbation approach based on the fact that thermal

energy is small compared to surface tension times molecular area and that the scavenging rate at which vapour condenses on droplets is large. Under these conditions, droplets of condensate are created in a narrow nucleation layer about the point x_M where the Zeldovich flux is maximum. The location of this point is unknown because it depends on the droplet density that has to be calculated as part of the problem. There is a wider condensation layer that may extend to the wall in which vapour is supersaturated and condenses on existing droplets. We find x_M from a trial vapour number density that optimizes the maximum number density of the condensate vapour, then we approximate the droplet density and the number of condensate molecules for $0 \leq x \leq x_M$ by using matched asymptotic expansions and obtain the vapour number density $c(x)$ and the deposition rates at the wall.

The rest of the section is organized as follows. Subsection 2.3.3 describes the model. In §2.1.3, the equations and boundary conditions of the model are written for the simple case of a Hiemenz stagnation point flow. In §2.1.4, we obtain upper and lower bounds of the vapour density profile. The numerical solution of the thermophysical model equations is described in §2.1.6. Subsection 2.1.5 contains a description of our singular perturbation approach. Lastly §2.1.7 contains the conclusions.

2.1.2 model

Consider a dilute vapour of number density $\tilde{c}(\tilde{\mathbf{x}})$ in a carrier gas. The mass fraction of vapour is sufficiently small with respect to the mass fraction of the carrier gas, so that the velocity and temperature fields (assumed to be stationary) $\tilde{\mathbf{u}}(\tilde{\mathbf{x}})$ and $\tilde{T}(\tilde{\mathbf{x}})$ are not affected by the condensation and deposition processes. The vapour will condense in droplets after a homogeneous nucleation process. Let $\tilde{\rho}(\tilde{\mathbf{x}})$ the number density of droplets and let $\tilde{n}(\tilde{\mathbf{x}})$ be the the number of condensed vapour molecules equal to the volume of a droplet divided by the molecular volume of the condensed vapour. Then $\tilde{\rho}(\tilde{\mathbf{x}})\tilde{n}(\tilde{\mathbf{x}})$ is the number density of the condensate. New droplets are generated by homogeneous condensation of vapour at a rate given by the stationary Zeldovich flux of clusters surpassing the size of a critical nucleus n_* to become droplets; cf. Eq. (1.19) of [115]. Thus the droplet density in a laminar flow varies according to

$$\tilde{\nabla} \cdot \left[\left(\tilde{\mathbf{u}} - \alpha\nu \frac{\tilde{\nabla}\tilde{T}}{\tilde{T}} \right) \tilde{\rho} \right] = \sqrt{\frac{2\tilde{v}^2\tilde{\sigma}}{\pi\tilde{m}_v}} \tilde{c}^2 (1 + n_*^{-1/3})^2 (1 + n_*^{-1})^{1/2} e^{-\frac{\sigma^3}{2\eta^2}} H(\tilde{c} - \tilde{c}_e), \quad (2.1)$$

$$\eta = \ln\left(\frac{\tilde{c}}{\tilde{c}_e}\right), \quad (2.2)$$

$$\sigma = \frac{2\tilde{\sigma}}{k_B\tilde{T}} \left(\frac{4}{3}\pi\tilde{v}^2\right)^{1/3}, \quad (2.3)$$

$$n_* = \left(\frac{\sigma}{\eta}\right)^3. \quad (2.4)$$

Here $\tilde{m}_v$, $\tilde{v}$ and $\tilde{\sigma}$ are the molecular mass, the molecular volume and the surface tension of the vapour, respectively. k_B, $\tilde{T}(\mathbf{x})$, η, σ and n_* are the Boltzmann constant, the temperature, the supersaturation, the nondimensional surface tension and the critical nucleus size, respectively. In Equation (2.1), the velocity of droplets equals the flow velocity plus the thermophoretic velocity $-\alpha\nu\tilde{\nabla}\ln\tilde{T}$, where ν is the kinematic viscosity of the carrier gas and the dimensionless thermophoretic coefficient α that depends on the droplet radius but will be considered here to be constant for simplicity. Droplets are produced only in supersaturated regions where the vapour density $\tilde{c}(\mathbf{x})$ is larger than its equilibrium value $\tilde{c}_e$, which is enforced by the Heaviside function $H(\tilde{c}-\tilde{c}_e)$ in the right hand side (RHS) of (2.1). We shall assume that the carrier gas is incompressible. This leads to simpler equations and asymptotic expressions [79] but it also overestimates the particle deposition rates, cf [31] for the case of heterogenous condensation. For wall temperatures larger than $\tilde{T}_\infty/2$, this effect is not too large and our asymptotic theory is applicable to more realistic models including compressibility of the carrier gas. For an incompressible carrier gas, $\tilde{\nabla}\cdot\tilde{\mathbf{u}}=0$ and (2.1) becomes

$$\begin{aligned}\left(\tilde{u}-\alpha\nu\frac{\tilde{\nabla}\tilde{T}}{\tilde{T}}\right)\cdot\tilde{\nabla}\tilde{\rho} &= \alpha\nu\tilde{\rho}\tilde{\nabla}\cdot\frac{\tilde{\nabla}\tilde{T}}{\tilde{T}} \\ &+ \sqrt{\frac{2\tilde{v}^2\tilde{\sigma}}{\pi\tilde{m}_v}}\,\tilde{c}^2(1+n_*^{-1/3})^2(1+n_*^{-1})^{1/2}e^{-\sigma^3/(2\eta^2)}H(\tilde{c}-\tilde{c}_e). \quad (2.5)\end{aligned}$$

Once the droplets are created, vapour condenses on them in supersaturation regions thereby increasing their size. The droplets, which grow from the nucleus size (which can be ignored), are much smaller than the mean free path[1] and therefore in a stationary flow we have [15, 31]

$$\left(\tilde{\mathbf{u}}-\alpha\nu\frac{\tilde{\nabla}\tilde{T}}{\tilde{T}}\right)\cdot\tilde{\nabla}\tilde{n}=(\tilde{c}-\tilde{c}_e)\sqrt{\frac{k_B\tilde{T}}{2\pi\tilde{m}_v}}(36\pi\tilde{v}^2)^{1/3}\tilde{n}^{2/3}H(\tilde{c}-\tilde{c}_e)\,H(\tilde{n}-n_*). \quad (2.6)$$

Both droplet nucleation and growth feed from the supersaturated vapour and therefore these processes acts as sinks in the balance equation for the vapour number density:

$$\begin{aligned}(\tilde{\mathbf{u}}\cdot\tilde{\nabla}-D\tilde{\Delta})\tilde{c} = -\sqrt{\frac{k_B\tilde{T}_\infty}{\tilde{m}_v}}\left(\frac{6v^4}{\pi}\right)^{1/6}\Bigg[&\sqrt{\frac{3\tilde{T}}{\tilde{T}_\infty}}(\tilde{c}-\tilde{c}_e)\tilde{\rho}\tilde{n}^{2/3}H(\tilde{n}-n_*) \\ &+\sqrt{\frac{\sigma_\infty}{2\pi}}n_*\tilde{c}^2(1+n_*^{-1/3})^2(1+n_*^{-1})^{1/2}e^{-\frac{\sigma^3}{2\eta^2}}\Bigg]H(\tilde{c}-\tilde{c}_e). \quad (2.7)\end{aligned}$$

[1] In this work we have adopted the simple thermophysical model described by [15] and applied it to the case of Na_2SO_4 vapours diluted in air with a mean free path of 0.34 μm at a temperature of 1400K [79]. A cluster of 400 molecules of Na_2SO_4 (the critical size for a supersaturation of 0.35 and a wall temperature of $1200K$) has a diameter of about 1 nm. This yields a Knudsen number of 340, much larger than 1. Hence the basic hypothesis of a free molecular condensation regime is applicable.

Here we have converted the Zeldovich flux of number of droplets per unit time in number density per unit time multiplying the RHS of (2.1) by the critical nucleus n_*. Likewise the number of molecules per droplet and per unit time in the RHS of (2.6) has been multiplied by $\tilde{\rho}$ to appear in the RHS of (2.7) as number density of vapour molecules per unit time adsorbed by droplets as they grow. In (2.7), we have defined a temperature-independent dimensionless surface tension $\sigma_\infty = 2\tilde{\sigma}(4\pi\tilde{v}^2/3)^{1/3}/(k_B\tilde{T}_\infty)$, where $\tilde{T}_\infty$ is a constant reference temperature, for example that far from the wall. We have $\sigma = \sigma_\infty\tilde{T}_\infty/\tilde{T}$ and the dimensionless surface tension in the Zeldovich exponential is inversely proportional to the temperature. In Eq. (2.7), the vapour follows the carrier gas flow and we neglect the Soret effect, [15, 79]. The solution of more detailed models (for example in OVD) show that changes due to the Soret effect are relatively small ([31], see also [35] for the case in which the Soret effect plays an important role).

In Eqs. (2.5)-(2.7), the equilibrium number density $\tilde{c}_e$ is given by the Clausius-Clapeyron relation which, for the case of an incompressible carrier gas, is:

$$\frac{\tilde{c}_e}{\tilde{c}_\infty} = \frac{\tilde{T}_d}{\tilde{T}} \exp\left[\left(\frac{\tilde{\Lambda}_K}{k_B\tilde{T}_d} - \frac{\tilde{\Lambda}_K}{k_B\tilde{T}}\right)\right], \tag{2.8}$$

$$\tilde{\Lambda}_K = \tilde{\Lambda} - 2\tilde{\sigma}\left(\frac{4\pi\tilde{v}^2}{3\tilde{n}}\right)^{1/3}, \quad \frac{\tilde{\Lambda}_K}{k_B\tilde{T}_\infty} = \frac{\tilde{\Lambda}}{k_B\tilde{T}_\infty} - \frac{\sigma_\infty}{\tilde{n}^{1/3}}. \tag{2.9}$$

Here $\tilde{c}_\infty$ is the vapour number density far from the wall, $\tilde{\Lambda}$ is the heat of vaporization and $\tilde{T}_d$ is the dew point temperature at which $\tilde{c}_\infty = \tilde{c}_e$ in the absence of flow. $\tilde{\Lambda}_K$ given by Eq. (2.9) contains the correction due to the finite size of the droplets (Kelvin effect) that is quite small even for the size of the critical nucleus n_*. Since n is usually much larger than n_*, we shall ignore the Kelvin effect, $\tilde{\Lambda}_K \approx \tilde{\Lambda}$ and, to be consistent, we shall also ignore the correction factor $(1 + n_*^{-1/3})^2(1 + n_*^{-1})^{1/2}$ in (2.1), (2.5) and (2.7).

In the presence of flow, the dew point temperature changes and to determine its shift is part of the problem we have to solve. If we have vapour density $\tilde{c}_\infty$ and temperature $\tilde{T}_\infty > \tilde{T}_d$ far from the wall, and lower the temperature locally below $\tilde{T}_d$, the vapour becomes supersaturated there. Hence nucleation becomes possible and the production of nuclei for further condensation is initiated. In the stationary flow we consider, the temperature satisfies the equation:

$$\tilde{\mathbf{u}} \cdot \tilde{\nabla}\tilde{T} = \kappa\,\tilde{\Delta}\tilde{T}, \tag{2.10}$$

where κ is the constant thermal diffusivity. In this equation, we have ignored the Dufour effect and also the effect of the latent heat of condensation because the vapour mass fraction is very small compared to that of the carrier gas. We will not specify here the equation for the velocity of the carrier gas because our theory can be used for different flow fields.

The boundary conditions for our problem are:

$$\tilde{T} = \tilde{T}_\infty,\ \tilde{c} = \tilde{c}_\infty,\ \tilde{\rho} = 0,\ \tilde{n} = 0 \quad \text{at infinity (far from the wall);} \tag{2.11}$$

$$\tilde{T} = \tilde{T}_w,\ \tilde{c} = \tilde{c}_e(\tilde{T}_w) \quad \text{at the wall.} \tag{2.12}$$

We consider $\tilde{T}_w < \tilde{T}_d < \tilde{T}_\infty$. Since the wall temperature is below the dew point, the vapour will condense on the cold wall where it will be in local equilibrium with the liquid coating it. Thus $\tilde{c} = \tilde{c}_e$ at the wall. At infinity, the vapour density is $\tilde{c}_\infty$. At some distance from the wall, there is an interface Γ (the dew surface) between the nucleation-condensation region where some vapour molecules condense forming droplets and some other molecules condense on the created droplets, and an outer region at a higher temperature where there is no vapour condensation. Locating Γ is part of the problem. On Γ, $\tilde{c}_* = \tilde{c}_e(\tilde{T}_*)$ (from now onwards, the asterisk will identify magnitudes on the interface), and the normal derivative of $\tilde{c}$ is continuous. Note that the dew point temperature at Γ will be different from the dew point temperature in absence of flow, $\tilde{T}_d$. We have

$$\tilde{T} = \tilde{T}_*,\ \tilde{c}_* = \tilde{c}_e(\tilde{T}_*),\ \mathbf{n}\cdot\tilde{\nabla}\tilde{c}|_{\Gamma-} = \mathbf{n}\cdot\tilde{\nabla}\tilde{c}|_{\Gamma+},\ \tilde{\rho} = 0,\ \tilde{n} = n_* \quad \text{at } \Gamma. \tag{2.13}$$

Assuming that we have calculated the carrier gas velocity field, $\tilde{\mathbf{u}}(\tilde{\mathbf{x}})$, in principle we have enough boundary conditions to determine $\tilde{T}$, $\tilde{c}$, $\tilde{\rho}$, $\tilde{n}$ and Γ.

(i) We solve the elliptic equation (2.10) for $\tilde{T}$ with one condition at infinity and another at the wall.

(ii) For a given location of Γ, the first order equations (2.5) and (2.6) for $\tilde{\rho}$ and $\tilde{n}$ in the condensation region have one boundary condition each at Γ. The elliptic equation (2.7) has Dirichlet boundary conditions (2.11) at infinity and $\tilde{c}_* = \tilde{c}_e(\tilde{T}_*)$ at Γ. Similarly, the solution of (2.7) for $\tilde{c}$ in the condensation region satisfies (2.12) at the wall and $\tilde{c}_* = \tilde{c}_e(\tilde{T}_*)$ at Γ.

(iii) Given an arbitrary location of Γ, the two elliptic problems for $\tilde{c}$ are solved inside and outside the condensation region. Then the location of Γ is changed until the additional condition (2.13) that the normal derivative of $\tilde{c}$ is continuous at Γ is satisfied. This determines the position of the dew point interface.

Note that the vapour density $\tilde{c}_*$ at the interface is smaller than $\tilde{c}_\infty$ because the condensation region is a vapour sink and the diffusion causes a vapour density deficit even in the dry region. Since $\tilde{c}_* = \tilde{c}_e(\tilde{T}_*)$ and $\tilde{c}_\infty = \tilde{c}_e(\tilde{T}_d)$, we have $\tilde{c}_e(\tilde{T}_*) < \tilde{c}_e(\tilde{T}_d)$. As $\tilde{c}_e(\tilde{T})$ is an increasing function, we obtain $\tilde{T}_* < \tilde{T}_d$; due to the flow, the temperature at the interface Γ is lower than the dew point temperature in the absence of flow $\tilde{T}_d$.

2.1.3 Hiemenz planar stagnation-point flow

We consider in this section the Hiemenz stagnation-point flow in the half space $\tilde{x} > 0$ depicted in Figure 1, [95]. There is a solid wall at $\tilde{x} = 0$ and the $\tilde{x}$-velocity of the incoming flow is asymptotic to $-\tilde{x}/\tau$ with a given strain rate τ^{-1}. The boundary layer thickness is $l_b = \sqrt{\nu\tau}$, which we shall adopt as the unit of length. Then the unit of velocity is $\nu/l_b = \sqrt{\nu/\tau}$. We shall adopt $\tilde{c}_\infty$ as the unit of $\tilde{c}$ and of $\tilde{\rho}$, and $\tilde{T}_\infty$ as the unit of temperature. Their values are given in Table 2.1. Since $\tilde{n}$ is dimensionless, we set $n(x) = \tilde{n}(l_b x)$.

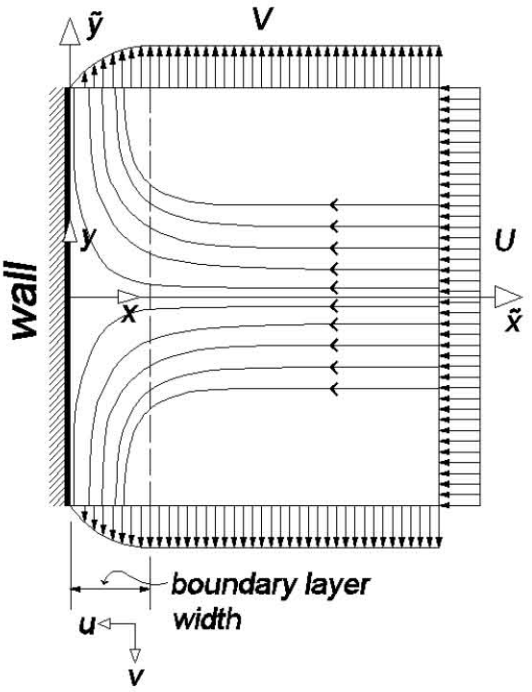

Figure 2.1: Sketch of plane stagnation-point flow.

The dimensionless x component of the velocity is a function of x, denoted by $-u(x)$, $u > 0$, whereas the dimensionless y component of the velocity is $u'(x)y$. (Here and in the rest of the paper, $f'(x)$ means df/dx.) Hence $u(x)$ is the parameter-free solution of the well-known Hiemenz boundary value problem (BVP) of stagnation in plane flow [95]:

$$u''' + u\,u'' + 1 - u'^2 = 0, \quad x > 0, \tag{2.14}$$

$$u(0) = u'(0) = 0\,; \quad u'(+\infty) = 1. \tag{2.15}$$

In nondimensional units, (2.10) becomes

$$T'' + P_r u T' = 0, \quad x > 0, \tag{2.16}$$

$\tilde{T}_\infty$ (K)	$\tilde{T}_d$ (K)	$[c] = [\rho] = \tilde{c}_\infty$ (cm^{-3})	$[n]$ (–)	l_b (mm)	ν/l_b (cm/s)	D (cm^2/s)	$\tilde{v}$ (cm^3)	$\tilde{m}_v$ (g)	$\tilde{\sigma}$ ($\mathrm{J/m}^2$)
1713	1400	1.9×10^{13}	1	6.26	0.24	0.083	8.87×10^{-23}	2.358×10^{-22}	0.05

Table 2.1: Typical parameters for homogeneous condensation of Na_2SO_4 in air, [15]

	α	$\frac{\epsilon}{\Lambda}$	P_r	S_c	ϵ	B
I	0.1	0.0515	0.7	1.8	0.0644	1.09×10^4
II	0.1	0.0515	0.7	1.8	0.0644	1.63×10^5

Table 2.2: Dimensionless parameters for I: $l_b = 6.26\ mm$, II: $l_b = 24.2\ mm$. Dimensionless wall temperatures are 0.467 (800 K), 0.5838 (1000 K) and 0.7006 (1200 K)

to be solved with the boundary conditions

$$T(0) = T_w = \tilde{T}_w/\tilde{T}_\infty\,; \quad T(+\infty) = 1, \tag{2.17}$$

where $P_r = \nu/\kappa$ is the Prandtl number (which is 0.7 for air). Equations (2.5) - (2.9) with the boundary conditions (2.11)-(2.13) become

$$U\rho' + \alpha\left(\frac{T'}{T}\right)'\rho = -\frac{Bc^2}{S_c\sqrt{6\pi\epsilon}}\exp\left(-\frac{1}{2\eta^2T^3\epsilon^3}\right)H(c-c_e), \quad x>0, \tag{2.18}$$

$$\rho(+\infty) = 0, \tag{2.19}$$

$$U = u + \alpha\frac{T'}{T}, \tag{2.20}$$

$$c_e(x) = \frac{T_d}{T(x)}\exp\left[\frac{\Lambda}{\epsilon}\left(\frac{1}{T_d} - \frac{1}{T(x)}\right)\right], \tag{2.21}$$

$$Un' = -\frac{B}{S_c}(c-c_e)T^{1/2}n^{2/3}H(n-n_*)\,H(c-c_e), \quad x>0, \tag{2.22}$$

$$n(+\infty) = 0, \tag{2.23}$$

$$n_* = \left(\frac{1}{\epsilon\eta T}\right)^3, \tag{2.24}$$

$$c'' + S_c u\,c' = B\left[\frac{\epsilon^{-7/2}c^2}{\sqrt{6\pi}\eta^3T^3}e^{-\frac{1}{2\eta^2T^3\epsilon^3}} + (c-c_e)\rho T^{1/2}n^{2/3}H(n-n_*)\right]H(c-c_e), \tag{2.25}$$

$$c(0) = c_e(0), \quad c(+\infty) = 1, \tag{2.26}$$

where

$$S_c = \frac{\nu}{D},\ \epsilon = \frac{k_B\tilde{T}_\infty}{2\tilde{\sigma}(\frac{4\pi}{3}\tilde{v}^2)^{1/3}},\ \frac{\Lambda}{\epsilon} = \frac{\tilde{\Lambda}}{k_B\tilde{T}_\infty}, \quad B = \frac{(3\tilde{v})^{2/3}\tilde{c}_\infty l_b^2}{D}\left(\frac{2}{\pi}\right)^{1/6}\sqrt{\frac{k_B\tilde{T}_\infty}{\tilde{m}_v}}. \tag{2.27}$$

Representative values for the dimensionless parameters of the problem are indicated in table 2.2 for Na_2SO_4 vapours in air as in [15]. $S_c = \nu/D$ is the Schmidt number, $\epsilon/\Lambda \ll 1$ measures how fast $c_e(x)$ decays as $x < x_*$ moves away from the dew point location x_*. In fact, from (2.21) we find

$$\frac{c_e(x)}{c_*} = \frac{T_*}{T(x)}\exp\left(\Lambda\frac{T(x)-T_*}{\epsilon T_*T(x)}\right) \approx \exp\left(-\frac{x_*-x}{\delta_e}\right),$$

and

$$\delta_e = \frac{\epsilon T_*^2}{\Lambda T_*'} \tag{2.28}$$

is the dimensionless decay length of $c_e(x)$ [79]. The inverse dimensionless surface tension $1/\sigma_\infty = \epsilon$ is small and therefore the Zeldovich flux in the RHS of (2.18) has a sharp maximum and it decays very rapidly to zero elsewhere. The maximum of the Zeldovich flux satisfies

$$\frac{c'}{c} = \frac{\frac{c_e'}{c_e} - \frac{3\eta T'}{2T}}{1 + 2\epsilon^3\eta^3 T^3} = \frac{1}{1 + 2\epsilon^3 T^3 \left(\ln \frac{c}{c_e}\right)^3} \left(\frac{\Lambda}{2\epsilon T} - 1 - \frac{3}{2}\ln\frac{c}{c_e}\right)\frac{T'}{T}, \tag{2.29}$$

in which we have used (2.21). This is quite close to the maximum of the supersaturation $\eta = \ln(c/c_e)$ whose location satisfies

$$\frac{c'}{c} = \frac{c_e'}{c_e} = \left(\frac{\Lambda}{2\epsilon T} - 1\right)\frac{T'}{T}. \tag{2.30}$$

Since $\epsilon \ll 1$, both these maxima should be close to the inflection point of c in which c' reaches a maximum. This can be appreciated in Figure 2 that shows c', η and J_Z (the Zeldovich flux in the RHS of (2.18)) normalized to their respective maxima taken from the solution of (2.14)-(2.26) for a wall temperature of 1000 K. Let $x_M < x_*$ be the common value of these maxima as $\epsilon \to 0$. Nucleation occurs only in a narrow interval about x_M inside the condensation region $0 < x < x_*$.

The parameter B is very large which, combined with the shape of the Zeldovich flux, means that the RHS of (2.18) behaves as a delta function source term whose role is to create rapidly a basal condensate number density near x_M. Let ρ_b and n_b be reference values for the basal droplet number density and basal number of condensed vapour molecules, respectively (so that $\rho_b n_b$ is the basal condensate number density). Compared to vapour condensation on droplets, little vapour is lost due to nucleation and therefore we can ignore the corresponding term in (2.25). As $B \gg 1$, $c \approx c_e$ except in a narrow condensation layer (that nevertheless includes the even narrower droplet nucleation region) whose length is obtained by balancing c'' and the RHS of (2.25). This yields a length

$$\delta = \frac{1}{\sqrt{B\rho_b n_b^{2/3}}} \tag{2.31}$$

that measures the width of the condensation layer in which there is supersaturation and therefore the vapour condenses on the droplets created about x_M. B plays an similar role to the scavenging parameter R in the case of heterogeneous condensation [79].

The boundary conditions (2.19) and (2.23) can be replaced by the following conditions at the location x_* of the dew point interface Γ,

$$\rho(x_*) = 0, \quad n(x_*) = 0. \tag{2.32}$$

Moreover at x_* we have

$$c(x_*) = c_e(x_*), \quad c'(x_*-) = c'(x_*+). \tag{2.33}$$

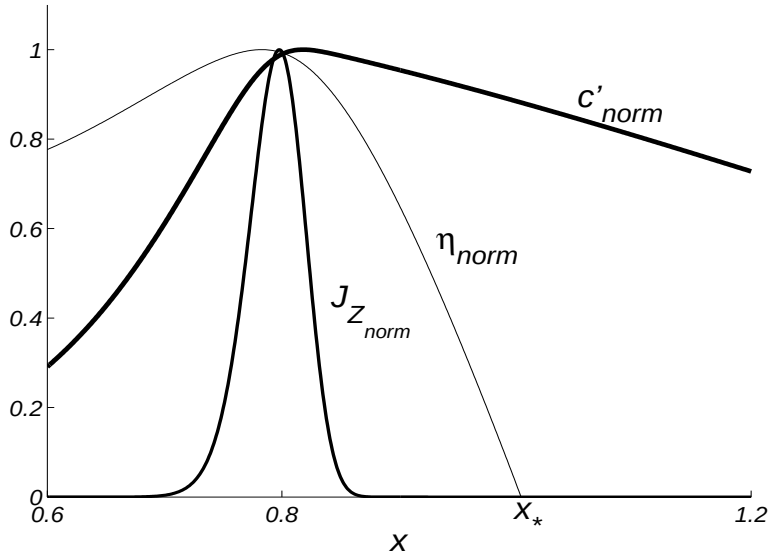

Figure 2.2: c', η and J_Z for $T_w = 1000K$. The three curves have been normalized so that their maxima always equal 1.

2.1.4 lower and upper bounds for c and x_* and deposition rates

Inside the condensation region $0 < x < x_*$ we have positive supersaturation and $c(x) > c_e(x)$ as shown in Fig. 2.3. The maximum possible value of x_* would be reached if $c(x)$ and $c_e(x)$ are tangent at x_*. In such a case, the width of the condensation layer with positive supersaturation is zero and the vapour density profile $c(x)$ reaches its lowest possible value. This profile is the solution of the BVP

$$c'' + S_c\, u\, c' = 0, \quad x > 0, \tag{2.34}$$

$$c(x_*) = c_e(x_*), \quad c'(x_*-) = c'(x_*+), \quad c(\infty) = 1. \tag{2.35}$$

The solution of the BVP (2.34)-(2.35) for $x > x_*$ and

$$c(x) = c_e(x), \quad x \le x_*, \tag{2.36}$$

is the 0-CL theory first proposed and studied by [16] for heterogeneous vapour condensation on solid particles. The solution of (2.34)-(2.35) can be written as [79]

$$c(x) = 1 + \frac{c_* - 1}{\Psi(x_*)}\,\Psi(x), \quad \text{where } \Psi \text{ solves:} \tag{2.37}$$

$$\Psi'' + S_c\, u\, \Psi' = 0, \quad \Psi(0) = 1, \quad \Psi(\infty) = 0. \tag{2.38}$$

To find x_*, we have to pick a trial value x_T, solve the BVP (2.38) and check whether the following relation, derived from the Clausius-Clapeyron relation (2.21), holds for x_T:

$$c_e'(x) = \left[1 - \frac{\epsilon T(x)}{\Lambda}\right] \frac{\Lambda T'(x)}{\epsilon T(x)^2}\, c_e(x). \tag{2.39}$$

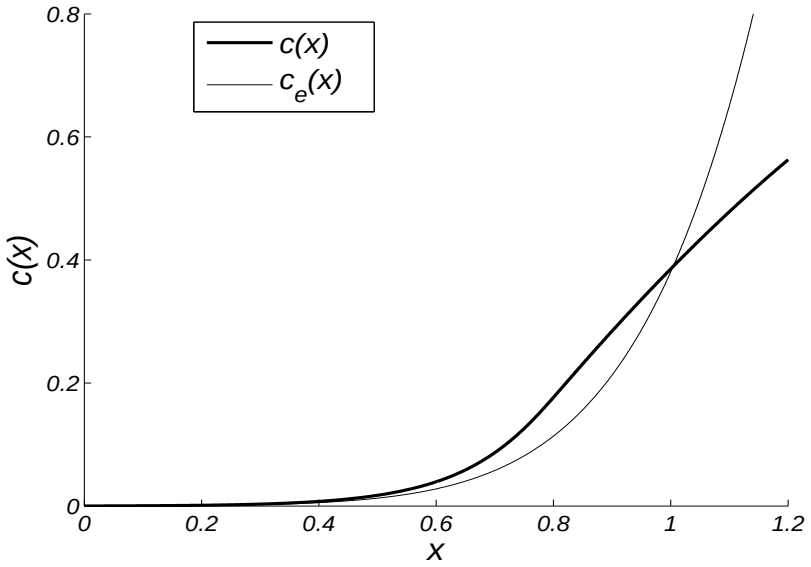

Figure 2.3: $c(x)$ (thick line) and $c_e(x)$ for $T_w = 1000K$.

If (2.39) does not hold for x_T, we change this point until it does. The resulting value is the sought x_*. The vapour number density and dew point location found by solving the BVP (2.34)-(2.35) will be denoted by $c_0(x)$ and x_{0*}, respectively.

An upper bound for the profile $c(x)$ is found by solving (2.34) with the lowest possible dew point location, $x_* = 0$. Fig. 2.4 compares this upper bound $c_s(x)$ to $c_0(x)$ and $c_e(x)$.

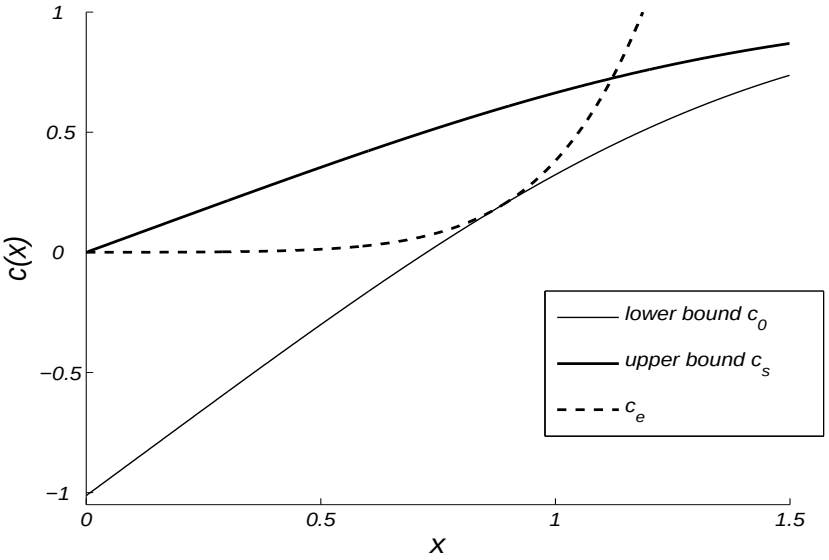

Figure 2.4: Upper and lower bounds for the vapour number density at $\tilde{T}_w = 1000$ K.

2.1.4.1 Deposition at the wall

Vapour directly condenses on the wall by diffusion and droplets of the condensate arrive there thermophoretically. The fluxes of vapour and condensate at the wall are

$$\tilde{J}_v = -D\tilde{c}'(0) = -\frac{D\tilde{c}_\infty}{l_b}c'(0), \tag{2.40}$$

$$\tilde{J}_c = -\tilde{\rho}(0)\tilde{U}(0)\tilde{n}(0) = -\frac{\alpha\nu\tilde{c}_\infty}{l_b}\frac{T'(0)\rho(0)n(0)}{T(0)}, \tag{2.41}$$

respectively, because $\tilde{u}(0) = 0$ and the thermophoretical velocity becomes $\tilde{U} = \alpha\nu\left(\frac{\tilde{T}'}{\tilde{T}}\right)'$ at the wall. Choosing $\nu\tilde{c}_\infty/l_b$ (4.56×10^{12} cm^{-3} for the parameter values in table 2.1) as the unit of flux, the non-dimensional fluxes are

$$J_v = \frac{c'(0)}{S_c}, \tag{2.42}$$

$$J_c = \alpha\frac{T'(0)\rho(0)n(0)}{T(0)}, \tag{2.43}$$

where we have omitted the minus sign. The total flux of condensate at the wall is

$$J = J_v + J_c = \frac{c'(0)}{S_c} + \rho(0)n(0)U(0). \tag{2.44}$$

2.1.4.2 Temperature profile

The temperature profile is a solution of (2.16) and (2.17) given by [79]

$$T(x) = 1 + (T_w - 1)\Phi(x), \quad \text{where } \Phi \text{ solves} \tag{2.45}$$

$$\Phi'' + P_r\, u\, \Phi' = 0, \quad \Phi(0) = 1, \quad \Phi(+\infty) = 0. \tag{2.46}$$

2.1.4.3 Maximum wall temperature at which there is a CL

As T_w increases x_* decreases until $x_* = 0$. This marks the absence of a CL of finite width. At the corresponding wall temperature $T_{w,M}$, which is independent of the model we use to describe vapour condensation on droplets, $J_c = 0$. At $T_{w,M}$, $\Phi_* = \Psi_* = 1$ and $T_{w,M}$ solves [79]

$$\frac{\Phi'(0)}{\Psi'(0)} = \frac{\epsilon T_{w,M}^2}{(1 - T_{w,M})(\Lambda - \epsilon T_{w,M})}\left\{\frac{T_{w,M}}{T_d}\exp\left[\frac{\Lambda}{\epsilon}\left(\frac{1}{T_{w,M}} - \frac{1}{T_d}\right)\right] - 1\right\}. \tag{2.47}$$

For $T_d = 0.817$ (1400 K) and $\epsilon/\Lambda = 0.0515$ (as in table 2.2), we obtain $T_{w,M} = 0.755$ (1293 K). For $T_{w,M} \le T_w < T_d$ there is no CL, $x_* = 0$, and we have $J_c = 0$. Making use of (2.37) and (2.38) with $\Psi_* = \Psi(0) = 1$, we get the following formula for the deposition at the wall

$$J = J_v = \frac{[1 - c_e(T_w)]\,\Psi'(0)}{S_c}. \tag{2.48}$$

2.1.5 numerical results

The BVP (2.16)-(2.26) is ill-conditioned. To solve it and obtain the c, n and ρ profiles, we first find the location of the dew surface, x_*, using the shooting method. In the condensation region, $0 \leq x \leq x_*$, the BVP is solved by finite differences using a relaxation method with a quite small time step. We have solved the BVP for wall temperatures $\tilde{T}_w$ ranging from 800 K to 1200 K. For lower $\tilde{T}_w$, compressibility effects of the carrier gas not contemplated in our thermophysical model are important [31]. For higher $\tilde{T}_w$, the condensation layer disappears.

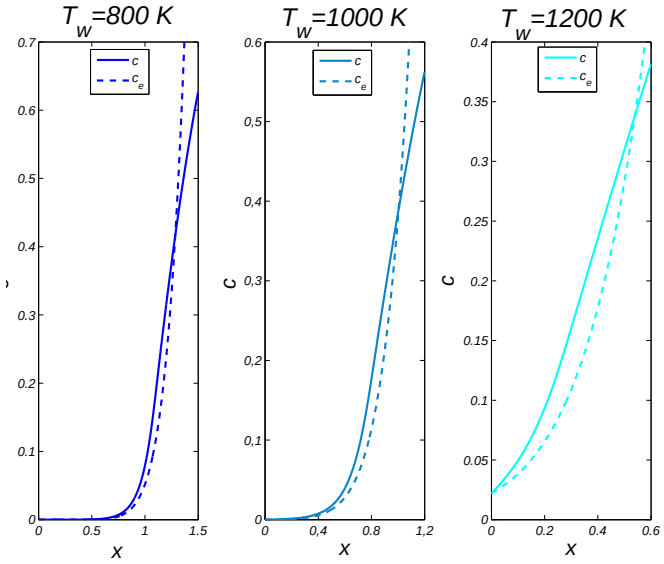

Figure 2.5: Profiles of the vapour number density $c(x)$ at three wall temperatures: $\tilde{T}_w =$ 800, 1000, 1200 K. The intersection between $c(x)$ (solid line) and the Clausius-Clapeyron equilibrium curve marks the location of the dew surface.

The profiles of the vapour and droplet number density profiles are depicted in Figures 5 and 6, respectively. Fig. 7 depicts the number of condensate molecules $n(x)$. Fig. 5 shows that the location of the dew surface approaches the wall as the wall temperature increases, as expected. Fig. 6 shows that the droplet density increases as the wall temperature decreases and that an appreciable number of droplets appears for $x < x_*$. Although there are less droplets at higher wall temperature, Fig. 7 shows that they are larger, as the number of condensate molecules carried by them increases with T_w.

Figure 8 depicts the consumption of vapour in (2.25) due to condensation on previously nucleated droplets. This is much more important than vapour consumption due to homogeneous nucleation of droplets. We observe how vapour scavenging by droplets changes with the wall temperature. For low T_w, nucleation is very active and the droplet density is very large but the droplet size is small. Nevertheless the net consumption of molecules to form and enlarge droplets is higher than that for larger T_w. Fig. 9 depicts the profile of the condensation number density. Deposition at the wall is almost constant

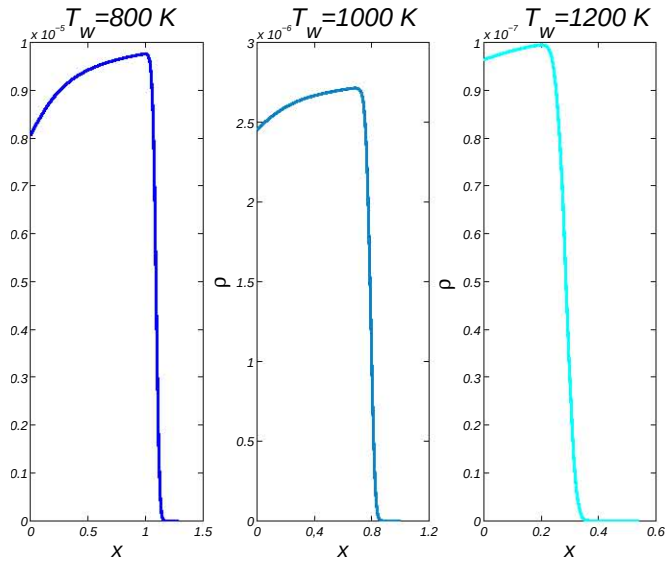

Figure 2.6: Profiles of the droplet number density $\rho(x)$ at three wall temperatures: $\tilde{T}_w =$ 800, 1000, 1200 K.

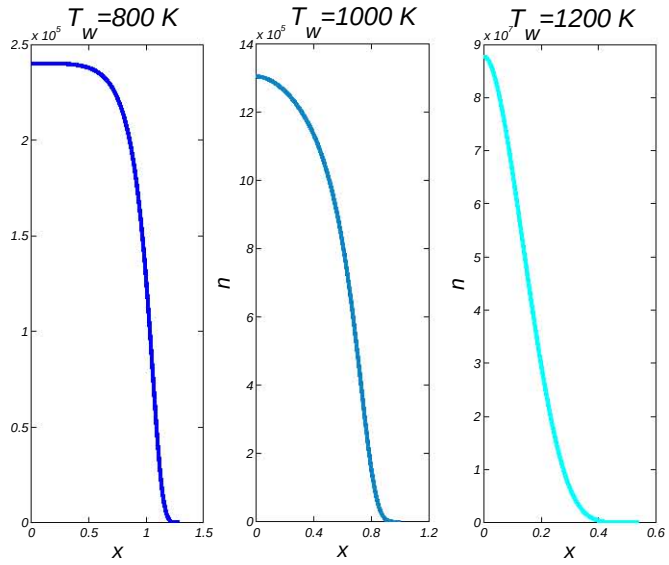

Figure 2.7: Profiles of the condensate number $n(x)$ at three wall temperatures: $\tilde{T}_w =$ 800, 1000, 1200 K.

for low wall temperature and, for each T_w, $\rho n = 1$ occurs at a point very close to the inflection point of all the curves. In turn, this point is very close to x_M where the Zeldovich flux is maximum. Droplets are created at a narrow region centered at x_M. According to (2.29), x_M depends strongly on the vapour density profile which, in turn, depends on the droplet density. The latter varies abruptly about x_M.

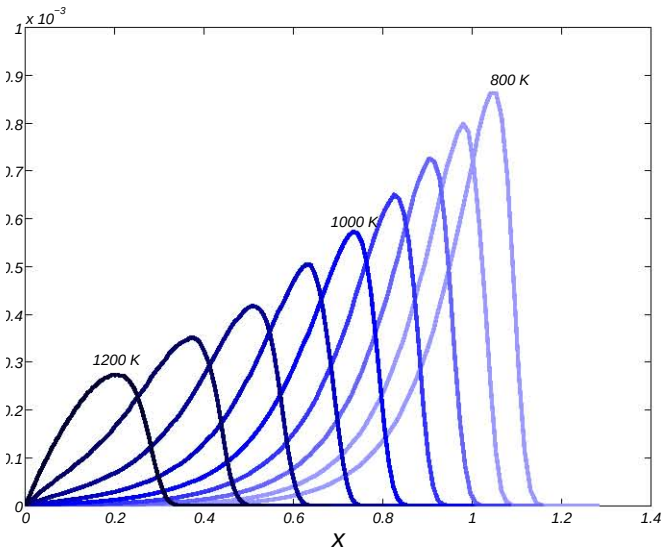

Figure 2.8: The function $(c - c_e)\rho n^{2/3}$ vs x for wall temperatures: $\tilde{T}_w = 800 + 50j$ K, with $j = 0, 1 \ldots 8$.

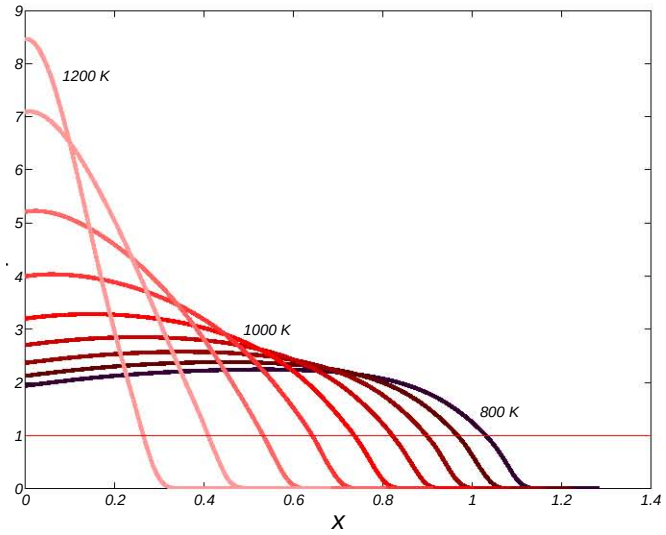

Figure 2.9: Condensate number density ρn vs x for wall temperatures: $\tilde{T}_w = 800 + 50j$ K, with $j = 0, 1 \ldots 8$.

Figure 10 depicts the deposition rates (2.42), (2.43) and (2.44) for different T_w. We observe that the deposition rate J_v due to direct condensation of vapour on the wall increases with T_w whereas the deposition rate J_c due to vapour condensation on droplets reaches a minimum at $T_w = 0.55$. In contrast with heterogeneous condensation (see figure 7 of [79]), the deposition rate shown in figure 10 is almost constant, except at high T_w close

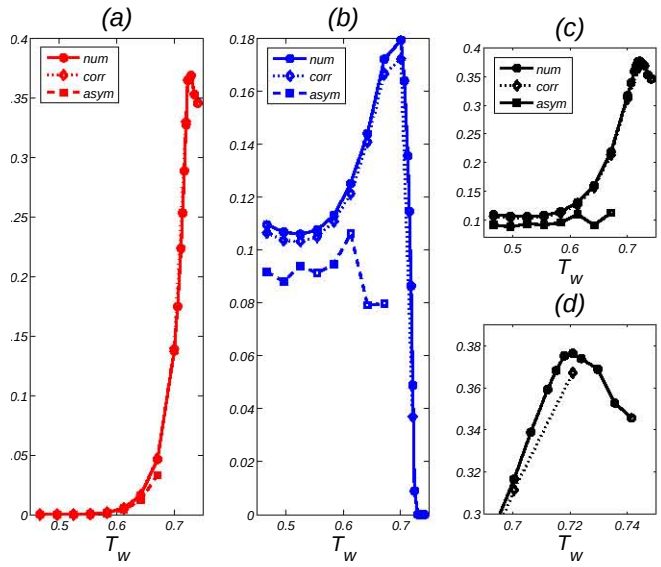

Figure 2.10: Deposition rates (a) J_v, (b) J_c and (c) $J = J_c + J_v$ versus wall temperature. (d) shows the total deposition rate J for an interval of T_w about the value at which J has a maximum. The deposition rates obtained by a direct numerical solution of the complete model is compared to approximations found by matched asymptotic expansions (marked as 'asymp') and by the corrected asymptotic theory of section 6 (marked as 'corr').

to that at which the condensation layer disappears. For low T_w, the nucleation process is very active and the droplet density is very large but the droplet size is small. The net consumption of vapour molecules to form and enlarge droplets is higher for low T_w. At higher wall temperatures, there are fewer nucleated droplets but their size is higher. In the case of heterogeneous condensation, the number of suspended solid particles that act as condensation sites is constant and they scavenge more vapour as T_w increases. Then the corresponding deposition rate increases with T_w except when the latter is very close to the temperature at which the vapour condenses only on the wall and no longer on the particles.

2.1.6 a singular perturbation approach

As explained in Section 2.1.3, droplets are created only in a very narrow nucleation region centered about x_M (where the Zeldovich flux is maximum) although the condensation region is wide, comprising the interval from the wall to the nucleation region. Let δ_M be the width of the nucleation region. For x on the interval $x_M + \delta_M/2 < x < x_*$ ending in the dew point x_*, the vapour could condense on droplets but there are none. For $0 < x < x_M - \delta_M/2$, the vapour condenses on the existing droplets but no new droplets are formed. Even when we ignore the contribution of droplet nucleation in the RHS of (2.25), locating x_M strongly depends on the vapour density profile which, in turn, is strongly affected by the droplet density. Thus the problem of finding an approximate

theory of homogeneous condensation is much more complex than that of heterogeneous condensation in which the droplet number density equals the number density of solid particles. For heterogeneous condensation, approximating the temperature and velocity fields by constant values throughout the *narrow* CL gave very good results. In the present case, (2.30) for the maximum of the supersaturation already shows that the variation of the temperature profile has to be taken into account.

In this section, we propose an asymptotic theory based upon a trial vapour density which interpolates between the upper and lower profiles $c_0(x)$ and $c_s(x)$ of Section 2.1.4.

2.1.6.1 Droplet density profile for a given $c(x)$

Let us rewrite the BVPs posed by equations (2.18)-(2.19), (2.22)-(2.23) and (2.25)-(2.26) respectively, as:

$$\rho' + \alpha\left(\frac{T'}{T}\right)'\frac{\rho}{U} = -\frac{Bc^2}{S_c U\sqrt{2\pi\epsilon}}\exp\left(-\frac{1}{2\epsilon^3\eta^2 T^3}\right), \tag{2.49}$$

$$C'' + S_c\, u\, C' + c_e'' + S_c\, u\, c_e' = B\, C\rho T^{1/2} n^{2/3}, \tag{2.50}$$

$$n' = -\frac{B}{S_c}\frac{C\,T^{1/2}n^{2/3}}{U}, \tag{2.51}$$

where we have ignored the loss of vapour used to form droplets in (2.25) because it is very small compared to the other term. According to (2.32), $\rho = n = 0$ at $x = x_*$ far from the nucleation layer. The vapour number density satisfies $c(+\infty) = 1$, $c(0) = c_e(0)$ and (2.33) at $x = x_*$.

Provided c is known, we can solve (2.49) by the method of matched asymptotic expansions. Let $x_M < x_*$ be the location of the global maximum of the RHS in (2.49). The latter is zero except in a narrow layer about x_M so that we can replace (2.49) by

$$\rho_{\rm in}' \sim -\frac{B\,c_M^2}{S_c U_M\sqrt{2\pi\epsilon}}\exp\left(-\frac{1}{2\epsilon^3\eta_M^2 T_M^3}\right)\exp\left(-\frac{|\beta_M|}{2\epsilon^3\eta_M^3 T_M^3}(x-x_M)^2\right), \tag{2.52}$$

$$\beta = \frac{\partial}{\partial x}\left[\frac{c'}{c} - \frac{c_e'}{c_e} + \frac{3\eta T'}{2T} + \epsilon^3\eta^3 T^3\left(\frac{2c'}{c} - \frac{U'}{U}\right)\right], \tag{2.53}$$

in the immediate neighborhood of x_M. Here $\rho_{\rm in}$ is the inner approximation to $\rho(x)$ and the subscripts M indicate that the corresponding functions are calculated at x_M. The solution of (2.52) that equals ρ_M at $x = x_M$ and tends to zero as $(x - x_M) \to +\infty$ is

$$\rho_{\rm in}(x) \sim \rho_M\,\mathrm{erfc}\left(\left|\frac{\beta_M}{2\epsilon^3\eta_M^3 T_M^3}\right|^{1/2}(x - x_M)\right), \tag{2.54}$$

$$\rho_M = \frac{\epsilon B\, T_M^{3/2}\eta_M^{3/2}c_M^2}{2S_c U_M|\beta_M|^{1/2}}\exp\left(-\frac{1}{2\epsilon^3\eta_M^2 T_M^3}\right). \tag{2.55}$$

The outer approximation to $\rho(x)$ obeys (2.49) with zero RHS

$$\rho'_{\rm out} + \alpha\left(\frac{T'}{T}\right)'\frac{\rho_{\rm out}}{U} = 0. \tag{2.56}$$

and the composite solution that approximates $\rho(x)$ uniformly in x is

$$\begin{aligned}\rho(x) &= 2\rho_M\left\{\exp\left[\alpha\int_x^{x_M}\left(\frac{T'}{T}\right)'\frac{{\rm d}x}{U}\right]-1\right\}H(x_M-x)\\ &+ \rho_M\,{\rm erfc}\left(\left|\frac{\beta_M}{2\epsilon^3\eta_M^3T_M^3}\right|^{1/2}(x-x_M)\right).\end{aligned} \tag{2.57}$$

2.1.6.2 Trial vapour number density $\gamma(x)$

In section 2.1.4 we found that the vapour number density lies between two limit curves $c_0(x)$ and $c_s(x)$given by solving equation (2.34) with boundary conditions (2.35) and with $c(0) = c_e(0)$, $c(+\infty) = 1$, respectively. Our trial vapour number density is

$$\gamma_j(x) = c_0 + (c_s - c_0)\frac{j}{N_1}, \quad j = 0,\, 1, \ldots N, \tag{2.58}$$

where N is an integer number. Out of these trial functions, we want to extract the best $\gamma_j(x)$ proceeding as follows. Firstly, we calculate the location of the maximum of the Zeldovich flux from the RHS of (2.49) with $c(x) = \gamma_j(x)$. This yields points x_{Mj}, $j = 0, 1, \ldots N$. Similarly, we can calculate the dew point locations x_{*j} where $\gamma_j(x) = c_e(x)$. We now solve (2.51) for $C(x) = \gamma_j(x) - c_e(x)$ with the boundary condition $n(x_{*j}) = 0$:

$$n_j(x) = \left(\frac{B}{3S_c}\int_x^{x_{*j}}\frac{\gamma_j - c_e}{U}T^{1/2}dx\right)^3. \tag{2.59}$$

The maximum value of n_j is reached at the wall, $n_j(0)$. Let $\rho_j(x)$ and $2\rho_{Mj}$ be the droplet density (2.57) and its maximum value (2.55) calculated using the trial vapour density $\gamma_j(x)$. We choose as the optimum value of j the one that makes the product $2\rho_{Mj}n_j(0)$ (maximum condensate number density) closest to $c_\infty = 1$ (maximum vapour density). We shall denote by J this optimum value of j. Figure 2.11 compares $\rho_J(x)$ to the droplet density obtained by numerically solving the whole problem for three different wall temperatures. We see that the agreement is fairly good and it improves as the wall temperature decreases. At higher temperatures, the method that we use to calculate $\rho_J(x)$ breaks down (e.g., at 1200 K).

2.1.6.3 Approximation for $n(x)$ and $c(x)$ in the condensation region

The optimal $\gamma_J(x)$ and $n_J(x)$ are reasonable approximations in the dry region $x > x_{MJ}$ but we need to improve them in the nucleation-condensation region $0 < x < x_{MJ}$. We

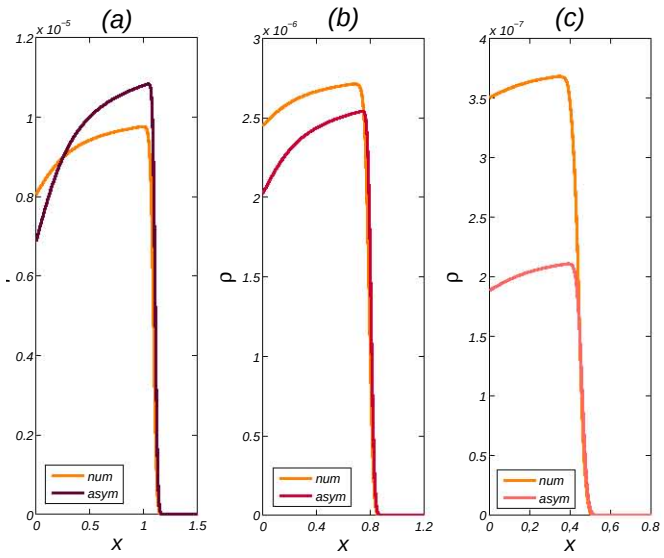

Figure 2.11: Numerically obtained and approximate droplet density profiles, $\rho(x)$ (marked as *num*) and $\rho_J(x)$ (marked as *asym*) at wall temperatures of (a) 800 K, (b) 1000 K, (c) 1150 K.

solve (2.50)-(2.51) using the composite droplet density $\rho_J(x)$ and the approximate location x_{MJ}. The boundary conditions at x_{MJ} will be given by the values of $\gamma_J(x)$ and $n_J(x)$ there to which $c(0) = c_e(0)$ is to be added. From (2.51), we obtain

$$C = -\frac{3S_c}{B}\frac{U}{T^{1/2}}Y', \quad Y = n^{1/3}. \tag{2.60}$$

Inserting this in (2.50), we get the third order equation:

$$Y''' + \left(\frac{2U'}{U} - \frac{T'}{T} + S_c u\right)Y'' + \left[\frac{\sqrt{T}}{U}\left(\frac{U}{T^{1/2}}\right)'' + S_c\left(\frac{uU'}{U} - \frac{uT'}{2T}\right) - B\rho_J\sqrt{T}Y^2\right]Y'$$
$$= \frac{B\sqrt{T}}{3S_cU}\left(c_e'' + S_c u c_e'\right), \tag{2.61}$$

to be solved with the boundary conditions

$$Y'(0) = 0, \quad Y'(x_{MJ}) = -\left.\frac{B}{3S_c}\frac{T^{1/2}}{U}(\gamma_J - c_e)\right|_{x_{MJ}}, \; Y(x_{MJ}) = [n_J(x_{MJ})]^{1/3}. \tag{2.62}$$

There is a narrow boundary layer near x_{MJ} in which Y satisfies the boundary conditions (2.62) and increases rapidly to some constant value. Rescaling x as $X = (x - x_{MJ})/\mu_x$ and assuming that $c_e'' = O(1)$, we find the scales of x, C and n from (2.50) and (2.51):

$$\mu_x = B^{-3/8}\rho_{MJ}^{-1/8}\delta_e^{1/4}, \quad \mu_C = B^{-3/4}\rho_{MJ}^{-1/4}\delta_e^{-1/2}, \quad \mu_n = B^{-3/8}\rho_{MJ}^{-9/8}\delta_e^{-3/4}. \tag{2.63}$$

For typical values of $B \approx 10^4$, $\rho_{MJ} \approx 10^{-6}$, $\delta_e \approx 0.16$, we get $\mu_x \approx 0.112$, $\mu_C \approx 0.08$, $\mu_n^{1/3} \approx 55.28$. Thus we may assume $\mu_C \ll \mu_x \ll 1 \ll \mu_n$ and $\mu_x = O(\delta_e)$. We now rescale $\rho = \rho_{MJ} r \approx \rho_{MJ} H(-X)$ (assuming a negligible width of the Zeldovich peak, $|2\epsilon^3 \eta_{MJ}^2 T_{MJ}^3/\beta_{MJ}|^{1/2} \ll \mu_x$), $Y = \mu_n^{1/3} y$, $X = (x - x_{MJ})/\mu_x$ and keep leading order terms in (2.61). The resulting equation and rescaled boundary conditions (2.62) are

$$\frac{\partial^3 y}{\partial X^3} - 2T_{MJ}^{1/2} y^2 \frac{\partial y}{\partial X} = \frac{\sqrt{T_{MJ}}}{3 S_c U_{MJ}} \delta_e (c_e'' + S_c u_{MJ} c_e'), \quad X < 0, \tag{2.64}$$

$$y(0) = B^{1/8} \rho_{MJ}^{3/8} \delta_e^{1/4} [n_J(x_{MJ})]^{1/3}, \quad \frac{\partial y}{\partial X}(0) = -\frac{\sqrt{T_{MJ}}}{3 S_c U_{MJ}} \frac{\gamma_J(x_{MJ}) - c_e(x_{MJ})}{\mu_C},$$

$$\frac{\partial y}{\partial X}\left(-\frac{x_{MJ}}{\mu_x}\right) = 0. \tag{2.65}$$

The BVP (2.64)-(2.65) has a unique solution that produces $y(-x_{MJ}/\mu_x) = y_w$, from which $n_w = B^{-3/8} \rho_{MJ}^{-9/8} \delta_e^{-3/4} y_w^3$ is an unscaled number of condensate molecules at the wall, $X_w = -x_{MJ}/\mu_x$ ($x_{MJ} \gg \mu_x$).

The boundary layer solution fixes ρ_J as the inner solution (2.54), thereby underestimating $n = Y^3$. y has an inflection point at $X = X_n$ and $\partial^2 y/\partial X^2$ and $\partial^3 y/\partial X^3$ become small for $X < X_n$. To correct this approximation to the solution of (2.61)-(2.62), we add to it a solution of the outer problem:

$$n' = -\frac{c_e'' + S_c u c_e'}{S_c \rho_J U}, \quad 0 < x < x_n \equiv x_{MJ} - \mu_x X_n, \tag{2.66}$$

$$n(x_n) = 0. \tag{2.67}$$

Eq. (2.66) follows from (2.61) if we ignore in the LHS of the former equation all terms except the last one and use $n = Y^3$ in the result. Thus the number of condensate molecules for $x < x_{MJ}$ is $n \approx n_0(x)$,

$$n_0 = \frac{H(x_n - x)}{S_c} \int_x^{x_n} \frac{c_e'' + S_c u c_e'}{\rho_J U}\, dx + \mu_n \left[y\left(\frac{x - x_{MJ}}{\mu_x} \right) \right]^3, \tag{2.68}$$

where the second term is the inner solution. The corresponding $C = c - c_e$, which we shall call $C_0(x)$, is given by (2.60) but it does not satisfy $C(0) = 0$. The correction is given by a boundary layer problem in which only C'' and the RHS of (2.50) are kept. Its solution is:

$$C_{0,B.L.}(x) = C_0(0) \left[1 - \exp\left(-x \sqrt{B\rho(0) T_w^{1/2} [n_0(0)]^{2/3}} \right) \right], \tag{2.69}$$

and the corresponding composite approximation becomes

$$C_{\text{unif}}(x) = C_0(x) - C_0(0) \exp\left(-x \sqrt{B\rho(0) T_w^{1/2} [n_0(0)]^{2/3}} \right). \tag{2.70}$$

The vapour density profile is compared to the asymptotic solution in Fig. 12. As in the case of the droplet density profile (Fig. 11), the asymptotic theory approximates better the vapour number density than the number of condensate molecules shown in Fig. 13.

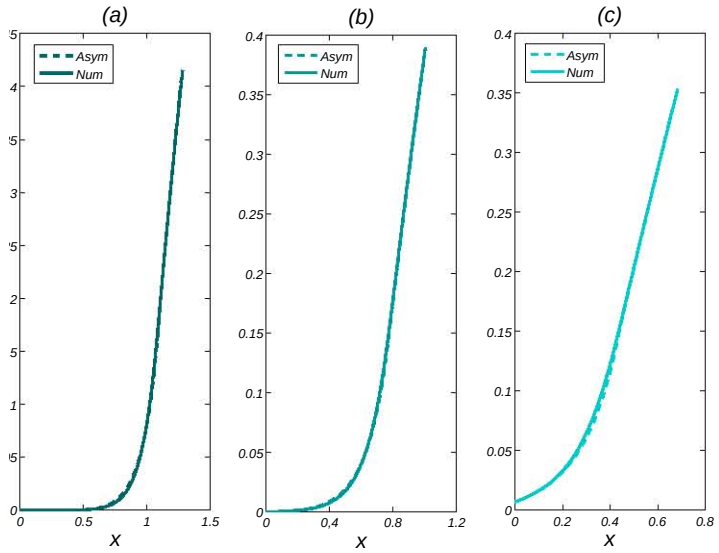

Figure 2.12: Numerically and asymptotically obtained vapour density profiles at wall temperatures of (a) 800 K, (b) 1000 K, (c) 1150 K.

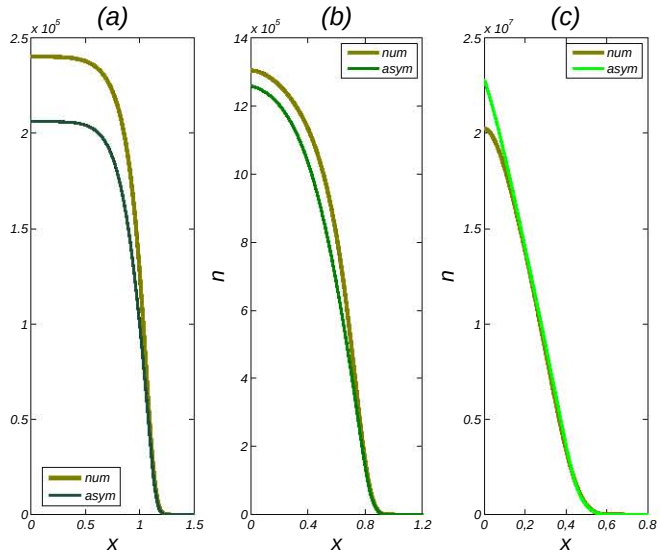

Figure 2.13: Numerically obtained and approximate number of condensate molecules, $n(x)$ at wall temperatures of (a) 800 K, (b) 1000 K, (c) 1150 K.

2.1.6.4 Corrected profiles for higher wall temperatures

The asymptotic theory described above is an acceptable approximation except when $\tilde{T}_w$ becomes larger and the width of the boundary layer decreases. Two shortcomings of the asymptotic theory come to the fore. Firstly, the calculation of the maximum Zeldovich

flux breaks down and we cannot find the optimal vapour profile $\gamma_J(x)$. Secondly, we cannot neglect $\partial^2 y/\partial X^2$ and $\partial y/\partial X$ in (2.61) when $\tilde{T}_w \geq 1000$ K. For $\tilde{T}_w$ close to 1200 K there is no boundary layer solution for n and C, although there is still one for ρ. As a result, the values of ρ and n at the wall differ appreciably from those given by the numerical solution of the thermophysical model.

We have developed a corrected asymptotic theory by improving the optimal trial vapour density and solving the complete third-order equation (2.61). We need to take into account that the maxima for c', η and J_z are not coincident, cf. Fig. 2. In the corrected theory, we obtain x_M graphically by solving the functional equation $\rho_{M1}(j,k) - \rho_{M2}(j,k) = 0$, whose terms are depicted in Fig. 14. $\rho_{M1}(j,k)$ is the maximum value of the droplet density profile found from Eq. (2.49) with ρ, $x_{Mk} = x_{*0}k/N$, $k = 0, 1, ..., N$, and x_{*0} given by the 0-CL Theory. $\rho_{M2}(j,k)$ is the maximum value of the droplet density profile given by the composite solution (2.57) with $x_M = x_{Mk}$ and $c(x) = \gamma_j(x)$.

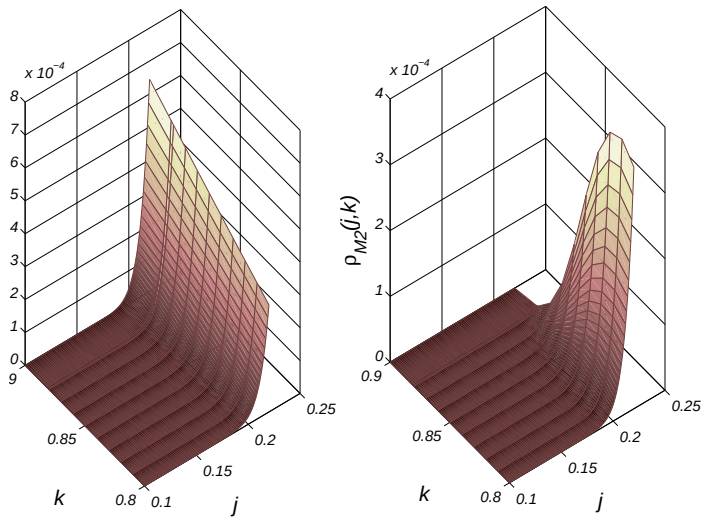

Figure 2.14: Functions $\rho_{M1}(j,k)$ and $\rho_{M2}(j,k)$ for $T_w = 1000\ K$. $\rho_{MK}(j)$ is the intersection curve of both surfaces.

Figure 15 compares the location of the point at which the Zeldovich droplet nucleation rate is maximum as given by the asymptotic theory of previous subsections, by the corrected theory and by numerical solution of the complete model equations. The earlier asymptotic theory performs poorly for higher T_w (and it gives no solution for $T_w > 0.7$) whereas the corrected theory still works for the whole range of T_w.

Figures 16 and 17 compare the corrected asymptotic theory and the numerical solution of the whole problem. In both cases, the corrected theory improves greatly the results of the earlier asymptotic theory. We have not shown the vapour number density profile given by the corrected asymptotic theory as it coincides within 1% relative error with that of the numerical solution of the whole problem. Both curves would overlap if depicted

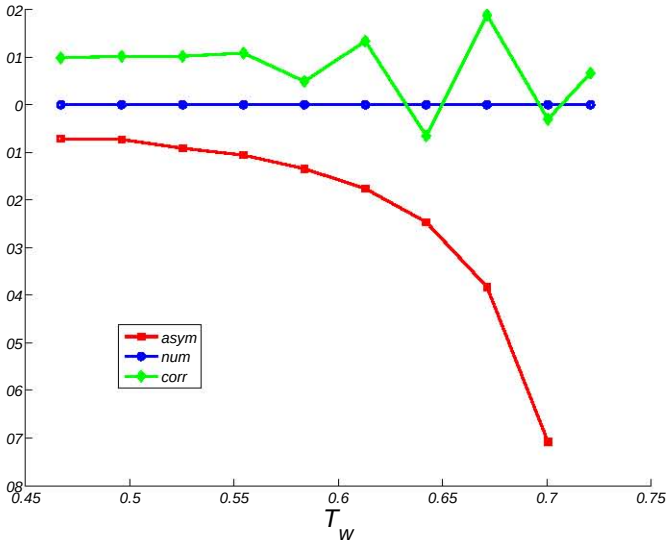

Figure 2.15: Estimated location x_{MJ} at which the Zeldovich droplet nucleation rate is maximum compared to the numerically obtained value x_M as a function of the wall temperature T_w.

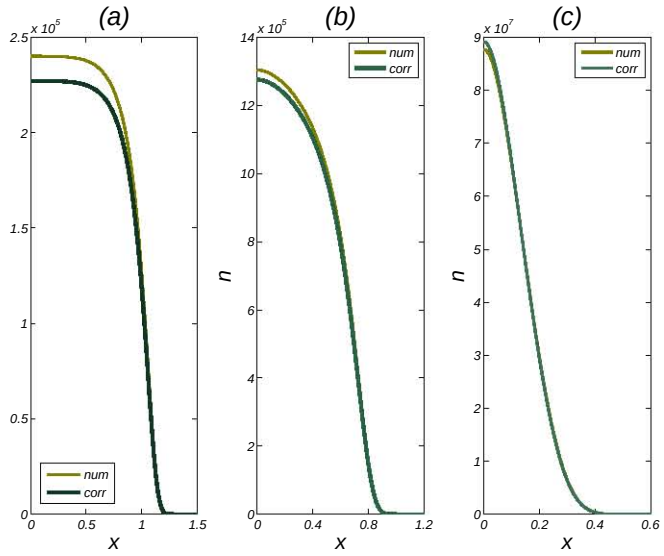

Figure 2.16: Corrected and numerical condensate number profiles for wall temperatures of (a) 800 K, (b) 1000 K, (c) 1200 K.

together. The deposition rates depicted in Fig. 10 are reasonably given by our earlier asymptotic theory except for quite high T_w for which this approximation breaks down. The corrected asymptotic theory gives quite accurate approximations for the deposition rates even at high T_w close to the maximum deposition rate.

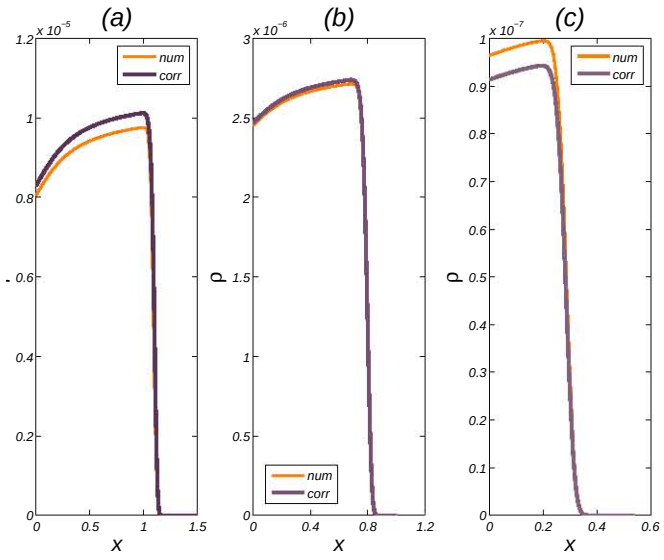

Figure 2.17: Corrected and numerical droplet number density profiles for wall temperatures of (a) 800 K, (b) 1000 K, (c) 1200 K.

2.1.7 conclusions

We have considered homogeneous condensation of single-species vapours mixed with a carrier gas in the stagnation point boundary layer flow near a cold wall. Droplets are homogeneously nucleated at the Zeldovich rate in a very narrow region and their size increases from the negligible size of the critical nucleus as they move towards the wall by thermophoresis. The mean free path is much larger than the droplet size and therefore the nucleated droplets capture vapour according to free-molecular-regime law. In our thermophysical model, we have ignored the Soret and Dufour effects and have assumed that the heat of vaporization is much larger than the Boltzmann constant times the temperature far from the wall. The carrier gas is assumed to be incompressible for the range of wall temperatures that we consider. Under these conditions, vapour condensation occurs in a condensation layer whose distance to the wall, width and characteristics depend on the parameters of the problem.

We have presented an asymptotic theory of the homogeneous condensation process, calculated the profiles of vapour density, droplet density and number of condensate molecules, and the deposition rates at the wall and compared them to direct numerical simulation of the equations governing the model. Elaborating a theory of homogeneous condensation is more complex than in the case of heterogeneous condensation where the number of droplets coincides with that of solid particles suspended in the gas. In the case of homogeneous condensation, the droplet density is higher than the equilibrium vapour density (the 0-CL theory in [79]) and lower than the vapour density profile in the absence of condensation. We select a trial vapour density which interpolates between these two bounds and satisfies the condition that the maximum number density of the condensate

be close to the maximum vapour number density. We then calculate the corresponding droplet density profile using that droplets nucleate in a very narrow region about the peak of the Zeldovich rate. With this profile, we solve the equations for the condensate number of molecules and the vapour density by matched asymptotic expansions. This process is iterated using the new vapour density until a reasonable convergence is reached. For large wall temperatures, the calculation of the maximum Zeldovich rate breaks down and we corrected our asymptotic procedure by selecting the optimal trial vapour density in a different way: we interpolate between vapour density profiles and locations of the dew surface. We also need to correct the equations in the condensation layer which is now very close to the wall. Our theory approximates very well the vapour number density and gives good approximations to the droplet density, the number of condensate molecules and the deposition rate.

We can extend our theory in several directions of engineering interest while keeping the paramount simplification that the condensible vapour is very diluted and therefore the velocity and temperature fields are independent from nucleation-condensation processes. In section 2 we will generalize our procedure for being applied to multi-species vapours. In section 3 we will consider self-similar boundary layer flows, such as wedge flows [35, 95], that are more general than the stagnation point flow. In an appropriate mass coordinate, the velocity field is described by a modified Falkner-Skan equation and the rest of the calculation is straightforward along the lines of the present work. We can also consider the case of a compressible carrier gas with temperature dependent viscosity, [31]. In this case, the equations for the temperature and velocity are coupled but their profiles are self-similar in the appropriate mass coordinate, [31]. Our methods can be applied to solve this more complete thermophysical model. Yet another scenario important for aerosols [21, 33, 50] and climate applications [87] is to consider what happens when a flow of air carrying supersaturated water vapour encounters a quiescent cold gas and condensation occurs. But the resulting boundary layer flow proves not to be similar to the case considered in this section which is not only the consequence of different boundary conditions at the "wall" formed by the quiescent cold gas but to the hydrodynamics ruling the external flow, that is, the flow beyond the boundary layer. In addition, solutions are not self-similar anymore and numerical calculations become more complex indeed. We will tackle this problem in chapter 5. In many applications, it is important to use nucleation rates that give a better description of experimental conditions than the Zeldovich rate we use here. Three such rates are discussed by [96] and references they cite. See also [81] for deviations from the classical nucleation rate at small sizes of the critical nucleus. Other improvements refer to the droplet growth law when the droplets are comparable or larger than the mean free path [96]. Our calculations can be repeated for these other nucleation and growth laws with the appropriate modifications. Validations and modifications of the classical nucleation theory may be seen in [46]. An alternative approach to modeling homogeneous nucleation in some special situations is described in [51].

2.2 Extended model for polydisperse cluster size distributions in a planar stagnation-point flow

2.2.1 introduction

The first model we have developed and is described in §2.1 has considered a monodisperse distribution of droplets, but droplet size distribution follows a cluster size distribution that is, in principle, polydisperse, namely, with multiple sizes. Polydisperse cluster size distribution results from the fact that nucleation is occurring at different points along the x-axis and each one of those nuclei evolves differently and give rise to a different-sized cluster. A monodisperse distribution is, therefore, an operational simplification but has not an *a priori* convincing physical support. Then, we have extended the model to the cluster size space that has, in principle, the same dimension as the physical space. Nucleation at each point is controlled by the corresponding critical size whose value depends on the temperature and the supersaturation at that point. When we discretize the cluster size space we will have as many equations for n and ρ as points are in the physical space, although concentration equation is still only one although having some terms that varies in the cluster size space, for instance, the sink term that is now a summation (see model equations below). In our previous monodisperse model we have been forced to use a relatively small h (physical step along x-axis) for obtaining numerical convergence, nevertheless, it doesn't seem reasonable to keep the same step for generating the size space. Because of that, we have assumed that nucleation is produced every $10\,h$ steps. This new polydisperse model uses the same basic equations for c, ρ and n as the previous one but adapting them to a two- dimensional space. What we wish to validate is how approximate is the monodisperse assumption respecting to the number of condensate and droplet number density at the wall.

The term 'size order' that we use in some plots refers to the position at which the cluster is created. It corresponds to the ordinal number of the element in the size space and is representative of the critical size. The higher the size order the closer the position to the wall.

2.2.2 model

Model equations are written as:

$$c(x)'' + S_c\, u(x)\, c'(x) = \frac{B\,\epsilon^{-7/2} c(x_i)^2}{\sqrt{6\pi}\,\eta(x_i)^3\,T(x_i)^3}\,\exp\left(\frac{-1}{2\eta(x_i)^2 T(x_i)^3 \epsilon^3}\right)\,H\big(c(x)-c_e(x)\big)$$

$$+\,B\,\big(c(x)-c_e(x)\big)\,T(x)^{1/2}\sum_{i=1}^{N}\big(\rho(i,x)\,n(i,x)^{2/3}\,H\big(n(i,x)-n_*(i)\big)\big)\,H\big(c(x)-c_e(x)\big),$$

$$c(0) = c_e(0), \quad c(+\infty) = 1$$

$$U(x)\,\rho'(i,x) + \alpha\left(\frac{T'(x)}{T(x)}\right)'\rho(i,x) = -\frac{B\,c(x_i)^2}{S_c\sqrt{6\pi\epsilon}}\exp\left(\frac{-1}{2\eta(x_i)^2T(x_i)^3\epsilon^3}\right)H\big(c(x)-c_e(x)\big),$$

$$\rho(x_i) = 0,$$

$$U(x) = u(x) + \alpha\,\frac{T'(x)}{T(x)}\,,$$

$$c_e(x) = \frac{T_d}{T(x)}\exp\left[\frac{\Lambda}{\epsilon}\left(\frac{1}{T_d}-\frac{1}{T(x)}\right)\right],$$

$$U(x)\,n'(i,x) = -\frac{B}{S_c}\big(c(x)-c_e(x)\big)\,T(x)^{1/2}\,n(i,x)^{2/3}\,H\big(n(i,x)-n_*(i)\big)\,H\big(c(x)-c_e(x)\big),$$

$$n(x_i) = 0,$$

$$n_*(i) = \left(\frac{1}{\epsilon\,\eta(x_i)\,T(x_i)}\right)^3,$$

where i denotes a variable in the cluster size space which determines the corresponding variable x_i in the physical space and N is the dimension of such space. x_i is the position at which the i^{th} nucleus is formed and, therefore, that variable controls the critical size from which each different cluster size at any position is produced by condensation. When we solve the system of equations by the shooting method, we start with only three equations at infinity, the equation for c and the equations for ρ and n corresponding to the position $x_i = x(\infty)$. Then, every $10\,h$ steps two new equations, for $n(i,x)$ and $\rho(i,x)$ respectively, are added to the system because every $10\,h$ steps a new nucleus might be created, which is controlled by the Heaviside function, that is, if $c_{x_i} \geq c_e(x_i)$.

2.2.3 numerical results

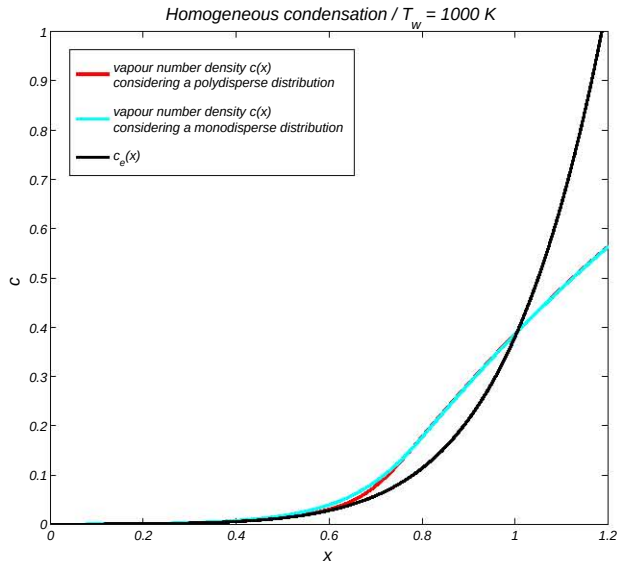

Figure 2.18: Vapour number density profiles obtained considering monodisperse and polydisperse droplet distributions, for a wall temperature of $1000\,K$

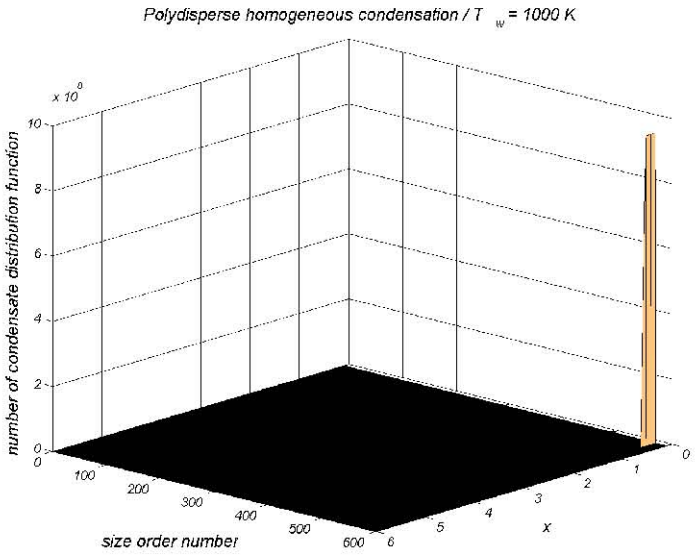

Figure 2.19: Polydisperse distribution function of the number of condensate $(n(x,i))$ for a wall temperature of $1000\,K$

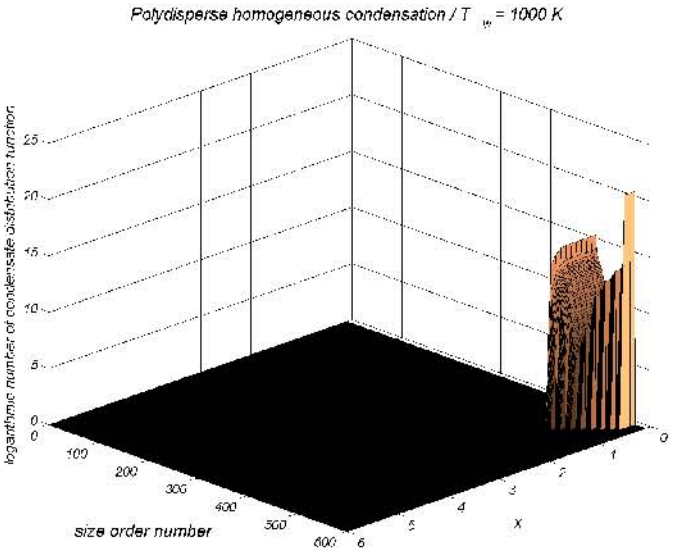

Figure 2.20: Logarithmic polydisperse distribution function of the number of condensate $(n(x,i))$ for a wall temperature of $1000\,K$

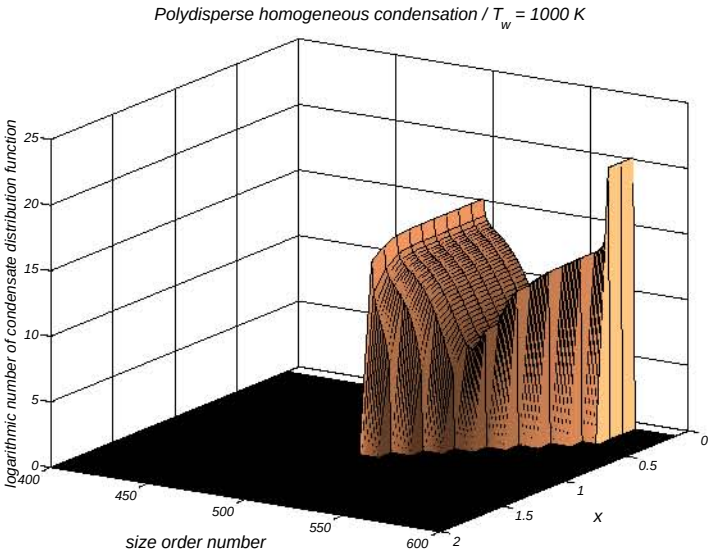

Figure 2.21: Enlarged view of the logarithmic polydisperse distribution function of the number of condensate $(n(x,i))$ for a wall temperature of $1000\,K$

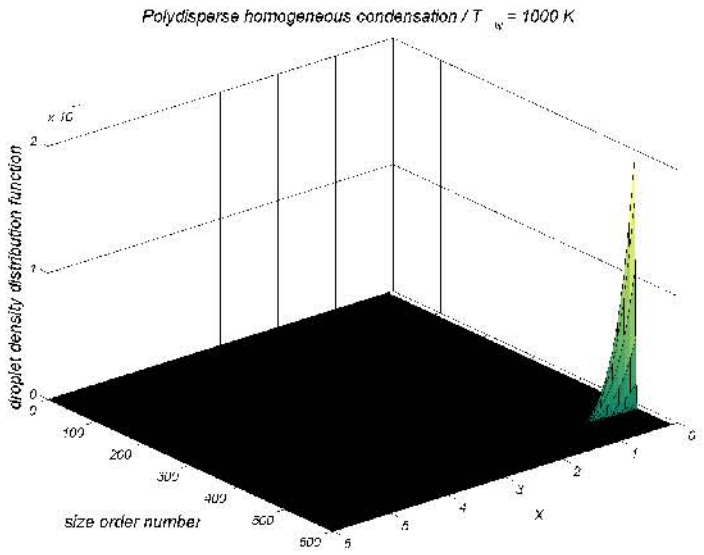

Figure 2.22: Polydisperse distribution function of the droplet number density ($\rho(x,i)$) for a wall temperature of $1000\,K$

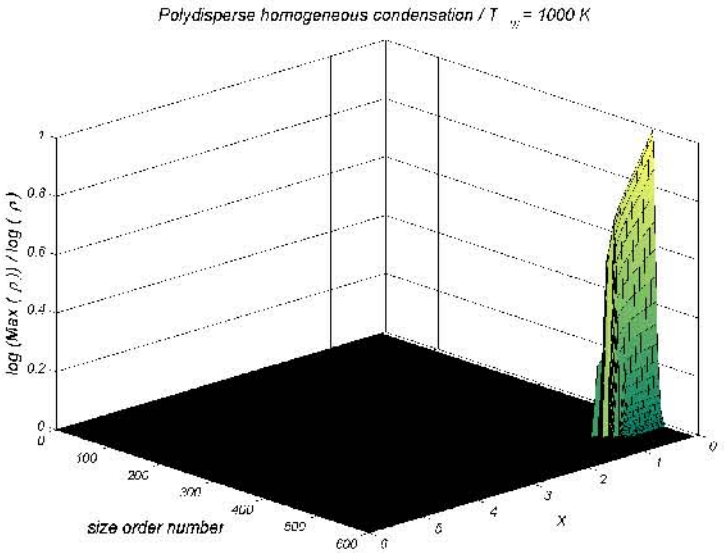

Figure 2.23: $log(Max(\rho(x,i)))/log(\rho(x,i))$ for a wall temperature of $1000\,K$

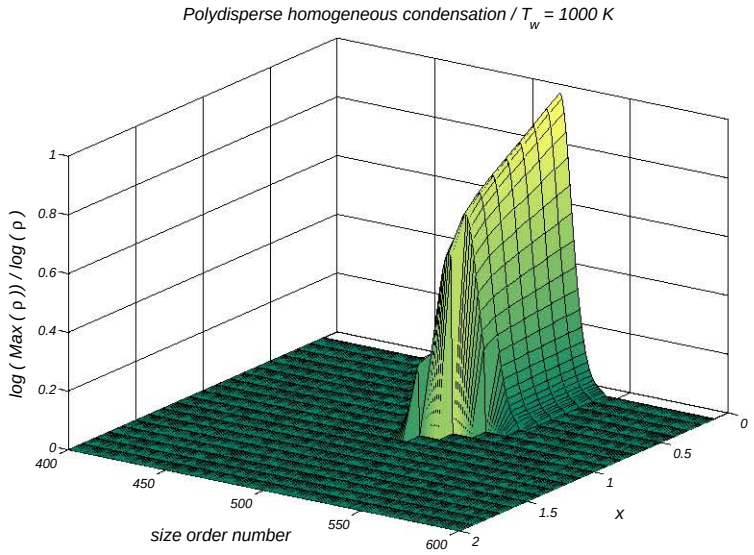

Figure 2.24: Enlarged view of $\log(\max(\rho(x,i)))/\log(\rho(x,i))$ for a wall temperature of $1000\,K$

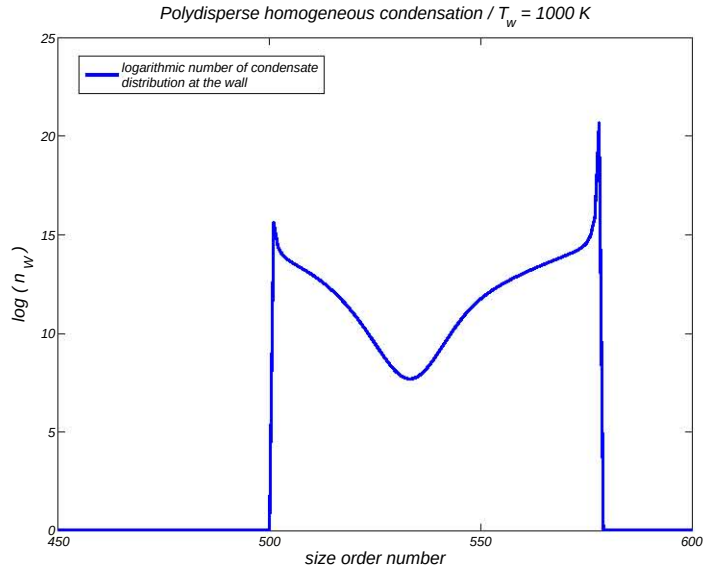

Figure 2.25: Logarithmic distribution function of the number of condensate at the wall $(n_w = n(0,i))$ for a wall temperature of $1000\,K$

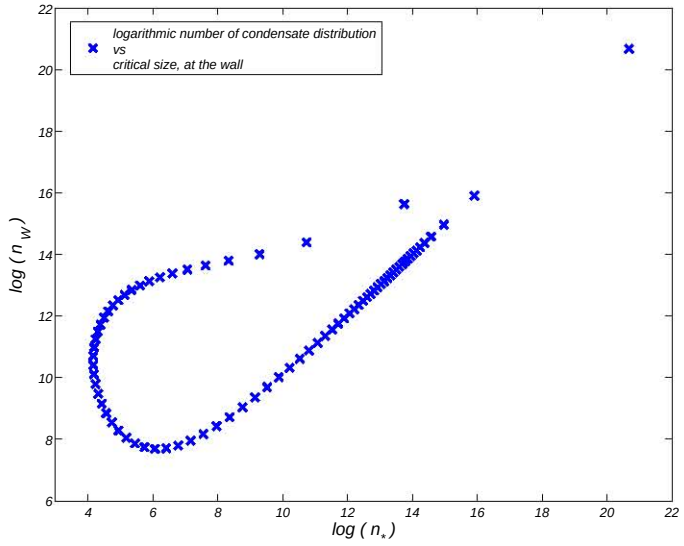

Figure 2.26: Logarithmic distribution function of the number of condensate at the wall ($n_w = n(0,i)$) *vs.* logarithmic critical size, for a wall temperature of $1000\,K$

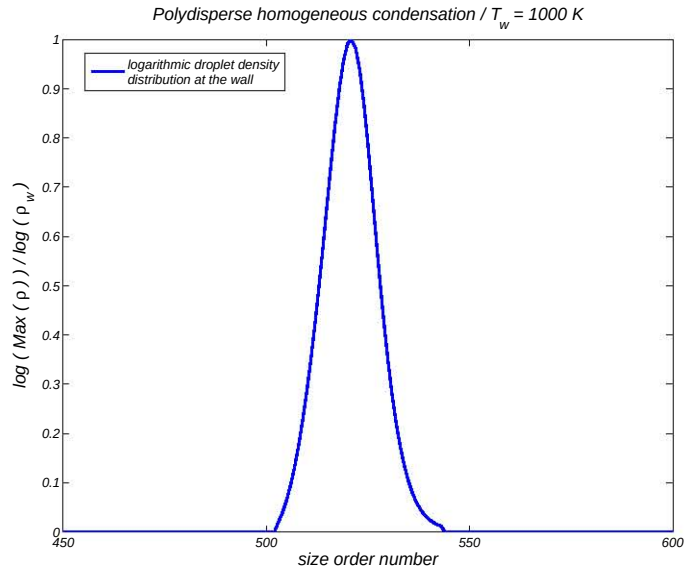

Figure 2.27: Logarithmic distribution function of the droplet number density at the wall ($\log(\max(\rho(0,i)))/\log(\rho(0,i))$), for a wall temperature of $1000\,K$

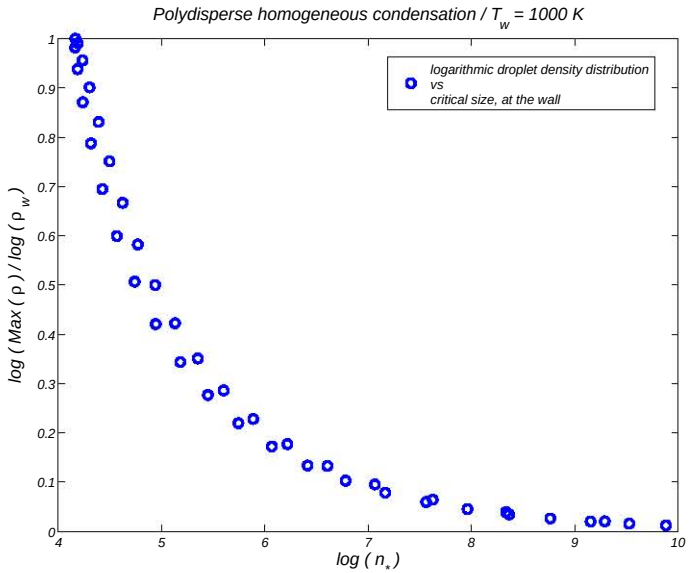

Figure 2.28: Logarithmic distribution function of the droplet number density at the wall $(\log(\max(\rho(0,i)))/\log(\rho(0,i)))$ *vs.* logarithmic critical size, for a wall temperature of $1000\,K$

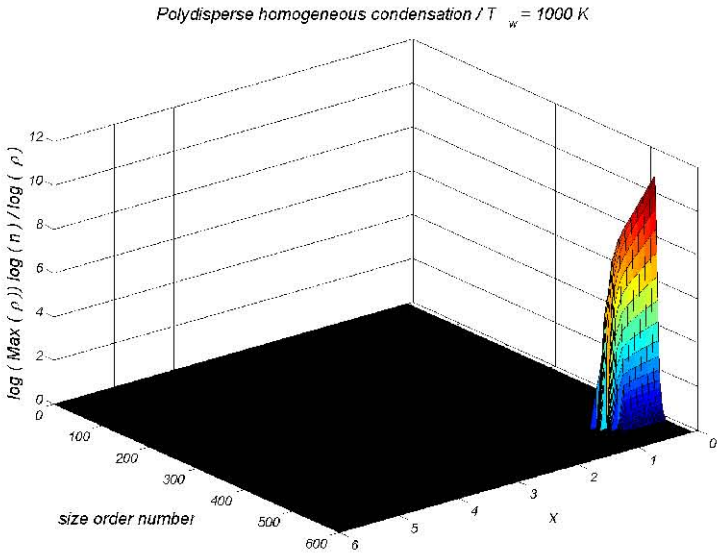

Figure 2.29: Logarithmic total condensate distribution function $\log(\max(\rho(x,i)))\log(n(x,i))/\log(\rho(x,i))$

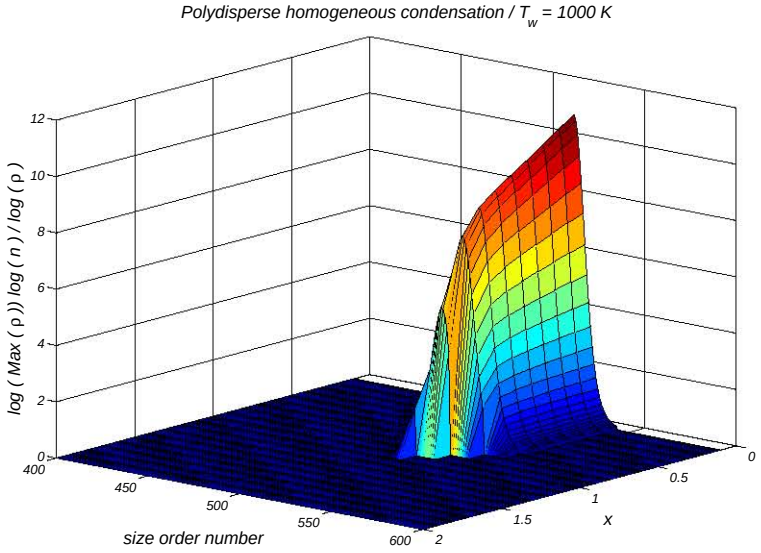

Figure 2.30: Logarithmic total condensate distribution function $\log(\max(\rho(x,i)))\log(n(x,i))/\log(\rho(x,i))$. Enlarged view

2.2.4 conclusions

It can be seen, as expected, that the nucleation region has broadened respecting to the monodisperse case, of course, to the humid side ($c(x) < c_e(x)$). Two maxima of the number of condensate may be observed (although that behavior of solution was already present in the previous simulation but the second maximum appearing closer to the wall was significantly smaller than the first). However, at the wall there is a main difference in the fact that the maximum of the droplet density occurs with the minimum of the number of condensate and owing to that, deposition at the wall may be overestimated with the first model.

2.3 Wedge flows and self-similar solutions

2.3.1 introduction

We have solved a model for homogeneous condensation in the specific case of a incompressible plane stagnation-point flow. A self- similar solution for the velocity field in such a flow may be obtained by defining a stretched variable $\zeta = \sqrt{\frac{1}{\tilde{\nu}\tilde{\tau}}}\,\tilde{y}$ across the streamwise direction (y-axis). This self-similarity is also extensible to the concentration equation of the condensation model. The unit of length $l_b = \sqrt{\tilde{\nu}\tilde{\tau}}$ is introduced in the parameter B whose inverse becomes a small parameter controlling the perturbative approach. For

wedge flows, the plane stagnation-point flow is a particular case of, a self-similar solution may be also obtained, but then, the stretched variable is a function of the streamwise coordinate x, whence $\zeta = \sqrt{\dfrac{(m+1)\tilde{u}_\infty}{2\,\tilde{x}\,\tilde{\nu}}}\,\tilde{y}$. This factor, if used as the unit of length, will make the new parameter B_w x-dependent and no self-similar solution would be possible for the concentration equation. The way to proceed is to re-scale the concentration (in fact, also the equilibrium concentration, the number of condensate and the droplet density) by a function of x to obtain a self-similar solution. Self-similar solution for wedge flow can also be extended to obliquely impinging stagnation-point flows.

2.3.2 Equations for ρ, n, c and c_e

equation for $\tilde{\rho}$

$$\tilde{U}\cdot\tilde{\nabla}\tilde{\rho} = \alpha\,\tilde{\nu}\tilde{\rho}\,\tilde{\nabla}\cdot\frac{\tilde{\nabla}\tilde{T}}{\tilde{T}} + \sqrt{\frac{2\tilde{v}^2\tilde{\sigma}}{\pi\tilde{m}_v}}\,\tilde{c}^2\exp\left(-\frac{\sigma^3}{2\eta^2}\right)$$

$$\left[\tilde{u}\,\overrightarrow{i} + \tilde{v}\,\overrightarrow{j} - \frac{\alpha\,\tilde{\nu}}{\tilde{T}}\left(\frac{\partial\tilde{T}}{\partial\tilde{x}}\,\overrightarrow{i} + \frac{\partial\tilde{T}}{\partial\tilde{y}}\,\overrightarrow{j}\right)\right]\cdot\left[\frac{\partial\tilde{\rho}}{\partial\tilde{x}}\,\overrightarrow{i} + \frac{\partial\tilde{\rho}}{\partial\tilde{y}}\,\overrightarrow{j}\right] =$$

$$\alpha\,\tilde{\nu}\,\tilde{\rho}\left[\frac{\partial}{\partial\tilde{x}}\left(\frac{1}{\tilde{T}}\frac{\partial\tilde{T}}{\partial\tilde{x}}\right) + \frac{\partial}{\partial\tilde{y}}\left(\frac{1}{\tilde{T}}\frac{\partial\tilde{T}}{\partial\tilde{y}}\right)\right] + \tilde{C}_\rho\,\tilde{c}^2\exp\left(-\frac{\sigma^3}{2\eta^2}\right)$$

Now we use the transformation from [95], p. 172, which reads:

$$\begin{aligned}\tilde{u} &= f'\,\frac{\tilde{a}}{\tilde{x}}\,x^{m-1},\\ \tilde{v} &= -\sqrt{\frac{(m+1)\,\tilde{\nu}\,\tilde{a}}{2}}\,x^{(m-1)/2}\left(f + \frac{m-1}{m+1}\,\zeta\,f'\right),\end{aligned}$$

where x^{m-1} and η are dimensionless. Transformed equations for momentum along x-axis and energy are:

$$\begin{aligned}f''' + f\,f'' + \left(\frac{2\,m}{m+1}\right)\left[1-(f')^2\right] &= 0\\ T'' + f\,\frac{\tilde{\nu}\,\tilde{\rho}\,c_P}{\tilde{\lambda}}T' &= 0\end{aligned}$$

where $'$ indicates derivative respect to ζ and $f = f(\zeta)$ is the dimensionless streamfunction.

The RHS of equation for $\tilde{\rho}$ becomes:

$$\left\{ \left(f' \, \tilde{a} \, \tilde{x} \, x^{m-1} - \frac{\alpha \, \tilde{\nu}}{\tilde{T}} \frac{\partial \tilde{T}}{\partial \tilde{x}} \right) \overrightarrow{i} + \left[-\sqrt{\frac{(m+1) \, \tilde{\nu} \, \tilde{a}}{2}} x^{(m-1)/2} \left(f + \frac{m-1}{m+1} \zeta \, f' \right) - \frac{\alpha \, \tilde{\nu}}{\tilde{T}} \frac{\partial \tilde{T}}{\partial \zeta} \frac{\partial \zeta}{\partial \tilde{y}} \right] \overrightarrow{j} \right\} \cdot$$

$$\left[\frac{\partial \tilde{\rho}}{\partial \zeta} \frac{\partial \zeta}{\partial \tilde{x}} \overrightarrow{i} + \frac{\partial \tilde{\rho}}{\partial \zeta} \frac{\partial \zeta}{\partial \tilde{y}} \overrightarrow{j} \right]$$

But, because T as same as f is self-similar, we can make $\dfrac{\partial \tilde{T}}{\partial \tilde{x}} = 0$. The scalar product is:

$$\left(\frac{m-1}{2} \right) \tilde{a} \, x^{m-1} \, f' \, \zeta - \left(\frac{m+1}{2} \right) \tilde{a} \, x^{m-1} \, f - \left(\frac{m-1}{2} \right) \tilde{a} \, x^{m-1} \, f' \, \zeta -$$

$$\left(\frac{m+1}{2} \right) \tilde{a} \, x^{m-1} \, \tilde{\nu} \, \frac{\tilde{T}'}{\tilde{T}} \, \frac{\alpha}{\tilde{\nu}} \, \tilde{\rho}',$$

where $'$ indicates again derivative respect to ζ.

Now, first and third terms cancel out and RHS reads:

$$-\left[\left(\frac{m+1}{2} \right) \left(f + \alpha \frac{\tilde{T}'}{\tilde{T}} \right) \tilde{a} \, x^{m-1} \right] \tilde{\rho}'$$

On the other hand, the LHS (ignoring also the derivative of T respect to x)

transforms into :

$$\left(\frac{m+1}{2} \right) \tilde{a} \, x^{m-1} \, \alpha \left(\frac{\tilde{T}'}{\tilde{T}} \right)' \tilde{\rho} + \tilde{C}_\rho \, \tilde{c}^2 \exp\left(-\frac{\sigma^3}{2\eta^2} \right)$$

Final equation for ρ is:

$$-\left(\frac{m+1}{2} \right) \tilde{a} \, x^{m-1} \left\{ f \, \tilde{\rho}' + \alpha \, \tilde{\rho} \left[\frac{\tilde{T}'}{\tilde{T}} + \left(\frac{\tilde{T}'}{\tilde{T}} \right)' \right] \right\} = \tilde{C}_\rho \, \tilde{c}^2 \exp\left(-\frac{\sigma^3}{2\eta^2} \right)$$

equation for ñ

$$\tilde{U} \cdot \tilde{\nabla} \tilde{n} = \sqrt{\frac{k_B}{2 \, \pi \tilde{m}_v}} \left(36 \, \pi \tilde{v}^2 \right)^{1/3} (\tilde{c} - \tilde{c}_e) \, \tilde{T}^{1/2} \tilde{n}^{2/3}$$

$$\left[\tilde{u} \overrightarrow{i} + \tilde{v} \overrightarrow{j} - \frac{\alpha \, \tilde{\nu}}{\tilde{T}} \left(\frac{\partial \tilde{T}}{\partial \tilde{x}} \overrightarrow{i} + \frac{\partial \tilde{T}}{\partial \tilde{y}} \overrightarrow{j} \right) \right] \cdot \left[\frac{\partial \tilde{n}}{\partial \tilde{x}} \overrightarrow{i} + \frac{\partial \tilde{n}}{\partial \tilde{y}} \overrightarrow{j} \right] = \tilde{C}_n \, (\tilde{c} - \tilde{c}_e) \, \tilde{n}^{2/3}$$

Final equation for $\tilde{n}$ is:

$$-\left(\frac{m+1}{2}\right)\tilde{a}\,x^{m-1}\left[f+\alpha\,\frac{\tilde{T}'}{\tilde{T}}\right]\tilde{n}' \;=\; \tilde{C}_n\,(\tilde{c}-\tilde{c}_e)\,\tilde{n}^{2/3}$$

equation for $\tilde{\mathbf{c}}$

$$\left(\tilde{\mathbf{v}}\cdot\tilde{\nabla}-D\,\tilde{\triangle}\right)\tilde{c} \;=\; -\sqrt{\frac{3k_B}{\tilde{m}_v}}\left(\frac{6\tilde{v}^4}{\pi}\right)^{1/6}(\tilde{c}-\tilde{c}_e)\,\tilde{T}^{1/2}\tilde{\rho}\,\tilde{n}^{2/3}$$

where the relatively smaller term due to nucleation has been ignored in the RHS.

$$\left(\tilde{u}\,\vec{i}+\tilde{v}\,\vec{j}\right)\cdot\left(\frac{\partial\tilde{c}}{\partial\tilde{x}}\,\vec{i}+\frac{\partial\tilde{c}}{\partial\zeta}\,\frac{\partial\zeta}{\partial\tilde{y}}\,\vec{j}\right)-D\left[\frac{\partial^2\tilde{c}}{\partial\tilde{x}^2}+\frac{\partial^2 c}{\partial\zeta^2}\left(\frac{\partial\zeta}{\partial\tilde{y}}\right)^2\right] \;=\; \tilde{C}_c\,(\tilde{c}-\tilde{c}_e)\,\tilde{\rho}\,\tilde{n}^{2/3}$$

Final equation for $\tilde{c}$ is

$$-\left(\frac{m+1}{2}\right)\tilde{a}\,x^{m-1}\left[f\,\tilde{c}\,'+\frac{D}{\tilde{\nu}}\,\tilde{c}\,''\right]-D\,\frac{\partial^2\tilde{c}}{\partial\tilde{x}^2} \;=\; \tilde{C}_c\,(\tilde{c}-\tilde{c}_e)\,\tilde{\rho}\,\tilde{n}^{2/3}$$

equation for $\tilde{\mathbf{c}}_\mathbf{e}$

$$\tilde{c}_e=\tilde{c}_\infty\frac{\tilde{T}_d}{\tilde{T}}\exp\left[\frac{\tilde{\Lambda}}{\tilde{\epsilon}}\left(\frac{1}{\tilde{T}_d}-\frac{1}{\tilde{T}}\right)\right]$$

2.3.3 self-similar solutions for small wedge angles

In order to obtain self-similar solutions we assume the following scalings for $\tilde{\rho}$, $\tilde{n}$, $\tilde{c}$ and $\tilde{c}_e$:

$$\begin{aligned}\tilde{\rho}^{ss} &= \Upsilon_\rho\,\tilde{\rho}\\ \tilde{n}^{ss} &= \Upsilon_n\,\tilde{n}\\ \tilde{c}^{ss} &= \Upsilon_c\,\tilde{c}\\ \tilde{c}_e^{ss} &= \Upsilon_{c_e}\,\tilde{c}_e\end{aligned}$$

where Υ_ρ, Υ_n, Υ_c and Υ_{c_e} are functions of $\tilde{x}$ to be determined. The x-dependence of $\tilde{c}_e$ comes through $\tilde{c}_\infty$, that is, $\tilde{c}_\infty^{ss}=\Upsilon_{c_e}\,\tilde{c}_\infty$. Substituting the former scalings we obtain:

$$-\left(\frac{m+1}{2}\right)\,\tilde{a}\,x^{m-1}\left\{f\;(\tilde{\rho}^{ss})' + \alpha\,\tilde{\rho}^{ss}\left[\frac{\tilde{T}'}{\tilde{T}} + \left(\frac{\tilde{T}'}{\tilde{T}}\right)'\right]\right\}\Upsilon_\rho \;=$$

$$\tilde{C}_\rho\;(\tilde{c}^{ss})^2\;\Upsilon_c^2\;\exp\left\{\frac{-\sigma^3}{2\left[\eta^{ss} + \log\left(\Upsilon_c/\Upsilon_{c_e}\right)\right]^2}\right\}$$

$$-\left(\frac{m+1}{2}\right)\,\tilde{a}\,x^{m-1}\left[f + \alpha\,\frac{\tilde{T}'}{\tilde{T}}\right]\;(\tilde{n}^{ss})'\,\Upsilon_n \;=\; \tilde{C}_n\;(\tilde{c}^{ss} - \tilde{c}_e^{ss})\;(\tilde{n}^{ss})^{\,2/3}\,\Upsilon_c\,\Upsilon_n^{2/3}$$

$$-\left(\frac{m+1}{2}\right)\,\tilde{a}\,x^{m-1}\left[f\;(\tilde{c}^{ss})' + \frac{D}{\tilde{\nu}}\;(\tilde{c}^{ss})''\right]\;\Upsilon_c - D\,\tilde{c}^{ss}\,\frac{\mathrm{d}^2\Upsilon_c}{\mathrm{d}\tilde{x}^2} \;=$$

$$\tilde{C}_c\;(\tilde{c}^{ss} - \tilde{c}_e^{ss})\;\tilde{\rho}^{ss}\;\left(\tilde{n}^{ss}\right)^{2/3}\;\Upsilon_c\,\Upsilon_\rho\,\Upsilon_n$$

In the equations for $\tilde{n}^{ss}$ and $\tilde{c}^{ss}$ (which depend on the difference between concentration and equilibrium concentration) we have assumed $\Upsilon_c \simeq \Upsilon_{c_e}$. Consistently, because $\log\left(\Upsilon_c/\Upsilon_{c_e}\right) \ll 1$, the 2nd exponential in the LHS of the equation for ρ may be approximated by:

$$\exp\left\{\frac{-\sigma^3}{2\left[\eta^{ss} + \log\left(\Upsilon_c/\Upsilon_{c_e}\right)\right]^2}\right\} \;\simeq\; \exp\left\{\frac{-\sigma^3}{2\left(\eta^{ss}\right)^2}\left[1 - 2\,\log\left(\frac{\Upsilon_c}{\Upsilon_{c_e}}\right)\,\frac{1}{\eta^{ss}}\right]\right\}$$

$$\simeq\; \exp\left[-\frac{\sigma^3}{2\left(\eta^{ss}\right)^2}\right]\;\exp\left[\frac{\sigma^3}{\left(\eta^{ss}\right)^3}\log\left(\frac{\Upsilon_c}{\Upsilon_{c_e}}\right)\right]$$

$$\simeq\; \exp\left[-\frac{\sigma^3}{2\left(\eta^{ss}\right)^2}\right]\;\left(\frac{\Upsilon_c}{\Upsilon_{c_e}}\right)^{(\sigma/\eta^{ss})^3}$$

For the equations for $\tilde{\rho}$, $\tilde{n}$, $\tilde{c}$ and $\tilde{c}_e$ to admit self-similar solutions we write the conditions to be hold by Υ_ρ, Υ_n, Υ_c and Υ_{c_e}:

$$\begin{aligned}
\Upsilon_c^2 \left(\frac{\Upsilon_c}{\Upsilon_{c_e}}\right)^{(\sigma/\eta^{ss})^3} - x^{m-1}\,\Upsilon_\rho &= 0 \\
\Upsilon_c - x^{m-1}\,\Upsilon_n^{1/3} &= 0 \\
\frac{\mathrm{d}^2\Upsilon_c}{\mathrm{d}\tilde{x}^2} - \frac{\tilde{a}}{D}\,x^{m-1}\,\Upsilon_c &= 0 \\
\Upsilon_\rho\,\Upsilon_n^{2/3} - x^{m-1} &= 0
\end{aligned}$$

There is not a general analytical solution for Υ_c but explicit expressions for Υ_ρ and Υ_n may be written as functions of Υ_c. Respecting to Υ_{c_e} it can only be known once the self-similar solution was obtained.

$$\begin{aligned}
\Upsilon_n &= \left(\frac{\Upsilon_c}{x^{m-1}}\right)^3 \\
\Upsilon_\rho &= \frac{x^{3(m-1)}}{\Upsilon_c^2} \\
\Upsilon_{c_e} &= \Upsilon_c \left[\frac{x^{m-1}}{\Upsilon_c}\right]^{4\left(\frac{\sigma}{\eta}\right)^3}
\end{aligned}$$

Concerning specifically the wedge flows, we are interested in a maximum value for m in the order of 10^{-1} (it would not be the case for obliquely impinging stagnation-point flows) for we shall only consider wedge angles rather smaller than $\pi/2$. Classical boundary layer solution for wedge flows near the stagnation point breaks down as angles become larger, due to the rough assumption that the boundary layer width goes to zero at the stagnation point which might only be true for an infinitely thin flat plate (a wedge of zero angle) and even that is approximate because width is really in the order of the Prandtl dimension (we will come back to this point in the next section). Thus, we might consider $m-1 \simeq -1$ and $x = \tilde{x}\sqrt{\dfrac{D}{\tilde{a}}}$, and equation for Υ_c becomes:

$$\frac{\mathrm{d}^2\Upsilon_c}{\mathrm{d}x^2} - \frac{\Upsilon_c}{x} = 0$$

Let us consider now both limit situations $x \ll 1$ and $x \gg 1$, defining the two new variables $\chi = \dfrac{1}{x}$ and $\xi = \sqrt{2\,x}$, respectively. With these transformations the equation for Υ_c gives rise to:

$$\frac{\mathrm{d}^2\Upsilon_c}{\mathrm{d}\chi^2} + 2\,\frac{\mathrm{d}\Upsilon_c}{\mathrm{d}\chi}\frac{1}{\chi} - \frac{\Upsilon_c}{\chi^3} = 0, \qquad x \to 0, \qquad \frac{\mathrm{d}^2\Upsilon_{c_i}}{\mathrm{d}\chi^2} + 2\,\frac{\mathrm{d}\Upsilon_{c_i}}{\mathrm{d}\chi}\frac{1}{\chi} = 0$$

$$\frac{\mathrm{d}^2\Upsilon_c}{\mathrm{d}\xi^2} - \frac{\mathrm{d}\Upsilon_c}{\mathrm{d}\xi}\frac{1}{\xi} - \Upsilon_c = 0, \qquad x \to \infty, \qquad \frac{\mathrm{d}^2\Upsilon_{c_o}}{\mathrm{d}\xi^2} - \Upsilon_{c_o} = 0$$

Whose solutions are:

$$\Upsilon_{c_i} = p\,x + q$$
$$\Upsilon_{c_o} = A\cosh(\sqrt{2x}) + B\sinh(\sqrt{2x})$$

Local behavior of the solution of equation $\dfrac{\mathrm{d}^2\Upsilon_c}{\mathrm{d}x^2} - \dfrac{\Upsilon_c}{x} = 0$ near $x = 0$ might also be obtained as a series in the form $\displaystyle\sum_{n=0}^{\infty} a_n\,x^n$ where a_n would be given by:

$$a_0 \quad \text{and} \quad a_1, \quad \text{arbitrary}$$
$$a_n = n \times (n-1)^2 \times (n-2)^2 \times \ldots \times 2^2 \times 1, \quad \text{for } n \geq 2$$

but a Taylor series is not a good option if we are dealing with regular singular points (and $x = 0$ is it). For $x = 0$ we would have to try a Frobenius series instead. However, for $x = \infty$, that is an irregular singular point, solution would have to be implemented as an asymptotic series.

Nevertheless, a solution can be written in terms of the modified Bessel functions because equation $\dfrac{\mathrm{d}^2\Upsilon_c}{\mathrm{d}x^2} - \dfrac{\Upsilon_c}{x} = 0$ may be obtained by transforming the modified Bessel equation:

$$\frac{\mathrm{d}^2\Upsilon_c}{\mathrm{d}x^2} + \frac{1}{x}\frac{\mathrm{d}\Upsilon_c}{\mathrm{d}x} - \left(1 + \frac{\nu^2}{x^2}\right)\Upsilon_c = 0$$

First transformation is classical and eliminates the first order derivative by means of the substitution $\Upsilon_c = Z\,\exp\left(-\dfrac{1}{2}\displaystyle\int\frac{\mathrm{d}x}{x}\right) = \dfrac{Z}{\sqrt{x}}$. After that, we have:

$$\frac{\mathrm{d}^2 Z}{\mathrm{d}x^2} - Z\left(1 + \frac{1}{4\,x^2} + \frac{\nu^2}{x^2}\right) = 0$$

Now, taking $\nu = 0$, defining the new independent variable ξ such that $\xi' = \dfrac{\mathrm{d}\xi}{\mathrm{d}x}$ equals the coefficient of the term in Z, and knowing the relations $\dfrac{\mathrm{d}Z}{\mathrm{d}x} = \dfrac{\mathrm{d}Z}{\mathrm{d}\xi}\,\xi'$ and $\dfrac{\mathrm{d}^2Z}{\mathrm{d}x^2} = \dfrac{\mathrm{d}^2Z}{\mathrm{d}\xi^2}\,(\xi')^2 + \dfrac{\mathrm{d}Z}{\mathrm{d}\xi}\,\xi''$, we arrive to:

$$\frac{\mathrm{d}^2Z}{\mathrm{d}\xi^2}\,(\xi')^2 + \frac{\mathrm{d}Z}{\mathrm{d}\xi}\frac{\xi''}{\xi'} - \frac{Z}{\xi'} = 0,$$

from which the term in $\mathrm{d}Z/\mathrm{d}\xi$ can also be removed by the same substitution as before, namely, $Z = \dfrac{\Omega}{\sqrt{\xi'}}$. Result is:

$$\frac{\mathrm{d}^2\Omega}{\mathrm{d}\xi^2} - \Omega\left[\frac{\xi'''}{2\,\xi'} - \frac{\xi''^2}{4\,\xi'^2} + \frac{1}{\xi'}\right] = 0$$

The coefficient of Ω may be arranged as:

$$\frac{1}{\xi'} + \frac{1}{x^4}\left(\frac{1}{\xi'^2} - \frac{1}{\xi'}\right)$$

and in the limit $x \to \infty$ we get:

$$\frac{1}{\xi'}$$

The solution of the modified Bessel equation is given by:

$$c_1\,I_0(z) + c_2\,K_0(z) \;=\; 0$$

$$I_0(z) \;=\; \sum_{k=0}^{\infty} \frac{\left(\frac{1}{4}z^2\right)^k}{(k!)^2}; \qquad K_0(z) \;=\; \int_0^{\infty} \frac{\cos(z,t)}{\sqrt{t^2+1}}\mathrm{d}t$$

2.4 Obliquely impinging flows

2.4.1 correction to boundary layer width near the stagnation point

In order to be able to apply the theory of wedge boundary layer flows to the case of obliquely impinging flows, we have to correct the boundary layer width in the neighborhood of the stagnation point, which is finite and not zero. Carrier and Lin [14] have solved the problem for a flat plate that is the minimum limit of a wedge. They tackled the boundary layer in the immediacy of the stagnation point by the whole Navier-Stokes written as a single biharmonic equation for the streamfunction. But, as velocity is very

low near the stagnation point, they looked for a Stokes (or slow flow) approximate solution which involves the same Blasius kind equation as the boundary layer solution, if the parabolic coordinates are used. Their solution is commented in a later work by S. Goldstein [39] about how to consider the immediacy of the leading edge in the Navier-Stokes equations. Other authors that have treated the same problem are S. Kaplun [52], P. Lagerstrom [56] and more recently van de Vooren [106] and Bichsel and Wittwer [5]. In general, the strategy is always to look for solutions including the boundary layer as well as the leading edge. However, it has to be said that most of these works deals with the stagnation point only tangentially because the main aim is usually the flow past the plate. Let's make a brief review of the main points:

All the authors adopt the Navier-Stokes equations for the streamfunction Ψ making the substitutions $x_1 = R_e\, x$, $y_1 = R_e\, y$ and $\psi_1 = R_e\, \Psi$ to reproduce the neighborhood of the leading edge, eliminating this way the Reynolds number in the biharmonic term:

$$\frac{1}{Re}\triangle^2 \Psi - \left(\frac{\partial \Psi}{\partial y}\frac{\partial \triangle \Psi}{\partial x} - \frac{\partial \Psi}{\partial x}\frac{\partial \triangle \Psi}{\partial y}\right) = 0$$

$$L(\Psi) = L^*(\Psi)$$

where L is the biharmonic operator and L^* is the rest.

Carrier and Lin propose a solution in the form of a series $\Psi = \Psi_0 + \Psi_1 + ...$, Ψ_0 being the solution of the biharmonic equation, Ψ_1 the solution of $L(\Psi_1) = L^*(\Psi_0)$ and so on. Boundary condition is $(u, v) = (0, 0)$. In polar coordinates their solution is:

$$\Psi = A\, r^{3/2}\left(\cos\frac{\theta}{2} - \cos\frac{3\,\theta}{2}\right) + \Psi_1 + ...$$

The leading term of the Blasius series solution for the dimensionless streamfunction f is $\alpha\,\eta^2/2$, with $\eta = \dfrac{y}{\sqrt{x}}$. The former function transforms into the streamfunction multiplying it by $\sqrt{x}$ obtaining $\alpha\, r^{3/2}\dfrac{(\sin\theta)^2}{2\sqrt{\cos\theta}}$. The corresponding term of Ψ_0 is $4\,A\,r^{3/2}\left(\cos\dfrac{\theta}{2} - \cos^3\dfrac{\theta}{2}\right)$. Both functions coincide for $\theta \ll 1$. That indicates the existence of a region of validity of both, the boundary layer solution and the solution of the biharmonic equation, close to the plate including the leading edge. Overlapping of boundary layer and slow flow solution becomes clearer when parabolic coordinates are used, (ξ, η). Since we're keeping the original notation, η must not be confused for the BL stretched variable η above. Carrier and Lin solve the corresponding convective biharmonic equation for two regions, namely, very close to the plate, where $\eta \ll 1$ and only

the biharmonic term applies, and the boundary layer where $\eta = 1$, obtaining:

$$\begin{aligned} \Psi &= K\,\xi\,\eta^2 \\ \Psi &= \xi\, f(\eta) \end{aligned}$$

for the two regions, respectively, where f is the solution of the Blasius equation. Carrier and Lin solution, however, doesn't include the external flow.

Nine years later Goldstein found an expansion for Ψ in the boundary layer, also in parabolic coordinates, that merges into the potential flow. But, in his own words, "...there is no reason to suppose the solution valid in a small enough sector near the plate at all distances from the leading edge. The nature of the solution near the leading edge will be re-examined". Expansion is the following:

$$\Psi = \xi\, f_0(\eta) + \xi^{-1}[f_2(\eta) + g_2(\eta)\log\xi] + O(\xi^{-2})$$

$$g_2 = b(\eta\, f_0' - f_0)$$

$$[d^4/d\eta^4 + f_0 d^3/d\eta^3 + (n+1)f_0' d^2/d\eta^2 + f_0'' d/d\eta - (n-1)f_{0'''}](f_2) = 2\,\eta\, f_0''\frac{g_2}{b} + b\, f_0''(f_0' - f_0^2)$$

where f_0 is the Blasius function. The operator applied to f_2 comes from the Navier-Stokes equation taking $\Psi = \xi\, f_0(\eta) \pm f_1(\eta) + f_2(\eta)/\xi \pm f_3(\eta)/\xi + ...$ for $\xi > 0$ or $\xi < 0$.

Another interesting approach was developed by van de Vooren and Dijkstra in 1970. They tackle the problem using the set of two partial differential equations in Ψ and Γ, Γ being vorticity, rather than the convective biharmonic equation in Ψ, written also in parabolic coordinates, and solve them numerically. For that, the unbounded domain is transformed into a rectangular region looking for guarantee stability of the calculation and keep derivatives of dependent variables, finite. Although their results seems convincing, in 1975 they produce a new paper [107] revisiting the situation near the leading edge and proposing a theory based on the Knudsen number where the no-slip condition is replaced by a different one taken from Schaaf (see references op.cit.).

A last comment is addressed to the rather recent work by Bichsel and Wittwer. Solution is obtained analytically but it is validated numerically. For their analysis they work with the equations of the vorticity:

$$\begin{aligned} -(\mathbf{u}\cdot\nabla)\omega + \triangle\omega &= 0 \\ \omega &= -\triangle\Psi \end{aligned}$$

Unlike Goldstein's their streamfunction is written as the sum of only three functions although they do not solve the equations by fixing the streamline but the vorticity functions,

that are called ω. These functions ω are taken as $\omega_0(x,y) = -\text{sign}(y)\frac{H(x)}{\sqrt{x}} f'' \frac{|y|}{\sqrt{x}}$, where f is the Blasius function, $\omega_1(x,y) = b\frac{H(x)}{x} f_1'' \frac{|y|}{\sqrt{x}}$ and $\tilde{\omega}_2(x,y) = -\text{sign}(y)\frac{H(x)}{(x)^{3/2}} \tilde{f}_2'' \frac{|y|}{\sqrt{x}}$, where f_1 and f_2 are obtained from the second equation of vorticity. First and third ω's are symmetric but the second one is even in y and that produces a symmetry break of the solution. While a symmetry breaking looks possible for a flow past a plate, it is not so when we think in wedge flows. Respecting to the numerical solution Bichsel and Wittwer proceed from the original boundary, for which the analytical study has been previously done providing the appropriate BC, to successively larger domains that approach the exterior infinite domain. Finally we have to say that although the authors declare "...we note that for a proper treatment of the problem one also has to discuss the behavior of the solution near $x = y = 0$ which is a singularity of the boundary **B**", such a discussion is not undertaken in the paper.

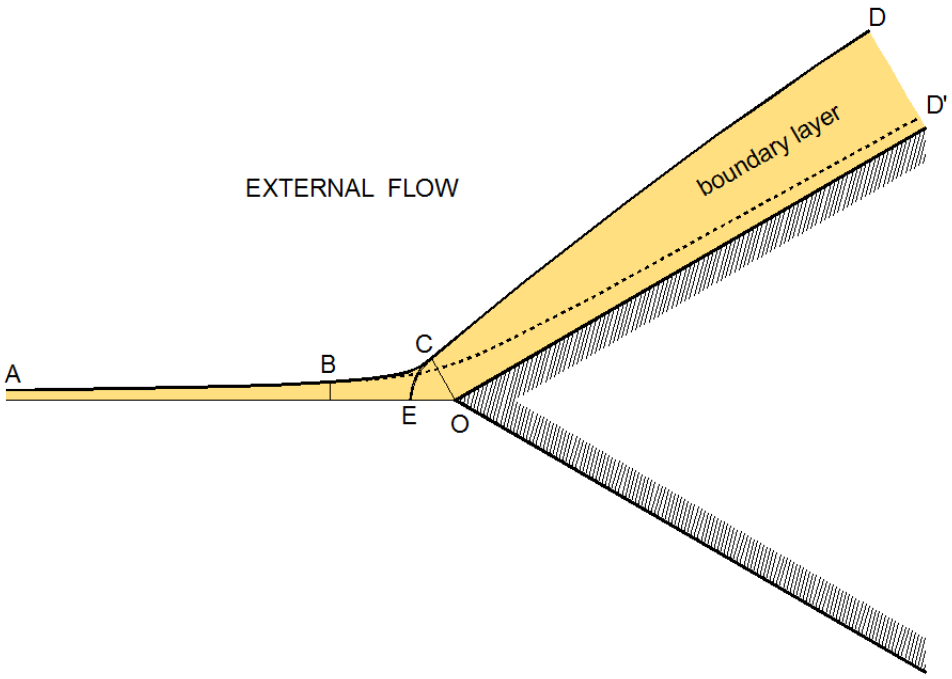

Figure 2.31: Proposed boundary layer for the flow ahead of and at the plate

A common feature of all the commented works is that $\delta(x) \sim x^{1/2}$, $\delta(x)$ being the BL width and that external flow doesn't appear for $x < 0$. However, in some works BC states that external velocity should reduce to 0 along the line $y = 0$ for $x < 0$ and it doesn't seem realistic (results contradicts that assumption [106]) because the point $(0,0)$ pertains to both, the line $y = 0$ and the edge of the BL that is a limit streamline of the external flow along which velocity cannot be zero. Shouldn't it being considered, on the contrary, a BL extended also ahead of the plate? This is the model we are specifically proposing.

Hence, the Navier-Stokes equations in compact form have to be solved incorporating the boundary conditions for the wall, the Falkner-Scan boundary layer and the external flow down and upstream, simultaneously. The upper boundary of the domain within which the inhomogeneous biharmonic equation has to be solved, is defined geometrically by the curves AB, BC and CD. AB is a streamline of the external upstream potential flow and CD is given by the function (in local axis: x measured along the wedge face and δ perpendicularly to it) $\delta(x) \sim \sqrt{\frac{2\,\nu\,x^{1-m}}{a(m-1)}}$ taking the external flow velocity as $a\,x^m$. BC is, then, a transition curve with i^{th}-order continuity at B and C to AB and CD, respectively.

Chapter 3

Theory of mixed vapour condensation from boundary layer flows

Simultaneous homogeneous and heterogeneous condensation (nucleation on presence of particles) of single-species vapours mixed with a carrier gas in the stagnation-point boundary layer flow near a cold wall is considered. Heterogeneous condensation of vapours mixed with a carrier gas in the stagnation point boundary layer flow near a cold wall had been previously considered in the presence of solid particles much larger than the mean free path of vapour particles [79]. The supersaturated vapour condensed on the particles by diffusion, and particles and droplets were thermophoretically attracted to the wall. It was assumed that the heat of vaporization was much larger than $k_B T_\infty$, where T_∞ is the temperature far from the wall, vapour condensation did occur in a condensation layer (CL). The CL width and characteristics depended on the parameters of the problem, and a parameter R yielding the rate of vapour scavenging by solid particles wa particularly important. Assuming that the CL is so narrow that temperature, particle density and velocity do not change appreciably inside it, an asymptotic theory had been found, the δ-CL theory, that approximates very well the vapour and droplet profiles, the dew point shift and the deposition rates at the wall for wide ranges of the wall temperature T_w and the scavenging parameter R.

The solid particles act as condensation sites for the vapour. Let n be the volume of a particle divided by the molecular volume of condensed vapour, so that a solid particle is equivalent to n molecules of vapour. Then a droplet of liquid coating on a solid particle is equivalent to $\tilde{n}(\tilde{x})$ vapour molecules, in the sense that $\tilde{n}$ equals the volume of a droplet (particle plus condensed vapour) divided by the molecular volume of condensed vapour. Thus, the number of liquid molecules coating a given solid particle is $\tilde{n}(\tilde{x})\tilde{n}$. Let $\tilde{\rho}(\tilde{x})$ be the number density of droplets, so that $\rho(\tilde{x})\,[\tilde{n}(\tilde{x})\tilde{n}]$ is the number density of the condensate. Since the number of droplets equals the number of solid particles, the continuity

equation for $\tilde{\rho}$ is:

$$\tilde{\nabla} \cdot \left[\left(\tilde{u} - \alpha \nu \frac{\tilde{\nabla}\tilde{T}}{\tilde{T}} \right) \tilde{\rho} \right] = 0 \tag{3.1}$$

In this equation, the velocity of droplets equals the flow velocity plus the thermophoretic velocity which is $\alpha \nu \tilde{\nabla} \ln \tilde{T}$ (ν is the kinematic viscosity of the carrier gas and α is a dimensionless thermophoretic coefficient which depends on the particle radius). For an incompressible carrier gas, (3.1) yields:

$$\tilde{\nabla} \cdot \left(\tilde{u} - \alpha \nu \frac{\tilde{\nabla}\tilde{T}}{\tilde{T}} \right) \cdot \tilde{\nabla}\tilde{\rho} = \alpha \nu \tilde{\rho} \tilde{\nabla} \cdot \frac{\tilde{\nabla}\tilde{T}}{\tilde{T}}$$

The mean free path Î»vg of vapours diluted in a carrier gas is small compared to the size of the particles suspended in the gas. In fact, for Na_2SO_4 vapours in air, the ratio of their molecular weights is $z = 142/28$, so that the mean free path λ_{vg} of vapours relative to that of pure air λ_g is (Davis 1983):

$$\lambda_{vg} = \sqrt{\frac{2}{1+z}} \frac{4\,\lambda_g}{(1+\sigma_v/\sigma_g)^2} \tag{3.2}$$

where σ_v and σ_g are the collision diameters of the vapour and of air molecules, respectively. We estimate $\sigma_g = 3.7 \times 10^8$ cm (based on the collision diameter of nitrogen) and $\sigma_v = 5.5 \times 10^8$ cm (based on the molecular volume of Na_2SO_4 in the solid phase). Hence, $\lambda_{vg}/\lambda_g = 0.371$, according to (3.2). At $T = 300\,K$, $\lambda_g = 0.065$ μm, and at $T = 1400\,K$ it is 1400/300 times this, or 0.3 μm. Equation (3.2) yields $\lambda_{vg} = 0.11$ μm. Instead of (3.2), we may use the average length over which a vapour molecule randomizes its momentum (loses its sense of direction), see (8) in Peeters, Luijten and van Dongen (2001):

$$\lambda_{vg} = \sqrt{\frac{1+z}{2}} \frac{4\,\lambda_g}{(1+\sigma_v/\sigma_g)^2}$$

which yields $\lambda_{vg} = 0.34$ μm at $T = 1400\,K$. This is still relatively small. Thus, we can consider that supersaturated vapour condenses on a spherical particle of radius 1 μm by diffusion. The diffusive flux of vapour diluted in the incompressible carrier gas is $\tilde{J}_v = D\,4\,\pi\,\tilde{r}^2 \partial c/\partial r$, which yields $\tilde{c}(\tilde{r}) = \tilde{c}\tilde{J}_v/(4\,\pi\,D\,\tilde{r})$ provided the flux is constant and $\tilde{c}$ is the vapour density far from the droplet whose radius is a. At the droplet, $\tilde{c}(a) = \bar{c} < \tilde{c}$, so that the diffusive flux towards the droplet is $\tilde{J}_v = 4\,\pi, , D\,a(\tilde{c}\bar{c})$, and it should equal the rate at which the droplet captures vapour molecules, $d\tilde{n}/d\tilde{t}$. In the stationary gas flow we consider, $d\tilde{n}/d\tilde{t} = (\tilde{u}\nu\,\alpha\tilde{\nabla}\ln\tilde{T}) \cdot \tilde{\nabla}\tilde{n}$. The simplest model for the vapour concentration at the surface of a droplet is that absorption and desorption of vapour molecules is so fast that $\tilde{c} = \tilde{c}e$, the equilibrium number density of vapour. Since $a = [3vn/(4)]1/3$ (v is the molecular volume of vapour), we have:

$$\tilde{u}\alpha\,\nu \frac{\tilde{\nabla}\tilde{T}}{\tilde{T}} \tilde{\nabla}\tilde{n} = D\,l\,\tilde{n}^{1/3}(\tilde{c}\tilde{c}_e)H(\tilde{c}\tilde{c}_e),$$

where $l = (48\,\pi^2\,v)^{1/3}$ and $H(x)$ is the Heaviside unit step function.

As we know, in the case of homogeneous condensation the condensation region is wide even when the rate of vapour scavenging by droplets is large. The vapour condenses in the free molecular regime on the droplets, which are thermophoretically attracted to the wall. In the case of heterogeneous condensation on spherical particles much larger than the mean free path of gas molecules (with a diameter of 1 μm), as it has being considered in [79], the vapour condenses in the continuum regime and the condensation region is narrow. We will see that homogeneous condensation is absolutely dominant over that case of the heterogeneous condensation. However, when another kind of heterogeneous condensation is included, that is, occurring on nanometric particles forming soot agglomerates, whose structure is open enough for the condensation on the free molecular regime to be applicable, situation changes producing an even more intense condensation process.

In all cases, the presence of vapours and suspended solid particles does not affect the laminar boundary layer flow of the carrier gas, which is described by coupled ordinary differential equations in a similarity variable. If the heat of vaporization is much larger than the thermal energy (temperature times the Boltzmann constant) far from the wall, vapour condensation occurs in a condensation layer (CL) whose distance to the wall, width and characteristics depends on the parameters of the problem. Outside the CL, the vapour is undersaturated and it cannot condense on the solid particles suspended in the carrier gas. In contrast to this dry region, there is a condensation region closer to the cold wall where condensation

3.1 Mixed condensation with heterogeneous condensation in the continuum regime

3.1.1 complete model

This model follows the basic lines of the previous homogeneous one and will be applied to the same kind of stagnation-point flow. We are adopting underlined and bar over for the heterogeneous and homogeneous specific variables respectively, while plain bold represent the concentration in the mixed case.

3.1.1.1 equations

$$
\begin{aligned}
&U\underline{\rho}' + \alpha\left(\frac{T'}{T}\right)'\underline{\rho} + \frac{B\,\mathbf{c}^2}{S_c\sqrt{6\pi\epsilon}}\exp\left(-\frac{1}{2\boldsymbol{\eta}^2T^3\epsilon^3}\right)H\left(\mathbf{c}-c_e\right) = 0\,, && \underline{\rho}\left(+\infty\right) = 0\\
&U\underline{n}' + \frac{B}{S_c}\left(\mathbf{c}-c_e\right)T^{1/2}\underline{n}^{2/3}H\left(\underline{n}-n_*\right)H\left(\mathbf{c}-c_e\right) = 0\,, && \underline{n}\left(+\infty\right) = 0
\end{aligned}
\tag{3.3}
$$

$$
\begin{aligned}
&U\bar{\rho}' + \alpha\left(\frac{T'}{T}\right)'\bar{\rho} = 0\,, && \bar{\rho}\left(+\infty\right) = 1\\
&U\bar{n}' + N\,G\left(\mathbf{c}-c_e\right)\bar{n}^{1/3}H\left(\mathbf{c}-c_e\right) = 0\,, && \bar{n}\left(+\infty\right) = 1\\
&G = \frac{1+K_n}{1+1.71K_n+1.333K_n^2}; \qquad K_n = \frac{l_p}{r_p}\\
&\mathbf{c}'' + S_c\,u\,\mathbf{c}' - B\left[\frac{\epsilon^{-7/2}\mathbf{c}^2}{\sqrt{6\pi}\boldsymbol{\eta}^3T^3}\exp\left(-\frac{1}{2\boldsymbol{\eta}^2T^3\epsilon^3}\right)H\left(\mathbf{c}-c_e\right)\right] -\\
&\qquad\left(\mathbf{c}-c_e\right)\left[RG\;\bar{\rho}\,\bar{n}^{1/3} + B\,T^{1/2}\underline{\rho}\,\underline{n}^{2/3}H\left(\underline{n}-n_*\right)\right]H\left(\mathbf{c}-c_e\right) = 0\\
&\qquad\qquad\qquad\qquad\qquad\qquad\qquad\qquad\qquad\qquad \mathbf{c}\left(0\right) = c_e(0); \qquad \mathbf{c}\left(+\infty\right) = 1
\end{aligned}
$$

3.1.1.2 numerical results

Vapour concentration and droplet sizes and densities profiles have been obtained for a wall temperature of 1000 K and are indicated in Figures 3.1 to 3.5. First noticeable thing is the dominance of the homogeneous condensation over the heterogeneous, mainly because the latter is occurring in the continuum regime. Differences may be observed in the droplets formed by nucleation, on one hand the density reduces and on the other the size increases, but the total number of condensate remains approximately the same. A consequence of that is the almost unaltered concentration profile. We can conclude that, curiously, the presence of the particles reduces the nucleation but not the condensation.

3.1.2 iterative procedure I

Another way for tackling the mixed condensation is by resorting of the previous models of heterogeneous and homogeneous condensation and combining them alternatively in

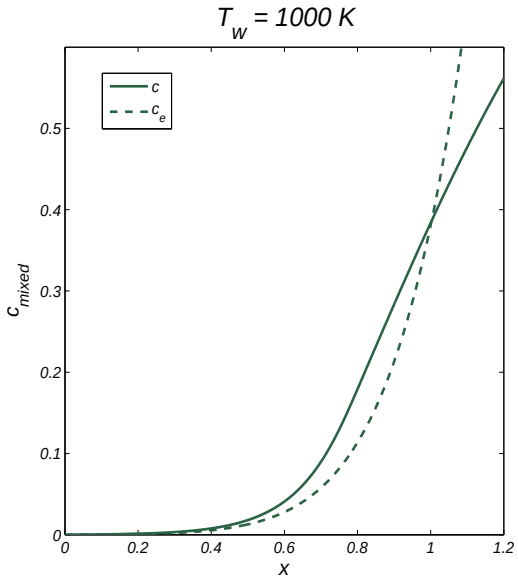

Figure 3.1: Profile of the vapour number density $c(x)$ for a wall temperature of $1000\,K$ as obtained from the complete model for mixed condensation. The profile for homogeneous condensation only, is indistinguishable from the former.

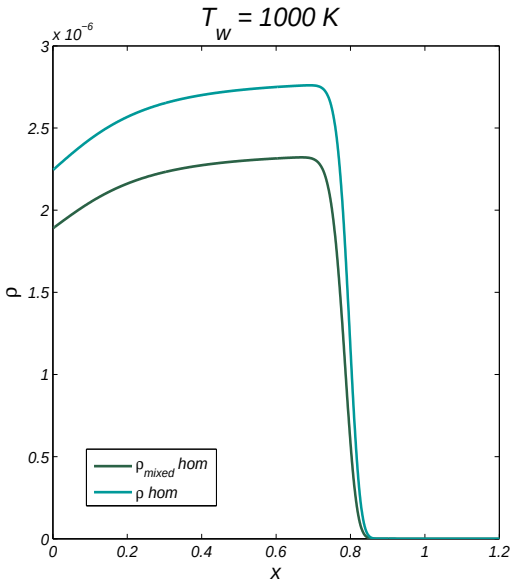

Figure 3.2: Profile of the droplet number density $\rho(x)\,hom$ for a wall temperature of $1000\,K$ as obtained from the complete model for mixed condensation and from homogeneous condensation only. This density refers to droplets resulting from condensation on the supercritical nuclei.

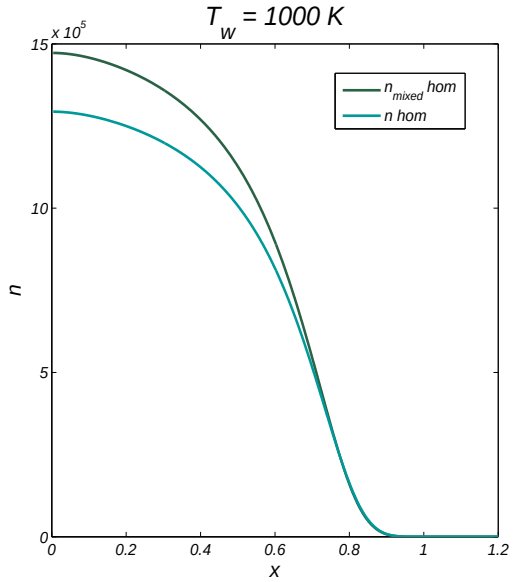

Figure 3.3: Profile of the condensate number $n(x)\,hom$ for a wall temperature of $1000\,K$ as obtained from the complete model for mixed condensation and from homogeneous condensation only. This number refers to condensate on the supercritical nuclei.

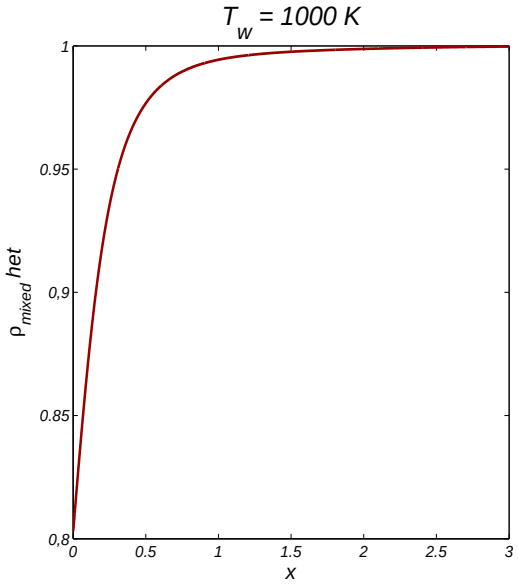

Figure 3.4: Profile of the droplet number density $\rho(x)\,het$ for a wall temperature of $1000\,K$ as obtained from the complete model for mixed condensation. This density refers to droplets resulting from condensation on solid particles. The profile for heterogeneous condensation only is indistinguishable from the former.

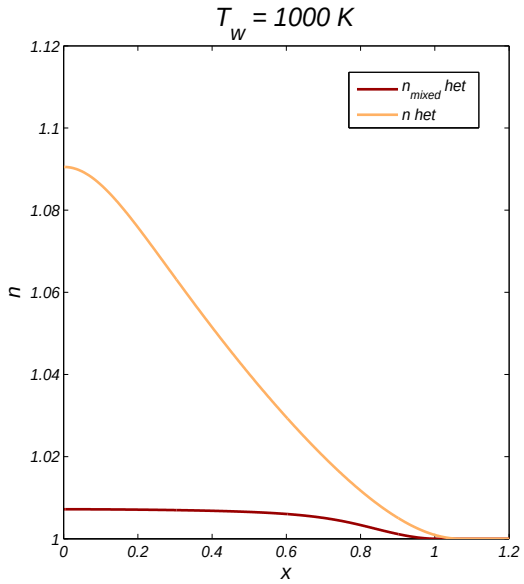

Figure 3.5: Profile of the condensate number $n(x)$ *het* for a wall temperature of $1000\,K$ as obtained from the complete model for mixed condensation and from heterogeneous condensation only. This number refers to condensate on solid particles.

an iterative scheme. Because of the extreme ill-posedness of the combined model, a less time consuming alternative procedure is advisable. Besides, the asymptotic approach will be probably more tractable if we attempt to manage heterogeneous and homogeneous condensation separately. On the other hand, consideration of the mixed condensation as split in two parts, an heterogeneous and an homogeneous ones, comes as a consequence of the linearity in c of the equations for the concentration in both models (if we except the relatively less important term due to nucleation in the homogeneous case). Equations for both separate models are written below:

Heterogeneous condensation

$$U\bar{\rho}' + \alpha\left(\frac{T'}{T}\right)'\bar{\rho} = 0\,, \qquad \bar{\rho}\,(+\infty) = 1$$

$$U\bar{n}' + N\,G\,(\bar{c} - c_e)\;\bar{n}^{\,1/3} H\,(\bar{c} - c_e) = 0\,, \qquad \bar{n}\,(+\infty) = 1$$

$$\bar{c}'' + S_c\,u\,\bar{c}' - R\,G\,(\bar{c} - c_e)\;\bar{\rho}\,\bar{n}^{\,1/3} H\,(\bar{c} - c_e) = 0\,, \qquad \bar{c}\,(0) = c_e(0); \quad \bar{c}\,(+\infty) = 1$$

Homogeneous condensation

$$U\underline{\rho}' + \alpha\left(\frac{T'}{T}\right)'\underline{\rho} + \frac{B\,\underline{c}^2}{S_c\sqrt{6\pi\epsilon}}\exp\left(-\frac{1}{2\eta^2 T^3\epsilon^3}\right) H\,(\underline{c} - c_e) = 0\,, \qquad \underline{\rho}\,(+\infty) = 0$$

$$U\underline{n}' + \frac{B}{S_c}\,(\underline{c} - c_e)\;T^{1/2}\,\underline{n}^{\,2/3} H\,(\underline{n} - n_*)\,H\,(\underline{c} - c_e) = 0\,, \qquad \underline{n}\,(+\infty) = 0$$

$$\underline{c}'' + S_c\,u\,\underline{c}' - B\left[\frac{\epsilon^{-7/2}\underline{c}^2}{\sqrt{6\pi}\eta^3 T^3}\exp\left(-\frac{1}{2\eta^2 T^3\epsilon^3}\right) + (\underline{c} - c_e)\;T^{1/2}\,\underline{\rho}\,\underline{n}^{\,2/3} H\,(\underline{n} - n_*)\right]$$

$$H\,(\underline{c} - c_e) = 0\,, \qquad \underline{c}\,(0) = c_e(0); \quad \underline{c}\,(+\infty) = 1$$

Equilibrium vapour density equation is common to both models

$$c_e(x) = \frac{T_d}{T(x)}\exp\left[\frac{\Lambda}{\epsilon}\left(\frac{1}{T_d} - \frac{1}{T(x)}\right)\right]$$

Mixed condensation

$$\mathbf{c} = \frac{\bar{c} + \underline{c}}{2}$$

$$\mathbf{c}'' + S_c\,u\,\mathbf{c}' - B\,\left[\frac{\epsilon^{-7/2}\mathbf{c}^2}{\sqrt{6\pi}\boldsymbol{\eta}^3 T^3}\exp\left(-\frac{1}{2\boldsymbol{\eta}^2 T^3\epsilon^3}\right) H\,(\mathbf{c} - c_e)\right] -$$

$$(\mathbf{c} - c_e)\left[R\,G\;\bar{\rho}\,\bar{n}^{\,1/3} + B\,T^{1/2}\,\underline{\rho}\,\underline{n}^{\,2/3} H\,(\underline{n} - n_*)\right] H\,(\mathbf{c} - c_e) = 0$$

$$\mathbf{c}\,(0) = c_e(0); \quad \mathbf{c}\,(+\infty) = 1$$

$$\mathbf{n} = \bar{n} + \underline{n}$$

$$U\mathbf{n}' + (\mathbf{c} - c_e)\left[\frac{B}{S_c}\,T^{1/2}\,\underline{n}^{\,2/3} H\,(\underline{n} - n_*) + N\,G\,\bar{n}^{\,1/3}\right] H\,(\mathbf{c} - c_e) = 0\,, \qquad \mathbf{n}\,(+\infty) = 1$$

Now, because of quasilinearity of the concentration equation we split it in two parts and solve them independent and iteratively assuming different possible initial stages (the 0 subscript will mean initial stage solution):

1.- The concentration in the condensation region equals the equilibrium concentration $\mathbf{c}(x) = c_e(x)$ (0-CL theory). 0-CL theory might be applied indistinctly to heterogeneous or homogeneous condensation but for the homogeneous case droplet density remains undetermined. So, 0-CL theory is only a good option if assuming heterogeneous condensation.

2.- Only heterogeneous condensation is being produced, so we consider the solution, $\mathbf{c} = \bar{c}_0$.

3.- Only homogeneous condensation is being produced, so we consider the solution, $\mathbf{c} = \underline{c}_0$.

3.1.2.1 first option for the initial stage

Considering the first option, we can write:

First iteration, heterogeneous part

$$U\bar{\rho}_0{}' + \alpha\left(\frac{T'}{T}\right)' \bar{\rho}_0 = 0$$

$$\bar{n}_0{}' = -\frac{N}{R}\int_0^{x_*} \left(\frac{c_e'' + S_c\, u\, c_e'}{U}\,\bar{\rho}_0\right) \mathrm{d}x\,, \quad \text{for } x \le x_*$$

$$\bar{c}_0 = c_e\,, \quad \text{for } x \le x_*$$

$$\bar{c}_0'' + S_c\, u\, \bar{c}_0' = 0\,, \quad \text{for } x > x_*$$

$$\bar{\rho}_0\,(+\infty) = 1; \quad \bar{n}_0\,(+\infty) = 1; \quad \bar{c}_0\,(+\infty) = 1; \quad \bar{c}_0{}'(x_*+) = \bar{c}_0{}'(x_*-)$$

where x_* indicates the location of the dew point interface

Once we have the first iteration solution corresponding to the first stage, that is, $\bar{\rho}_0$, $\bar{n}_0$ and $\bar{c}_0$, we use it as an input for the next (homogeneous) solution.

Second iteration, homogeneous part

$$U\underline{\rho}_1{}' + \alpha\left(\frac{T'}{T}\right)'\underline{\rho}_1 + \frac{B\left(\bar{c}_0+\underline{c}_1\right)^2}{4S_c\sqrt{6\pi\epsilon}}\exp\left(-\frac{1}{2\eta_1^2T^3\epsilon^3}\right)H\left(\frac{\bar{c}_0+\underline{c}_1}{2}-c_e\right)=0$$

$$U\underline{n}_1{}' + \frac{B}{S_c}\left(\frac{\bar{c}_0+\underline{c}_1}{2}-c_e\right)T^{1/2}\underline{n}_1^{\,2/3}H\left(\underline{n}_1-n_{*0}\right)H\left(\frac{\bar{c}_0+\underline{c}_1}{2}-c_e\right)=0$$

$$\underline{c}_1'' + S_c\,u\,\underline{c}_1' - 2B\left[\frac{\epsilon^{-7/2}\left(\bar{c}_0+\underline{c}_1\right)^2}{4\sqrt{6\pi}\eta_0^3T^3}\exp\left(-\frac{1}{2\eta_1^2T^3\epsilon^3}\right)H\left(n_{*0}-\underline{n}_1\right)H\left(\frac{\bar{c}_0+\underline{c}_1}{2}-c_e\right)\right] -$$

$$\left(\underline{c}_1-c_e\right)H\left(\frac{\bar{c}_0+\underline{c}_1}{2}-c_e\right)\left[BT^{1/2}\underline{\rho}_1\underline{n}_1^{\,2/3}H\left(\underline{n}_1-n_{*0}\right)+RG\,\bar{\rho}_0\bar{n}_0^{1/3}\right]=0$$

$$\eta_1=\log\left(\frac{\bar{c}_0+\underline{c}_1}{2c_e}\right);\quad \underline{\rho}_1\left(+\infty\right)=0\,;\quad \underline{n}_1\left(+\infty\right)=0\,;\quad \underline{c}_1\left(0\right)=c_e(0);\quad \underline{c}_1\left(+\infty\right)=1$$

Now, process goes on iteratively up to some ith iteration:

ith iteration, heterogeneous part

$$U\bar{\rho}_{i-1}{}' + \alpha\left(\frac{T'}{T}\right)'\bar{\rho}_{i-1}=0$$

$$U\bar{n}_{i-1}' + N\left(\frac{\bar{c}_{i-1}+\underline{c}_{i-2}}{2}-c_e\right)G\,\bar{n}_{i-1}^{1/3}H\left(\frac{\bar{c}_{i-1}+\underline{c}_{i-2}}{2}-c_e\right)=0$$

$$\bar{c}_{i-1}'' + S_c\,u\,\bar{c}_{i-1}' - \left(\bar{c}_{i-1}-c_e\right)H\left(\frac{\bar{c}_{i-1}+\underline{c}_{i-2}}{2}-c_e\right)\left[R\,\bar{\rho}_{i-1}\,G\,\bar{n}_{i-1}^{1/3}+BT^{1/2}\underline{\rho}_{i-2}\underline{n}_{i-2}^{\,2/3}\right]=0$$

$$\bar{\rho}_{i-1}\left(+\infty\right)=1;\quad \bar{n}_{i-1}\left(+\infty\right)=1;\quad \bar{c}_{i-1}\left(0\right)=c_e(0);\quad \bar{c}_{i-1}\left(+\infty\right)=1$$

ith+1 iteration, homogeneous part

$$U\underline{\rho}_i{}' + \alpha\left(\frac{T'}{T}\right)'\underline{\rho}_i + \frac{B\left(\bar{c}_{i-1}+\underline{c}_i\right)^2}{4S_c\sqrt{6\pi\epsilon}}\exp\left(-\frac{1}{2\eta_i^2T^3\epsilon^3}\right)H\left(\frac{\bar{c}_{i-1}+\underline{c}_i}{2}-c_e\right)=0$$

$$U\underline{n}_i{}' + \frac{B}{S_c}\left(\frac{\bar{c}_{i-1}+\underline{c}_i}{2}-c_e\right)T^{1/2}\underline{n}_i^{2/3}H\left(\underline{n}_i-n_{*i}\right)H\left(\frac{\bar{c}_{i-1}+\underline{c}_i}{2}-c_e\right)=0$$

$$\underline{c}_i'' + S_c\,u\,\underline{c}_i' - 2B\left[\frac{\epsilon^{-7/2}\left(\bar{c}_{i-1}+\underline{c}_i\right)^2}{4\sqrt{6\pi}\eta_i^3T^3}\exp\left(-\frac{1}{2\eta_i^2T^3\epsilon^3}\right)H\left(n_{*i}-\underline{n}_i\right)H\left(\frac{\bar{c}_{i-1}+\underline{c}_i}{2}-c_e\right)\right] -$$

$$\left(\underline{c}_i-c_e\right)H\left(\frac{\bar{c}_{i-1}+\underline{c}_i}{2}-c_e\right)\left[T^{1/2}\underline{\rho}_i\,\underline{n}_i^{2/3}H\left(\underline{n}_i-n_{*i}\right)+RG\,\bar{\rho}_{i-1}\,\bar{n}_{i-1}^{1/3}\right]=0$$

$$\eta_i=\log\left(\frac{\bar{c}_{i-1}+\underline{c}_i}{2c_e}\right);\quad \underline{\rho}_i\left(+\infty\right)=0;\quad \underline{n}_i\left(+\infty\right)=0;\quad \underline{c}_i\left(0\right)=c_e(0);\quad \underline{c}_i\left(+\infty\right)=1$$

3.1.2.2 second and third options for the initial stage

Let us see now the last two options. Terms $\underline{\rho}\underline{n}^{2/3}$ and $\bar{\rho}\bar{n}^{1/3}$ at the equation of the concentration of the mixed model, are $O(1)$. So, because $B \gg R$, it is clear that homogeneous condensation is dominant respecting to heterogeneous, validating in principle the righteousness of the proposed iterative method as far as we take the homogeneous condensation as the initial stage. (heterogeneous and homogeneous condensation, because they are treated separately, shall develop dew point interfaces at different locations and it might be expected that such a circumstance yields specific numerical difficulties but numerical difficulties arise in fact depending on the relative dominance of each kind of condensation). Process can be written now, as:

First iteration, homogeneous part

$$U\underline{\rho}_0{}' + \alpha\left(\frac{T'}{T}\right)'\underline{\rho}_0 + \frac{B\,\underline{c}_0^2}{S_c\sqrt{6\pi\epsilon}}\exp\left(-\frac{1}{2\eta_0^2T^3\epsilon^3}\right)H\left(\underline{c}_0 - c_e\right) = 0\,, \qquad \underline{\rho}_0\left(+\infty\right) = 0$$

$$U\underline{n}_0{}' + \frac{B}{S_c}\left(\underline{c}_0 - c_e\right)T^{1/2}\underline{n}_0^{2/3}H\left(\underline{n}_0 - n_*\right)H\left(\underline{c}_0 - c_e\right) = 0\,, \qquad \underline{n}_0\left(+\infty\right) = 0$$

$$\underline{c}_0{}'' + S_c\,u\,\underline{c}_0{}' - B\left[\frac{\epsilon^{-7/2}\underline{c}_0^2}{\sqrt{6\pi}\eta_0^3T^3}\exp\left(-\frac{1}{2\eta_0^2T^3\epsilon^3}\right)H\left(n_* - \underline{n}_0\right) + \left(\underline{c}_0 - c_e\right)T^{1/2}\underline{\rho}_0\,\underline{n}_0^{2/3}H\left(\underline{n}_0 - n_*\right)\right]$$

$$H\left(\underline{c}_0 - c_e\right) = 0\,, \qquad \underline{c}_0\left(0\right) = c_e(0); \quad \underline{c}_0\left(+\infty\right) = 1$$

Second iteration, heterogeneous part

$$U\bar{\rho}_1{}' + \alpha\left(\frac{T'}{T}\right)'\bar{\rho}_1 = 0$$

$$U\bar{n}_1' + N\left(\frac{\bar{c}_1 + \underline{c}_0}{2} - c_e\right)G\,\bar{n}_1^{1/3}H\left(\frac{\bar{c}_1 + \underline{c}_0}{2} - c_e\right) = 0$$

$$\bar{c}_1'' + S_c\,u\,\bar{c}_1' - \left(\bar{c}_1 - c_e\right)H\left(\frac{\bar{c}_1 + \underline{c}_0}{2} - c_e\right)\left[R\,\bar{\rho}_1\,G\,\bar{n}_1^{1/3} + B\,T^{1/2}\underline{\rho}_0\underline{n}_0^{2/3}\right] = 0$$

$$\bar{\rho}_1\left(+\infty\right) = 1; \quad \bar{n}_1\left(+\infty\right) = 1; \quad \bar{c}_1\left(0\right) = c_e(0); \quad \bar{c}_1\left(+\infty\right) = 1$$

and so on.

3.1.3 some simplifications in the iterative procedure I

Next, two alternative simplifications are described, although they have only a theoretical interest for touching complementary aspects of the aforementioned procedure.

3.1.3.1 first simplification when using the second option

Another approach can be made for the latter option transforming the differential into algebraic equations. The basic idea is that the variables of the previous homogeneous condensation in the mixed condensation also satisfy the corresponding equations of isolated homogeneous condensation. Same occurs for the heterogeneous condensation:

In the mixed condensation, equation for the concentration reads

$$\bar{c}'' + \underline{c}'' + S_c\, u\, \bar{c}' + S_c\, u\, \underline{c}' - B\left[\frac{\epsilon^{-7/2}\,(\bar{c}+\underline{c})^2}{2\sqrt{6\pi}\boldsymbol{\eta}^3 T^3}\exp\left(-\frac{1}{2\boldsymbol{\eta}^2 T^3\epsilon^3}\right) H\left(\frac{\bar{c}+\underline{c}}{2}-c_e\right)\right]$$

$$-(\bar{c}-c_e)\left[R\,G\;\bar{\rho}\,\bar{n}^{\,1/3} + B\,T^{1/2}\underline{\rho}\,\underline{n}^{\,2/3} H\,(\underline{n}-n_*)\right] H\left(\frac{\bar{c}+\underline{c}}{2}-c_e\right)$$

$$-(\underline{c}-c_e)\left[R\,G\;\bar{\rho}\,\bar{n}^{\,1/3} + B\,T^{1/2}\underline{\rho}\,\underline{n}^{\,2/3} H\,(\underline{n}-n_*)\right] H\left(\frac{\bar{c}+\underline{c}}{2}-c_e\right) = 0$$

but

$$\underline{c}'' + S_c\, u\, \underline{c}' = B\left[\frac{\epsilon^{-7/2}\,\underline{c}^2}{2\sqrt{6\pi}\underline{\eta}^3 T^3}\exp\left(-\frac{1}{2\underline{\eta}^2 T^3\epsilon^3}\right) + (\underline{c}-c_e)\;T^{1/2}\underline{\rho}\,\underline{n}^{\,2/3} H\,(\underline{n}-n_*)\right] H\,(\underline{c}-c_e)$$

and

$$\bar{c}'' + S_c\, u\, \bar{c}' = R\,G\;(\bar{c}-c_e)\;\bar{\rho}\,\bar{n}^{\,1/3} H\,(\bar{c}-c_e)$$

because we assume that $\bar{c}$ and $\underline{c}$ are solutions of independent homogeneous and heterogeneous condensation processes.

Otherwise, in the mixed condensation, equation for the cluster density is

$$U\underline{\rho}' + \alpha\left(\frac{T'}{T}\right)'\underline{\rho} + \frac{B\,\mathbf{c}^2}{S_c\sqrt{6\pi\epsilon}}\exp\left(-\frac{1}{2\boldsymbol{\eta}^2 T^3\epsilon^3}\right) H\,(\mathbf{c}-c_e) = 0$$

but $\quad \underline{\rho}' + \alpha\left(\frac{T'}{T}\right)'\underline{\rho} + \frac{B\,\underline{c}^2}{2\sqrt{6\pi\epsilon}\underline{\eta}^3 T^3}\exp\left(-\frac{1}{2\underline{\eta}^2 T^3\epsilon^3}\right) H\,(\underline{c}-c_e) = 0$

which leads to $\quad H(\mathbf{c}-c_e) = \dfrac{-4\,H\,(\underline{c}-c_e)\;\underline{c}^2}{(\underline{c}+\bar{c})^2}\dfrac{\log\left(\dfrac{\underline{c}}{c_e}\right)}{\log\left(\dfrac{\underline{c}+\bar{c}}{2\,c_e}\right)}$

so, if we also assume $\bar{\rho}\,\bar{n}^{1/3} \approx 1$, we finally obtain an algebraic equation for $\bar{c}$, where $\underline{\rho}$, $\underline{n}$ and $\underline{c}$ are the solutions of the previous homogeneous condensation:

$$H(x)\left[B(x)+Z(x)\right]+\frac{\log\left(\dfrac{\underline{c}}{c_e}\right)}{\log\left(\dfrac{\underline{c}+\bar{c}}{2\,c_e}\right)}H(x)\left[Z(x)+\frac{\underline{c}+\bar{c}-2c_e}{(\underline{c}+\bar{c})^2}\left(R+\frac{B(x)}{\underline{c}-c_e}\right)\underline{c}^2\right]$$

$$+R\,(\bar{c}-c_e)\,H\,(\bar{c}-c_e)=0$$

being $\quad H(x)=H\,(\underline{c}-c_e)$

$$B(x)=B\,(\underline{c}-c_e)\;T^{1/2}\underline{\rho}\,\underline{n}^{2/3}H\,(\underline{n}-n_*)$$

$$Z(x)=\frac{B\,\underline{c}^2}{S_c\sqrt{6\pi\epsilon}}\exp\left(-\frac{1}{2\underline{\eta}^2T^3\epsilon^3}\right)$$

3.1.3.2 another simplification when using the second option

A different and conceptually clearer way to solve the heterogeneous condensation problem as the second stage after a previous homogeneous condensation, is based in the linearity of the concentration equation given that $\bar{\rho}\,\bar{n}^{1/3} \approx 1$. Besides, this equation is inhomogeneous due to the equilibrium concentration term:

$$c_{het}{}'' + S_c\,u\,c_{het}{}' + R\,G\,c_{het} - R\,G\,c_e = 0$$

Previous homogeneous condensation produces the appearance of a new inhomogeneous term:

$$c_{het_1}{}'' + S_c\,u\,c_{het_1}{}' + R\,G\,c_{het_1} - R\,G\,c_e + \left[c_{hom}{}'' + S_c\,u\,c_{hom}{}' + B\,T^{1/2}\rho_{hom}\,n_{hom}^{2/3}\right] = 0$$

In order to obtain the solution c_{het_1} without solving the second equation we should know the solution c_{het_0} of the homogeneous equation:

$$c_{het_0}{}'' + S_c\,u\,c_{het_0}{}' + R\,G\,c_{het_0} = 0$$

as a function of the known solution c_{het}. To do that, first, we have to seek another linearly independent solution of the inhomogeneous equation. Let this solution to be $f(x)\,c_{het}$, where $f(x)$ is unknown for the moment. Substituting in the first (inhomogeneous) equation, $f(x)$ can be found:

$$f(x)'' + f(x)'\left[\frac{2\,c'_{het}}{c_{het}} + S_c\,u\right] = 0$$

$$f(x) = Q + K\int \exp\left[-\frac{2\,c'_{het}}{c_{het}} - S_c\,u\right]\mathrm{d}x$$

Making use of the method of variation of parameters we write c_{het_0} as $a(x)\,c_{het} + b(x)\,f(x)\,c_{het}$ and substitute it in the homogeneous equation, imposing the condition $a(x)'c_{het} + b(x)'f(x)\,c_{het} = 0$. Thus, the following system is obtained:

$$a(x)'\,c_{het} + b(x)'\,f(x)\,c_{het} = 0$$

$$a(x)'\,c_{het}{}' + b(x)'\,\big(f(x)\,c_{het}\big)' - C(x)\Big(a(x) + b(x)\Big) = 0$$

$$C(x) = -R\,G\,c_e\,,$$

that may be arranged as the linear ODE's system:

$$a(x)' + \frac{C(x)}{c_{het}}\Big(a(x) + b(x)\Big) = 0$$

$$b(x)' + \frac{C(x)}{f(x)\,c_{het}}\Big(a(x) + b(x)\Big) = 0\,,$$

and therefore,

$$\Big(a(x) + b(x)\Big)' + \Big(a(x) + b(x)\Big)\frac{C(x)}{c_{het}}\left(1 - \frac{1}{f(x)}\right) = 0$$

$$a(x) + b(x) = \exp\left[-\int \frac{C(x)}{c_{het}}\left(1 - \frac{1}{f(x)}\right)\mathrm{d}x\right]$$

$$a(x) = \int \frac{C(x)}{c_{het}}\exp\left[-\int \frac{C(x)}{c_{het}}\left(1 - \frac{1}{f(x)}\right)\mathrm{d}x\right]\mathrm{d}x$$

$$b(x) = \int \frac{C(x)}{f(x)\,c_{het}}\exp\left[-\int \frac{C(x)}{c_{het}}\left(1 - \frac{1}{f(x)}\right)\mathrm{d}x\right]\mathrm{d}x$$

Once a solution of the homogeneous equation is known, it is possible to obtain another one and after, apply the method of variation of parameters again to solve any inhomogeneous equation, for instance, with $C(x) = -R\,G\,c_e + \left[{c_{hom}}'' + S_c\,u\,{c_{hom}}' + B\,T^{1/2}\rho_{hom}\,n_{hom}^{2/3} \right]$ that is what we're looking for.

3.1.4 iterative procedure II

Unfortunately, the iterative procedure I proved to be numerically non-convergent. For that reason we look for another procedure considering the mixed condensation in terms of the variation of concentration rather than of concentration itself. This way we assume the function c_s defined in §1.4, as the initial vapour number density. This function represents the solution of the advection-diffusion problem without neither nucleation nor condensation. Then, subsequent independent heterogeneous and homogeneous condensations will produce alternate variations Δc_{het} and Δc_{hom} that will reduce the function c_s.

3.1.4.1 equations

Model equations as a function of the total variation $\Delta c = \Delta c_{het} + \Delta c_{hom}$ read as follows:

$$
\begin{aligned}
&{c_s}'' - \Delta c'' + S_c\,u\,({c_s}' - \Delta c') - B\left[\frac{\epsilon^{-7/2}(c_s-\Delta c)^2}{\sqrt{6\pi}\eta^3 T^3}\exp\left(-\frac{1}{2\eta^2T^3\epsilon^3}\right)H(c_s-\Delta c-c_e)\right] - \\
&\qquad -(c_s-\Delta c-c_e)\left[R\,G\,\bar\rho\,\bar n^{1/3} + B\,T^{1/2}\underline{\rho}\,\underline{n}^{2/3}H(\underline{n}-n_*)\right]H(c_s-\Delta c-c_e) = 0 \\
&\qquad\qquad \Delta c\,(0) = \Delta c\,(+\infty) = 0 \quad \text{because } c_s\,(0) = c_e \text{ and } c_s\,(\infty) = 1 \\
&U\,\underline{n}' + (c_s-\Delta c-c_e)\,\frac{B}{S_c}\,T^{1/2}\underline{n}^{2/3}H(\underline{n}-n_*)\,H(c_s-\Delta c-c_e) = 0\,, \qquad \underline{n}\,(+\infty) = 1 \\
&U\,\bar n' + (c_s-\Delta c-c_e)\,N\,G\,\bar n^{1/3}H(c_s-\Delta c-c_e) = 0\,, \qquad \bar n\,(+\infty) = 1 \\
&U\underline{\rho}' + \alpha\left(\frac{T'}{T}\right)'\underline{\rho} + \frac{B\,(c_s-\Delta c)^2}{S_c\sqrt{6\pi\epsilon}}\exp\left(-\frac{1}{2\eta^2T^3\epsilon^3}\right)H(c_s-\Delta c-c_e) = 0\,, \qquad \underline{\rho}\,(+\infty) = 0 \\
&U\bar\rho' + \alpha\left(\frac{T'}{T}\right)'\bar\rho = 0\,, \qquad \bar\rho\,(+\infty) = 1
\end{aligned}
$$

From those equations we may implement the following iterative procedure assuming that heterogeneous condensation is the first to occur:

first iteration: $\Delta c_{_{hom}} = 0; \quad \Delta c_{_{het}} = \Delta c^1_{_{het}}$

$$-\Delta c^1_{_{het}}{}'' - \Delta c^1_{_{het}}{}' - \left(c_s - \Delta c^1_{_{het}} - c_e\right) N\, G\, \bar{n}^{1/3} H\left(c_s - \Delta c^1_{_{het}} - c_e\right) = 0,$$

because $c_s'' + S_c\, u\, c_s' = 0$

$$U\, \bar{n}^1{}' + \left(c_s - \Delta c^1_{_{het}} - c_e\right) N\, G\, (\bar{n}^1)^{1/3} H\left(c_s - \Delta c^1_{_{het}} - c_e\right) = 0$$

second iteration: $\Delta c_{_{hom}} = \Delta c^1_{_{hom}}; \quad \Delta c_{_{het}} = \Delta c^1_{_{het}}; \quad c^1 = c_s - \Delta c^1_{_{het}}$

$$-\Delta c^1_{_{hom}}{}'' - \Delta c^1_{_{hom}}{}' - \left(c^1 - \Delta c^1_{_{hom}} - c_e\right) B\, T^{1/2} \underline{\rho}^1 \left(\underline{n}^1\right)^{2/3} H\left(c^1 - \Delta c^1_{_{hom}} - c_e\right)$$

$$+\Delta c^1_{_{hom}} R\, G\, \bar{\rho}^1 \left(\bar{n}^1\right)^{1/3} - B\left[\frac{\epsilon^{-7/2}(c^1 - \Delta c_{_{hom}})^2}{\sqrt{6\pi}\eta^3 T^3} \exp\left(-\frac{1}{2\eta^2 T^3 \epsilon^3}\right) H\left(c^1 - \Delta c^1_{_{hom}} - c_e\right)\right] = 0;$$

$$\eta = \log\left(\frac{c^1 - \Delta c^1_{_{hom}}}{c_e}\right)$$

$$U\, \underline{n}^1{}' + \left(c^1 - \Delta c^1_{_{hom}} - c_e\right) \frac{B}{S_c} T^{1/2} \left(\underline{n}^1\right)^{2/3} H\left(c^1 - \Delta c^1_{_{hom}} - c_e\right) = 0$$

$$U\underline{\rho}^1{}' + \alpha\left(\frac{T'}{T}\right)' \underline{\rho}^1 + \frac{B\,(c^1 - \Delta c^1_{_{hom}})^2}{S_c\sqrt{6\pi\epsilon}} \exp\left(-\frac{1}{2\eta^2 T^3 \epsilon^3}\right) H\left(c^1 - \Delta c^1_{_{hom}} - c_e\right) = 0$$

and so on.

3.1.4.2 numerical results

The first four iterations profiles for the vapour concentration, the droplet number density and the number of condensate have been obtained for a wall temperature of 1000 K, and are shown in Figures 3.6 to 3.8. In the case of the fourth iteration, calculations have demanded an accuracy higher than the Matlab standard one, and, for that reason, we have used the Multiprecision Computing Toolbox from Advanpix, instead. However, fourth iteration doesn't improve absolutely the convergence but the third one had already produced very good results for the vapour number density and the number of condensate profiles respecting to the complete model, as it can be seen in Figures 3.6 and 3.8, while the droplet number density, indicated in Figure 7, is a little higher than the corresponding to the complete model. Maximum absolute relative error for the vapour number density in the third iteration respecting to the second, is below 0.04, thus, process can be stopped at that point. Failure of iterations beyond the third one is due to the non-realistic, although still relatively small, reduction of the vapour density profile around the condensation

layer, when condensation is split and analyzed separately in a sequential process, because condensate number and droplet density are extremely sensitive to variations in the vapour density.

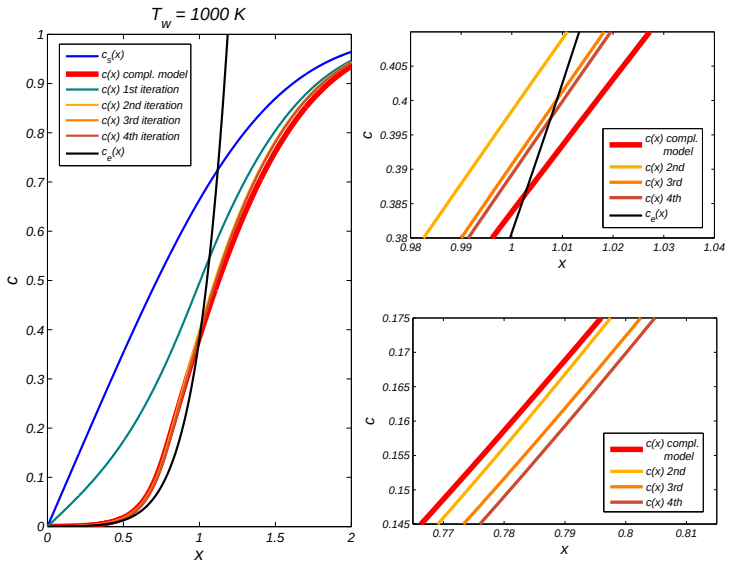

Figure 3.6: Left: 1st to 4th iterations profiles of the vapour number density $c(x)$ for a wall temperature of $1000\,K$. The 1st and 3rd iterations correspond to heterogeneous condensation while the 2nd and the 4th correspond to homogeneous condensation. Right: enlarged views of two zones, around the condensation layer and within it respectively, for noticing the difference between 2nd to 4th profiles.

3.2 Mixed condensation with heterogeneous condensation in the molecular regime

All the aforesaid applies when heterogeneous condensation is occurring in the continuum regime. Now we will discuss how to include the heterogeneous condensation in the molecular regime but in the case of fractal-like agglomerates (that represents the most general scenario) whose primary particles satisfy the condition $d_p \lesssim\ll \lambda\, K_n$, d_p, λ and K_n being the particle diameter, the mean free path of the condensible vapour molecules and the Knudsen number respectively. Condensation on the agglomerate is the simultaneous process of condensation on every particle pertaining it. Effective condensation on the particle is not proportional to its whole surface but to a reduced one, due to the screening effect of its neighbors. So, we have to start by characterizing in some way the structural geometry of the agglomerate in order to quantify the net surface to take in account for obtaining the condensation rate. In principle, it is not a trivial task and we will delay a

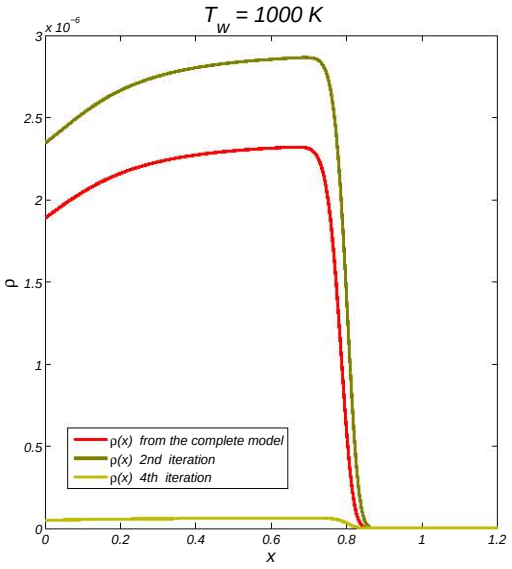

Figure 3.7: 2nd and 4th iterations profiles of the condensate number $n(x)$ for a wall temperature of $1000\,K$. Let notice that the 1st and 3rd iterations do not produce nucleation.

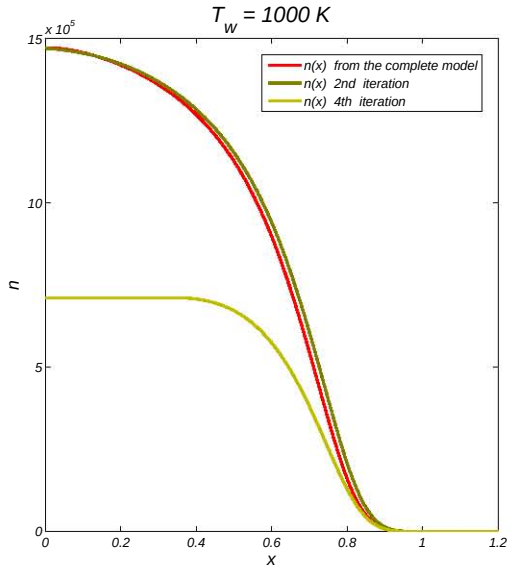

Figure 3.8: 2nd and 4th iterations profiles of the droplet number density $\rho(x)$ for a wall temperature of $1000\,K$. Let notice that the 1st and 3rd iterations do not produce nucleation.

more complete description of the agglomerate geometry for chapter 4 and look for a preliminary approximation considering chain-like agglomerates. Model follows the preceding one in the continuum regime.

3.2.1 complete model: chain-like agglomerates

Chain-like agglomerates have the simplest structure and the highest scavenging capacity. However, condensation rate becomes much more complex respecting to the isolated spherical particle. Condensation in the molecular regime results from a balance between vapour molecules hitting and escaping the particle surface, whose distributions are assumed to be Maxwellian. Direct incidence on a particle is affected by the presence of its neighbors in the chain. So, first thing is to obtain the incidence pattern of such a particle. It is reflected in Figure 3.9 by the red envelope around the black spherical particle, whose radial distances to the sphere represent, on each point of it, the number of incoming molecules per unit time and surface (We'll come back in detail to that calculation in chapter 4). Now, we haven't considered neither specular nor diffuse reflections because assume that every vapour molecule that hits the surface condenses on it.

3.2.1.1 model

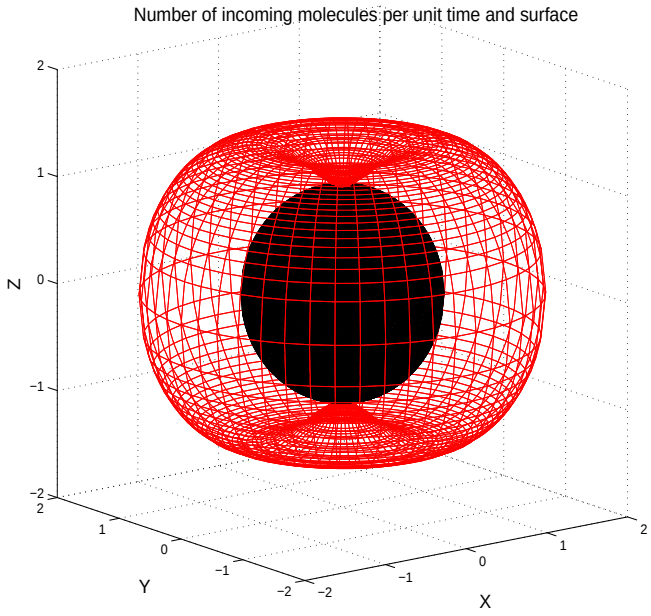

Figure 3.9: Incidence pattern on a spherical particle in a chain-like array.

As it can be seen in Figure 3.9, condensation rate on some point depends on its position over the surface. This way, thickness of condensate should vary from zero in the poles (contact points between particles) to a maximum in its equator, but it is reasonable to think that surface tension will produce an undulating surface with constant radii rather than a discontinuous one (see Figure 3.10).

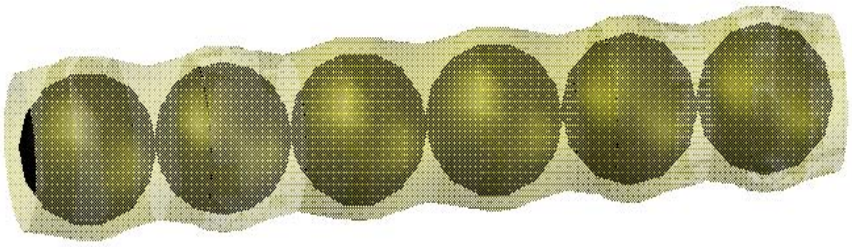

Figure 3.10: Condensate over a chain-like agglomerate.

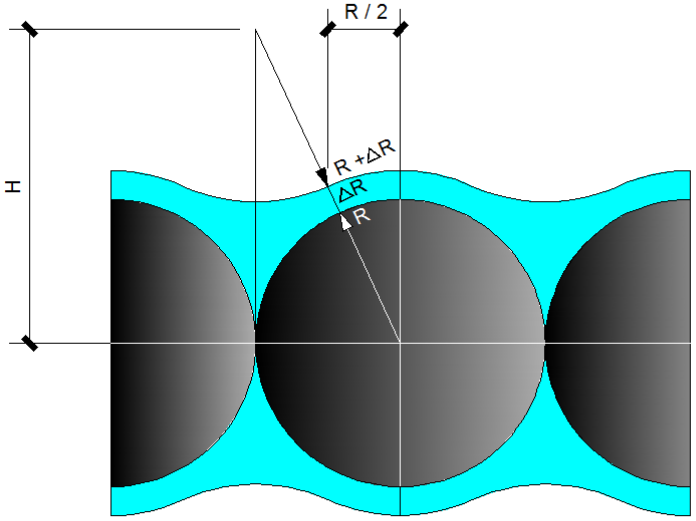

Figure 3.11: Transverse section of a chain-like agglomerate with condensed vapour around (cyan).

Denoting by V and S the volume and the lateral surface of the condensate unit corresponding to one particle (see Figure 3.11), we have:

$$H = 2(R+\Delta R)\sqrt{1+\left(\frac{R}{2(R+\Delta R)}\right)^2}$$

$$V = \pi\left[\frac{R\,H^2}{4} - H\,(R+\Delta R)^2 \arcsin\left(\frac{R}{2(R+\Delta R)}\right) + R\,(R+\Delta R)^2 - \frac{R^3}{12}\right]$$

$$S = 4\pi\,H\,(R+\Delta R)\arcsin\left(\frac{R}{2(R+\Delta R)}\right)$$

Expanding the square root in H and $\arcsin(z/2)$ in V by Taylor series, z being equal to $\dfrac{R}{R+\Delta R}$ and using $V = n\,\tilde{v}$, we obtain an approximate equation for z:

$$z^4 - z^2\left(248 + \frac{384\,n\,\tilde{v}}{\pi\,R^3}\right) + 1152 = 0$$

That is what has been considered in the proposed model whose equations (where particle radius R has been substituted by r_p) are:

$$U\underline{\rho}\,' + \alpha\left(\frac{T'}{T}\right)'\underline{\rho} + \frac{B\,\mathbf{c}^2}{S_c\sqrt{6\pi\epsilon}}\exp\left(-\frac{1}{2\boldsymbol{\eta}^2T^3\epsilon^3}\right)H\left(\mathbf{c}-c_e\right) = 0$$

$$U\underline{n}\,' + \frac{B}{S_c}\left(\mathbf{c}-c_e\right)T^{1/2}\underline{n}^{\,2/3}H\left(\underline{n}-n_*\right)H\left(\mathbf{c}-c_e\right) = 0$$

$$U\bar{\rho}\,' + \alpha\left(\frac{T'}{T}\right)'\bar{\rho} = 0$$

$$U\bar{n}\,' + N\,G\left(\mathbf{c}-c_e\right)\bar{n}^{\,1/3}H\left(\mathbf{c}-c_e\right) = 0$$

$$Un_g\,' + N_g\left(\mathbf{c}-c_e\right)S\,T^{1/2}\,H\left(\mathbf{c}-c_e\right) = 0$$

$$S = 8\pi r_p^2\left(\frac{1}{z}\right)^2\sqrt{1-\left(\frac{z}{2}\right)^2}\arcsin\left(\frac{z}{2}\right)$$

$$z = \sqrt{124 + \frac{192\,n_{gr}\,n_g\,\tilde{v}}{\pi\,r_p^3} - \sqrt{\left(62 + \frac{96\,n_{gr}\,n_g\,\tilde{v}}{\pi\,r_p^3}\right)^2 - 1152}}$$

$$\mathbf{c}'' + S_c\,u\,\mathbf{c}\,' - B\left[\frac{\epsilon^{-7/2}\mathbf{c}^2}{\sqrt{6\pi}\boldsymbol{\eta}^3T^3}\exp\left(-\frac{1}{2\boldsymbol{\eta}^2T^3\epsilon^3}\right)H\left(\mathbf{c}-c_e\right)\right] -$$

$$\left(\mathbf{c}-c_e\right)\left[RG\;\bar{\rho}\,\bar{n}^{\,1/3} + BT^{1/2}\underline{\rho}\,\underline{n}^{\,2/3}H\left(\underline{n}-n_*\right) + Bg\,\rho_g\,S\,T^{1/2}\right]H\left(\mathbf{c}-c_e\right) = 0$$

Other parameters and functions are:

$$B_g = \frac{\rho_{gr}\, l_b^2}{4\, D} \sqrt{\frac{8\, k_B\, T_\infty}{\pi\, m_V}}$$

$$N_g = \frac{B_g\, c_\infty}{S_c\, \rho_{gr}\, n_{gr}}$$

$U_g = u + \alpha_g \dfrac{T'}{T}$, flow velocity plus thermophoretic velocity of the agglomerate

$$\alpha_g = .75 \left(\frac{1 + \dfrac{a}{8(\pi/3 - 2)}}{1 + \dfrac{a}{8(\pi - 2)}} \right), \quad \text{agglomerate thermophoretic coefficient according to [37]}$$

$a = 0.75$, accommodation coefficient;

$r_p = 25\ nm$, particle radius

$n_{gr} = 0.7379 \times 10^6$, number of vapour molecules in a particle

$\rho_{gr} = 10^{12}\ m^{-3}$, agglomerate reference density

3.2.1.2 numerical results

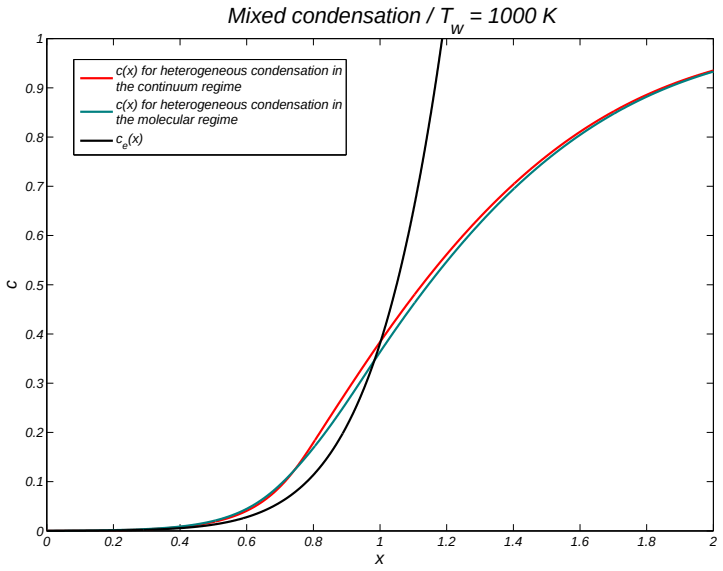

Figure 3.12: Vapour number density profiles for mixed condensation with and without condensation on nano-particulate agglomerates, for a wall temperature of $1000\,K$.

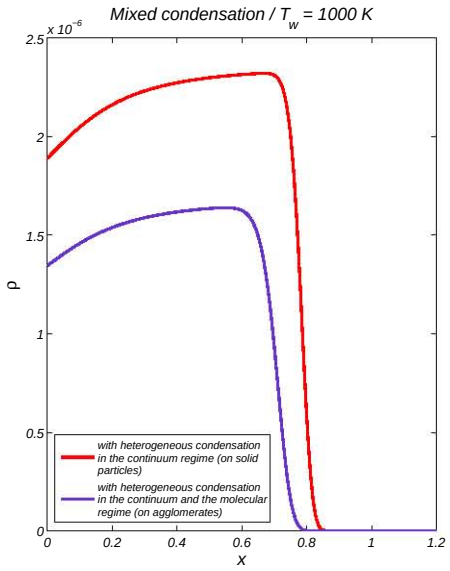

Figure 3.13: Droplet number density profiles for mixed condensation with and without condensation on nano-particulate agglomerates, for a wall temperature of $1000\,K$.

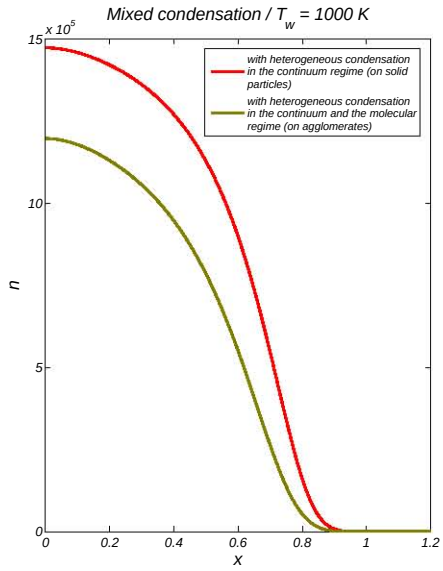

Figure 3.14: Number of condensate profiles for mixed condensation with and without condensation on nano-particulate agglomerates, for a wall temperature of $1000\,K$. We're referring here to condensate on supercritical nuclei.

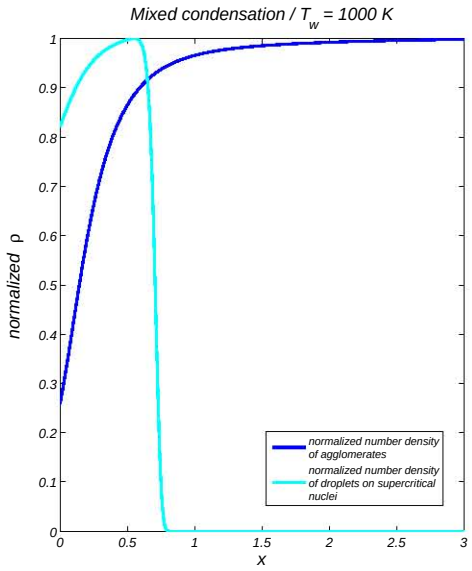

Figure 3.15: Comparison of normalized number density of agglomerates and droplets on supercritical nuclei, for a wall temperature of $1000\,K$

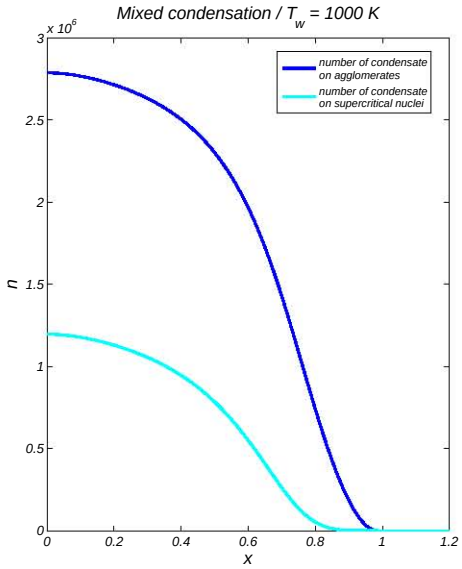

Figure 3.16: Comparison of normalized number of condensate on agglomerates and on supercritical nuclei, for a wall temperature of $1000\,K$

3.2.2 complete model: cylindrical approximation to chain-like agglomerates

Chain-like agglomerates can be treated as cylinders over which condensation is occurring longitudinally at an uniform rate. This approximation simplifies the calculations considerably and yields quite identical results.

3.3 conclusions

Some preliminary conclusions can be worked out from the mixed condensation model we have developed in this chapter. It has to de pointed out, nevertheless, that the model has only been applied to a wall temperature of $1000\,K$, considering from the results obtained from our precedent theory of homogeneous condensation (see §2.1) that it produces some kind of 'mean' behavior for the total range of interest $800\,K < T_w < 1200\,K$. The next step has to be, absolutely, to carry out simulations for the whole range of wall temperatures. Two points are, however, remarkable:

1. Presence of solid particles much larger than the mean free path of vapour particles reduces the nucleation process but not the condensation on the supercritical nuclei resulting from the former.

2. Presence of solid nanoparticles in the order of the mean free path of vapour particles (in the form of fractal-like agglomerates) reduces, as it could be expected, substantially both, the nucleation and the consequent condensation on the supercritical nuclei.

3. Mixed condensation may be approximated satisfactorily as a sequence of alternate homogeneous and heterogeneus condensation processes which might be useful for tackling a singular perturbation approach to the problem that is missing at the moment and we consider an important future task.

Chapter 4

The agglomeration process stochastically considered

Agglomeration processes take place in many different scenarios concerning colloid and aerosol formation. In this chapter we have modeled the creation of fractal-like soot agglomerates from primary nanoparticles inside a combustion chamber. The agglomeration process has been simulated by applying a random- diffusive mixed procedure in the 3D-space, consisting on calculate the mean translational diffusion coefficient of the agglomerate any time a new bond is formed. Particle-particle, particle-cluster and cluster-cluster aggregations have been considered for a cubic homogeneous volume with periodic boundary conditions at the six sides for typical residence times of soot inside a combustion chamber. The resulting agglomerate distributions for different times are characterized geometrically and it is proven that stable lognormal distribution functions are obtained. In addition to the classic ones, we are proposing two new parameters for characterizing the geometrical structure of the agglomerates, namely, the tree-ness and the eccentricity indexes. Results indicate a very interesting behavior of these parameters in the whole simulation.

4.1 Introduction

Given the complexity of interwoven phenomena present in the problem, we shall start by carefully depicting the context and the sequence of stages experienced by condensible molecules, aerosols and droplets in a physical space. Considering the wide scope we are attempting to cover with our theory, we have, in addition, to particularize for different geometrical scales. Lastly and for the sake of clarity, we have also preferred to point and comment, in advance to any reference to them, the bunch of terms, sometimes not too precisely delimited, usually found in aerosol classic literature. What are we strictly meaning with nucleation, condensation, collision, coalescence, coagulation and agglomeration, and which of these processes are expected to occur in our problem?

1. Nucleation means creating a new phase (liquid or solid) from vapour molecules giving rise to molecular clusters. A cluster become stable and, therefore, can undergo further growth, if it reaches some critical size. Then, they are called nuclei. Nuclei are primary particles (solid or liquid) but they are not usually called this way.

2. Condensation means creating a liquid phase on a nuclei (solid or liquid) or an aerosol (solid), from vapour molecules. This leads to the appearance of wholly liquid droplets or liquid droplets with a solid core. In general, we will call them droplets.

3. Collision is a kind of interaction (more precisely contactation) resulting from Brownian motion, laminar shear flow and turbulence. Collisions occur between droplets and/or aerosols.

4. Coalescence and coagulation are merging processes undergone by droplets and/or aerosols as a result of collisions, diffusion (if solid) or viscous flow (if liquid). New particles formed through these merging processes, can be properly called primary particles (liquid or solid). The process leading to them, in case collision has taken place, is specifically known as coagulation. In other case it is simply known as coalescence. Primary particles (if solid) may be spherical or not. Primary particles comprehend two size groups that are known as the ultrafine mode (size of less than 100 nm) and the accumulation or fine mode (size from 100 nm to 1 micron). Sometimes coalescence cannot be seen as a merging process because it is not the case of small particles giving rise to a larger one but exactly the opposite. This kind of coalescence leads to what is called the coarse mode (size larger than 1 micron but normally less than 100 microns) and occurred, for instance, in the flyash formation when inorganic contaminants fuse and coalesce during coal particles combustion.

5. Some spherical primary particles (liquid or solid) produce bigger spherical particles by further collision or viscous flow in the contact zone. Those primary particles are called coalescing.

6. A different merging process is undergone by the other kind of spherical primary particles (called noncoalescing) and the nonspherical primary particles, both solid. Spherical noncoalescing particles, by collision between them, by collision with nonspherical ones or by diffusion in the contact zone, produce agglomerates (solid). Agglomerates are never spherical but fractal-like. The process leading to them is specifically known as agglomeration. Agglomerates belongs to the coarse mode.

A term in aerosol vocabulary that hasn't a sole accepted meaning is aggregation. For some authors it refers to a process in the largest scale, concerning the entanglement of agglomerates and for others is simply a synonym for merging.

Initially we have a gas (air) carrying multi-species condensible dilute vapours and aerosols with some known size distribution function, whose giving-rise processes (natural or man-made) can be ignored. Gas is flowing in the neighborhood of a solid wall to which the flow obliquely impinges at an angle ϕ respect to the wall normal vector. Original scenario is assumed to be isothermal but very close to the wall (assumed to be colder than the air) a boundary layer where temperature strongly decreases will be developed. In a first stage the initial known aerosol distribution will change due to coagulation process up to the temperature boundary layer (TBL). A velocity boundary layer (VBL) will be also developed. Positions of both TBL and VBL are, in principle, different, but for Prandtl number around unity (which is the case for air) TBL and VBL are of the same order of magnitude and for simplicity we shall consider them as coincident. Another question is the wall temperature. In steam boilers, wall temperature can be assumed to be constant because of the water evaporation process is taking place over there. A tall building on the seafront is presumably provided with air-conditioning or heating systems, so the assumption of constant wall temperature would be also acceptable.

Respecting to the aerosol size distribution, a big difference exists between the atmospheric and combustion chamber scales. In the latter case, soot, ashes and chemicals production are localized at the flame surroundings where a particle size distribution function may be known and we expect that a transition zone with high coagulation activity will exist before primary particles reach the wall; it is also possible that nucleation of some species starts at this zone, still far from the boundary layer, with very large supersaturation ratios [105]. In the open space on the seafront, situation is much less defined. On the marine atmospheric boundary layer intensive water evaporation and sea spray production due to wave-wind interaction are occurring, giving rise to saline aerosols, although it is very difficult to obtain measurement data of size distributions. However, some good attempts have been made for numerically modeling the structure of sea-salt aerosols (SSA) by means of what is known as the source function [27]. The source function is the sea-salt emission rate close to the surface of the sea and it depends on local wind speed over a whitecap area, taken conventionally at 10 m height. SSA usually range from tens of nanometers to several hundred microns. Coagulation seems not to be an important process in the formation of SSA.

Combustion byproducts in the atmosphere range from a few nanometers to tens of microns but at that moment, due to long residence times, substantial changes in size distribution have been produced. Residence times for combustion process are, of course, much lower, in the order of a few minutes.

When fuel combustion takes place, soot is the first aerosol to appear as results of hydrocarbons vaporization, with characteristic formation time of 10^{-4} sec. [68]. Its size is about tens of nanometers (ultrafine mode, [13, 59, 111]) but soot particles have a tendency to agglomerate forming larger particles and becoming primary particles for further coagulation-condensation processes. Soon after, vaporization of inorganic fuel impurities starts with subsequent chemical activity (sulphur, alkali and heavy metals compounds react and oxydize) which is followed by a nucleation-coagulation-condensation process mainly fed by heaviest molecules, in which submicron flyash or fine mode (under 0.1 μm size) is produced. Final product of combustion are flyash particles or coarse mode that, when assumed that an original coal particle of about $10 - 100$ μm has completely burnt, are in the range of $0.1 - 50$ μm.

Multi-species condensible vapours to be considered will depend on the situation we are trying to model but a distinction has to be made from alkalis and other metals [61, 62]. It is known that some salts when vaporize do not stay necessarily as a single-component (e.g. alkali halides) [58]. When $NaCl$ (quite abundant on the seafront atmosphere) evaporates, Na, Cl, $NaCl$ and Na_2Cl_2 vapours can exist simultaneously although decomposition in Na and Cl is not likely at weather temperatures. In other scenario, $NaCl$ is also responsible for most of alkali sulphates originated by fuel combustion in power sources, but in this case $NaCl$ impurities evaporate from the pulverized- coal particles surface and react with water vapour, O_2 (considering good air-fuel mixing) and SO_2 (from the oxidation of sulphur impurities) to produce Na_2SO_4 directly in the gaseous phase. Total reaction time is less than 2 sec. [68]. $NaCl$ is not the only source of Na in combustion process, because coal also contents it in atomic form (organically bound) and as NaO_2, so Na fate in combustion chambers is solid sodium silicates, $Na_xSi_yO_z$, (for combustion temperatures in the middle range, $1300 - 1850$ K, in case of coals with low chloride contents [112] or in the high one, > 1900 K, for silica-rich coals [80], coming mainly from reactions between atomic sodium and silica) and solid sodium oxide, both in flyashes, and liquid sodium sulphate and chloride in the form of droplets, in the cooler zones. Now, respecting to nucleation-coagulation-condensation processes, the problem that moves to controversy is whether the sodium sulphate is created from the sodium chloride in the gaseous or the liquid phase [68] [112]. In the latter case $NaCl$ has to previously nucleate in order to be able to react and no Na_2SO_4 condensation will be produced. Another possibilities are coalescence from Na and SO_x vapours or chemical reactions between condensed phases of $NaOH$ and SO_x [4].

4.2 Aerosols in a combustion context

Combustion processes with subsequent aerosol formation are present in everyday's life and industry. Specially relevant are the undesired side-effects of particulate matter, as the corrosion of boiler surfaces caused by deposition with chemical activity (*fouling*) and deposition with chemical activity and fusion (*slagging*) [4], pp. 300-301, or the appearance of serious health problems in the form of pneumoconiosis or lung cancer [41].

Particulate matter is profusely generated in the combustion of hydrocarbons, mostly of those with a high number of carbons in their chemical composition (coal, diesel, biomass, etc.). These hydrocarbons, when burning, form a wide variety of carbonated byproducts: gaseous hydrocarbons, hydrogen, oxygenated species like CO or CO_2 and tars [113], p. 58, but also inorganic compounds, because of the presence of inorganic impurities such as alkalies, chlorine or sulphur, which lead to the formation of inorganic gases (SO_x, NO_x) and salts ($NaCl$, Na_2SO_4).

The composition and geometry of the final products is a function of the combustion time stages and although a complete description is far from been depicted, the general features are understood [113], p. 58. Aliphatic and aromatic compounds of the hydrocarbons (present in tars) volatilize very quickly (with a characteristic time of about 10^{-4} *sec* [68], p. 184) and undergo subsequent chemical reactions, leading to the formation of soot particles (mainly aggregates of thousands of graphitic crystallites [113], p. 59), which have lost most of their original hydrogen, and polyaromatic hydrocarbons (PAH). Primary soot particles [48], whose size is about tens of nanometers, tends to stick together immediately after their formation (such a process is known as agglomeration), forming "fractal-like" structures. Further processes like coagulation and condensation will affect the shape and properties of the agglomerates at much larger times and it is precisely the study of those subsequent processes, the motivation of our work.

We shall consider a pulverized coal-fired boiler with a maximum combustion temperature of 1900 K and working at a pressure of 1 atm. Combustion of pulverized coal leads mainly to:

1. Soot primary noncoalescing spheres ($10-50$ nm) and soot fractal-like agglomerates of those spheres (in a very wide range of size, $0.01-1$ μm). Had the size distribution function of primary soot [19, 60, 117] be known the final distribution resulting from an agglomeration process could be modeled for different residence times [70].

2. Submicron flyash particles (size under 0.1 μm) produced by nucleation, condensation and coagulation of vaporized inorganic elements and compounds. Assuming a first monodisperse distribution of different inorganic molecules we can find a size distribution function for the submicron aerosols due to a nucleation-condensation-coagulation combined process [71], also for different residence times. For the species

considered at this step, nucleation will be regarded as a coagulation between single molecules instead of an energy-dependent process.

3. Large flyash particles (from 1 to 100 μm) produced by coalescence of coal inorganic mineral inclusions during combustion. This mode can scavenge particles from the submicron bin size [34]. An approximation for estimating the size distribution function for these large flyash particles is the assumption of full coalescence which means that all the ash in the char from a coal particle coalesces to form a single ash particle [4].

4.2.1 Submicron flyash formation: a model of coagulation

Dynamics of submicron flyash formation is determined by the general particulate balance equation [33]. Terms in the RHS correspond to nucleation, condensation, transport and coagulation respectively, but we shall assume nucleation as a single-particles-coagulation process so there will be three rather than four terms in the RHS. Species to be considered are metal oxides, i. e., CaO, and MgO formed from Ca and Mg that volatilize during the first stage of coal burning. We also assume that the oxidation reaction time is significantly smaller than the coagulation or condensation times so oxidation will always occur (if the environment contains O_2) in the gaseous state.

Some approaches to the coagulation process combines dynamic equations and experimental work [69]; another way to undertake the submicron flyash formation is by doing a stochastic simulation [93, 102]. A very simplified model rely in considering that coagulation occurs any time two particles come closer than two diameters center to center and it is assumed that coalescence is immediate, so the two particles transform into a new bigger one. We have considered two cubic lattices shifted in the 3D space containing 10^3 and 8^3 particles with diameters of 50 nm and 100 nm respectively. Results of the simulation are shown in Figures 4.1 to 4.4.

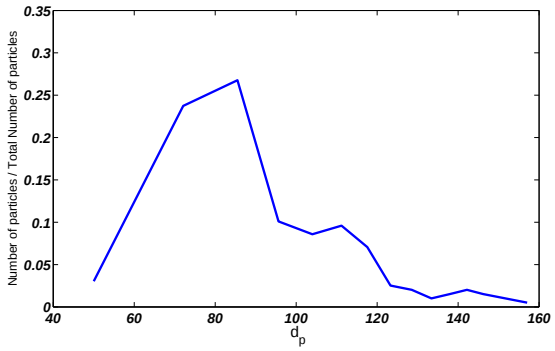

Figure 4.1: Size frequency distribution function of particle diameters

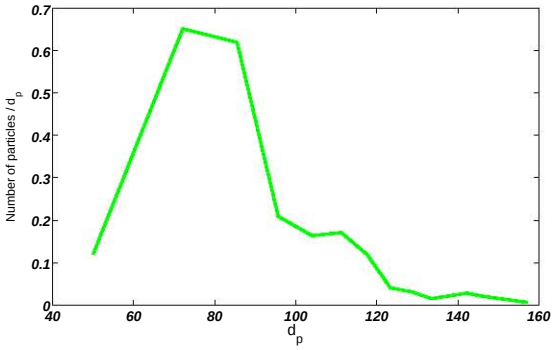

Figure 4.2: Size distribution function of particle diameters

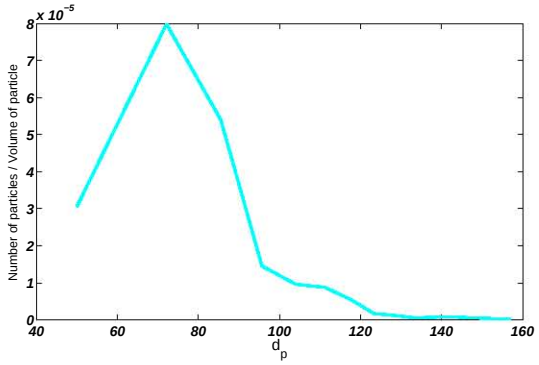

Figure 4.3: Size distribution function of particle volumes

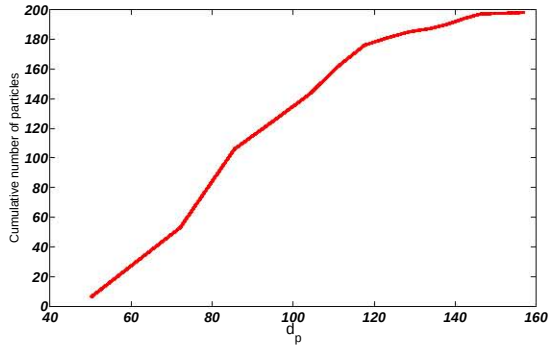

Figure 4.4: Cumulative size distribution function of particle diameters

4.2.2 Soot agglomeration

Primary soot particles agglomerate because of numerous collisions that take place under different mechanisms occurring in the system: Brownian motion, laminar shear and

turbulence [33], pp. 188 & 222, which all together constitutes a very complex nonlinear dynamic process. Let us imagine, for instance, a typical pulverized coal-fired boiler with a maximum combustion temperature of 1900 K and working at a pressure of 1 atm. A low-velocity forced ventilation is maintained for avoiding unburned particles to be dragged and thus, working regime in the combustion chamber is laminar. Under this conditions the movement of the agglomerating soot particles may be mainly described by a Brownian motion. There are different ways to obtain agglomerate size distributions: by numerical simulations of the agglomerate formation based on some random-like collision algorithms, by solving a kinetic (Smoluchowski) equation written in terms of a collision frequency factor [33] p. 230, [120] or by experimental measurements. Agglomerates are formed both by cluster-particle (primary) and cluster-cluster aggregation, however, the behavior for each one of these possibilities is slightly different, because of diffusion effects that are more important for particle-cluster than for cluster-cluster aggregation (particles can move within the clusters but clusters cannot do the same) [72]. Diffusion properties of particles can be taken in account through the equations but are absent from the numerical simulations; on the other hand, structural properties of the agglomerates can be devised from the numerical simulations but are invisible in the equations. One way to circumvent that situation is to obtain particle and cluster positions by solving the Langevin equation for each time step movement rather than by a random number generator [75] [25], modeling previously by some way the frictional resistance of the carrier gas in which agglomeration is occurring. Although, at a first sight, it looks contradictory to apply Langevin equation to the Brownian movement, whose velocity has no derivative, it is not if the Langevin differential equation is transformed into an integral one [20]. For describing soot agglomeration we must introduce in the Langevin equation not only the velocity due to Brownian movement but the bulk velocity of the gas too. Classical solution to Langevin equation has to be seen on a strictly probabilistic scope [18] nevertheless it is possible [18] [23] [25] to express this probabilistic scope through formal expressions for particle velocity and position (averaged values).

Another possible way is to carry out a Monte Carlo simulation based on the solution of the integral form of the Langevin equation (averaged values of the particle's position and velocity) [20] and this is the method we have used in this work. Models based on stochastic behavior may be found in [74, 84]. The adequacy of the stochastic fractal-like representation of soot agglomerates has been validated by several experimental works [76, 82, 94, 97].

There is still an additional problem concerning the description of the frictional resistance of the carrier gas. Theoretical calculations [32] are based in a virtual mathematical representation of the agglomerate by means of geometrical parameters but because of its strong dependence on the agglomerate structure that changes as the agglomerate grows, it would be necessary to calculate its diffusivity as the agglomerate is being created, based solely upon its structure . This can to be done either by determining hydrodynamics interactions (forces and/or torques), produced between primary particles in the agglomerate, from the Riseman-Kirkwood theory [90] (which is an extension of Langevin equation

to the configuration space of the agglomerate) or by solving Navier-Stokes equations for viscous flows close to and through the agglomerate, at low Reynolds numbers and neglecting inertial terms [57]. First of those methods seems to be more expeditious and, in fact, has been used satisfactorily for calculating viscoelastic properties of aerosols and polymer chains [116] and for computer program simulations of fractal aerosol dynamics [77]. Diffusive mobility of fractal aggregates has also been obtained through laboratory measurements leading to empirical expressions [109] or by assimilating the agglomerate to a porous media [100, 101]. The problem of those alternative methods is that in some step of the process the agglomerates have to be virtualized by their geometry. We tried to avoid that as far as possible.

In that follows we simulate soot agglomeration by applying a random-diffusive mixed procedure. It consists in calculate the mean translational diffusion coefficient anytime a new bond is formed and use it to control the subsequent movement random process through a weighted parameter which affects the displacement of the agglomerate. This way, we don't need to establish any *a priori* condition for the agglomerate structure. Calculations are done for different residence times. Initially size distribution function of soot particles is assumed to be monodisperse. Particle movement can occur in any spatial direction because displacements are given by real integers (randomly produced) times the particle path length (considered as Brownian) [33] and for that reason sticking condition is taken as $d_{pa} < 2d_p$, d_{pa} being the distance between particle centers and d_p their diameter, that is, two particles will bond when they are closer than the particle size.

Evolution of soot primary particles (with an initial monodisperse distribution) into agglomerates is given in terms of the number density, the fractal dimension and the radius of gyration of soot agglomerates at any time, $N_a(t)$, $R_a(t)$ and $E_f(t)$. Last two properties are defined as:

$$R_a = \sqrt{\frac{1}{n_a}\sum_i R_i^2} \qquad \text{radius of gyration of the agglomerate}$$

$$E_f = \frac{\ln(n_a)}{\ln(k_a R_a / r_p)} \qquad \text{agglomerate fractal dimension,}$$

where n_a is the number of particles per agglomerate, R_i is the distance from the center of mass to i^{th} particle and k_a is a proportionality constant known as the prefactor of the fractal scaling. Both E_f and k_a have to be obtained from the simulations [98].

4.3 Time step determination

Since the integral form of the Langevin equation does not take into account the interactions between the particles and the surrounding gas, a more complete description

including this effect can be obtained by using Hinch's theory [43], which introduce hydrodynamic considerations for calculating the averaged particle position.

It is important to precise that quite different approaches have been made to consider the hydrodynamic effect in the Langevin equation. Besides Hinch's, Batchelor [2] and Ermak and McCammon [26] works about the subject can be cited. Difference rests in which scale of interaction is being taken in account. Hinch studies the interaction between particles and fluid, so his approach is local, in a short range scale (we're referring here to a spatial and not to a time scale). But when a particle moves through a fluid produces alterations in it due to viscosity, vorticity, etc. and these alterations affect other particles (singles or not) present in the fluid. This is the long range effect that Batchelor considers. In dilute suspensions that effect is negligible.

For fixing the unit time step we obtain the time-dependent mean-square displacement of a particle according to two different approaches to Brownian motion, the simplest theory (1) and a more complex full hydrodynamic theory (2) [110] and compare them with the path length of a Brownian particle. As long as the theory of Riseman-Kirkwood applies in a medium range because it considers the interactions only between particles of the same agglomerate, we are considering short range effects for the Brownian dynamics of single particles that are corrected to the medium range as agglomeration is taken place.

$$\zeta = \frac{6\pi\mu_a r_p}{C} \qquad \text{particle friction coefficient}$$

$$C = 1 + \frac{l_a}{r_p}\left[1.257 + 0.4\exp\left(\frac{-1.1 r_p}{l_a}\right)\right] \qquad \text{slip correction factor}$$

$$l_a = \frac{1}{4\sqrt{2}\pi r_p^2 \rho_a} \qquad \text{mean free path of air molecules}$$

$$l_p = \frac{\sqrt{m k_B T}}{\zeta} \qquad \text{path length of a Brownian particle}$$

$$D_p = \frac{k_B T}{\zeta} \qquad \text{particle diffusion coefficient}$$

where m is the particle mass, T is air temperature, ρ_a is air number density and μ_a is air viscosity. Slip correction factor makes the first expressions to be valid for both the continuum and the free molecular regimes.

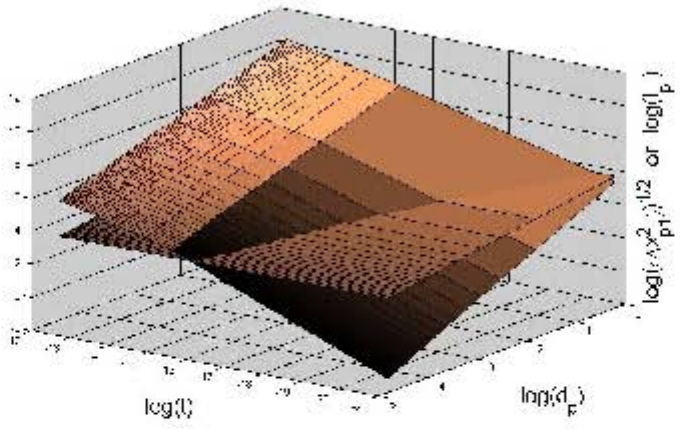

Figure 4.5: Square root of the mean-square displacement of soot primary particles according to theory (1) of Brownian motion (steepest surface) compared with their path length.

First theory gives:

$$\langle \Delta x_{p1}^2(t) \rangle = 2D_p \left\{ t + \Theta \left[\exp\left(-\frac{t}{\Theta} \right) - 1 \right] \right\}$$

$$\Theta = \frac{m}{\zeta} \qquad \text{particle relaxation time}$$

$$\tau = 2r_p \sqrt{\frac{m}{k_B\, T}} \qquad \text{freely stream time,}$$

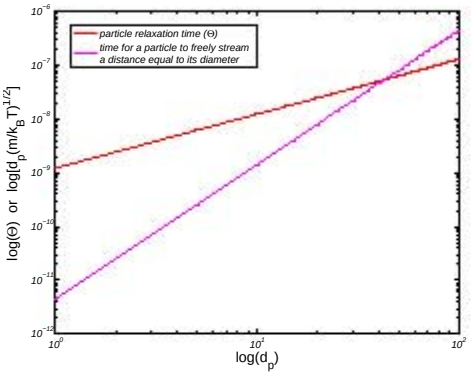

Figure 4.6: Particle relaxation time vs. freely stream time.

while the second one gives:

$$\langle \Delta x_{p2}^2(t) \rangle =$$

$$2D_p \left\{ t - 2\sqrt{\frac{\tau\, t}{\pi}} + \frac{2\tau}{9}\left(1 - \frac{\rho_p}{\rho_a}\right) + \frac{3}{\sqrt{\tau(5 - 8\rho_p/\rho_a)}} \left[\frac{1}{a_+^3} \mathrm{e}^{a_+^2 t} \mathrm{erfc}(a_+\sqrt{t}) - \frac{1}{a_-^3} \mathrm{e}^{a_-^2 t} \mathrm{erfc}(a_-\sqrt{t}) \right] \right\}$$

$$a_\pm = \frac{3}{2}\left[\frac{3 \pm \sqrt{5 - 8\rho_p/\rho_a}}{\sqrt{\tau}(1 + 2\rho_p/\rho_a)} \right]$$

$$\tau = \frac{r_p^2\, \rho_a}{\mu_a} \qquad \text{time for diffusion of vorticity across a particle radius}$$

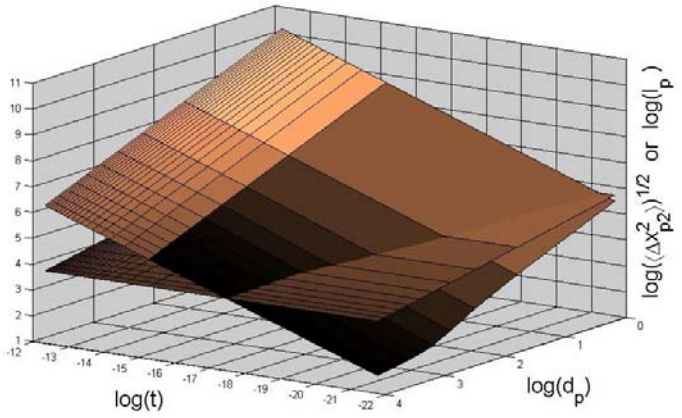

Figure 4.7: Square root of the mean-square displacement of soot primary particles according to theory (2) of Brownian motion (steepest surface) compared with their path length.

Figure 4.6 shows that particle relaxation time (characteristic time in Theory (1)) and freely stream time are of the same order of magnitude in the long range and they coincide for a particle diameter of 50 nm. Otherwise, Figure 4.8 indicates that the time scale for diffusion of vorticity (characteristic time in Theory (2)) is much smaller than the freely stream time. A consequence of the former is shown in Figures 4.7 and 4.9. It can be seen that the mean displacement according to Theory (2) is shifted to the short range zone if compared to mean displacement according to Theory (1). Figure 4.9 resumes the situation for the particle diameter of 50 nm. Curves for theories (1) and (2) join for long times. 50 nm is a soot diameter average and we will use it for the simulations.

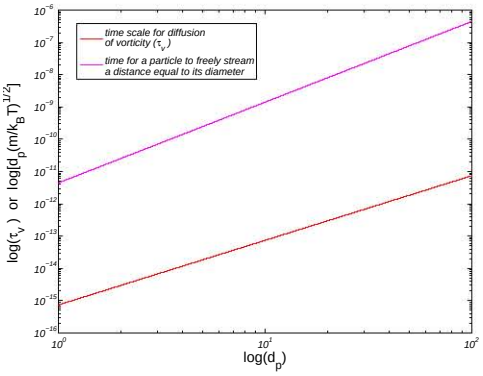

Figure 4.8: Time scale for diffusion of vorticity vs. freely stream time.

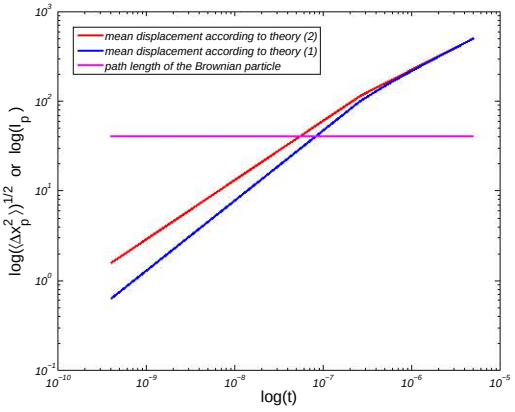

Figure 4.9: Comparison of theories (1) and (2) for a particle diameter of 50 nm.

4.4 Simulation details

Soot agglomeration process is simulated by applying a random-diffusive mixed procedure inside a small fraction of the total volume of a combustion chamber.

Initial particle configuration consist on a cubic lattice formed by $(N_p + 1)^3 = 8000$ particles with an inter-distance $S_p = 60\, d_p$ (see Figures 4.10 and 4.11 for more details). The number particle density in the domain according to these parameters happens to be $10^{12}\ cm^{-3}$, which is in the range expected in combustion chambers. Periodic boundary conditions has been fixed in the domain to preserve the particle density during the whole simulation, that is, particles that move out of the domain shall be re-injected from the opposite boundary.

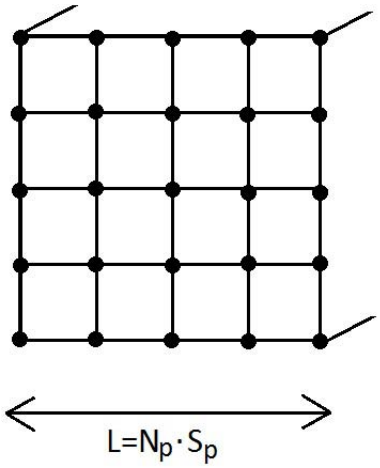

Figure 4.10: Cubic distribution of particles inside the domain

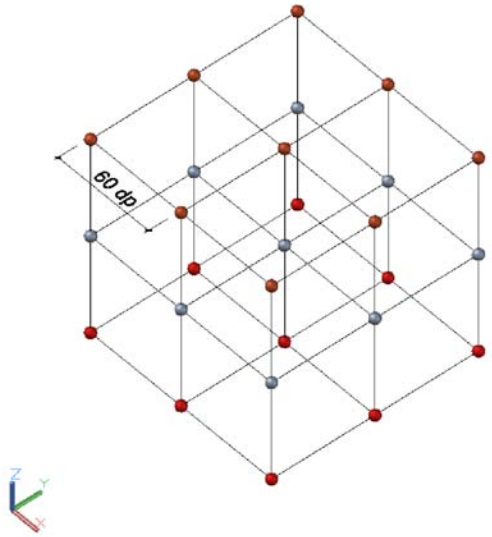

Figure 4.11: spacing in the cubic lattice

The number of computer iterations chosen for each simulation is 3×10^7. As the physical average time of each iteration is 2×10^{-7} seconds, according to Hinch's theory, the corresponding real time of our simulations is 6 seconds.

The agglomeration process is defined by considering that two particles whose centres are closer than $2d_p$ will agglomerate. Diffusion effects are taking into account by the mean translational diffusion coefficient [116] that is calculated anytime a new bond is formed

and is used to control the subsequent random movement process through a weighted parameter which affects the displacement of the agglomerate. The diffusion coefficients of the agglomerates (D_a) is estimated following Riseman-Kirkwood theory:

$$D_a = \frac{D_p}{n_a}\left(1 + \frac{r_p}{n_a}\sum_i \sum_j \left\langle \frac{1}{R_{ij}} \right\rangle\right)$$

where D_p is the particle diffusion coefficient, D_a is the agglomerate mean translational diffusion coefficient and R_{ij} is the distance from i^{th} to j^{th} particles in the agglomerate.

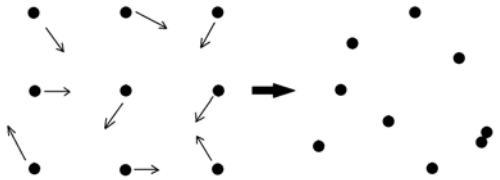

Figure 4.12: Random movement of particles at each time step. If two particles get close enough they are linked together

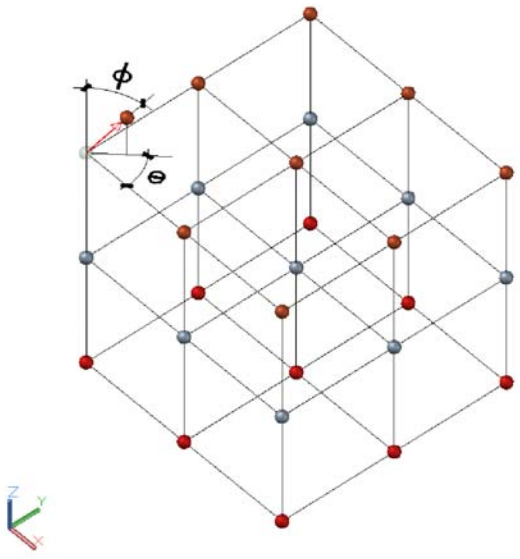

Figure 4.13: Random variables ϕ and θ

Every single particle has a certain constant diffusivity in the media which controls its (Brownian) motion and, thus, its spatial jump is fixed at the beginning of the simulation

($\langle \Delta x_{p2}^2 \rangle_p$) but diffusion coefficient of the agglomerates decreases as they increase their size, making their motion gradually slower in the media. This effect is simulated by multiplying the local spatial jump of the single particle ($\langle \Delta x_{p2}^2 \rangle_a$) by a decreasing factor defined as the ratio of the agglomerate and particle diffusivities:

$$\langle \Delta x_{p2}^2 \rangle_a = \langle \Delta x_{p2}^2 \rangle \frac{D_a}{D_p}$$

4.5 Numerical results

4.5.1 Parameters and constants

Numerical values of the constants and parameters that have been used are indicated in Table 3 with the following meanings: ρ_{soot} is the soot density, d_p the soot particle diameter, $N_{\rho_{\text{soot}}}$ the soot particle number density, T the air temperature, P_{air} the air pressure, μ_a the air viscosity (calculated using Sutherland relation), ρ_{air} the air density (considered as an ideal gas) and k_B the Bolztmann constant.

ρ_{soot} (g cm^{-3})	d_p (nm)	N_{soot} (cm^{-3})	T (K)	P_{air} (Pa)	μ_a (N s m^{-2})	ρ_{air} (kg m^{-3})	k_B (kg m^2 s^{-2})
2	50	10^{12}	1900	1.01325×10^5	6.20×10^{-5}	0.173	1.38×10^{-23}

Table 4.1: Constants and parameters used in the simulation

4.5.2 Statistical validation

A total of 120 simulations have been performed, that have allowed to obtain accurate statistic information about the temporal evolution of the radius of gyration and the number of particles per agglomerate, and consequently about the fractal dimension too. It is important to evaluate how the boundary conditions influence the simulation results. Periodic boundary conditions are normally fixed in order to preserve the soot number density, in other words, to simulate a small representative sub-volume of an homogeneous particle system. As it has already been pointed, we have also considered periodic boundary conditions, expecting that the combustion chamber (where the chemical reaction is taking place) may be approximated by successive repetitions of the simulation. However, this approximation may introduce errors in the simulation results if the size is small. On the other hand, a very large size of the simulation brings about a very high computational cost. Thus, the number of particles must be chosen considering a balance

between some acceptable computation time and some acceptable accuracy in the results. A good orientation shall be provided by studying the time evolution of the distribution function moments. An adequate size of the simulation should allow the moments to reach a quasi-steady zone. In this zone, simulation is expected to give rise to self-similar size distributions, a fact which has been widely observed for soot particles in diverse situations [33]. Statistical moments (geometric an logarithmic) can be obtained as follows:

$$
\begin{aligned}
N(t) &= \int_0^\infty n(v,t)\,\mathrm{d}v \\
f(\eta,t) &= \frac{n(v,t)\,\bar{v}(t)}{N(t)}, \qquad \text{size distribution function} \\
\langle v^k \rangle &= \int_0^\infty v\,n(v,t)\,\mathrm{d}v, \qquad k^{th} \text{ geometric moment of } n(v,t) \\
\langle \eta^k \rangle &= \frac{\langle v^k \rangle}{(\langle v \rangle)^k}\,N^{k-1}, \qquad k^{th} \text{ geometric moment of } f(\eta,t) \\
\langle \log^k(\eta) \rangle &= \int_0^\infty [\log(\eta)]^k\ f(v,t)\,\mathrm{d}\eta, \qquad k^{th} \text{ logarithmic moment of } f(\eta,t)
\end{aligned}
$$

where v is the agglomerate volume or the number of particles forming it, $n(v)$ is the number of agglomerates with volume v, $\bar{v}$ is the average volume of the agglomerates and $\eta = \dfrac{v}{\bar{v}}$ is the normalized volume. Significant moments are the corresponding to $k \geq 2$.

For studying the dynamics of the system during the simulation, data from 61 time points equally distributed during the whole simulation, were gathered. The global behavior of the system is followed by calculating the k^{th} discretized geometric and logarithmic moments of the agglomerate size distribution function, that we have called $\langle \eta^k \rangle$ and $\langle \ln^k(\eta) \rangle$ respectively, from the collected data:

$$
\begin{aligned}
\eta_i &= \frac{v_i}{\bar{v}} \\
\langle \eta^k \rangle &= \frac{\langle v^k \rangle}{(\langle v \rangle)^k}\,N^{k-1} \\
\langle v^k \rangle &= \sum_i v_i^k\,n_i(t) \\
\langle \ln^k(\eta) \rangle &= \frac{\bar{v}(t)}{N(t)} \sum_i \ln^k(\eta_i)\ n_i(t)
\end{aligned}
$$

$v_i(t)$ being the i^{th} agglomerate size (number of particles forming the agglomerate type i), $n_i(t)$ the number of agglomerates of the type i, $\bar{v}$ the average size of the agglomerates and $N(t)$ the total number of agglomerates, at a certain time.

Figure 4.14 show the averaged geometric (left) and logarithmic (right) moments from the 2^{th} to the 6^{th} order, for a total number of 8000 particles. It may be observed that, for the time considered, lower order geometric moments reach a steady state and higher order logarithmic moments show a slight asymptotic tendency (geometric and logarithmic moment orders stabilize in opposite directions). We may consider acceptable the adopted size of 8000 particles for the simulations although the time interval should be extended beyond 3×10^7.

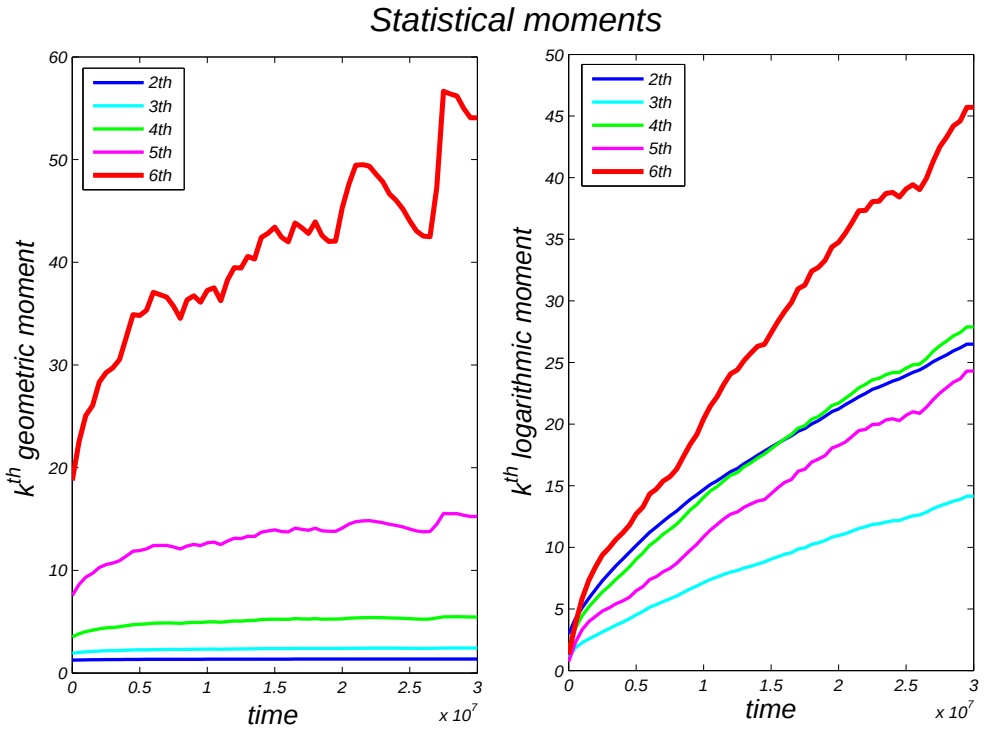

Figure 4.14: *Time evolution of the averaged geometric (left) and logarithmic (right) k^{th} moments, from the simulations.*

Agglomerate size distribution evolves in time to a lognormal pattern, with a maximum size of about 80 particles and a smooth decay as the size increases (see Figure 4.15). The maximum and the minimum sizes that have been obtained for the agglomerates are XXX and XXX particles respectively.

Normalized accumulated size distribution function of the agglomerate size distribution has also been obtained (see Figure 4.16).

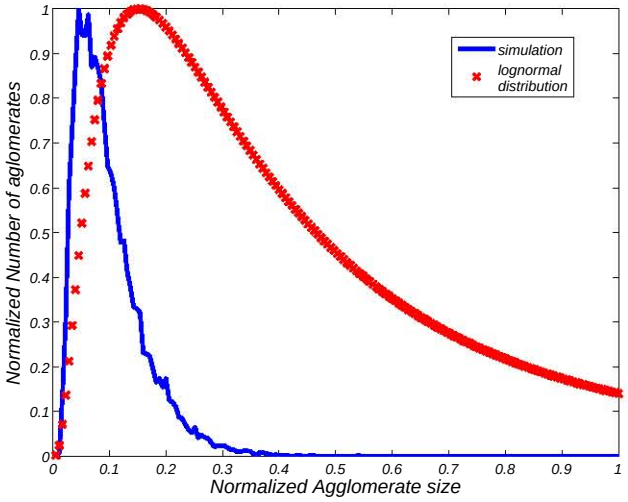

Figure 4.15: *Size distribution function of the simulation (blue) at time* $t = 5E6\Delta t$ *compared with a lognormal distribution. Similarity of the patterns may be observed.*

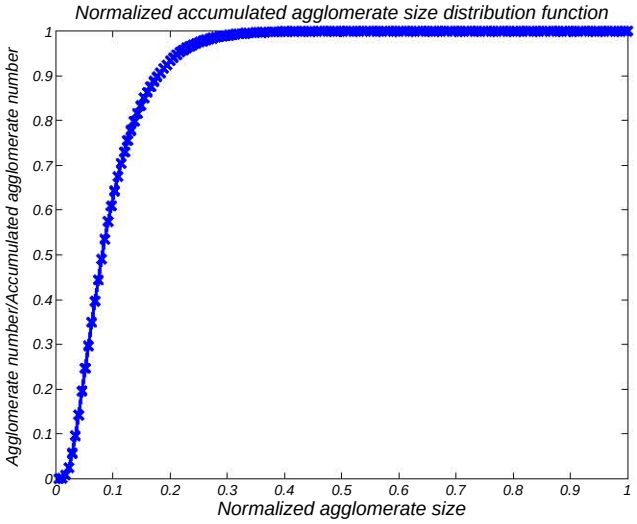

Figure 4.16: *Normalized accumulated size distribution function obtained from simulations.*

4.5.3 Geometrical characterization of the agglomerates

Comparing the agglomerate geometries only slight differences can be observed. Agglomerates obtained from our simulations show very open fractal-like structures (see figures

4.17 and 4.18) if compared with other simulations performed in lattices, with much longer times. Agglomerates are characterized in terms of the known fractal dimension (E_f) and radius of gyration (r_g). Both E_f and k_a are obtained by fitting the results from the simulations into a logarithmic relation:

$$\log(N_p) = \log(k_a) + E_f \log(r_g)$$

Figure 4.17: *Agglomerate containing 396 particles exhibits typical fractal-like structure. Radius of gyration*=27.75 d_p

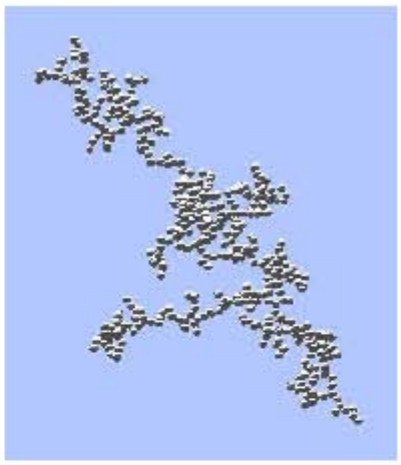

Figure 4.18: *Agglomerate containing 542 particles exhibits typical fractal-like structure. Radius of gyration*=31.08 d_p

By making a logarithmic fitting of the data (see figure 4.19) at different times, a curve of the fractal dimension vs. time may be obtained (see figure 4.20). The results show

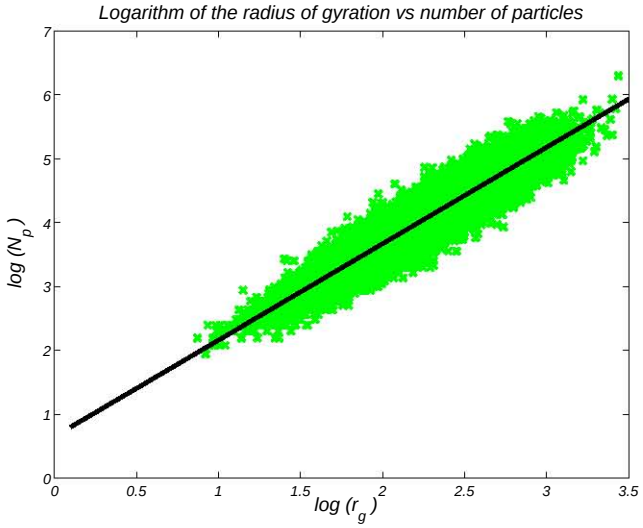

Figure 4.19: *Logarithmic relation between the radius of gyration and the number of particles per agglomerate, for a residence time of* $t = 6$ *seconds.*

values approaching asymptotically to 1.5. This dimension is lower than others reported as much as numerically as experimentally. It should be noticed that we are interested in simulating real soot agglomeration in the early stages of coal combustion whose typical residence times are in the order of a few seconds, with soot number densities around $10^{12}\, cm^{-3}$ (which gives particle spacing of around $60\, d_p$). Oppositely, in many other works the soot formation time is much longer (in the range of dozens of minutes) and the initial soot density is conveniently reduced for computational reasons to values giving smaller inter-distances of around $10\, d_p$.

For having a more intuitive insight into the geometrical structure of the agglomerates, two new parameters are proposed: the tree-ness and the eccentricity indexes (See Figures 4.21 and 4.22). They are defined as follows:

$$i_t^j = \frac{n_g^j}{12}, \qquad \text{tree-ness index of } j^{th} \text{ particle}$$

$$i_e^j = \frac{X_{CM} - X^j}{r_p}, \qquad \text{eccentricity index of } j^{th} \text{ particle}$$

where n_g^j is the number of particles tangent to j^{th}, X_{CM} are the generalized coordinates of the center of mass of the center of mass of j^{th} particle and its tangent neighbors and X^j are the generalized coordinates of j^{th} particle.

If we plot $i_t(N_a) - \lim_{N_a \to \infty}(i_t)$ versus N_a it can be seen that i_t evolves as $\frac{1}{N_a}$.

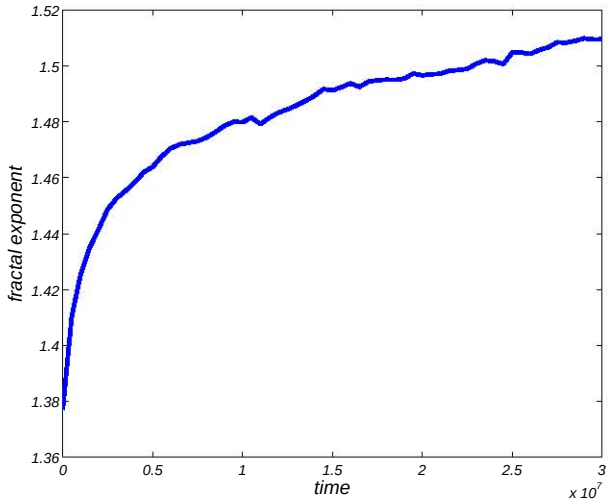

Figure 4.20: *Time evolution of the fractal exponent. For the considered time interval it may be observed an asymptotic tendency to a value close to 1.5.*

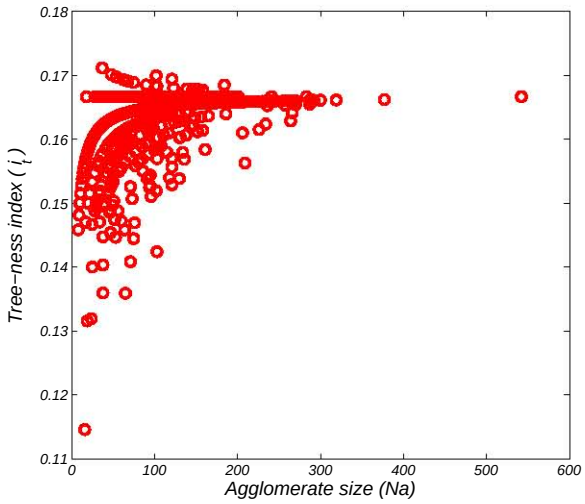

Figure 4.21: Tree-ness index resulting from our simulations.

4.6 Conclusions

In this chapter a Monte Carlo method for simulating the agglomeration of newborn soot particles inside a combustion chamber, is described. The volume is a cubic domain with periodic boundary conditions (to preserve particle density) and is filled with a total number of 8000 particles equally distributed modeling real soot particle densities in

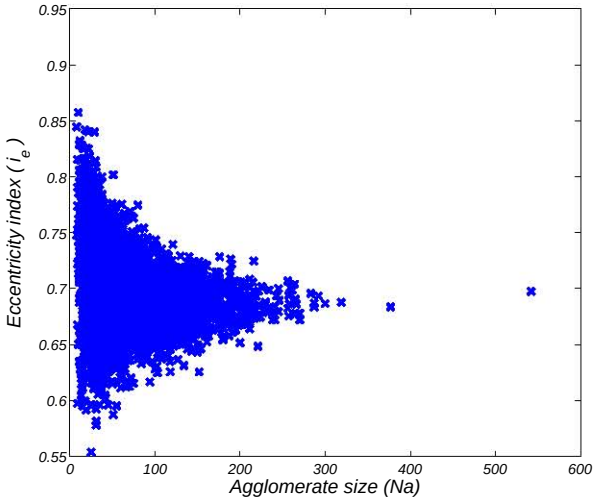

Figure 4.22: Eccentricity index resulting from our simulations.

combustion chambers. This size seems reasonable as the curves distribution function moment suggest, allowing to obtain a realistic particle distribution in the results, avoiding an excessive error by the use of periodic boundary conditions and ensuring an acceptable computational time (2 days) per simulation. The total number of iterations was 120, which is enough for providing statistically reliable results.

Particles jump a certain fixed distance in random directions defined by azimuthal and polar angles generated at each time step. As particles agglomerates the diffusion coefficient decreases and hence the mean distance they are able to cover. We model that by taking the jump of an agglomerate as a function of the ratio between the diffusion coefficient of the agglomerate (calculated following the Riseman-Kirkwood theory) and the diffusion coefficient of the single particle.

Physical time step was calculated by using the Hinch's hydrodynamic theory leading to a representative residence time of the simulations of about 6 seconds, which is in the order of the initial stages of soot production in combustion chambers.

We focused on studying the dynamic evolution of the radius of gyration against the number of particles in order to obtain the fractal dimension as a major soot geometric characterization parameter. Results show that, as expected, the fractal dimension increases with an asymptotic tendency to a value of 1.5 at the end of the time interval. Something has to be said about this apparently low fractal exponent if compared with the values closer to 2 that have been profusely found experimentally or by numerical simulations. The problem is that most studies in the matter are generally concerned with

environmental implications of soot production for which residence times are much larger than those controlling our problem, dealing with condensation on the chamber walls in the very beginning of combustion process. A not usual geometrical characterization of the agglomerates is presented by defining the tree-ness and the eccentricity indexes that evolves in time as the inverse of the agglomerate size.

This simple model may be extended to more complex situations involving, for instance, thermophoretic action over the agglomerates. A model for that situation is presented in the appendix A.

Chapter 5

Theory of homogeneous vapour condensation from counterflow boundary layers

5.1 Preliminars

We have developed a nucleation-condensation theory for the stagnation-point flow due to the impingement of an uniform flow against a wall (solid boundary). For the purpose, we have taken the classical solution of a potential flow in an infinite plane around an stagnation point ([1], pp. 105-106). But in fact it has been a first approximation to the problem of BL flows because it is know that that solution is only locally valid in the neighborhood of the stagnation point and it doesn't represent any real flow. Actually that kind of stagnation-point flow can only be the result of the impingement of a jet (=uniform flow of finite width) on a wall (or equivalently the impingement of two equal and opposite jets), whose solution has been usually obtained through conformal transformations. That solution gives a streamline equation slightly different to that of the classical plane stagnation-point flow we have employed ([73], pp. 303-304).

Now, we shall apply the former nucleation-condensation theory to another kind of flow where a BL without solid boundaries could be developed. The most general case we can consider for studying BL without solid boundaries is the impingement of two unequal (different breadths and velocities) coaxial jets. However, this case doesn't lead to a potential solution ([7], pp. 47-49 and 64-65). Solution for the case of different breadths but equal velocities can be found in ([73], pp. 305-306) and ([91], 11.3), obtained by using the formula of Schwarz. When the breadth of one jet is much larger than the breadth of the other, the first one becomes a stream (or in general a fluid body) and it is more properly to talk of jet penetration. Solution using conformal transformations for the case of a jet penetrating a stream, moving with velocity smaller than that of the jet, is obtained in [45].

The solution of the flow due to the impingement of two jets is a free-streamline one. A free-streamline is a streamline separating fluid in motion from fluid at rest and along it pressure and velocity are constant. It's worthy to say that in [45] solution has been obtained assuming that the jet velocity decreases up to the stream's one, along a free-streamline, which is not consistent. In general free-streamline solutions are harder to obtain and some approximations have been systematically done. If we intend to write down the equations of the problem of the impingement of tho unequal and opposite jets we shall have a clear evidence of the former statement. Unknowns are not only confined to the flow itself but to the boundary conditions too. We have to obtain, in addition to the velocity field, the equations for the free streamlines (FS) produced between each flow and the surrounding still fluid, the equation for the dividing streamline (DS) between the flows and the velocity of the diverging jets. If we tried to satisfy all the boundary conditions, equations for the irrotational flow are not sufficient so we would have to write, for instance, the biharmonic equation for the streamfunction.

Since we are interested specifically in the mixing layers appearing along the FS and the DS (and consequent nucleation and condensation on it), we can use the Boundary Layer Theory for studying them, by making some assumptions about the flows beyond the BL without solving the general rotational flow due to the impingement of two unequal jets. In that flow, either longitudinal or transverse BL (referred to the direction of the injection flow) shall appear depending whether we are looking to the FS or the DS. The longitudinal BL appears along the FS's. Now, we shall assume that jet velocities are uniform at the outlet. Very close to the jet outlet (at a distance from the edge of the outlet, larger than the Navier-Stokes limit, ν_I/V_I, ν_I and V_I being the viscosity and the velocity of the injected fluid, respectively), a BL, where longitudinal velocity decreases from V_I to 0, starts to develop. On the following we are considering Reynolds number not larger than 700, in order to assume laminar behavior on the BL. The general problem of the mixing layer between two parallel flows with different velocities is treated in [95]. We'd be focusing in the $\lambda = 0$ case. Let notice that, because of the uniform velocity, intereresting case is not the free jet (op. cit., 7.2.6), but the mixing layer problem (op. cit., 7.2.4).

In terms of its application to the nucleation-condensation theory, the former case poses a difference respecting to the transverse BL (that we shall see below). It refers to the lack of a characteristic time.

Now, we shall keep attention to the DS. Flows beyond the thin mixing layer along the DS are plane (not uniform as before) and we can assume in a first approximation that velocities parallel to the DS are linear in s (s being the coordinate along the DS). The reason for that assumption is that DS is a streamline (common to both fluids) and tangential velocity along it will reach a maximum equal to the velocity of the diverging jet at a distance very large compared to the jet radius. Thus, velocity is a monotonic increasing function of s. In a very narrow region close to the stagnation point (that is located at

some position on the common jet's axis and is the centerline of the DS) tangential velocities may be written as $U_e = A\,s$. Parameter A (that could be experimentally obtained) characterizes the external flows (flows beyond the BL) in that narrow region and is of the order of V_I/R_I, R_I being the jet radius. External velocities, or rigourously, velocities along the DS, obtained through the hypothetical solution of the whole problem shall be equal or be in the ratio of the flow densities (because of the constancy of pressure through the DS). But for the BL approximation of the mixing layer, the external velocities shall differ (in terms of A that is different for each flow) even in case the fluids have the same density. Parameter A provides the characteristic time for the nucleation-condensation process.

We have to say that a similarity solution of the dimensionless streamfunction equation for the BL is in principle possible since we are assuming the linear relation $U_e = A\,s$ for the outer flow. However, no similar solution can be found for which the conditions that results from that linear relation, holds. Thus, external velocity cannot be a linear function of s. Next, we give a proof of that:

Let's assume that such a linear relation does really exist. If f is the dimensionless streamfunction and η the stretched coordinate across the BL, f will satisfy the Hiemenz equation where derivative respecting to η is denoted by a prime:

$$f''' + f''f + 1 - (f')^2 = 0$$

Two B.C. are compulsory, namely, $f'(\infty) = 1$ and $f'(-\infty) = \lambda$. Some other conditions are possible:

1. $\partial u/\partial\eta = \partial U_e/\partial y$ for $\eta = \pm\infty$ implies $f''(\pm\infty) = 0$.

2. f is unknown at both boundaries but it is expected that at some inner point I, whose position is unknown too, $f = 0$ because $f > 0$ for $y > 0$ and $f < 0$ for $y < 0$. Let notice that f is equivalent to transverse velocity.

3. The condition $f = 0$ never implies that f' is a maximum or a minimum because $abs(f)$ is a monotonic increasing function with no inflection points.

4. Finally, it is expected that at some other inner point II, whose position is equally unknown, f'' reaches a maximum because $f'' = 0$ at both ends, so $f''' = 0$ there.

Resuming all above we have the following situation:

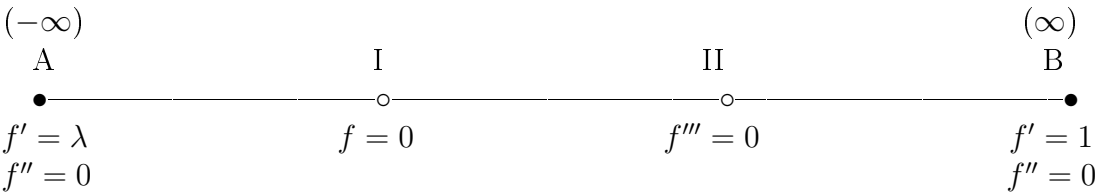

For points A, B and I third derivatives are $f'''_A = \lambda - 1$; $f'''_B = 0$; $f'''_I = (f')^2 - 1$, and Hiemenz equation in their neighborhood may be written as:

$$f''' \simeq (f')^2 - 1$$

Dimensionless streamfunction f and its derivatives according to the previous are depicted in Figure 5.1.

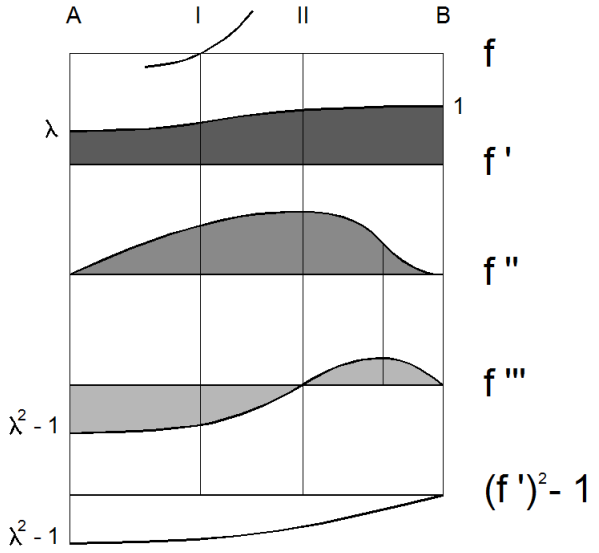

Figure 5.1: Dimensionless streamfunction f and its derivatives

Two contradictions are evident. The first one appears at point B where the functions f''' and $(f')^2 - 1$ are not coincident as it follows from above. The other one is that, according to the figure, the slope of f'' is positive between A and I but, on the contrary, f''' is negative between those points. A possibility to avoid the first contradiction is to

introduce a null point for f''' between points II and B but that would introduce a new inflection point in f' without a physical explanation. Conclusion is that f'' cannot be zero at the boundaries implying a dependence on y of the external velocity U_e.

A flow of air containing supersaturated water vapour that encounters a quiescent cold gas is a common phenomenon of undoubted meteorological interest occurring in the low atmosphere. In that case a free shear boundary layer is produced causing the deceleration of the air flow and an abrupt decrease of its temperature. A very close related precedent of this problem is the mixing layer flow that called a lot of attention during almost the whole twentieth century with the works by W. Tollmien (1926), A. M. Kuethe (1935), H. Gortler (1942), R. C. Lock (1951), L. J. Crane (1957), L. Ting (1959) [104], J. Steinheuer (1968), R. D. Mills (1968) and K. Gersten-H. Herwig (1992). With the exception of Crane, none of these authors treats the turbulent regime that has appeared a little later in the literature, see, for instance, A. J. Yule (1972) [118]. Amongst all them, Ting's paper is significant because it is focused in obtaining, through asymptotic expansions, a reasonable third boundary condition for solving the differential equation, however, the third boundary condition found by Ting breaks down when the slower fluid is at rest. Another more recent reference is the case of opposite impinging streams [99], whose study has been mainly motivated by its industrial applications. This latter case is really a limit situation of the problem we are dealing with, thus, firstly, we will look at it with some detail for illuminating a more general approach.

Would it be possible to obtain a perturbative solution (in the way Ting does [104] for the longitudinal BL) for the external velocities U_e and V_e in the transverse BL described above? For that be possible we'd have to be able either to:

-Guess a valid functional relation for V_e (linear in the coordinate orthogonal to s?) as we have done for U_e,

or to:

-Solve the equations for a rotational flow finding the adequate B. C. It has to be noted that the integration region for the external flow is a subregion of the whole domain, for which B. C. are not, in principle, available.

The classical stagnation-point flow solution, $\Psi = Axy$, is a trivial solution of the biharmonic equation:

$$\frac{1}{Re}\triangle^2\Psi - \left(\frac{\partial\Psi}{\partial y}\frac{\partial\triangle\Psi}{\partial x} - \frac{\partial\Psi}{\partial x}\frac{\partial\triangle\Psi}{\partial y}\right) = 0$$

but we are looking for other solutions. Let's take the streamfunction as the perturbative series:

$$\Psi = \Psi^{(0)} + \epsilon\,\Psi^{(1)} + \epsilon^2\,\Psi^{(2)} + ...,$$

The zeroth order biharmonic equation is obtained disregarding the bilaplacian, that is multiplied by the small parameter $\epsilon = 1/Re$, and its solution might be written as a Taylor expansion around the stagnation point (It is exactly what Ting does not only for the zeroth but for all orders). The question is whether the zeroth order biharmonic equation accepts a polynomic solution or perhaps, whether that equation has an analytic solution.

The answer is yes. The equation has the following stagnation-point flow solution:

$$\Psi^{(0)} = x\left(\frac{e^{y} - e^{-y}}{2}\right) + y\left(\frac{e^{x} - e^{-x}}{2}\right)$$

whose behavior is very similar to the classical stagnation-point. In fact, classical stagnation-point solution results from linearizing the former equation (and dividing by two). In Figures 5.2 to 5.13 velocities and streamfunctions for the classical stagnation-point solution and the solution with vorticity are depicted. It can be seen that in a very close region near the stagnation point, the solution with vorticity approaches the classical stagnation-point one. Streamline functions $y(x)$ are obtained by solving the corresponding equations for two different vectors of the parameter K, ranging from 1 to 16 for the classical stagnation-point solution and from 1 to 8 for the solution with vorticity.

$$\frac{\mathrm{d}y}{\mathrm{d}x} = -K\frac{y}{x} \quad \text{for the stagnation-point classical solution}$$

$$\frac{\mathrm{d}y}{\mathrm{d}x} = K\frac{-e^{y} - e^{-y} + y\left(e^{x} + e^{-x}\right)}{e^{x} - e^{-x} + x\left(e^{y} + e^{-y}\right)} \quad \text{for the solution with vorticity}$$

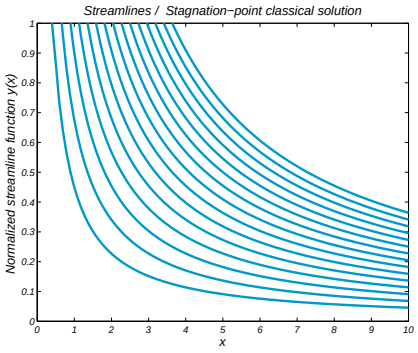

Figure 5.2: Streamlines for the classical stagnation-point solution

We can consider a subregion immediately close to the BL whose length is in the order of R_I, for which the flow is represented by the dimensional (scaled) streamfunction (where

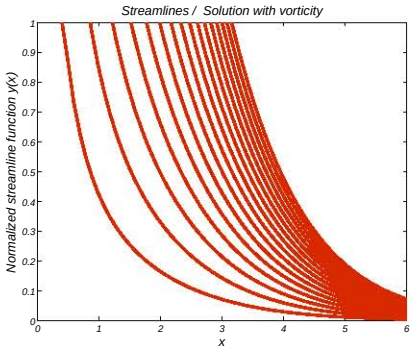

Figure 5.3: Streamlines for the solution with vorticity

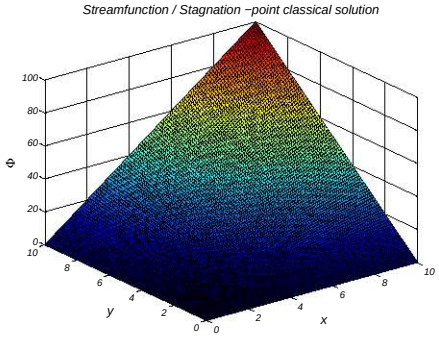

Figure 5.4: Streamfunction for the classical stagnation-point solution

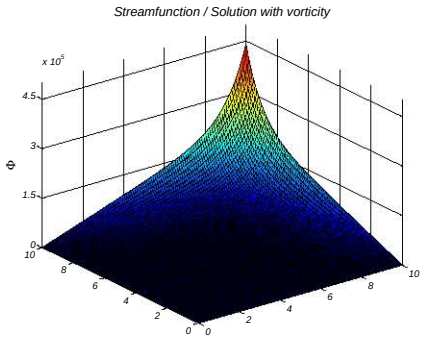

Figure 5.5: Streamfunction for the solution with vorticity. The streamfunction coincides with the vorticity

V_I is the free jet velocity):

$$\bar{\Psi} = \frac{V_I}{2}\left[x\left(\exp\frac{y}{L_I} - \exp^{-1}\frac{y}{L_I}\right) + y\left(\exp\frac{x}{R_I} - \exp^{-1}\frac{x}{R_I}\right)\right],$$

$$\bar{\Psi} = V_I\left[x\sinh\left(\frac{y}{L_I}\right) + y\sinh\left(\frac{x}{R_I}\right)\right]$$

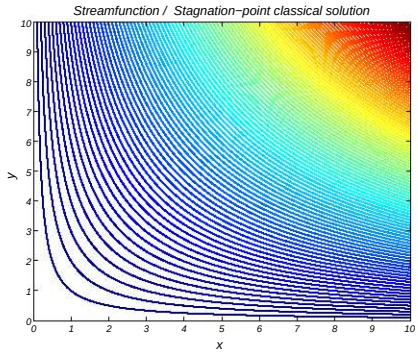

Figure 5.6: Streamfunction contour lines for the classical stagnation-point solution. x ranges from 0 to 10

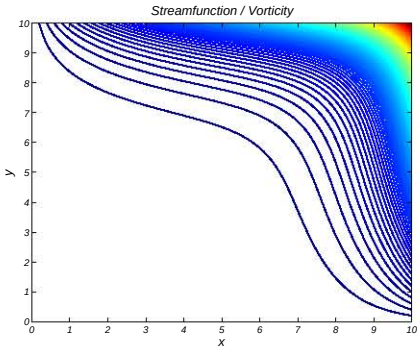

Figure 5.7: Streamfunction contour lines for the solution with vorticity. x ranges from 0 to 10

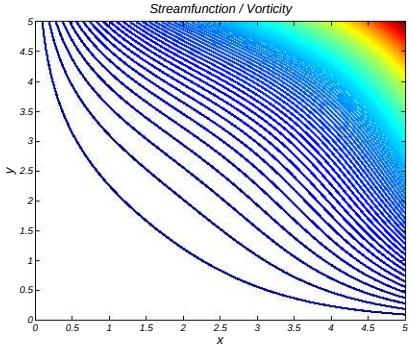

Figure 5.8: Streamfunction contour lines for the solution with vorticity. x ranges from 0 to 5

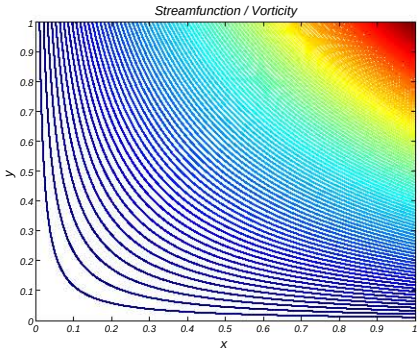

Figure 5.9: Streamfunction contour lines for the solution with vorticity. x ranges from 0 to 1

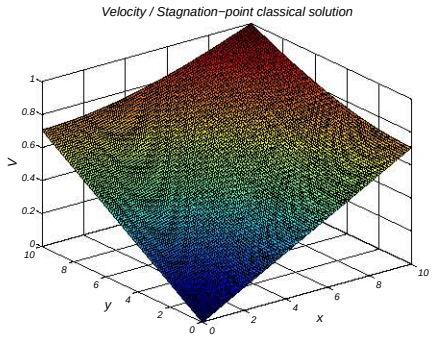

Figure 5.10: Velocity for the classical stagnation-point solution

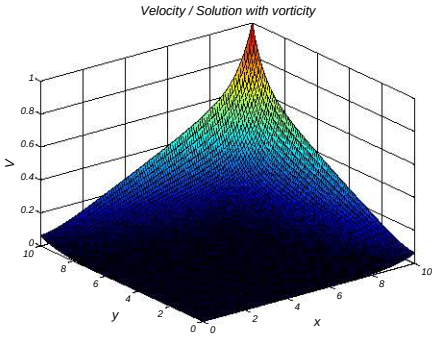

Figure 5.11: Velocity for the solution with vorticity

that is locally valid (as the classical solution is valid) and describes the external flow beyond the BL. R_I and L_I are characteristic dimensions of the free jet. From this stream-

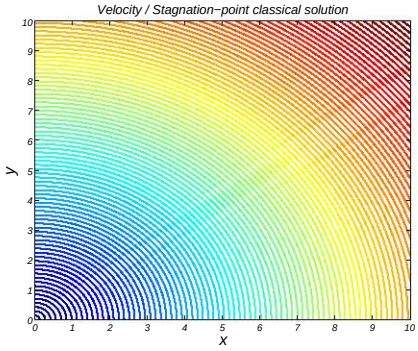

Figure 5.12: Velocity contour lines for the classical stagnation-point solution. x ranges from 0 to 10

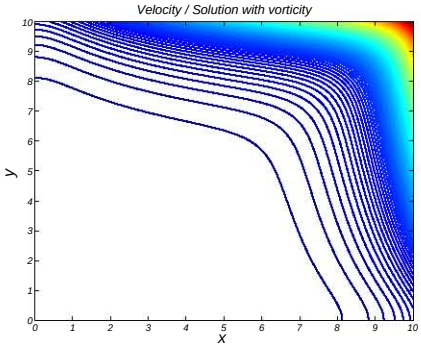

Figure 5.13: Velocity contour lines for the solution with vorticity. x ranges from 0 to 10

function we obtain the velocities:

$$u_e = \frac{\partial \bar{\Psi}}{\partial y} = V_I \left[\frac{x}{L_I} \cosh\left(\frac{y}{L_I}\right) + \sinh\left(\frac{x}{R_I}\right) \right]$$

$$v_e = -\frac{\partial \bar{\Psi}}{\partial x} = -V_I \left[\sinh\left(\frac{y}{L_I}\right) + \frac{y}{R_I} \cosh\left(\frac{x}{R_I}\right) \right]$$

If we analyze the expression we have obtained, let's say, for u_e, some inconsistency draws attention. Assuming x is very small we should recover a function very close to $a\,x$ and it is not the case. For that, we have to scale the dimensional x in the first term with $\frac{L_I}{R_I}$.

Something similar occurs for velocity v_e. Resulting expressions are:

$$u_e = \frac{\partial \bar{\Psi}}{\partial y} = V_I \left[\frac{x}{R_I} \cosh\left(\frac{y}{L_I}\right) + \sinh\left(\frac{x}{R_I}\right) \right]$$

$$v_e = -\frac{\partial \bar{\Psi}}{\partial x} = -\frac{V_I}{R_I} \left[L_I \sinh\left(\frac{y}{L_I}\right) + y \cosh\left(\frac{x}{R_I}\right) \right]$$

5.2 The Hiemenz solution

Let us assume that the Hiemenz equation were still valid for describing the problem. It would be the same as approximating u_e and v_e in the former expressions, for $x \ll R_I$ and $y \ll L_I$.

Hiemenz equation has to be solved with B.C. in $f^{'}$ for $\eta \to \infty$ and $\eta \to -\infty$. Those conditions are imposed by the longitudinal velocities of the external flows. The third B.C. might be taken in $f^{''}$ and because there are two flows there would be two possible choices. But in fact, both conditions must be taken in account, so it seems we have to differentiate the original third order equation to produce a fourth order new one.

The fourth order equation following from the Hiemenz equation is:

$$f^{IV} + f^{'''} f - f^{''} f^{'} = 0$$

and may be transformed into the system:

$$\begin{aligned} f^{''} &= w \\ w^{''} + w^{'} f - w f^{'} &= 0 \end{aligned}$$

However, if we try to solve that system no solution can be found.

It would be also possible to use other transformations. For instance, the following derived from Gortler's ([95],pag. 182):

$$\begin{aligned} \hat{\Psi} &= \nu\sqrt{2\xi} f(\xi,\eta) \\ \hat{u} &= u_e f_\eta \\ \hat{v} &= -\left[f \frac{u_{e(x)}}{\sqrt{2\xi}} + f_\xi u_{e(x)} \sqrt{2\xi} + f_\eta \nu \sqrt{2\xi} \frac{\partial \eta}{\partial x} \right] \end{aligned}$$

where $\xi = \frac{1}{\nu}\int_0^x u_{e(x)}\,\mathrm{d}x$ and $\eta = \frac{1}{\nu\sqrt{2\xi}}\int_0^y u_e\,\mathrm{d}y$ are the dimensionless coordinates. Let notice that ξ doesn't depends on u_e but on its component along x-axis, $u_{e(x)}$.

$$\begin{aligned}
\frac{\partial u_e}{\partial x} &= V_I\left[\frac{1}{R_I}\cosh\left(\frac{y}{L_I}\right)+\frac{1}{R_I}\cosh\left(\frac{x}{R_I}\right)\right]\\
\frac{\partial u_e}{\partial y} &= \frac{V_I\,x}{R_I\,L_I}\sinh\left(\frac{y}{L_I}\right)\\
\frac{\partial^2 u_e}{\partial y^2} &= \frac{V_I\,x}{R_I\,L_I^2}\cosh\left(\frac{y}{L_I}\right)\\
\frac{\partial u}{\partial x} &= \frac{\partial u_e}{\partial x}\,f_\eta + u_e\,f_{\eta\xi}\,\frac{u_{e(x)}}{\nu} + u_e\,f_{\eta\eta}\,\frac{\partial \eta}{\partial x}\\
\frac{\partial u}{\partial y} &= \frac{\partial u_e}{\partial y}\,f_\eta + \frac{u_e^2}{\nu\sqrt{2\xi}}\,f_{\eta\eta}\\
\frac{\partial^2 u}{\partial y^2} &= \frac{\partial^2 u_e}{\partial y^2}\,f_\eta + \frac{3\,u_e}{\nu\sqrt{2\xi}}\frac{\partial u_e}{\partial y}\,f_\eta + \frac{u_e^3}{2\xi\,\nu^2}\,f_{\eta\eta\eta}
\end{aligned}$$

Transformation leads to:

$$f_{\eta\eta\eta} + f_{\eta\eta}\left[f\frac{u_{e(x)}}{u_e} + \frac{3\sqrt{2\xi}\nu}{u_e}\left(\frac{1}{u_e}\frac{\partial u_e}{\partial y}\right)\right] + f_\eta\frac{2\xi\nu^2}{u_e^2}\left(\frac{1}{u_e}\frac{\partial^2 u_e}{\partial y^2}\right) =$$
$$\frac{2\xi\nu}{\rho^* u_e^3}\frac{\partial p^*}{\partial x} + \frac{\sqrt{2\xi}\,u_{e(x)}}{u_e}\left[\sqrt{2\xi}\Big(f_\eta f_{\eta\xi} - f_{\eta\eta}f_\xi\Big) + \frac{\nu}{u_e^2}\frac{\partial u_e}{\partial y}\Big(f f_\eta + 2\xi f_\xi f_\eta\Big)\right]$$

For regions relatively far from the stagnation point, that is, for $x \gg y$, $u_{e(x)} \simeq u_e$ and the former equation gives:

$$f_{\eta\eta\eta} + f_{\eta\eta}\left[f + \frac{3\sqrt{2\xi}\nu}{u_e}\left(\frac{1}{u_e}\frac{\partial u_e}{\partial y}\right)\right] + f_\eta\frac{2\xi\nu^2}{u_e^2}\left(\frac{1}{u_e}\frac{\partial^2 u_e}{\partial y^2}\right) =$$
$$\frac{2\xi\nu}{\rho^* u_e^3}\frac{\partial p^*}{\partial x} + \sqrt{2\xi}\left[\sqrt{2\xi}\Big(f_\eta f_{\eta\xi} - f_{\eta\eta}f_\xi\Big) + \frac{\nu}{u_e^2}\frac{\partial u_e}{\partial y}\Big(f f_\eta + 2\xi f_\xi f_\eta\Big)\right]$$

However, $u_{e(x)} \simeq u_e$ doesn't mean that $\dfrac{\partial u_e}{\partial y}$ can be taken as zero. The last were the

case equation would be:

$$f_{\eta\eta\eta} + f f_{\eta\eta} + \frac{2\xi\nu}{u_e}\left[\left(\frac{1}{\rho^* u_e^2}\right)\frac{\partial p^*}{\partial x} - \left(\frac{1}{u_e}\frac{\partial u_e}{\partial x}\right)(f_\eta)^2\right] = 2\xi\left(f_\eta f_{\eta\xi} - f_{\eta\eta} f_\xi\right)$$

that is a kind of generalized Hiemenz equation.

5.3 Compressible Flows: Levy-Lees and a first alternative transformation

Until now we have dealt with jets at equal temperature but this is only a particular case. Jets at different temperatures is the most common situation if we intend to model atmospheric activity. Different temperatures implies different density and viscosity. Then, we have to write the Navier-Stokes equations for a compressible flow. According to [95], pag. 233, we have:

$$\begin{aligned}
\rho^*\left(u^*\frac{\partial u^*}{\partial x} + v^*\frac{\partial u^*}{\partial y}\right) &= -\frac{\partial p^*}{\partial x} + \frac{\partial}{\partial y}\left(\mu^*\frac{\partial u_i^*}{\partial y}\right) \\
\frac{\partial \rho^* u^*}{\partial x} + \frac{\partial \rho^* v^*}{\partial y} &= 0 \\
\rho^* c_p^*\left(u^*\frac{\partial T^*}{\partial x} + v^*\frac{\partial T^*}{\partial y}\right) &= \frac{\partial}{\partial y}\left(\frac{\mu^* c_P^*}{Pr}\frac{\partial T^*}{\partial y}\right) + u^*\frac{\partial p^*}{\partial x} + \mu^*\left(\frac{\partial u^*}{\partial y}\right)^2
\end{aligned}$$

where λ (thermal conductivity in reference [95] notation) has been substituted by $\mu^* c_P^*/Pr$ and the relation $\beta T^* = 1$, valid for an ideal gas, has been considered (β is the coefficient of thermal expansion in reference [95] notation). Now we are using $(.)^*$ for denoting BL variables, instead of $\hat{(.)}$.

In case the external velocity is only a function of x we may obtain similarity solutions by introducing the dimensionless streamfunction f such that:

$$\begin{aligned}
\Psi^* &= f(x,\eta)\, F(x,y); \quad F = \sqrt{u_e x \rho^* \mu^*} \\
\eta &= \sqrt{\frac{u_e}{x}}\int_0^y \sqrt{\frac{\rho^*}{\mu^*}}\,\mathrm{d}y \\
u^* &= \frac{1}{\rho^*}\frac{\partial \Psi^*}{\partial y}; \qquad v^* = -\frac{1}{\rho^*}\frac{\partial \Psi^*}{\partial x}
\end{aligned}$$

The following expressions are obtained for $\partial\Psi^*/\partial y$ and $\partial\Psi^*/\partial x$ respectively:

$$\begin{aligned}
\frac{\partial \Psi^*}{\partial y} &= \left[f_\eta + \frac{f}{2}\left(\frac{1}{\rho^*}\frac{\partial \rho^*}{\partial \eta} + \frac{1}{\mu^*}\frac{\partial \mu^*}{\partial \eta} + \frac{1}{u_e}\frac{\partial u_e}{\partial \eta} \right) \right] u_e\, \rho^* \\
&= \mathbf{P}_\eta u_e\, \rho^* \\
\frac{\partial \Psi^*}{\partial x} &= \left\{ \left(f_x + \mathbf{P}_\eta \frac{\partial \eta}{\partial x} \right) + \frac{f}{2}\left[\frac{1}{\rho^*}\frac{\partial \rho^*}{\partial x} + \frac{1}{\mu^*}\frac{\partial \mu^*}{\partial x} + \frac{1}{u_e}\frac{\partial u_e}{\partial x} + \frac{1}{x} \right] \right\} \sqrt{u_e x \rho^* \mu^*} \\
&= \left[\left(\mathbf{P}_\eta \frac{\partial \eta}{\partial x} + \mathbf{P}_x \right) + \frac{f}{2}\left(\frac{1}{x} + \frac{1}{u_e}\frac{\partial u_e}{\partial x} \right) \right] \sqrt{u_e x \rho^* \mu^*}
\end{aligned}$$

Navier-Stokes equations for that problem are the following:

$$\begin{aligned}
&\mathbf{P}_{\eta\eta\eta} + \frac{\mathbf{P}_{\eta\eta}}{2}\left[f + (m-1)\frac{\boldsymbol{\theta}_\eta}{\boldsymbol{\theta}} \right] + \frac{x}{u_e}\frac{\mathrm{d}u_e}{\mathrm{d}x}\left[\boldsymbol{\theta} + \frac{\mathbf{P}_{\eta\eta} f}{2} - (\mathbf{P}_\eta)^2 \right] = \\
&\qquad x(\mathbf{P}_\eta \mathbf{P}_{\eta x} - \mathbf{P}_x \mathbf{P}_{\eta\eta}) \\
&\boldsymbol{\theta}_{\eta\eta} + \frac{(\boldsymbol{\theta}_\eta)^2}{\boldsymbol{\theta}}\left(\gamma + \frac{m-1}{2} \right) + Pr\left[\frac{f\boldsymbol{\theta}_\eta}{2}\left(1 + \frac{x}{u_e}\frac{\mathrm{d}u_e}{\mathrm{d}x} \right) + \frac{u_e^2}{c_P^* T_e}(\mathbf{P}_{\eta\eta})^2 \right] = \\
&\qquad xPr\left[(\mathbf{P}_\eta \boldsymbol{\theta}_x - \mathbf{P}_x \boldsymbol{\theta}_\eta) + \mathbf{P}_\eta \boldsymbol{\theta}\frac{\mathrm{d}H_e}{\mathrm{d}x}\frac{1}{c_P^* T_e} \right] \\
&\mathbf{P}_x = f_x + \frac{f}{2}\left(\frac{1}{\rho^*}\frac{\partial \rho^*}{\partial x} + \frac{1}{\mu^*}\frac{\partial \mu^*}{\partial x} \right); \qquad \mathbf{P}_\eta = f_\eta + \frac{f}{2}\left(\frac{1}{\rho^*}\frac{\partial \rho^*}{\partial \eta} + \frac{1}{\mu^*}\frac{\partial \mu^*}{\partial \eta} \right)
\end{aligned}$$

where $\boldsymbol{\theta}(x,\eta) = T^*(x,\eta)/T_e(x)$ is a dimensionless temperature, $T_e(x)$ is the temperature field in the external region, $\mu^* = M(T^*)^m$ and $c_P^* = \Gamma(T^*)^{-\gamma}$, $H_e = c_P^* T_e + u_e^2/2$; $(\mathbf{P}_\eta - f_\eta)/f$ in the motion equation has been replaced by $\dfrac{\boldsymbol{\theta}_\eta}{\boldsymbol{\theta}}\left(\dfrac{m-1}{2} \right)$ making use of $\rho^* = \dfrac{p^*(x)}{\mathrm{R}T^*}$.

Because the external velocity is a function of x solely, it follows that $u_e\dfrac{\mathrm{d}u_e}{\mathrm{d}x} = -\dfrac{1}{\rho^*}\dfrac{\partial p^*}{\partial x}$. The former implies that the B.C. $f_{\eta\eta} = 0$ for $\eta \to \pm\infty$, has to yield a solution.

Situation is quite different for a compressible flow when external velocity depends on both, x and y. Firstly, η has to be taken as $\dfrac{1}{\sqrt{x}}\displaystyle\int_0^y \sqrt{\frac{u_e \rho^*}{\mu^*}}\,\mathrm{d}y$. When substituting that expresion in the Navier-Stokes equations the result is rather intricate.

So, we should ask ourselves whether it would be possible to obtain simpler equations for the compressible BL with a plane external flow. Two subsequent questions (or suggestions) arise:

1. Would it be profitable to substitute u_e by $u_{e(x)}$ in the streamfunction definition?

2. Would it be profitable to use the Levy-Lees transformation instead of the first one?

Answer to the first question is no. The streamfunction cannot loose the connection with u_e if the B.C. in u^* has to be satisfied. Substitution makes sense in the definition of ξ, for that reason is only applicable to the Levy-Lees transformation or any other else in which ξ is not taken explicitly as x. It must be said that the advantage of taking $\xi = x$ rests on the consequent simplification of numerical calculation when no similarity solution is attainable. Von Mises transformation also uses $\xi = x$ ([95], p.183).

Now it's the time for the second suggestion. Let's have:

$$\begin{aligned} \hat{\Psi} &= \sqrt{2\xi} f(\xi,\eta) \\ \xi &= \int_0^x \rho_e \mu_e u_{e(x)}\, \mathrm{d}x; \quad \eta = \frac{1}{\sqrt{2\xi}} \int_0^y \rho^* u_e\, \mathrm{d}y \\ \mathbf{C}(\xi,\eta) &= \frac{\rho^*(\xi,\eta)\mu^*(\xi,\eta)}{\rho_e(x)\mu_e(x)} \end{aligned}$$

which transform Navier-Stokes motion equation into:

$$\begin{aligned} &(\mathbf{C} f_{\eta\eta})_\eta + \frac{u_{e(x)}}{u_e} f f_{\eta\eta} = \\ &\left(\frac{2\xi\mathbf{C}}{\mu^*\rho^* u_e^3}\right)\frac{\partial p^*}{\partial x} + \frac{\sqrt{2\xi}\, u_{e(x)}}{u_e}\left[\sqrt{2\xi}\Big(f_\eta f_{\eta\xi} - f_{\eta\eta} f_\xi\Big) - \frac{\partial u_e}{\partial y}\frac{1}{\rho^* u_e^2}\Big(f f_\eta + 2\xi f_\xi f_\eta\Big)\right] \\ &-\frac{\sqrt{2\xi}}{\rho^* u_e^2}\mathbf{C}\left(3 f_{\eta\eta}\frac{\partial u_e}{\partial y} + f_\eta \frac{\sqrt{2\xi}}{\rho^* u_e}\frac{\partial^2 u_e}{\partial y^2}\right) \end{aligned}$$

5.4 A second transformation

5.4.1 Equations

Equations obtained using Levy-Lees are much simpler than those coming from the first transformation. Handicap is that in case numerical integration is done by using a mesh,

the step $\Delta\xi$ shall not be constant. The main difference between Levy-Lees's and the 1st transformation is, precisely, the treatment of that coordinate along x-axis. For that reason, the transformations differ in the way the streamfunction is defined: while Levy-Lees take $\Psi = \sqrt{2\xi(x)}f(\xi,\eta)$ we do $\Psi = F(x,\eta)f(x,\eta)$, where both, $\sqrt{2\xi}$ and F, are dimensional streamfunctions respectively. However, modifying a little bit the transformation we have used above, motion equation simplifies significantly. In effect:

$$\Psi = x\sqrt{a\rho^*\mu^*}; \qquad \eta = \frac{1}{x}\int_0^y u_e\sqrt{\frac{\rho^*}{\mu^* a}}\mathrm{d}y; \qquad a = \frac{V_I}{R_I}$$

leads to

$$\boldsymbol{\Phi}_{\eta\eta} + \boldsymbol{\Phi}_\eta\left[\left(\frac{m-1}{2}\right)\frac{\boldsymbol{\theta}_\eta}{\boldsymbol{\theta}} + \frac{1}{2\,p^*}\frac{\partial p^*}{\partial \eta} + 3\,y_\eta\,\lambda_y\right] + \boldsymbol{\Phi}\left[m\,y_\eta\,\lambda_y\,\frac{\boldsymbol{\theta}_\eta}{\boldsymbol{\theta}} + (y_\eta)^2\,\lambda_{2y}\right] =$$

$$\left(\frac{ax^2}{\rho^* u_e^3}\right)\frac{\partial p^*}{\partial x} + \frac{ax^2}{u_e}\Big(\boldsymbol{\Phi}\,\boldsymbol{\Phi}_x - \boldsymbol{\Omega}\,\boldsymbol{\Phi}_\eta - y_\eta\,\lambda_y\,\boldsymbol{\Omega}\,\boldsymbol{\Phi}\Big)$$

$$\boldsymbol{\Phi} = f_\eta + f\left(\frac{m-1}{2}\right)\frac{\boldsymbol{\theta}_\eta}{\boldsymbol{\theta}} + \frac{1}{2\,p^*}\frac{\partial p^*}{\partial \eta}; \qquad \boldsymbol{\Omega} = \frac{f}{x} + f_x + f\left(\frac{m-1}{2}\right)\frac{\boldsymbol{\theta}_x}{\boldsymbol{\theta}} + \frac{1}{2\,p^*}\frac{\partial p^*}{\partial x}$$

which seems to be even simpler than the Levy-Lees result.

When $\dfrac{\partial u_e}{\partial y} = 0$ $\left(\text{and } \dfrac{\partial p_e}{\partial y} = 0 \text{ too}\right)$ the equation is slightly different:

$$\boldsymbol{\Phi}_{\eta\eta} + \boldsymbol{\Phi}_\eta\left[\left(\frac{m-1}{2}\right)\frac{\boldsymbol{\theta}_\eta}{\boldsymbol{\theta}} + \frac{ax}{u_e}f\right] - \left(\frac{ax^2}{u_e}\right)\lambda_x\,(\boldsymbol{\Phi})^2 = \left(\frac{ax^2}{\rho^* u_e^3}\right)\frac{\partial p^*}{\partial x} + \frac{ax^2}{u_e}\Big(\boldsymbol{\Phi}\,\boldsymbol{\Omega}_\eta - \boldsymbol{\Omega}\,\boldsymbol{\Phi}_\eta\Big)$$

$$\boldsymbol{\Omega} = f_x + f\left(\frac{m-1}{2}\right)\frac{\boldsymbol{\theta}_x}{\boldsymbol{\theta}} + \frac{1}{2\,p^*}\frac{\partial p^*}{\partial x}$$

which, when $u_e = ax$, reduces finally to:

$$\boldsymbol{\Phi}_{\eta\eta} + \boldsymbol{\Phi}_\eta\left[\left(\frac{m-1}{2}\right)\frac{\boldsymbol{\theta}_\eta}{\boldsymbol{\theta}} + f\right] - (\boldsymbol{\Phi})^2 = \left(\frac{1}{\rho^* a^2 x}\right)\frac{\partial p^*}{\partial x} + x\Big(\boldsymbol{\Phi}\,\boldsymbol{\Omega}_\eta - \boldsymbol{\Omega}\,\boldsymbol{\Phi}_\eta\Big)$$

The energy equation with the former transformation reads:

$$\boldsymbol{\theta}_{\eta\eta} + \boldsymbol{\theta}_\eta\left[\left(\frac{m-1}{2} - \gamma\right)\frac{\boldsymbol{\theta}_\eta}{\boldsymbol{\theta}} + Pr\left(\frac{ax}{u_e}\right)f + y_\eta\,\lambda_y + \frac{1}{2\,p^*}\frac{\partial p^*}{\partial \eta}\right] + Pr\left(\frac{u_e^2}{c_P T_e}\right)\Big(\boldsymbol{\Phi}_\eta + \boldsymbol{\Phi}\,y_\eta\,\lambda_y\Big)^2 =$$

$$-Pr\left(\frac{ax^2}{u_e c_P T_e}\right)\boldsymbol{\Phi}\left(\frac{\partial p^*}{\partial x}\right) + Pr\left(\frac{ax^2}{u_e}\right)\Big(\boldsymbol{\Phi}\,\boldsymbol{\theta}_x - \boldsymbol{\Omega}\,\boldsymbol{\theta}_\eta + \tau_e\boldsymbol{\theta}\,\boldsymbol{\Phi}\Big)$$

$$\tau_e = \frac{1}{T_e}\frac{\partial T_e}{\partial x}$$

When $\dfrac{\partial u_e}{\partial y} = 0$ $\left(\dfrac{\partial p_e}{\partial y} = 0\right)$ the equation reduces to:

$$\boldsymbol{\theta}_{\eta\eta} + \boldsymbol{\theta}_\eta \left[\left(\frac{m-1}{2} - \gamma \right) \frac{\boldsymbol{\theta}_\eta}{\boldsymbol{\theta}} + Pr \left(\frac{ax}{u_e} \right) f \right] + Pr \left(\frac{u_e^2}{c_P T_e} \right) (\boldsymbol{\Phi}_\eta)^2 =$$
$$Pr \left(\frac{ax^2}{u_e} \right) \Big(\boldsymbol{\Phi}\, \boldsymbol{\theta}_x - \boldsymbol{\Omega}\, \boldsymbol{\theta}_\eta \Big) + Pr \left(\frac{ax^2}{u_e c_P T_e} \right) \boldsymbol{\Phi} \left(c_P \boldsymbol{\theta} \frac{\partial T_e}{\partial x} - \frac{1}{\rho^*} \frac{\partial p^*}{\partial x} \right)$$

and finally, when $u_e = ax$, to:

$$\boldsymbol{\theta}_{\eta\eta} + \boldsymbol{\theta}_\eta \left[\left(\frac{m-1}{2} - \gamma \right) \frac{\boldsymbol{\theta}_\eta}{\boldsymbol{\theta}} + Pr\, f \right] + Pr \left(\frac{u_e^2}{c_P T_e} \right) (\boldsymbol{\Phi}_\eta)^2 =$$
$$Pr\, x \Big(\boldsymbol{\Phi}\, \boldsymbol{\theta}_x - \boldsymbol{\Omega}\, \boldsymbol{\theta}_\eta \Big) - Pr \left(\frac{x}{c_P T_e} \right) \boldsymbol{\Phi} \left(c_P \boldsymbol{\theta} \frac{\partial T_e}{\partial x} - \frac{1}{\rho^*} \frac{\partial p^*}{\partial x} \right)$$

noticing that $\left(c_P \boldsymbol{\theta} \dfrac{\partial T_e}{\partial x} - \dfrac{1}{\rho^*} \dfrac{\partial p^*}{\partial x} \right) = \boldsymbol{\theta}\, \dfrac{\partial H_e}{\partial x}$ (H_e being the external enthalpy), considering $\dfrac{\partial p^*}{\partial x} = \rho_e u_e \dfrac{\partial u_e}{\partial x}$ and taking in account that $\boldsymbol{\theta} = \dfrac{T^*}{T_e} = \dfrac{\rho_e}{\rho^*}$ (constant pressure across the BL).

The system of momentum along x-axis and energy equations can be written as usual as a system of first order equations (where we have used $p^* = p_e$):

$$\begin{aligned}
\boldsymbol{\Phi}_1 &= \boldsymbol{\Phi}' \\
\boldsymbol{\theta}_1 &= \boldsymbol{\theta}' \\
\boldsymbol{\Phi}_1' + \boldsymbol{\Phi}_1 \left(\alpha \frac{\boldsymbol{\theta}_1}{\boldsymbol{\theta}} + 3C \right) + \boldsymbol{\Phi} \left(m\, C \frac{\boldsymbol{\theta}_1}{\boldsymbol{\theta}} + D \right) &= E\, \boldsymbol{\theta} + G \Big(\boldsymbol{\Phi}\, \frac{\partial \boldsymbol{\Phi}}{\partial x} - \boldsymbol{\Omega}\, \boldsymbol{\Phi}_1 - C\, \boldsymbol{\Omega}\, \boldsymbol{\Phi} \Big) \\
\boldsymbol{\theta}_1' + \boldsymbol{\theta}_1 \left(\kappa \frac{\boldsymbol{\theta}_1}{\boldsymbol{\theta}} + C \right) + J \Big(\boldsymbol{\Phi}_1' + C\, \boldsymbol{\Phi}_1 \Big)^2 &= -L\, \boldsymbol{\theta}\, \boldsymbol{\Phi} + P_r\, G \left(\boldsymbol{\Phi} \frac{\partial \boldsymbol{\theta}}{\partial x} - \boldsymbol{\Omega}\, \boldsymbol{\theta}_1 \right) \\
-\boldsymbol{\Phi} + \boldsymbol{f}' + \boldsymbol{f}\, \alpha \frac{\boldsymbol{\theta}_1}{\boldsymbol{\theta}} &= 0 \\
0 &= -\boldsymbol{\Omega} + \frac{\boldsymbol{f}}{x} + \frac{\partial \boldsymbol{f}}{\partial x} + \boldsymbol{f}\, \alpha\, \frac{1}{\boldsymbol{\theta}} \frac{\partial \boldsymbol{\theta}}{\partial x} + \frac{f}{2} \frac{1}{p_e} \frac{\partial p_e}{\partial x},
\end{aligned}$$

with the following meanings:

$$C = \frac{x}{u_e(x,y)}\sqrt{\frac{\mathrm{R}\,\mu_e\,T_e\,a}{p_e(x)}}\sqrt{\boldsymbol{\theta}^{m+1}}\,\lambda_y\,;\quad D = \left(\frac{C}{\lambda_y}\right)^2\lambda_{2y}\,;\quad G = \frac{a\,x^2}{u_e(x,y)}\,;$$

$$E = \frac{a\,x^2 R\,T_e}{u_e(x,y)^3\,p_e(x)}\frac{\partial p_e(x)}{\partial x}\,;\quad J = \frac{Pr\,u_e(x,y)^2}{c_P(\boldsymbol{\theta})T_e}\,;\quad L = \frac{x^2\,P_r\,a\,R}{c_P(\boldsymbol{\theta})p_e(x)\,u_e(x,y)}\frac{\partial p_e(x)}{\partial x}\,;$$

$$\alpha = \frac{m-1}{2}\,;\quad \kappa = \alpha - \gamma\,;\quad \lambda_y = \frac{1}{u_e(x,y)}\frac{\partial u_e(x,y)}{\partial y}\,;\quad \lambda_{2y} = \frac{1}{u_e(x,y)}\frac{\partial^2 u_e(x,y)}{\partial y^2}\,;$$

$$\int_0^y u_e\,\mathrm{d}y = x\sqrt{\frac{\mathrm{R}\,\mu_e\,T_e\,a}{p_e}}\int_0^\eta \sqrt{\boldsymbol{\theta}^{m+1}}\,\mathrm{d}\eta\,;\qquad c_P(\boldsymbol{\theta}) = c_{P_e}\,\boldsymbol{\theta}^{\gamma};\qquad c_{P_e} = \Gamma\,T_e^{\gamma}$$

where variables in bold font are dimensionless. Equation for θ has been particularized for a constant external temperature field, that is, $\dfrac{\partial T_e}{\partial x} = 0$. If we substitute the expression for u_e in §5.1 (but without the scaling, because when integrating in y the streamfunction Ψ is recovered) we get an equation for y as a function of the RHS:

$$x\,\sinh\frac{y}{L_I} + y\,\sinh\frac{x}{R_I} = \frac{x}{V_I}\sqrt{\frac{\mathrm{R}\,\mu_e\,T_e\,a}{p_e}}\int_0^\eta \sqrt{\boldsymbol{\theta}^{m+1}\,\mathrm{d}\eta}$$

5.4.2 Detailed algebra

Transformation:

$$\Psi = x\sqrt{a\rho^*\mu^*}$$

$$\eta = \frac{1}{x}\int_0^y u_e\sqrt{\frac{\rho^*}{\mu^* a}}\mathrm{d}y$$

Velocities:

$$\begin{aligned} u = \frac{1}{\rho^*}\frac{\partial\Psi}{\partial y} &= \frac{1}{\rho^*}\,x\,\sqrt{a}\left[\frac{1}{2\sqrt{\rho^*\mu^*}}\left(\rho^*\frac{\partial\mu^*}{\partial\eta} + \mu^*\frac{\partial\rho^*}{\partial\eta}\right)f + \sqrt{\rho^*\mu^*}f_\eta\right]\frac{\partial\eta}{\partial y} \\ &= u_e\left(f_\eta + \frac{F_\eta f}{2}\right) \\ &= u_e\,\boldsymbol{\Phi} \end{aligned}$$

$$v = -\frac{1}{\rho^*}\frac{\partial \Psi}{\partial x} = -\frac{1}{\rho^*}\left[\sqrt{a\,\rho^*\,\mu^*}\,f + x\,f\,\frac{\partial\sqrt{\rho^*\,\mu^*}}{\partial x}\right]$$
$$= -\frac{x\,\sqrt{a\,\rho^*\,\mu^*}}{\rho^*}\left[\frac{f}{x} + \left(f_\eta + \frac{F_\eta f}{2}\right)\frac{\partial\eta}{\partial x} + \left(f_x + \frac{F_x f}{2}\right)\right]$$
$$= -\frac{x\,\sqrt{a\,\rho^*\,\mu^*}}{\rho^*}\left(\mathbf{\Phi}\frac{\partial\eta}{\partial x} + \mathbf{\Omega}\right)$$
$$F_\eta = \frac{\rho^*_\eta}{\rho^*} + \frac{\mu^*_\eta}{\mu^*}; \qquad F_x = \frac{\rho^*_x}{\rho^*} + \frac{\mu^*_x}{\mu^*}$$

Momentum equation along x-axis

LHS:

$$\frac{\partial u}{\partial x} = \mathbf{\Phi}_x\,u_e + \mathbf{\Phi}_\eta\frac{\partial\eta}{\partial x}u_e + \mathbf{\Phi}\frac{\partial u_e}{\partial x}$$

$$\frac{\partial u}{\partial y} = \mathbf{\Phi}_\eta\frac{\partial\eta}{\partial y}u_e + \mathbf{\Phi}\frac{\partial u_e}{\partial y}$$

$$\rho^*\left(u\frac{\partial u}{\partial x} + v\frac{\partial u}{\partial y}\right) =$$
$$\rho^*\,u_e\,\mathbf{\Phi}\left(\mathbf{\Phi}_x\,u_e + \mathbf{\Phi}_\eta\frac{\partial\eta}{\partial x}u_e + \mathbf{\Phi}\frac{\partial u_e}{\partial x}\right) - x\,\sqrt{a\,\rho^*\,\mu^*}\left(\mathbf{\Phi}\frac{\partial\eta}{\partial x} + \mathbf{\Omega}\right)\left(\mathbf{\Phi}_\eta\frac{\partial\eta}{\partial y}u_e + \mathbf{\Phi}\frac{\partial u_e}{\partial y}\right) =$$
$$\rho^*\,u_e^2\,(\mathbf{\Phi}\,\mathbf{\Phi}_x - \mathbf{\Omega}\,\mathbf{\Phi}_\eta) - x\,\sqrt{a\,\rho^*\,\mu^*}\;\frac{\partial u_e}{\partial y}\,\mathbf{\Omega}\,\mathbf{\Phi}$$

RHS:

$$\frac{\partial}{\partial y}\left(\mu^*\frac{\partial u}{\partial y}\right) = \frac{\partial\mu^*}{\partial\eta}\frac{\partial\eta}{\partial y}\frac{\partial u}{\partial y} + \mu^*\frac{\partial^2 u}{\partial y^2} =$$
$$\mu^*_\eta\frac{u_e^2}{x}\sqrt{\frac{\rho^*}{a\,\mu^*}}\left[\mathbf{\Phi}_\eta\frac{u_e}{x}\sqrt{\frac{\rho^*}{a\,\mu^*}} + \mathbf{\Phi}\left(\frac{1}{u_e}\frac{\partial u_e}{\partial y}\right)\right] +$$
$$\mu^*\left[\mathbf{\Phi}_{\eta\eta}\frac{u_e^2\,\rho^*}{x^2\,\mu^*\,a} + \mathbf{\Phi}_\eta\frac{u_e^2}{x}\sqrt{\frac{\rho^*}{\mu^*\,a}}\left(\frac{G_\eta}{2} + \frac{3}{u_e}\frac{\partial u_e}{\partial y}\right) + \mathbf{\Phi}\frac{\partial^2 u_e}{\partial y^2}\right]; \qquad G_\eta = \frac{\rho^*_\eta}{\rho^*} - \frac{\mu^*_\eta}{\mu^*}$$
$$= \frac{u_e^3\,\rho^*}{a\,x^2}\left[\mathbf{\Phi}_{\eta\eta} + \mathbf{\Phi}_\eta\left(\frac{F_\eta}{2} + \frac{3\,x}{u_e^2}\sqrt{\frac{\mu^*\,a}{\rho^*}}\frac{\partial u_e}{\partial y}\right) + \mathbf{\Phi}\left(\frac{x}{u_e^2}\sqrt{\frac{\mu^*\,a}{\rho^*}}\frac{\mu^*_\eta}{\mu^*}\frac{\partial u_e}{\partial y} + \frac{x^2\,\mu^*\,a}{u_e^3\,\rho^*}\frac{\partial^2 u_e}{\partial y^2}\right) - \frac{\partial p^*}{\partial x}\right]$$

Last steps to the final equation

$$F_\eta = (m-1)\frac{\boldsymbol{\theta}_\eta}{\boldsymbol{\theta}} + \frac{\boldsymbol{p}^*_\eta}{\boldsymbol{p}^*}; \qquad F_x = (m-1)\frac{\boldsymbol{\theta}_x}{\boldsymbol{\theta}} + \frac{\boldsymbol{p}^*_x}{\boldsymbol{p}^*};$$

Because the pressure gradients along x-axis has to match at $\eta = 0$, in principle, the pressure should change across the BL. Thus, $p^* = p^*(x, \eta)$ and has to be differentiated too. The following substitutions:

$$\mu^* = \mu_e \left(\frac{T}{T_e}\right)^m \quad \text{and} \quad \rho^* = \frac{p^*}{\mathrm{R}\,T}$$

lead to the coefficients C and D.

Energy equation

Transformation:

$$T = \boldsymbol{\theta}(x, \eta)\, T_e(x)$$

LHS:

$$\frac{\partial T}{\partial x} = \frac{\partial \boldsymbol{\theta}}{\partial x} T_e + \boldsymbol{\theta} \frac{\partial T_e}{\partial x} + \boldsymbol{\theta}_\eta \frac{\partial \eta}{\partial x} T_e$$

$$\frac{\partial T}{\partial y} = \boldsymbol{\theta}_\eta \frac{\partial \eta}{\partial y} T_e$$

$$u\frac{\partial T}{\partial x} + v\frac{\partial T}{\partial y} = \boldsymbol{\Phi}\frac{\partial \boldsymbol{\theta}}{\partial x}\, u_e\, T_e - \boldsymbol{\Omega}\, \boldsymbol{\theta}_\eta\, u_e\, T_e + \boldsymbol{\Phi}\, \boldsymbol{\theta}\, u_e \frac{\partial T_e}{\partial x} = \rho^*\, c_P\, u_e\, T_e \Big(\boldsymbol{\Phi}\, \boldsymbol{\theta}_x - \boldsymbol{\Omega}\, \boldsymbol{\theta}_\eta + \boldsymbol{\Phi}\, \tau_e \Big)$$

$$\tau_e = \frac{1}{T_e}\frac{\partial T_e}{\partial x}$$

RHS:

$$\frac{\partial}{\partial y}\left(\frac{\mu^*\, c_P}{P_r}\frac{\partial T}{\partial y}\right) =$$

$$\frac{T_e}{x\, P_r\, \sqrt{a}}\frac{\partial}{\partial y}\Big(\boldsymbol{\theta}_\eta\, c_P\, \sqrt{\mu^*\, \rho^*}\, u_e\Big) = \frac{c_P\, \rho^*\, T_e\, u_e^2}{x^2\, P_r\, a}\left(\frac{F_\eta\, \boldsymbol{\theta}_\eta}{2} + \boldsymbol{\theta}_{\eta\eta} - \gamma\, \frac{\boldsymbol{\theta}_\eta^2}{\boldsymbol{\theta}} + \boldsymbol{\theta}_\eta\, y_\eta\, \lambda_y\right) =$$

$$\frac{c_P\, \rho^*\, T_e\, u_e^2}{x^2\, P_r\, a}\left(\frac{F_\eta\, \boldsymbol{\theta}_\eta}{2} + \boldsymbol{\theta}_{\eta\eta} - \gamma\, \frac{\boldsymbol{\theta}_\eta^2}{\boldsymbol{\theta}} + \boldsymbol{\theta}_\eta\, y_\eta\, \lambda_y\right) + \boldsymbol{\Phi}\, u_e\, \frac{\partial p^*}{\partial x} + \mu^*\left(\boldsymbol{\Phi}_\eta \frac{\partial \eta}{\partial y} u_e + \boldsymbol{\Phi}\frac{\partial u_e}{\partial y}\right)$$

$$= \left[\boldsymbol{\theta}_{\eta\eta} + \left(\frac{m-1}{2} - \gamma \right) \frac{\boldsymbol{\theta}_\eta^2}{\boldsymbol{\theta}} + \boldsymbol{\theta}_\eta \left(y_\eta \, \lambda_y + \frac{p_\eta^*}{2p^*} \right) \right] + \boldsymbol{\Phi} \, \frac{\partial p^*}{\partial x} \, u_e + \frac{\rho^* \, u_e^4}{x^2 \, a} \Big(\boldsymbol{\Phi}_\eta + \boldsymbol{\Phi} \, y_\eta \, \lambda_\eta \Big)^2$$

$$c_P = \Gamma \, T^{-\gamma}$$

5.5 Solving the equations

At a first sight two methods seem adequate for solving the former system:

1. The Quasilinearization Method [3].

2. A finite difference approach based on Keller's box scheme [53].

Although it only looks evident in the second one, both methods are implemented by using finite differences. As we are dealing with non-similar flow solutions and functionally scaled coordinates, the grid has not an uniform spacing (in our case, only along η direction). In addition, boundary layer width depends, in general, on the longitudinal coordinate. The second method is able to cope with non-constant spacing of the grid but the first one needs a coordinate transformation for obtaining a uniform grid. Otherwise, the second method needs the system to be written as a set of first order differential equations (6 eqs.) while the first one can operate with the original equations (4 eqs.). In our case, this last point makes no big difference.

However, we shall proceed in another way, mainly due to the presence of boundary conditions that have to be hold by both flows at $\eta = 0$. Instead of the global finite differences approach we split the bidimensional grid in a row of linear problems that are solved successively along the longitudinal direction. The integration might be repeated in a sort of iterative sweeping in order to refine the solution but we conjecture that probably it wouldn't be necessary. Each linear problem is solved by the shooting method aiming from both sides of the B. L. at the point $\eta = 0$.

5.5.1 The pressure gradient

Before to tackle the method of solution we need to express the BL pressure gradient in terms of the external flow. For that, we have to write the momentum equation for the outer edge of the BL, where velocities and their derivatives coincide with those corresponding to the external flow:

$$\rho_e \left(u_e^* \frac{\partial u_e^*}{\partial x} + v_e^* \frac{\partial u_e^*}{\partial y} \right) = -\frac{\partial p_e^*}{\partial x} + \mu_e \frac{\partial^2 u_e^*}{\partial y^2},$$

and we have:

$$u_e^* = \frac{\partial \bar{\Psi}}{\partial y} = V_I \left(\frac{x}{R_I} \cosh \frac{y}{L_I} + \sinh \frac{x}{R_I} \right)$$

$$v_e^* = -\frac{\partial \bar{\Psi}}{\partial x} = -\frac{V_I}{R_I} \left(L_I \sinh \frac{y}{L_I} + y \cosh \frac{x}{R_I} \right)$$

with $L = O\left(\sqrt{\frac{\nu R}{V}}\right) = O\left(\frac{R}{\sqrt{Re}}\right)$.

Whence, we obtain:

$$\frac{\partial u_e^*}{\partial x} = \frac{V_I}{R_I} \left(\cosh \frac{y}{L_I} + \cosh \frac{x}{R_I} \right)$$

$$\frac{\partial u_e^*}{\partial y} = V_I \left(\frac{x}{R_I L_I} \sinh \frac{y}{L_I} \right); \qquad \frac{\partial^2 u_e^*}{\partial y^2} = V_I \left(\frac{x}{R_I L_I^2} \cosh \frac{y}{L_I} \right)$$

which leads to:

$$\frac{V_I^2}{R_I} \left(\frac{x}{R_I} \cosh \frac{y}{L_I} + \sinh \frac{x}{R_I} \right) \left(\cosh \frac{y}{L_I} + \cosh \frac{x}{R_I} \right) -$$

$$\frac{V_I^2 x}{R_I^2 L_I} \sinh \frac{y}{L_I} \left(L_I \sinh \frac{y}{L_I} + y \cosh \frac{x}{R_I} \right) = -\frac{1}{\rho_e^*} \frac{\partial p_e^*}{\partial x} + \frac{\mu_e^* V_I x}{\rho_e^* R_I L_I^2} \cosh \frac{y}{L_I}$$

$$\frac{V_I^2 x}{R_I^2} \left(1 - \frac{\nu_e^* R_I}{V_I L_I^2} \cosh \frac{y}{L_I} \right) + \frac{V_I^2 x}{R_I^2} \left(\cosh \frac{y}{L_I} - \frac{y}{L_I} \sinh \frac{y}{L_I} \right) +$$

$$\frac{V_I^2}{R_I} \sinh \frac{x}{R_I} \left(\cosh \frac{y}{L_I} + \cosh \frac{x}{R_I} \right) = -\frac{1}{\rho_e^*} \frac{\partial p_e^*}{\partial x}$$

If $x \ll R_I$

$$\frac{\partial p_e^*}{\partial x} \simeq -\frac{V_I^2 \rho_e^* x}{R_I^2} \left[2 + \cosh \frac{y}{L_I} \left(2 - \frac{\nu_e R_I}{V_I L_I^2} \right) - \frac{y}{L_I} \sinh \frac{y}{L_I} \right]$$

We can integrate the last equation, making use of $\rho_e^* = \frac{p_e^*}{\mathrm{R}\, T_e^*}$. Denoting by $G(y)$ the terms inside the brackets we arrive to:

$$p_e^* = P_0 \, \exp\left(-\frac{V_I^2 \, G(y) \, x^2}{2 \, \mathrm{R} \, T_e^* \, R_I^2}\right)$$

where P_0 is the pressure at the stagnation point. The obtained expression for p_e^* depends on y which contradicts the approximation about the constancy of pressure across the B. L. Otherwise, the condition of continuity for the pressure gradients at the plane of contact between the flows ($\eta = 0$) has to hold. We may allow this condition to hold by properly scaling the boundary layer characteristic dimension L. This dimension must be of the order of the inverse of the Reynolds number. If we assume the gradients to be equal at $y = 0$, and neglect the variation in density between the flows, we can write:

$$\begin{aligned}
\left(\frac{\partial p_e^*}{\partial x}\right)_I &= \left(\frac{\partial p_e^*}{\partial x}\right)_{II} \\
-\frac{V_I^2 \, x}{R_I^2}\left(4 - \frac{\nu_e \, R_I}{V_I \, L_I^2}\right) &= -\frac{V_{II}^2 \, x}{L_{II}^2}\left(4 - \frac{\nu_e \, R_{II}}{V_{II} \, L_{II}^2}\right) \\
\frac{4}{\nu_e}\left(\frac{V_I^2}{R_I^2} - \frac{V_{II}^2}{R_{II}^2}\right) &= \frac{V_I}{R_I \, L_I^2} - \frac{V_{II}}{R_{II} \, L_{II}^2}
\end{aligned}$$

We can obtain the length scale L_I if we fix the other one, that is, L_{II}. As it has been said, those lengths are in the order of $\frac{R}{\sqrt{R_e}}$. This way, L_{II} being $\frac{R_{II}}{\sqrt{R_{e_{II}}}}$, we calculate:

$$L_I = \sqrt{\frac{\dfrac{V_I}{R_I}}{\dfrac{V_{II}}{R_{II} \, L_{II}} + \dfrac{4}{\nu_e}\left(\dfrac{V_I^2}{R_I^2} - \dfrac{V_{II}^2}{R_{II}^2}\right)}}$$

that should be in the order of $\frac{R_I}{\sqrt{R_{e_I}}}$. We shall verify it at §5.5.2.4.

5.5.2 The Iterative Sweeping Method

5.5.2.1 Equations

The system of equations the method shall be applied to, is what has been obtained at §5.4.1.

$$\boldsymbol{\Phi}'' + \boldsymbol{\Phi}'\left(\alpha\frac{\boldsymbol{\theta}'}{\boldsymbol{\theta}} + 3C\right) + \boldsymbol{\Phi}\left(m\,C\frac{\boldsymbol{\theta}'}{\boldsymbol{\theta}} + D\right) = E\,\boldsymbol{\theta} + G\Big(\boldsymbol{\Phi}\,\frac{\partial \boldsymbol{\Phi}}{\partial x} - \boldsymbol{\Omega}\,\boldsymbol{\Phi}' - C\,\boldsymbol{\Omega}\,\boldsymbol{\Phi}\Big)$$

$$\boldsymbol{\theta}'' + \boldsymbol{\theta}'\left(\kappa\frac{\boldsymbol{\theta}'}{\boldsymbol{\theta}} + C\right) + J\Big(\boldsymbol{\Phi}'' + C\,\boldsymbol{\Phi}'\Big)^2 = -L\,\boldsymbol{\theta}\,\boldsymbol{\Phi} + P_r\,G\,\left(\boldsymbol{\Phi}\frac{\partial \boldsymbol{\theta}}{\partial x} - \boldsymbol{\Omega}\,\boldsymbol{\theta}'\right)$$

5.5.2.2 Boundary conditions

Boundary conditions are the following:

Velocity along x-axis

$\boldsymbol{x = 0}$

$\left(\frac{\partial^2 u}{\partial x^2}\right)_{x=0} = 0,$ because longitudinal velocity has an inflection point at $x = 0$

$\left(\frac{\partial^2 \boldsymbol{\Phi}}{\partial x^2} u_e + 2\frac{\partial \boldsymbol{\Phi}}{\partial x}\frac{\partial u_e}{\partial x} + \boldsymbol{\Phi}\frac{\partial^2 u_e}{\partial x^2}\right)_{x=0} = 0,$ but $u_e = 0$ and $\frac{\partial^2 u_e}{\partial x^2} = 0$ at $x = 0$,

therefore

$\left(\frac{\partial \boldsymbol{\Phi}}{\partial x}\right)_{x=0} = 0,$ which may be reduced to:

$\left[f_{\eta x} + \frac{(m-1)}{2}\frac{\boldsymbol{\theta}_\eta}{\boldsymbol{\theta}} f_x\right]_{x=0} = 0,$ because, due to symmetry, $\frac{\partial \boldsymbol{\theta}}{\partial x} = 0$; $\frac{\partial \mathbf{p}^*}{\partial x} = 0$;

$\frac{\partial}{\partial \eta}\left(\frac{\partial \boldsymbol{\theta}}{\partial x}\right) = 0$ at $x = 0$. We make also $\mathbf{p}^*_\eta = 0$

$\boldsymbol{x = \infty}$

$\left(\frac{\partial u}{\partial x}\right)_{x=\infty} = 0,$ assuming that longitudinal velocity yields uniform at $x = \infty$

$\left(u_e \frac{\partial \boldsymbol{\Phi}}{\partial x}\right)_{x=\infty} = -\left(\boldsymbol{\Phi}\frac{\partial u_e}{\partial x}\right)_{x=\infty},$ but $\lim_{x\to\infty}\left(\frac{u_e}{\frac{\partial u_e}{\partial x}}\right) \approx x$, and assuming $\frac{\partial \mathbf{p}^*}{\partial x} = 0$

condition may be written as:

$f_{\eta x} + \frac{(m-1)}{2}\frac{\boldsymbol{\theta}_\eta}{\boldsymbol{\theta}} f_x = -x\left[f_\eta + \frac{(m-1)}{2}\frac{\boldsymbol{\theta}_\eta}{\boldsymbol{\theta}} f\right]$ for $x = \infty$

Temperature along x-axis

$\left(\frac{\partial \boldsymbol{\theta}}{\partial x}\right)_{x=0} = 0,$ because of symmetry

$\left(\frac{\partial \boldsymbol{\theta}}{\partial x}\right)_{x=\infty} = 0,$ assuming that temperature yields uniform at $x = \infty$

Velocity along η-axis

$f_\eta(\eta = \infty) = 1$, longitudinal velocity at $\eta = \infty$ passes over into that for external flow I

$f(\eta = 0) = 0$, both flows stop at $\eta = 0$

$f_\eta(\eta = -\infty) = \dfrac{V_{II}}{V_I}$, longitudinal velocity at $\eta = -\infty$ passes over into that for external flow II

Temperature along η-axis

$\boldsymbol{\theta}(\eta = \infty) = 1$, temperature at $\eta = \infty$ passes over into that for external flow I

$\boldsymbol{\theta}(\eta = -\infty) = \dfrac{T_{II}}{T_I}$ temperature at $\eta = -\infty$ passes over into that for external flow I

Because the problem is of first order in x (unless we include the momentum equation in the y direction) B.C. along x-axis are redundant (duplicated). It would be necessary to discriminate between $x = 0$ and $x = \infty$ or try to hold both B.C. minimizing the total error. Eventually conditions at $x = 0$ are chosen as the most reasonable, because of the symmetry conditions.

5.5.2.3 Solving equations

As the problem is advective in x, solution is initiated by writing the equations for $x_0 = 0$ making use of $u_e(x, y) \sim x$ for $x \to 0$ (which leads to $G(0) = J(0) = L(0) = 0$):

$$\boldsymbol{\Phi}_0'' + \boldsymbol{\Phi}_0' \left(\alpha \frac{\boldsymbol{\theta}_0'}{\boldsymbol{\theta}_0} + 3C_0 + \frac{\boldsymbol{f}_0}{1 + \cosh \dfrac{y}{L_I}} \right) + \boldsymbol{\Phi}_0 \left(m\, C_0 \frac{\boldsymbol{\theta}_0'}{\boldsymbol{\theta}} + D_0 + \frac{\boldsymbol{f}_0\, C_0}{1 + \cosh \dfrac{y}{L_I}} \right) = E_0\, \boldsymbol{\theta}_0$$

$$\boldsymbol{\theta}_0'' + \boldsymbol{\theta}_0' \left(\kappa \frac{\boldsymbol{\theta}_0'}{\boldsymbol{\theta}_0} + C_0 + P_r \frac{\boldsymbol{f}_0}{1 + \cosh \dfrac{y}{L_I}} \right) = 0$$

$$\boldsymbol{\Phi}_0 = \boldsymbol{f}_0' + \alpha\, \boldsymbol{f}_0 \frac{\boldsymbol{\theta}_0'}{\boldsymbol{\theta}_0},$$

that allows us to obtain $\boldsymbol{\Phi}_0(\eta)$, $\boldsymbol{\theta}_0(\eta)$ and $\boldsymbol{f}_0(\eta)$. Let notice that C_0, D_0 and E_0 are functions of $\boldsymbol{\theta}_0$. For calculating those functions, y has to be obtained (because u_e, u_{e_y} and $u_{e_{yy}}$ depend on y), solving an integral at each η step. At the same time, that integral depends on $\boldsymbol{\theta}_0$, that is a variable of the problem. The explicit expressions for C_0, D_0 and

E_0 are:

$$C_0 = \frac{\sinh\frac{y}{L_I}\sqrt{\boldsymbol{\theta}^{m+1}}}{L_I\left(1+\cosh\frac{y}{L_I}\right)^2}\sqrt{\frac{R\,\mu_e\,T_e}{a\,P_0}}$$

$$D_0 = \frac{\cosh\frac{y}{L_I}\,\boldsymbol{\theta}^{m+1}}{L_I^2\left(1+\cosh\frac{y}{L_I}\right)^3}\left(\frac{R\,\mu_e\,T_e}{a\,P_0}\right)$$

$$E_0 = -\frac{G(y)}{\left(1+\cosh\frac{y}{L_I}\right)^3}$$

where $G(y)$ is explained in §5.5.1.

Next, we write the equations for $x_1 = \Delta x$ and approximate first derivatives by backward finite differences:

$$\boldsymbol{\Phi}_1'' + \boldsymbol{\Phi}_1'\left(\alpha\frac{\boldsymbol{\theta}_1'}{\boldsymbol{\theta}_1} + 3C_1\right) + \boldsymbol{\Phi}_1\left(m\,C_1\frac{\boldsymbol{\theta}_1'}{\boldsymbol{\theta}} + D_1\right) = E_1\,\boldsymbol{\theta}_1 + G_1\Big(\boldsymbol{\Phi}_1\frac{\boldsymbol{\Phi}_1-\boldsymbol{\Phi}_0}{\Delta x} - \boldsymbol{\Omega}_1\,\boldsymbol{\Phi}_1' - C_1\,\boldsymbol{\Omega}_1\,\boldsymbol{\Phi}_1\Big)$$

$$\boldsymbol{\theta}_1'' + \boldsymbol{\theta}_1'\left(\kappa\frac{\boldsymbol{\theta}_1'}{\boldsymbol{\theta}_1} + C_1\right) + J_1\Big(\boldsymbol{\Phi}_1'' + C_1\,\boldsymbol{\Phi}_1'\Big)^2 = -L_1\,\boldsymbol{\theta}_1\,\boldsymbol{\Phi}_1 + P_r\,G_1\left(\boldsymbol{\Phi}_1\frac{\boldsymbol{\theta}_1-\boldsymbol{\theta}_0}{\Delta x} - \boldsymbol{\Omega}_1\,\boldsymbol{\theta}_1'\right)$$

$$\boldsymbol{\Phi}_1 = \boldsymbol{f}_1' + \alpha\,\boldsymbol{f}_1\frac{\boldsymbol{\theta}_1'}{\boldsymbol{\theta}_1},$$

$$\boldsymbol{\Omega}_1 = \frac{\boldsymbol{f}_1}{x_1} + \frac{\boldsymbol{f}_1-\boldsymbol{f}_0}{\Delta x} + \alpha\,\frac{\boldsymbol{f}_1}{\boldsymbol{\theta}_1}\left(\frac{\boldsymbol{\theta}_1-\boldsymbol{\theta}_0}{\Delta x}\right) + \frac{\boldsymbol{f}_1}{2\,p_e(x_1)}\left.\frac{\partial p_e}{\partial x}\right|_{x=x_1}$$

that allows us to obtain $\boldsymbol{\Phi}_1(\eta)$, $\boldsymbol{\theta}_1(\eta)$, $\boldsymbol{f}_1(\eta)$ and $\boldsymbol{\Omega}_1(\eta)$, C_1, D_1, E_1, G_1, J_1 and L_1 being functions of $\boldsymbol{\theta}_1$.

B.C.: $f_i'(+\infty) = 1; \quad f_i'(-\infty) = \frac{V_{II}}{V_I}\lambda; \quad \theta_i(+\infty) = 1; \quad \theta_i(-\infty) = \tau = \frac{T_{II}}{T_I}$

Besides: $\theta_i'(+\infty) = \theta_i'(-\infty) = 0$, because external temperature is constant

This way, the discretized system equivalent to equations for $\boldsymbol{\Phi}$, $\boldsymbol{\theta}$, $\boldsymbol{f}$ and $\boldsymbol{\Omega}$ can be integrated in x and η, separately. Once a reasonable x_∞ is reached, integration might be refined by starting a second sweep where first derivatives in x are approximated as $\frac{x_{i+1}^1 - x_{i-1}^2}{2\,\Delta x}$. A reasonable x_∞ should produce an asymptotic behavior for u along x-axis.

5.5.2.4 Integration details

Integration is implemented for two unequal jets labeled as I and II, with the following parameters:

-Jet velocities: $V_I = 30\ m/s$; $V_{II} = 10\ m/s$.

-Jet widths: $R_I = 500\ m$; $R_{II} = 1000\ m$.

-Jet temperatures (T_e): $T_I = 303\ K$; $T_{II} = 233\ K$.

-Boundary layer characteristic dimensions (according to §5.5.1): $L_I = 1.2 \times 10^{-2}\ m$; $L_{II} = 6 \times 10^{-2}\ m$. Those values can be compared with $R_I/\sqrt{R_{e_I}} = 2.4 \times 10^{-2}\ m$ and $R_{II}/\sqrt{R_{e_{II}}} = 5.7 \times 10^{-2}\ m$.

-x domain (from 0 to ∞): $(0, 10)$; $\Delta x = 1$

-η domain (from $-\infty$ to ∞): $(-5, 2)$ (minus sign corresponds to jet I); $\Delta\eta = 1e-2$. This domain probably needs to be adjusted during the numerical calculation.

Physical parameters:

$P_r = 0.7$; Jet dynamic viscosities (μ_e): $\mu_I = 1.983 \times 10^{-5}\ kg/m.s$; $\mu_{II} = 1.412 \times 10^{-5}\ kg/m.s$; $m = 0.7$; $c_{P_e} = 10^{-3}\ J/kg.K$; $\gamma = 0$.

Equations for $\mathbf{\Phi}(\eta)$, $\boldsymbol{\theta}(\eta)$, $\boldsymbol{f}(\eta)$ and $\mathbf{\Omega}(\eta)$ are integrated by the shooting method at each x step. Shooting is made from $-\infty$ and ∞, for which values for $f(-\infty)$ and $f(\infty)$ have to be guessed (these values are in the order of η at $-\infty$ and η at ∞, respectively). Conditions at $\eta = 0$, that is, $f(\eta = 0) = 0$ and $f_\eta(0-) = f_\eta(0+)$, must be satisfied.

5.5.2.5 The particular case of an incompressible flow

Since the numerical calculation of the compressible flow equations seems some troublesome we may start analyzing the uncoupled equation for the velocity field (differential equation in f) resulting from the incompressible flow. Such equation reads as follows:

$$f''' + 3\,f''\,\lambda_y \frac{\partial y}{\partial \eta} + f'\,\lambda_{2y} \left(\frac{\partial y}{\partial \eta}\right)^2 = -\frac{a\,x^3}{u_e^3} \left(\frac{V_I}{L_I}\right)^2 - \frac{a\,x\,f}{u_e}\left(f'' + \lambda_y \frac{\partial y}{\partial \eta}\,f'\right)$$

where the first term in the RHS correspond to the pressure gradient.

Solving for $x_0 = 0$ (keeping the aforementioned scheme for the compressible case), we

get:

$$\lambda_y \frac{\partial y}{\partial \eta} = \frac{R_I}{V_I\, L_I} \sqrt{\frac{\mu_e\, a}{\rho_e}} \frac{\sinh \dfrac{y}{L_I}}{\left(1 + \cosh \dfrac{y}{L_I}\right)^2}$$

$$\lambda_{2y} \left(\frac{\partial y}{\partial \eta}\right)^2 = \left(\frac{R_I}{V_I\, L_I}\right)^2 \frac{\mu_e\, a}{\rho_e} \frac{\cosh \dfrac{y}{L_I}}{\left(1 + \cosh \dfrac{y}{L_I}\right)^3}$$

$$\frac{a\, x^3}{u_e^3} \left(\frac{V_I}{L_I}\right)^2 = \frac{2 + \cosh \dfrac{y}{L_I} \left(2 - \dfrac{\nu_e\, R_I}{V_I\, L_I^2}\right) - \dfrac{y}{L_I} \sinh \dfrac{y}{L_I}}{\left(1 + \cosh \dfrac{y}{L_I}\right)^3}$$

$$\frac{a\, x}{u_e} = \frac{1}{1 + \cosh \dfrac{y}{L_I}}$$

approximating $\sinh \dfrac{x}{R_I}$ by $\dfrac{x}{R_I}$ and remembering that $a = \dfrac{V_I}{R_I}$. Now we can solve the third order differential equation for f with the boundary conditions detailed at §5.52.2.

5.6 Momentum equation along y-axis

Although we have obtained the pressure change across the BL we have evaded the consideration of the boundary condition at the plane of contact between the flows ($\eta = 0$) (see §5.1) by relating the widths of the BL at each side of that plane. It was acceptable, anyway, because variation of the pressure with η is considerably smaller respecting to its variation along x-axis. Other way to proceed for considering the pressure across the BL is to write:

$$\begin{aligned} \boldsymbol{p}^* &= \boldsymbol{P}^*(x) + O(\delta) \\ &= \boldsymbol{P}^*(x) + x\, e^{-\eta}\, \boldsymbol{Q}^*(\eta) \end{aligned}$$

where δ represents the maximum value of the coordinate η, that is, the width of the BL. In that case $\dfrac{\partial p^*}{\partial y}$ is $O(\delta)$ and momentum equation in the y direction is incorporated in order to calculate the unknown function $\boldsymbol{Q}^*(\eta)$ while function $\boldsymbol{P}^*(x)$ is determined as before by the momentum equation in the x direction at the outer edge of the BL. Then, we have:

$$\frac{\partial \boldsymbol{p}^*}{\partial x} = \frac{\mathrm{d}\boldsymbol{P}^*}{\mathrm{d}x} + e^{-\eta}\,\boldsymbol{Q}^*(\eta)$$

$$\frac{\partial \boldsymbol{p}^*}{\partial x} = \frac{\mathrm{d}\boldsymbol{P}^*}{\mathrm{d}x} \quad \text{for } \eta \to \infty \quad \text{and} \quad \frac{\partial \boldsymbol{p}^*}{\partial x} = \frac{\mathrm{d}\boldsymbol{P}^*}{\mathrm{d}x} + \boldsymbol{Q}^*(\eta) \quad \text{for } \eta = 0$$

5.7 Condensation

Cooling of air carrying supersaturated water vapour ignites a parallel process of nucleation and condensation of water molecules due to the fact that both, vapour and equilibrium vapour densities decreases. Vapour density decreases because of diffusion-convection of the vapour in the air flow and equilibrium vapour density because the vapour cools as it moves. Which is the spatial scale of this process? In other words, it is confined to the boundary layer? Probably is not and temperature in the inner edge of the transition region might be substantially low and therefore, condensation is already taking place before to reach the boundary layer. We will refer now to a previous work about homogeneous vapour condensation from boundary layers [12]. Homogeneous means in this context that condensation takes place on nuclei created by nucleation of vapour molecules instead of on particles suspended in the flow. Non-dimensional equations controlling the nucleation-condensation process are indicated below (considering a free molecular regime) assuming that a self-similar solution for the concentration is possible:

$$\begin{aligned}
G\rho' + \alpha\left(\frac{T'}{T}\right)'\rho &= -\frac{Bc^2}{S_c\sqrt{6\pi\epsilon}}\exp\left(-\frac{1}{2\beta^2 T^3\epsilon^3}\right)H(c-c_e),\\
B &= \frac{(3\tilde{v})^{2/3}\tilde{c}_\infty l_b^2}{D}\left(\frac{2}{\pi}\right)^{1/6}\sqrt{\frac{k_B\tilde{T}_\infty}{\tilde{m}_v}},\\
\epsilon &= \frac{k_B\tilde{T}_\infty}{2\tilde{\sigma}_{lv}(\frac{4\pi}{3}\tilde{v}^2)^{1/3}},\\
\beta &= \ln\left(\frac{\tilde{c}}{\tilde{c}_e}\right),\\
l_b &= \sqrt{\frac{\nu}{a_1}},\\
G &= F + \alpha\frac{T'}{T},\\
c_e(\eta) &= \frac{T_d}{T(\eta)}\exp\left[\frac{\Lambda_v}{\epsilon}\left(\frac{1}{T_d} - \frac{1}{T(\eta)}\right)\right],\\
\frac{\Lambda_v}{\epsilon} &= \frac{\tilde{\Lambda}_v}{k_B\tilde{T}_\infty},
\end{aligned}$$

$$
\begin{aligned}
Gn' &= -\frac{B}{S_c}\,(c-c_e)T^{1/2}n^{2/3}H(n-n_*)\,H(c-c_e),\\
n_* &= \left(\frac{1}{\epsilon\beta T}\right)^3,\\
c''+S_cF\,c' &= B\left[\frac{\epsilon^{-7/2}c^2}{\sqrt{6\pi}\beta^3T^3}e^{-\frac{1}{2\beta^2T^3\epsilon^3}}+(c-c_e)\rho T^{1/2}n^{2/3}H(n-n_*)\right]H(c-c_e),
\end{aligned}
$$

where α is the thermophoretic coefficient, $S_c=\dfrac{\nu}{D}$ is the Schmidt number, $\tilde{v}$ is the vapour molecular volume, $\tilde{m}_v$ is the mass of a vapour molecule, k_B is the Boltzmann constant, $\tilde{\sigma}_{lv}$ is the liquid-vapour surface tension, T_d is the dew point temperature and $\tilde{\Lambda}_v$ is the heat of vaporization of water. $\tilde{c}_\infty$ is the reference vapour density at the outer edge of the boundary layer and $\tilde{T}_\infty=\tilde{T}_f$.

The three variable of the problem are the water vapour density (c), the droplet density (ρ) and the number of molecules per droplet (n). Droplets are produced by condensation of vapour monomers on the supercritical nuclei. One thing that hadn't been considered in the aforementioned previous work and that we will consider now is the thermal inertia of the droplets. That will bring some changes into the above listed equations specifically because the equilibrium vapour density will not be controlled anymore by the flow temperature but by the new variable Θ or droplet temperature. The droplet temperature is related with the rest of variables, specifically with c and n, by the equation [114]:

$$
\begin{aligned}
N[c-c_e(\Theta)]f_c &= L(\Theta-T)f_h,\\
N &= \frac{c_\infty l_b^2(48\pi^2\tilde{v})^{1/3}}{S_c}\\
L &= \frac{\lambda\tilde{T}_\infty(48\pi^2\tilde{v})^{1/3}}{a_1\tilde{\Lambda}},
\end{aligned}
$$

where λ is the thermal conductivity of the gas-vapour mixture and f_c and f_h are factors depending on the Knudsen number. The first of the latter equations is written for the continuum limit. In our case (free molecular regime) it should be:

$$
\frac{B}{S_c}\,T^{1/2}n^{1/3}[c-c_e(\Theta)]f_c = L(\Theta-T)f_h
$$

(Let notice that the term $T^{1/2}$ doesn't change because it comes from the Maxwellian corresponding to the ambient temperature)

But condensation is a temperature-varying process. Droplet absorbs heat in dependance of its specific heat and mass, thus, droplet temperature is time-dependent, although its characteristic time is much smaller than that of the convection-diffusion process. The mechanism is graphically described in Figure 5.14.

For that reason, equation above is a particular case of a more general integro-differential equation (in which it was supposed that C is not temperature-dependent and $\Delta\Theta=0$,

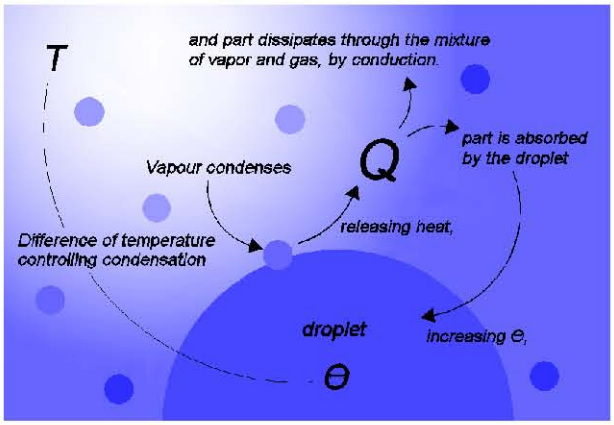

Figure 5.14: Mechanism of heat exchange in condensation process

making the RHS to vanish):

$$\begin{aligned} \frac{B}{S_c} T^{1/2} n^{2/3} [c - c_e(\Theta)] f_c - L n^{1/3} (\Theta - T) f_h &= \int_{\Theta_1}^{\Theta_2} C \mathrm{d}\Theta, \\ c_P &= \left(\frac{\partial C}{\partial m} \right)_P, \end{aligned}$$

where C and c_P are the droplet's heat and specific heat capacities respectively. Now, the second equation is transformed into $C = c_P \tilde{m}_v n$ and substituted in the first one, leading to:

$$\frac{B}{S_c} T^{1/2} n^{2/3} [c - c_e(\Theta)] f_c - L n^{1/3} (\Theta - T) f_h = c_P \tilde{m}_v \int_{\Theta_1}^{\Theta_2} n \mathrm{d}\Theta,$$

Assuming that vapours are diluted, T is not affected by the heat conduction through the mixture and $\Theta_1 = T$, $\Theta_2 = \Theta$. Resuming, we have the five basic equations:

$$\begin{aligned} G\rho' + \alpha \left(\frac{T'}{T} \right)' \rho &= -\frac{B c^2}{S_c \sqrt{6\pi\epsilon}} \exp\left(-\frac{1}{2\beta^2 T^3 \epsilon^3} \right) H(c - c_e), \\ c_e(\eta) &= \frac{T_d}{\Theta(\eta)} \exp\left[\frac{\Lambda_v}{\epsilon} \left(\frac{1}{T_d} - \frac{1}{\Theta(\eta)} \right) \right], \\ c_P \tilde{m}_v \int_T^{\Theta} n \mathrm{d}\Theta &= \frac{B}{S_c} T^{1/2} n^{2/3} [c - c_e(\Theta)] f_c - L n^{1/3} (\Theta - T) f_h, \\ G n' &= -\frac{B}{S_c} (c - c_e) T^{1/2} n^{2/3} H(n - n_*)\, H(c - c_e), \\ c'' + S_c F\, c' &= B \left[\frac{\epsilon^{-7/2} c^2}{\sqrt{6\pi} \beta^3 T^3} e^{-\frac{1}{2\beta^2 T^3 \epsilon^3}} + (c - c_e) \rho T^{1/2} n^{2/3} H(n - n_*) \right] H(c - c_e), \end{aligned}$$

5.8 Ice formation

Is it condensation the end of the process? When the temperature of the quiescent cold gas approaches 240 K, it is expected that a second phase transition will take place and the droplet or part of it, will freeze. Droplet freezing starts normally when isolated ice nuclei, already present within the droplet or coming from the surrounding gas, contact the outside of the droplet, and this occur at temperatures equal or a little lower than 273 K. Outer undercooled water vapour may cristallize directly on these nuclei or, as the water in the droplet is supercooled, droplet may also freeze as soon as an exterior nucleus reaches its surface. But homogeneous freezing of a liquid droplet (that is, without the aid of an ice nucleus) happens if temperature is lower than 240 K [47]. At those temperatures it would seem also possible that a vapour-to-ice process (with no liquid transition) takes place, but in fact, from a practical point of view, nucleation of ice crystals directly from the vapour phase doesn't occur, at least for temperatures above 173 K [87].

Ignoring the presence of any ice-forming nucleus, situation can be summarized as follows: In a first stage flowing water vapour cools and it nucleates producing liquid droplets by further condensation. After that, vapour and droplets cools even more and when temperature go below 240 K a parallel process of droplet freezing and vapour-to-ice nucleation is initiated. Considering only temperatures above 173 K the latter process of vapour-to-ice nucleation may be neglected. In addition, when droplets start freezing the mechanism of subsequent growth by accretion of vapour molecules becomes a crystallization process as vapour molecules pass direclty to the solid phase. So, at the same time, droplet solidifies by (internal) freezing and (external) growth.

While ice nucleation may be described by a similar mechanism to that of nucleation in the liquid phase, droplet freezing is a more delicate task. The first question that arises is "..whether the liquid, when confined to small dimensions, can be regarded as true liquid water". First works, as those by Turnbull & Fisher (1949) and Buckle (1961) considered the freezing of supercooled water in bulk form. Later, Wood & Walton (1970) tackled the problem of freezing of liquid droplets and their results are cited by Huang & Bartell [47].

5.8.1 Ice nucleation from the supercooled water

The rate of production of critical ice nuclei in the supercooled droplet can be expressed by [87]:

$$\tilde{J} = 2\tilde{N}_c \left(\frac{k_B \tilde{\Theta}\, \tilde{g}_w}{h\, \tilde{g}_i} \right) \sqrt{\frac{\tilde{\sigma}_{sl}}{k_B \tilde{\Theta}}} \exp\left(-\frac{\Delta \tilde{F}_g}{k_B \tilde{\Theta}} - \frac{\Delta \tilde{A}_w}{k_B \tilde{\Theta}} \right)$$

where $\tilde{N}_c$ is the number of water molecules in contact with unit area of the ice surface (in the order of 10^{12} cm^{-2}, see reference), $\tilde{g}_w$ and $\tilde{g}_i$ are the mass densities of water and ice respectively, h is Planck's constant, $\tilde{\sigma}_{sl}$ is the solid-liquid surface tension and $\Delta \tilde{F}_g$ and $\Delta \tilde{A}_w$ are the free energy for the formation of a critical nucleus (or germ) and the activation energy for diffusion of water molecules across the water-ice boundary, respectively.

The energy $\Delta\tilde{F}_g$ differs from that of nucleation from the vapour phase because the free energy difference between the two phases (in the denominator of $\Delta\tilde{F}_g$) is now a function of the heat of fusion at the melting point, $\Delta\tilde{H}_m$. Several ways for obtaining $\Delta\tilde{H}_m$ may be considered. Here we shall use [44, 47]:

$$\begin{aligned}
\Delta\tilde{H}_m &= \int_{\tilde{\Theta}}^{\tilde{\Theta}_m} \Delta\tilde{S}_m(\tilde{\Theta})\mathrm{d}\tilde{\Theta} \\
\Delta\tilde{S}_m(\tilde{\Theta}) &= \frac{\Delta\tilde{h}_m}{\tilde{\Theta}_m} - \int_{\tilde{\Theta}}^{\tilde{\Theta}_m} \frac{\Delta\tilde{c}_p}{\tilde{\Theta}}\mathrm{d}\tilde{\Theta} \\
\tilde{c}_{pw} &= 30.7259 - 0.1129\,(\tilde{\Theta} - 226) + \frac{41.7}{[1 + 0.0072\,(\tilde{\Theta} - 226)^2]} \\
\tilde{c}_{pi} &= 37.9091 + 0.1319\,\tilde{\Theta}
\end{aligned}$$

where $\Delta\tilde{S}_m(\tilde{\Theta})$ is the change in entropy between ice and supercooled water, $\tilde{\Theta}_m$ is the melting temperature, $\Delta\tilde{h}_m$ is the water enthalpy of fusion (in J/mol), $\Delta\tilde{c}_p$ is the difference in spacific heat capacity of the water and the ice, $\tilde{c}_{pi}(\tilde{\Theta})$ is the function for hexagonal ice molar specific heat capacity [87] and $\tilde{c}_{pw}(\tilde{\Theta})$ is the function for supercooled water molar specific heat capacity [47], both expressed in J/mol with $\tilde{\Theta}$ in K. Temperature range considered was $230\ K \leq \tilde{\Theta} \leq 273\ K$. Once we have $\Delta\tilde{H}_m$, $\Delta\tilde{F}_g$ is obtained as follows [47]:

$$\Delta\tilde{F}_g = \frac{16\pi\tilde{\sigma}_{sl}^3}{3\left(\dfrac{\Delta\tilde{H}_m}{N_A\tilde{v}_w} + \dfrac{2\tilde{\sigma}_l(\tilde{g}_w - \tilde{g}_i)}{\tilde{g}_w}\right)^2}$$

where surface tension of water, $\tilde{\sigma}_l$, is temperature-dependent.

Another way to deal with $\Delta\tilde{F}_g$ could have been by means of the critical nucleus size, obtained from the thermodynamical equilibrium between solid and liquid phases [24].

The other quantity, $\tilde{A}_w$, can be estimated by experimental work [87] or, on the contrary, assuming to be related with the viscosity through the Eyring's expression [89].

$$\Delta\tilde{A}_w = k_B\tilde{\Theta}\ln\left(\frac{\mu_w\tilde{v}_w}{h}\right)$$

where μ_w is the water absolute viscosity.

5.8.2 Growth of ice nuclei and droplet freezing

As soon as the critical size nucleus is reached, ice crystals accrete water molecules from the droplet and grow at a rate that depends basically on the supercooling. At the same time, the droplet continues accreting vapour molecules from the outside and growing too. For assuming that the droplet growth results from a vapour-to-ice nucleation process (dry growth regime), latent heat of freezing has to be dissipated by conduction with the

surroundings. Thus, initially supercooled droplet will increase its temperature because of freezing, and only if it keeps below T_m the process will be continued.

To deal with the droplet growth and freezing process we shall propose a very simplified model on the main following lines (see also Figure 5.15):

1. Homogeneous water-to-ice nucleation, at a rate given by $\tilde{J}$ above, will start when droplet temperature goes below 240 K. Droplet temperature doesn't mean necessarily a uniform temperature but the temperature of the droplet in a region close to its surface.

2. Homogeneous water-to-ice nucleation will proceed until a shell (assuming spherical droplets) of ice, with a constant width equal to the critical nucleus size, is formed in the outside of the droplet. This will be called the first stage. At this moment temperature inside the droplet (unfrozen water) has risen above the initial temperature.

3. Subsequent droplet growth and freezing will be determined by the heat exchange process between supercooled air, ice shell and inner unfrozen water at temperature 240 $K \leqq \tilde{\Theta} \leqq 273$ K ($\tilde{\Theta} = \Theta_w$). This will correspond to the second stage. Water inside the droplet warms up owing to the heat released by the ice shell as it grows but, at the same time, heat is conducted to the outside through the shell itself, reaching a balance that allows the droplet for keep freezing inside.

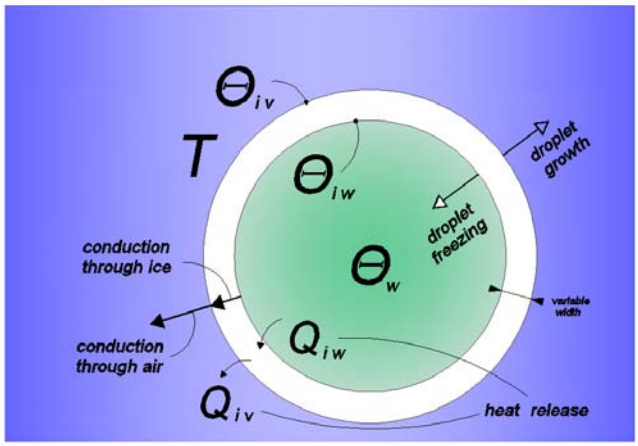

Figure 5.15: Mechanism of heat exchange in freezing process. $\Delta T = T - \Theta_{iv}$ controls the droplet growth and $\Delta T = \Theta_{iw} - \Theta_w$ controls the internal ice shell growth.

Time for completing the first stage can be roughly obtained by [64, 65]:

$$t_1 = \frac{\delta a}{G}$$

as the time for the critical size nuclei to cover the whole surface of the droplet. Therefore, δa is the thickness of the external layer of mixed ice and water which equals critical nucleus size (r_g) according to our proposed model. Dufour and Defay [24] gives:

$$r_g = \frac{2\,\sigma_w\,v_w}{\bar{\Lambda}_c\,\ln(T_{e_{wv}}/T)}$$

where σ_w, v_w, $\bar{\Lambda}_c$ and $T_{e_{wv}}$ are surface tension, molecular volume, mean heat of condensation and liquid-vapour equilibrium temperature, corresponding to water, respectively.

G is the growth rate of ice that depends on how process of accretion is conceived [8, 10, 11, 40, 42, 66, 86], more specifically in which regime it is occurring depending on the molecular mechanism of crystal formation. In general:

$$G \sim \frac{D_w\,\bar{\Lambda}_m}{a_0\,k_B\,T_0}\Delta T_s$$

where D_w is the water-water diffusivity (that is a consequence of the appearance of a clustered structure in supercooled water [87]), $\bar{\Lambda}_m$ is the mean heat of fusion, a_0 is the molecular spacing in ice, k_B is Boltzmann constant, $T_0 = 273\,K$ and ΔT_s is the supercooling.

However, we may also obtain first stage duration in a much simpler way by means of previously calculated rate of production of supercritical nuclei (J) inside the droplet, as:

$$t_1 = \frac{16\,\pi\,R^2\,r_g}{3\,J}$$

R being the droplet radius.

We shall consider that the ice-water interface has the same temperature as the water inside the ice shell, namely, $\Theta_{iw} = \Theta_w$ (see Figure 5.15) and also that a quasi-steady state is reached, then, heat released by the water (Q_{iw}) and conducted through ice equals the heat released by the droplet to the environment (Q_{iv}). On the other hand, Q_{iv} is the summation of two terms: the heat conducted through air and the heat released by the droplet freezing process. Denoting by r the shell internal radius, balance heat equations for the droplet interfaces at the second stage, reads:

$$4\,\pi\,\rho_w\,\Lambda_m\,r^2\,\frac{\mathrm{d}r}{\mathrm{d}t} = \frac{4\,\pi\,\lambda_i\big[T_0 - \Theta_{iv}(r)\big]\,R\,r}{R-r}$$

$$\frac{4\,\pi\,\lambda_i\big[T_0 - \Theta_{iv}(r)\big]\,R\,r}{R-r} = 4\,\pi\,R\,\lambda_a\big[\Theta_{iv}(r) - T\big] + 4\,\pi\,R\,\Lambda_s\,D_v\big(c - c_e\big)$$

through which the duration of the second stage may be calculated, when r is integrated between $R - 2\,r_g$ and 0. In the former equations ρ_w is water number density, λ_i and λ_a are the thermal conductivities of ice and air respectively, Λ_s is the heat of sublimation of ice and D_v is the water vapour diffusivity in air.

Chapter 6

General conclusions

6.1 Reaching the goals?

This is the time the circle has been closed or, much better, the angle of departure has been reached and we hope, at some point above the initial one. We will proceed by summarizing aims and achievements.

6.2 Boundary layer incompressible flows: the combustion chamber

The combustion chamber is a scenario where condensation and subsequent deposition play a very important and practical role.

6.2.1 homogeneous condensation

1. A theory of homogeneous condensation and deposition near a cold wall has been developed for the specific case of a stagnation-point flow and a complete model has been solved numerically obtaining deposition rates and vapour number density, droplet number density and number of condensate profiles for wall temperatures ranging from $800\,K$ to $1200\,K$.

2. A very satisfactory singular perturbation approach of the same problem has been made making use of some simplifications resulting from the precedent work.

3. The aforementioned model where a monodisperse droplet size distribution was assumed, has been extended to the general case of a polydiperse distribution. Results validate the monodisperse approach in terms of the profiles that have been obtained but allow to recognize some distinctions that affect in some degree the deposition rates.

4. The more general case of a wedge flow (accepting self-similar solutions as the particular stagnation-point flow) was theoretically undertaken producing a slight different differential equation for the vapour number density. This equation, valid for small wedge angles, hasn't been solved and we think it should be the matter of a future work.

5. A model is proposed to describe the behavior of wedge flows for any wedge angle based in extending the boundary layer classical behavior to the flow upstream and solving the whole problem in terms of the inhomogeneous biharmonic compact form of the Navier-Stokes equations. This model would make applicable the theory of wedge flows to oblique impinging flows. This is also apoint needed to continuation and numerical vallidation.

6.2.2 mixed condensation

1. A complete model for describing simultaneous heterogeneous (in the continuum and molecular regimes) and homogeneous condensation (in the molecular regime) has been developed but it hasn't been applied to the whole range of wall temperatures as the homogeneous case.

2. The mixed condensation was described also by means of independent alternate homogeneous and heterogeneous model with good results. We think that will allow to develop a singular perturbation approach resorting in our previous work.

6.2.3 the agglomeration process

1. A Monte Carlo simulation of the diffusively controlled agglomeration process has been implemented obtaining geometrical characterization of the agglomerates for the early stages of the process (residence times of a few seconds in a combustion chambers). These structures differ (are more chain-like or less fractal-like) than those usually described in the literature because of the smaller residence times.

2. We are proposing two new indexes for characterizing geometrically the agglomerates that taken together may allow to describe more accurately the agglomerates considered in a larger (non-local) scale.

6.2.4 something else about the agglomeration process

We are proposing and analytically advancing a model for the agglomeration process taking in account stochastic and thermophoretic motion of particles and clusters. As we know it hasn't been undertaken up to now.

6.3 Counterflow boundary layers in compressible flows: atmospheric scenarios

The problem of impinging jets has a solution as ideal plane flows only for the case of equal jet velocities, equal also to the velocities of the two outgoing flows [7]. The case of interest, however, is the problem of two unequal impinging jets for which only a solution with vorticity is possible. What we have intended here is to approach a meteorological problem of two flows at different temperatures that collide developing a boundary layer in the plane of contact. External flow solution is an approximation to zeroth-order of the Navier-Stokes equations in compact form. Problem has been tackled in two steps:

First, we write the equations for modelling a compressible flow with temperature-dependent properties for obtaining the velocity and temperature fields. Considering the problem is advective-diffusive across the boundary layer but only convective along it, the plane boundary layer problem is numerically undertaken by decomposing it in a series of linear boundary layer problems matched together. A finite difference scheme is used to discretize the x-derivatives. Linear problem for each x is solved by the shooting method.

Second, we study the nucleation and condensation of water vapour taking in account the droplet thermal inertia. We have also extended the model to include the ice formation and freezing process of the droplets.

Appendix A

The agglomeration process stochastically and thermophoretically considered

As part of the work of heterogeneous and homogeneous condensation in combustion chambers and subsequent deposition on boundary-layer flows, we have tackled the creation of fractal-like soot agglomerates. Process of agglomeration has been classically faced by stochastic simulations. In a previous chapter we have simulated the agglomeration process by applying a random-diffusive mixed procedure. But Brownian forces, that are very important during the initial stages, tends to reduce significantly with growth. At that time, thermophoretic forces are expected to have the most important role and will therefore affect the geometric structure of the agglomerate. In this appendix we propose a model where both, stochastic and thermophoretic forces, drive the agglomeration process assuming the agglomerates reach translational and rotational equilibrium at each time step of the simulation. As we are talking about primary particles of about 50 nm, and the fractal-like agglomerates we have previously obtained feature a rather open structure, the free molecular regime has been considered. Now, in addition to stochastic motion we consider the thermophoresis, calculating the net force on the agglomerate at each time step. This net force is obtained estimating the screen effect on each particle forming the agglomerate due to the presence of the others. The process would be run for different residence times, for obtaining, both, the parameters characterizing the agglomerate geometry and the thermophoretic velocities.

A.1 Introduction

Calculation of thermophoretic forces on a particle immersed in a gas when particle size is considerably smaller than the mean free path of the gas molecules is nowadays a classic problem that can be tackled by the theory developed by L. Waldmann in 1959 [108]. First thing it has to be commented is whether such a theory is applicable to the agglomeration process we are dealing with. All agglomerate configurations may be confined in a region bounded by the curves: $\frac{L}{d_p} = N_p$, applying for a chain-like agglomerate, and $\frac{L}{d_p} = (N_p)^{1/3}$, applying for an absolutely dense sphere, L being the distance between the two farthest particles in the agglomerate, d_p the particle's diameter and N_p, the number of particles in the agglomerate. Thus, N_p exponent becomes a measure of how spatially extended the agglomerate happens to be. For a chain-like agglomerate, the characteristic dimension for the agglomeration process in indeed the particle's diameter d_p, while for a sphere with $L \gg d_p$, it shall be L, that is, the problem, for very big agglomerates, moves from the molecular to the continuum regimes. Results of our previous stochastic model is reflected by a cloud of blue circles in Figure A.1, where enveloping volume (E_v) means $\frac{4\,\pi\,L^3}{3}$.

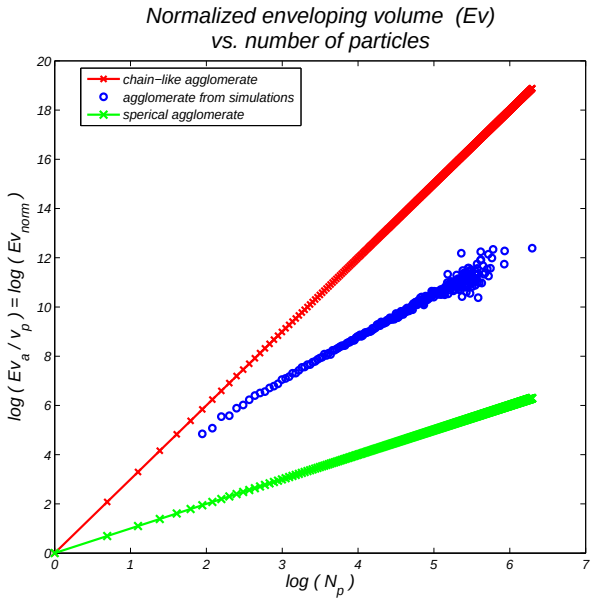

Figure A.1: Comparison of enveloping volume vs. number of particles per agglomerate, for different kinds of agglomerate.

Points in the immediacy of the upper curve (green straight line) suggest a molecular regime approximation for the whole process. We shall assume that thermophoretic forces shall not affect substantially the agglomerates configuration for the molecular regime being still valid. Any case, the results obtained through the simulation have to confirm that assumption. Additionally, we get also information about the agglomerate structure

through the tree-ness index. Our simulations yield a mean tree-ness index that asymptotically tends to $2/12 = 0.167$ (see Figure 4.21 in chapter 4) that is the corresponding to a chain-like agglomerate.

Calculation of the effect that thermophoretic actions (forces and torques) produce on the agglomerates may be undertaken from two different sides:

1. By considering those actions through an external potential and solving with it the Langevin equation for each time step.

2. By directly calculating the displacements and rotations those actions provoke in the agglomerate, assuming that mechanical equilibrium is achieved at each time step.

Of course, second way to proceed is considerably more expeditious than the first one. However, the first method seems to be more appropriate for the initial stages of the agglomeration process when Brownian effect is still important, because calculation of the diffusion tensor is incorporated in the scheme, making unnecessary to resort to any particular approximation [26]. When Brownian effect has considerably diminished, diffusion is less relevant and it is not so important which specific tensor expression will be used (in our first model it was taken from the Riseman-Kirkwood theory [116]). On the other hand, time steps producing displacements in the order of the particle diameter (approximately 2×10^{-7} s) are not so much smaller than the particle relaxation time (approximately 6×10^{-8} s) and the second method with the equilibrium assumption is not realistic, but as the agglomerate grows its diffusivity decreases and consequently its relaxation time does too, hence, second method is adequate for advanced stages of the agglomeration process.

Once we have decided which method to use for calculating how the agglomerates are thermophoretically moved at each time step, we face the next difficulty coming from the fact that thermophoretic actions change as the agglomerates move (mainly the torques). Shall we calculate displacements and rotations as if the actions were mean values for the very small time step? It seems to be a sensible option, specially because we are assuming local mechanical equilibrium. The force is balanced with the translational friction and the torque with the rotational friction, so linear and angular velocities may be obtained and thereby displacements and rotations. Viscous media response to rotation and translation of agglomerates has been studied by different ways, for instance, see references [30, 36, 49, 54, 55, 67]. For translational and rotational frictional coefficients see references [28, 29].

A.1.1 simulation

Soot agglomeration process is simulated by applying a random-diffusive mixed procedure inside a small fraction of the total volume of a combustion chamber. Initial particle

configuration consist on a cubic lattice formed by $(N_p + 1)^3 = 8000$ particles with an interdistance $S_p = 60\, d_p$. The number particle density in the domain according to these parameters is $10^{12}\ cm^{-3}$, which is in the range expected in combustion chambers. Periodic boundary conditions has been fixed in the domain to preserve the particle density during the whole simulation, that is, particles that escape the domain shall be re-injected from the opposite boundary. Hitherto we are keeping the same scenario as in our former model. The only new thing is to take in account the existence of a temperature field $T(z)$ characterized by a temperature gradient along z-axis.

Single particles will move during the simulation describing a Brownian motion in random directions but fixing the step length as $2d_p$ (All the details concerning the Brownian simulation follow the former reduced model described in chapter 4. However, in the present model the total displacement will be obtained by summing up to the Brownian jump the displacement due to thermophoresis. Of course, for the single particles that displacement is negligible but, as agglomerates are created and grow, the Brownian jump is diffusively reduced and an each time larger thermophoretic displacement has to be added. Besides, the agglomerates not only shift but also rotates. It is rotation that makes thermophoresis important in the evolution of the process because rotation alters the position of the agglomerate in the temperature field. Calculation of thermophoretic forces is done considering that the distribution function of the gas molecules is not affected by the presence of the particles (single or in the agglomerates). We will come immediately to this point.

In fact, it is not only an approximation concerning the smallness of the particles compared to the mean free path of gas molecules (MFP), but the relative position of the particles too: the molecules striking rate is calculated assuming an infinite bath surrounding the particles but it is not the case when the agglomeration leads to the appearance of narrow coves whose widths are smaller than the MFP. Hits cannot be considered anymore as "memoryless" because continuous diffuse and specular reflections shall be produced between the faces of very near particles. We expect not to deal with such situations because of the quite open configurations we have obtained before. Anyway, the presence of other particles will certainly affect the total force due to molecular collisions. This is a "screen effect" and it has to be considered, indeed. Particles situated no farther than the MFP respecting to a particular one contribute to reduce the total force on it, and contribute in a way that we quantify by means of the net shadow (deducting overlapping) thrown by the particles. The term shadow is strictly literal assuming that beyond a sphere centered in any particle of an agglomerate with a radius equal to the MFP there is no other obstacles affecting the particle. Since the agglomerate configuration is known at every time step, the shadow over each particle can be calculated and, whence, the net thermophoretic force on it. In the following we shall consider only equal particles in the agglomerates.

A very simple rule for obtaining the net force reduction due to shadows is to calculate

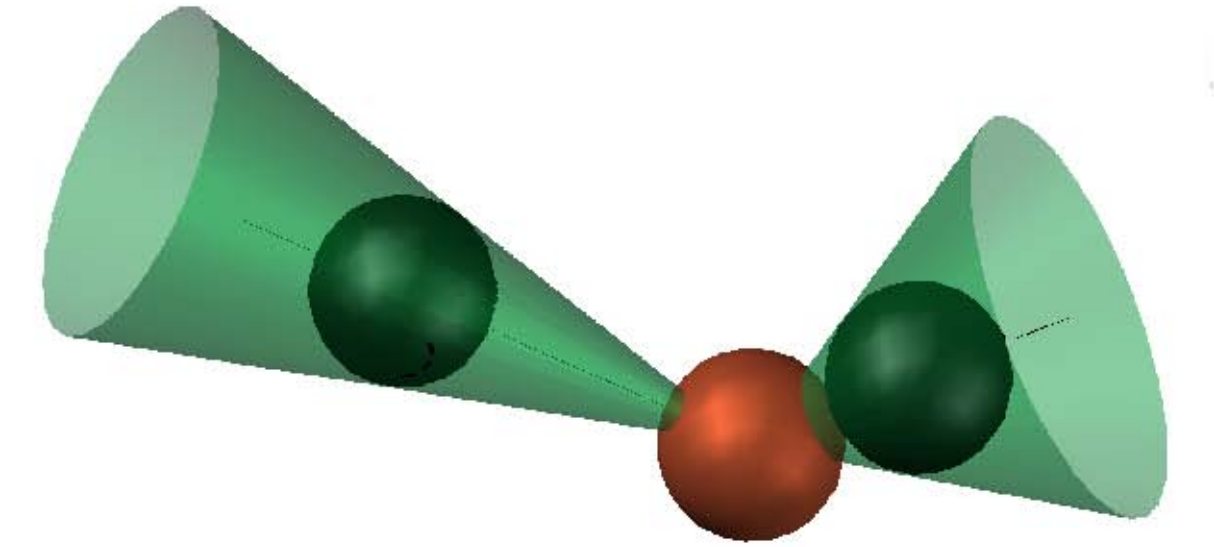

Figure A.2: Shadow effect rule for obtaining the net force on a particle

the net thermophoretic force on a spherical particle in the presence of another particle tangent to the first one and, then, fit the results parabolically between the two limit cases:

1. Reduction equal to zero for a net shadow equal to zero (free particle).

2. Reduction equal to one for a net shadow equal to $4\pi r_p^2$ (particle completely surrounded).

A.1.2 thermophoretic velocity of the agglomerates

Thermophoretic force on the agglomerate is a resultant of the forces acting on different particles but not all the spherical particles composing the agglomerate experience the thermal gradient of the gas because many of them are isolated by the most external particles. Agglomerate has its own thermal gradient. Nevertheless, the forces acting on the particles cannot be either obtained assuming them as single ones. The proper way should be to solve the Navier-Stokes equations for the agglomerate itself but, considering that this calculation has to be done at each time step, the whole model would be computationally unfeasible. We need to make some hypothesis for sake of simplification. As the agglomerates are not dense sets of particles, we shall assume that their thermal gradient is determined by their geometrical configuration, namely, the position of each of their particles respecting to the external temperature field.

Now, we have to obtain all the forces acting on any particle of the agglomerate. These

forces come from three actions (every one with a different range of directions):

1. Direct incidence of the surrounding gas molecules.

2. Specular reflections of gas molecules from the neighbor particles.

3. Diffuse reflections of gas molecules from the neighbor particles.

While the rate of collisions on a particle due to direct incidence or diffuse reflection admits a straightforward calculation, the case of specular reflection demands particular expressions for each reflection making the calculations very troublesome. The main function determining the net collision rate on a particle is the distribution function of the molecules in the surrounding gas. This function is obtained from the Boltzmann equation that, in the case of small Knudsen numbers, can be solved by the Chapman-Enskog approximation leading to the very known expanded expression where the leading term has to do with the equilibrium distribution and the second one with the thermal effect. Next, we will see that in some detail.

A.1.3 distribution function through the Boltzmann equation

The leading term of the distribution function in the Chapman-Enskog expansion coincides with the equilibrium distribution known as the Maxwellian. It is a direct consequence of taking equal to zero the collision term in the Boltzmann equation implying that the logarithm of the distribution function is a collisional invariant which leads to the equilibrium condition. The second term derives from the first order approximation. However, use of Chapman-Enskog expansion is justified provided the Knudsen number is small ($\lesssim 0.01$) and it is not the case when we are dealing with nanometric scales (particle's diameter) with the same order of magnitude as the mean free path of the gas molecules (Mean free path of air at $1000\,K$ is 190 nm approximately,assuming the VHS model, and particle's diameter is 50 nm). Surprisingly, based on the assumption that for large Knudsen numbers the distribution function of the gas molecules is not affected by the presence of the particles, Waldmann [108] obtains the same results for the thermal force than the second term of the CE expansion (the upper limit of an infinite Knudsen number corresponds to a collisionless flow). Nevertheless, doubt still remains respecting to the distribution function. Can it be taken as a Maxwellian or not?

The first thing to comment is that the coincidence of the CE zeroth order term with the Maxwellian f_M is physically consistent but cannot be seen as a result of the method itself. The scale length L is introduced in the dimensionless Boltzmann equation through the variables t and x (scale length of the macroscopic gradients [6]), therefore, a small Knudsen number means, in terms of the CE expansion, that temporal and spatial variations of f are occurring in a scale much larger than the mean free path of gas molecules. Otherwise, equilibrium involves a homogeneous, stationary state where the collision term reduces to zero because f derivatives are zero and there are no external forces; it is an

equivalent matter. But, assuming a Maxwellian distribution function for the gas molecules has nothing to do with the further applicability of the Chapman-Enskog method. Even in rarefied gases, with large Knudsen numbers, a Maxwellian distribution also applies [6] pp. 2, 148, [17] pp. 41, 278. First of equations (9.2) from [17] admits $f_0 = f_M$ assuming T is a smooth function of $\mathbf{x}$. Of course, things will also depend on how the Knudsen number is defined as we will see below. In our case, the thermal force, according to Waldmann's theory, also coincides with CE's. Next approximation will surely disagree but we will stop at this point, that is, at the thermophoretic term.

Second thing to comment is that the distribution function f for the gas molecules is not only influenced by the Knudsen number associated with the particle size but also with the particle inter-distances because that dimension will define how far the molecules can move after hitting once the particle [17] pp. 271. The smaller the distance, the stronger the memory. Respecting to particle size $K_n \simeq 190/50 \simeq= 4$ but if we consider particle inter-distances in the order of $10\,d_p$, the Knudsen number becomes 0.4 and the distribution function of the gas molecules may be affected by the presence of other particles. Would it be valid to keep assuming a Maxwellian distribution function? Probably not. It would be necessary to obtain f through the Boltzmann equation, maybe introducing a simplified collision term, for instance, in terms of the probability of collisions between particle and molecules. Let imagine a volume whose center is occupied by a particle. The surrounding space is filled with a gas. The probability of a gas molecule to hit the particle can be calculated as the sum of the probabilities of the molecule to be at any position around the particle times the quotient between the effective solid angle measured from the molecule and $4\,\pi$. By effective solid angle (Θ) we mean the angle subtended by the particle as seen from the molecule and it will depend, of course, on the position of the molecule. The sum of the probabilities of the molecule to be at any position i is the inverse of the number of all possible positions and that one is approximated by the difference between the volume of reference (V_r) and the volume of the particle (v_p), divided by the volume occupied by the molecule (V_i). Resuming:

$$P_i = \frac{V_i}{4\,\pi(V_r - v_p)} \sum_{i=1}^{I} \Theta(r_i)$$

The probability of $N = \sum_{i=1}^{I} N_i$ molecules inside the volume of reference to hit the particle (neglecting the probability of inter-molecular collisions) is:

$$P_N = 1 - \left(1 - \frac{N_i\,P_i}{N}\right)^N$$

Each sub-volume i inside the reference one will have N_i molecules given by the still unknown distribution function f. Now it corresponds to write the sum in the form of an

integral of the distribution function and introduce the probability P_N as a measure of the collision frequency in the Boltzmann equation. But because, as it has been already pointed out, we are considering rather open fractal-like structures, the Maxwellian distribution function is a consistent option for calculating the rate of collisions and we will disregard in the following the former considerations. Then, to first order we will have the following expression for f^- [37]:

$$f^- = N\left(\frac{m}{2\,k_B\,T}\right)^{3/2}\exp\left(-\frac{m\,\mathbf{C}^2}{2\,k_B\,T}\right)\left[1-\frac{3\,\mu}{2\,N\,k_B\,T}\left(\frac{m\,\mathbf{C}^2}{2\,k_B\,T}-\frac{5}{2}\right)\overrightarrow{\mathbf{C}}\,.\,\overrightarrow{\nabla}T\right],$$

that, expanding the exponentials and neglecting second order terms,

may be transformed into:

$$f^- = N\left(\frac{m}{2\,k_B\,T}\right)^{3/2}\exp\left(-\frac{m\,\mathbf{c}^2}{2\,k_B\,T}\right)\left[1-\frac{m\,\overrightarrow{\mathbf{c}}\cdot\overrightarrow{\mathbf{V}}}{k_B\,T}-\frac{3\,\mu}{2\,k_B\,T}\left(\frac{m\,\mathbf{c}^2}{2\,k_B\,T}-\frac{5}{2}\right)\overrightarrow{\mathbf{c}}\cdot\overrightarrow{\nabla}T\right]$$

where N is the number density of gas molecules, m is the molecular mass, T is temperature, μ is dynamic viscosity, $\overrightarrow{\mathbf{c}} = \overrightarrow{\mathbf{C}} - \overrightarrow{\boldsymbol{V}}$, and $\overrightarrow{\mathbf{c}}$ and $\overrightarrow{\boldsymbol{V}}$ are the molecule and the agglomerate velocities respectively.

A.2 Force calculation

For making things easier we will split the force calculations in two parts: the one due to the leading term of the distribution function, that is not direction-dependent, and the part due to the thermal effect that depends on the vector $\overrightarrow{\nabla}T$. A single particle (because it is spherical) is not affected by those considerations whereas its neighbors (because of the screen effect) produce the resultant force to have any direction.

A.2.1 forces on a particle due to direct incidence in presence of one or more neighbors. Leading term of the distribution function

When a particle has neighbors particles tangent to it, the direct incidence on the first one will be reduced. First we shall calculate the reduction produced on a particle by two neighbors placed forming a right angle (particularization for a single particle is straightforward) and will generalize after for two neighbors placed at an arbitrary angle Ω measured from the particle.

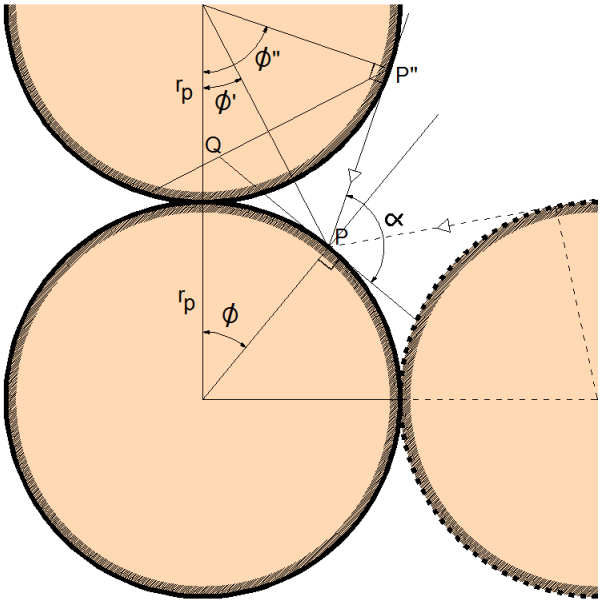

Figure A.3: Obstruction produced by two neighbor particles placed at a right angle.

A.2.1.1 two particles at a right angle

$$\begin{aligned}
\alpha &= \arcsin\left[\frac{2}{5-4\,\cos\phi}\left(\sin\phi \pm \sqrt{1-5\,\cos\phi+8\,\cos^2\phi-4\,\cos^3\phi}\right)\right] \\
\phi' &= \arctan\left(\frac{\sin\phi}{2-\cos\phi}\right) \\
\phi'' &= \alpha-\phi
\end{aligned}$$

Rate of impinging molecules per unit area (n_i) and force exerted per unit area ($\mathbf{f}_i$) on any point P on the surface of the particle are given by the following integrals:

$$\begin{aligned}
n_i &= 2\int_\alpha^\pi \int_0^{\gamma(\delta)} \int_0^\infty N\,m\left(\frac{h}{\pi}\right)^{3/2} (\mathbf{c}\cdot\mathbf{n})\,e^{-h\,\mathbf{c}^2}\mathbf{c}^2\,\cos\delta\,\mathrm{d}\delta\,\mathrm{d}\gamma\,\mathrm{d}\mathbf{c} \\
\gamma(\delta) &= \arccos\left(A\,\csc\delta + B\,\cot\delta\right) \\
A &= \frac{\sin(\phi''-\phi')}{\sin(\alpha-\phi''+\phi')}; \qquad B = \frac{1}{\sin\alpha}\left[\frac{\sin(\phi''-\phi')}{\sin(\alpha-\phi''+\phi')}-\cos(\pi-\alpha)\right]
\end{aligned}$$

where $\mathbf{c}\cdot\mathbf{n} = \mathbf{c}\sin\delta$ and angles δ and γ are showed in Figure A.4. Expression above for γ comes from $\dfrac{PT}{PT''}$ where PT and PT" are written in terms of angles α, δ, ϕ' and ϕ''.

Integral of $\mathbf{c}$ is $\dfrac{N}{2\sqrt{\pi\, h}}$, being $h = \dfrac{m}{2\, k_B\, T}$. Integration in δ is done numerically taking 91 points for the discrete vector $\phi = (0, \pi/2)$. In Figure A.5 the pattern of incidence along a meridian with obstruction produced by one and two particles at right angles, respectively, are shown. Both curves represent only half of the particle because of symmetry.

$$\mathbf{f}_i = n_i \frac{2\sqrt{\pi\, h}}{N} \int_0^{\infty} \overrightarrow{\mathbf{c}}\, (\mathbf{c} \cdot \mathbf{n})\, e^{-h\, \mathbf{c}^2} \mathbf{c}^2\, \mathrm{d}\mathbf{c}$$

$$\mathbf{f}_i = \frac{m\, N^2}{8\, h \sqrt{\pi}}\, n_i$$

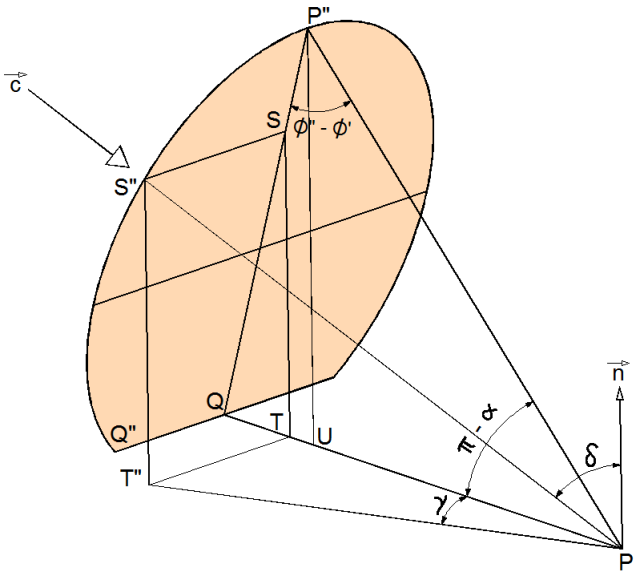

Figure A.4: Axonometric view of the tangent cone from point P to upper particle. Hatched zone is the basis of the cone

A.2.1.2 two particles at any angle

Minimum angle Ω is $\pi/3$ and we shall consider a maximum of $\pi/2$. When the angle between the particles is smaller than $pi/2$ each particle interferes the other being necessary to calculate the angle ϕ_{lim} that allows to carry out the calculation by means of two slight different integrals. That angle ϕ_{lim} is indicated in Figure A.6. For the region between T_1 and P_{lim} the same integral as above is applicable. For the region between P_{lim} and T_2 the expression for γ has to be modified in the corresponding integral. This new expression for γ is written below after the equation for obtaining ϕ_{lim}.

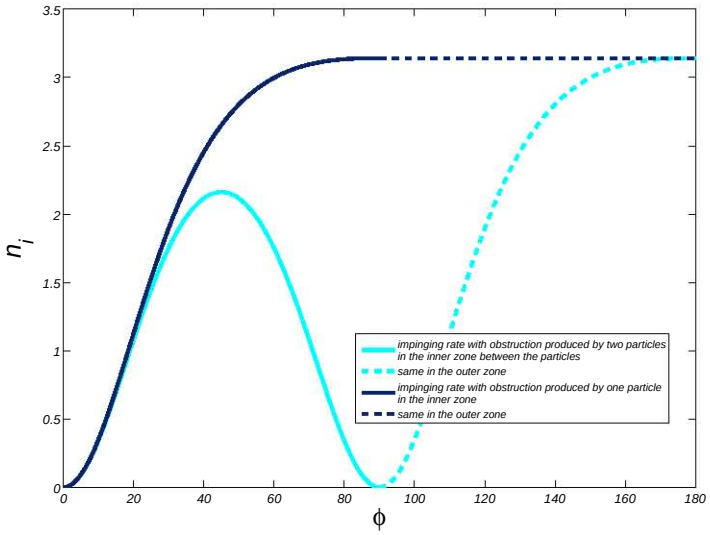

Figure A.5: Curves of the impingement rate for any point P on the surface of a particle (given by its angle ϕ) considering the obstruction produced by one and two particles tangent to the first. The two particles are placed at a right angle.

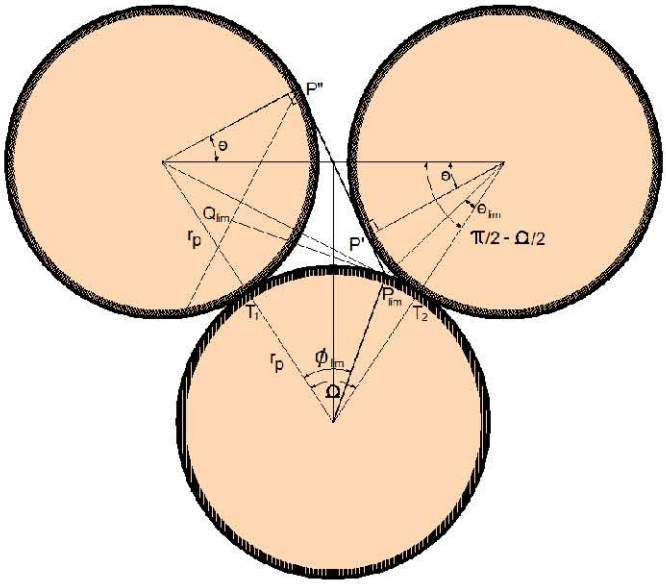

Figure A.6: Obstruction produced by two neighbor particles placed at an angle Ω arbitrary. Angle ϕ_{lim} divide the surface in between the particles in two regions for which different integrals apply.

$$\sin^4 X\,(a^2+b^2)+\sin^3 X\,(c\,a+2\,b\,d)+\sin^2 X\,(c^2-2\,e\,a+d^2-b^2)+\sin X\,(2\,b\,d-2\,e\,c)$$
$$+(e^2-d^2)=0$$

$$X = \Omega - \phi_{\lim} \qquad \theta = \arccos\left[\frac{1}{2\,\sin(\Omega/2)}\right]$$

$$a = \sin\Omega - 2\sin^2(\Omega/2)\cot(\Omega/2+\theta)$$

$$b = \sin\Omega\cot(\Omega/2+\theta) + 2\sin^2(\Omega/2)$$

$$c = 1 - 4\,\sin^2(\Omega/2) - \cot(\Omega/2+\theta)\left[2\,\sin\Omega - \sqrt{4\,\sin^2(\Omega/2)-1}\right]$$

$$d = 2\left[6\,\sin\Omega - \sqrt{4\,\sin^2(\Omega/2)-1} - \cot(\Omega/2+\theta)\right]$$

$$e = 2\left(\cot(\Omega/2+\theta) + \sqrt{4\,\sin^2(\Omega/2)-1} - 5\,\sin\Omega\right.$$

$$\gamma(\delta) = \arccos\left(A'\,\csc\delta + B'\,\cot\delta\right)$$

$$A' = \frac{\cos\left[\arctan\left(1/P_{\lim}\,P''\right)\right]\,\sin\left(2\pi/3-\alpha+\phi-\phi'\right)}{\cos\left(\alpha-\pi/6+\phi'-\phi\right)\,\sin\left(\pi/3-\phi+\phi'\right)} \qquad B' = \frac{1}{\tan\left(\pi/3-\phi-\phi'\right)}$$

$$P_{\lim}\,P'' = \sqrt{\left[\sqrt{3}-\cos(\pi/6-\phi)\right]^2 + \left[1+\sin(\pi/6-\phi)\right]^2 - 1}$$

In Figure A.7 appears the angle $\phi_{\lim}$ as a function of angle Ω and, as an example, in Figure A.8 the impingement rate function for an angle $\Omega = 5\pi/12$, is shown.

$$\begin{aligned}
\mathbf{f}_i &= 2\,m\int_\alpha^\pi\int_0^{\gamma(\delta)}\int_0^\infty N\,m\left(\frac{h}{\pi}\right)^{3/2}\overrightarrow{\mathbf{c}}\,(\mathbf{c}\cdot\mathbf{n})\,e^{-h\,\mathbf{c}^2}\mathbf{c}^2\,\cos\delta\,\mathrm{d}\delta\,\mathrm{d}\gamma\,\mathrm{d}\mathbf{c}\\
\gamma(\delta) &= \arccos\left(A\,\csc\delta + B\,\cot\delta\right)\\
A &= \frac{\sin(\phi''-\phi')}{\sin(\alpha-\phi''+\phi')}; \qquad B = \frac{1}{\sin\alpha}\left[\frac{\sin(\phi''-\phi')}{\sin(\alpha-\phi''+\phi')} - \cos(\pi-\alpha)\right]
\end{aligned}$$

A.2.2 forces on a particle due to reflections. Leading term of the distribution function

The neighbors not only obstruct the direct incidence of the surroundings molecules on a particle, they also produce, by reflections, that molecules with a external trajectory could

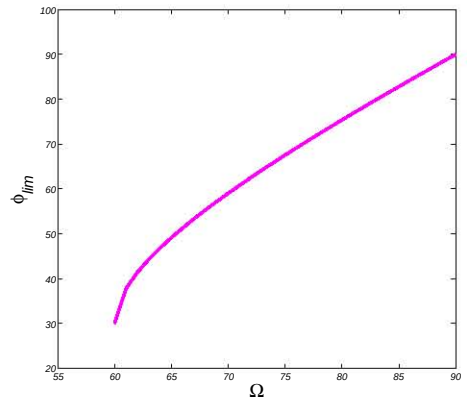

Figure A.7: Angle ϕ_{lim} used in the calculation of the net impingement rate on a particle obstructed by other two tangent to the first one, as a function of the angle Ω.

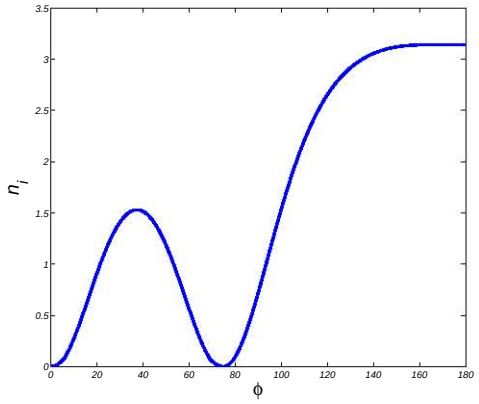

Figure A.8: Impingement rate on a particle by direct incidence taking in account the obstruction produced by other two tangent to the first one and placed at a relative angle of $\Omega = 5\pi/12$

reach, nevertheless, the particle. Particle, at once reflects the molecules that hit its surface. Then, there are molecules coming from the surroundings (that have probably "forgotten" where they come from) and some others rebounding many times between the closest particles. Reflections are of two kinds, specular and diffuse. The so called accommodation factor, ranging from 0 to 1, controls the proportion between molecules specularly reflected and scattered. While successive diffuse reflections can be systematically managed it is not the case for the specular ones that have to be analyzed particularly. Given the geometrical complexity of such analysis we shall limit ourselves to describe the calculation of the first specular reflection and give some details about the second.

A.2.2.1 first specular reflections

Specular reflection between two particles is graphically described in Figure A.9. Tangent plane at P in the upper particle produces a shadowed zone (in gray) in the lower particle. The cone of radiations from the point P (in blue) and the boundary of the shadowed zone define the zone where the reflections are effective. The basic idea for obtaining the impingement rate due to specular reflections from a neighbor particle, is the following:

Let's consider a generic point P in the upper particle, where rays will impact originally, and another generic point P' in the lower particle who will receive specular reflections from P. Position of P will vary in latitude and longitude and at the same time rays will vary their angle of attack δ_P in the plane $n - t_2$ and also around n-axis. Variations in the angle δ_P will produce reflections on points above or below P', so that variations may be ignored. If now, angle δ_P is kept unchanged and we consider variations in the angle around n-axis locus of reflections is represented by the black dotted line in Figure A.9, so, they are all below P' and can be ignored too. Same occurs if angle δ_P increases. But situation is different if angle δ_P decreases and at the same time angle around n-axis varies. Situation is represented by the red dotted line. We will have a pair of points P_i and P_d on the same latitude of P. We can argue that points P_i and P_d have no particular effect on P. But the problem is that these points will coincide with P' when the incidence point P moves along its latitude. Hence, the effect of a change in latitude of point P is equivalent to a change in the angle of attack of rays at that point. Therefore, we can calculate this effect by summing up the reflections on every pair of points P_i and P_d along the latitude of point P'. Of course, not along the whole latitude circle but in an arc less than $2\,\pi$ that we shall call influence arc of generic point P on generic point P'. Integration of all effective points P on the upper sphere will give the impingement rate on a point P' as a function of its latitude ϕ'. Effective points P means logically that there are some limits beyond which incident rays on P don't produce reflections on P'. Figures A.10 and A.11 clarifies the procedure.

The limit angle ϕ_T is easy to see and its expression rather simple. However, limit angle ϕ_K depends on the way the incidence on the upper particle is produced and that will curiously depend on the lower particle because, on the other hand, it is obstructing the upper one. In case $\phi' = \pi/3$, $\phi_K = \pi/6$. Equations for calculating the angles ϕ_T, ϕ_K for $\phi' > \pi/3$ and ϕ_K for $\phi' < \pi/3$ are written below. Notice that they consists in nonlinear algebraic systems that have to be solved numerically:

$$\phi_T = \arcsin\left(\frac{\sin\,\phi' + 2\,\sqrt{4 - 8\,\cos\,\phi' + 5\,\cos^2\phi' - \cos^3\phi'}}{5 - 4\,\cos\,\phi'}\right)$$

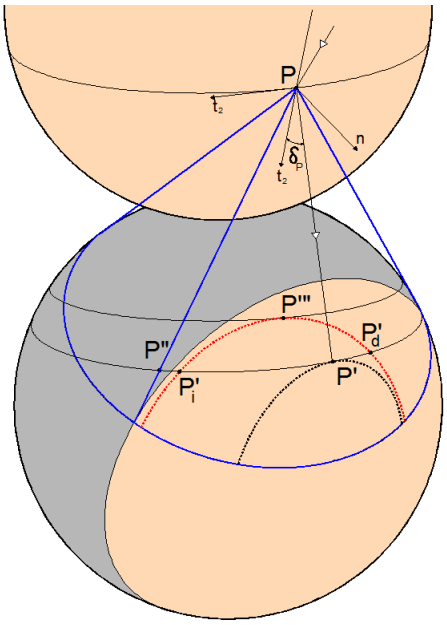

Figure A.9: Impacts on a particle by specular reflection from an upper one.

System of equations for obtaining ϕ_K if $\phi' < \pi/3$

$$r_p \cos\phi_K + KP' \sin(\phi_K + \delta_K) + r_p \cos\phi' = 2\, r_p$$

$$r_p \sin\phi_K - KP' \cos(\phi_K + \delta_K) = r_p \sin\phi'$$

$$(r_p \sin\phi_K)^2 + r_p^2 (2 - \cos\phi_K)^2 = KP'^2 + r_p^2$$

System of equations for obtaining ϕ_K if $\phi' < \pi/3$

$$r_p \cos\phi_K + KP' \sin(\phi_K + \delta_K) + r_p \cos\phi' = 2r_p$$

$$r_p \sin\phi_K - KP' \cos(\phi_K + \delta_K) = r_p \sin\phi'$$

$$(r_p \sin\phi_K)^2 + r_p^2 (2 - \cos\phi_K)^2 = KT'^2 + r_p^2$$

$$r_p \cos\phi_K - KT' \sin(\phi_K - \delta_K) + r_p \cos\phi_{T'} = 2r_p$$

$$r_p \sin\phi_K + KT' \cos(\phi_K - \delta_K) = r_p \sin\phi_{T'}$$

For solving the 3×3 system we rewrite the equations in the following form and proceed iteratively:

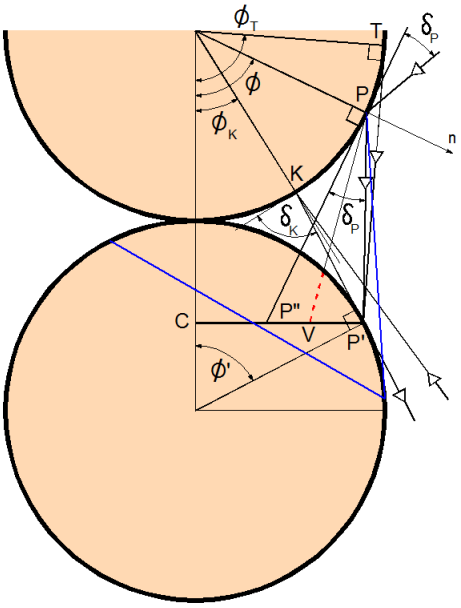

Figure A.10: Limit angle ϕ_T, and limit angle ϕ_K for $\phi' > \pi/3$

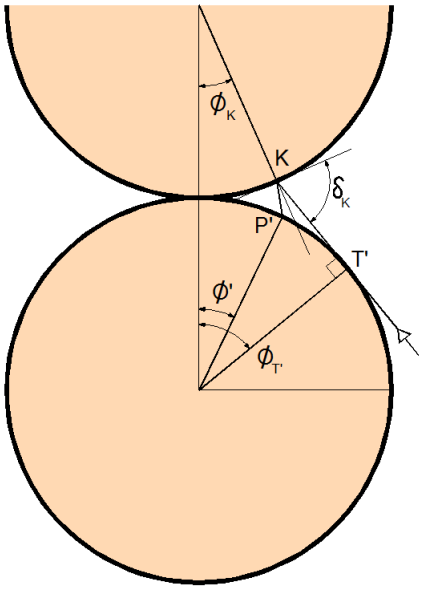

Figure A.11: Limit angle ϕ_K for $\phi' < \pi/3$

$$\phi_K^{(i+1)} = \arccos\left[1 - \left(\frac{KP'^{(i)}}{2\,r_p}\right)\right]$$

$$\delta_K^{(i+1)} = \arctan\left[\frac{1 + \cos\left(\phi' - \phi_K^{(i)}\right) - 2\,\cos\,\phi_K^{(i)}}{\sin\,\phi_K^{(i)} - \sin\left(\phi' - \phi_K^{(i)}\right)}\right]$$

$$KP'^{(i+1)} = \frac{r_P\left(\sin\,\phi_K^{(i)} - \sin\,\phi'\right)}{\cos\left(\phi_K^{(i)} + \delta_K^{(i)}\right)}$$

with a starting point $KP'^{(0)} = .75\,r_p$ and a lower limit $KP'_{min} = .5\,r_p$. That minimum value is used for substituting $KP'^{(0)} = KP'^{(1)}$ by $KP'^{(0)} = .5\,(KP'^{(0)} + KP'_{min})$ in order to be used in a next iteration just in case some of the two exceptions $\delta_K^{(1)} < 0$ or $(KP'^{(1)}/r_p)^2 > 4$ (which would imply $\cos\phi_K > 1$) happen. If not, we keep $KP'^{(0)} = KP'^{(1)}$ and put $KP'_{min} = KP'^{(0)}$. This way, process is convergent.

For the 5×5 system process is a little more sophisticated but a solution is also found. Next and final step is graphically exposed in Figure A.12. We have to calculate the impingement rate per unit area (of the lower particle) $\mathrm{d}n_r$ on P' from some position P, integrating the projections on $n_{P'}$ of the rates per unit area on every generic points P'_i and P'_d along the arc of influence $P''_i - P' - P''_d$. After that, we have to integrate the impingement rate per unit area $\mathrm{d}n_r$ for all the points P between P_T and P_K.

$$\mathrm{d}n_r = \frac{\partial F(\delta_P, \phi')}{\partial \phi'}\,\mathrm{d}\delta_P$$

$$\frac{\partial F(\delta_P, \phi')}{\partial \phi'} = 4\,\pi\,\sin\phi' \int_0^{\theta_{P''_d}} \int_0^{\infty} N\,m \left(\frac{h}{\pi}\right)^{3/2} (\mathbf{c}' \cdot n_{P'})\, e^{-h\,\mathbf{c}'^2}\,\mathbf{c}'^2\,\mathrm{d}\theta\,\mathrm{d}\mathbf{c}'$$

$$n_r(\phi') = \int_{\delta_T}^{\delta_K} \frac{\partial F(\delta_P, \phi')}{\partial \phi'}\,\mathrm{d}\delta_P,$$

$n_r^{(1)} = n_r$, impingement rate per unit area of the lower particle due to first specular reflection from the upper particle.

where:

1. $\mathbf{c}'$ is the generic denomination of the velocity vector along the lines $P\,P'_d$, from $P\,P'$ to $P\,P''_d$.
2. $(\mathbf{c}' \cdot n_{P'})$ is $\left(0, -\cos\delta_{P'}, \sin\delta_{P'}\right) \cdot \left(\dfrac{V\,P'_d}{P\,P'_d}, \dfrac{P\,P''}{P\,P'_d}, \dfrac{V\,P''}{P\,P'_d\,\sin\phi}\right)$.
3. $\delta_{P'} = \delta_P + \phi + \phi' - \pi/2$
4. $(V\,P'')^2 + (V\,P'_d)^2 = (P\,P''\tan\gamma_P)^2$.
5. $\theta_{P''_d} = \arcsin\left(\dfrac{P\,P''\,\tan\gamma_P}{r_p\,\sin\phi'}\right)$.
6. $\gamma_P = \gamma_P(\delta_P)$.
7. $P\,P'' = \dfrac{r_p(2 - \cos\phi - \cos\phi')}{\cos\phi}$.

8. $\delta_K = \frac{\pi}{2} - \phi_K - \arctan\left(\frac{\sin\phi_K - \sin\phi}{2 - (\cos\phi_K + \cos\phi)}\right)$ and $\delta_T = 0$.

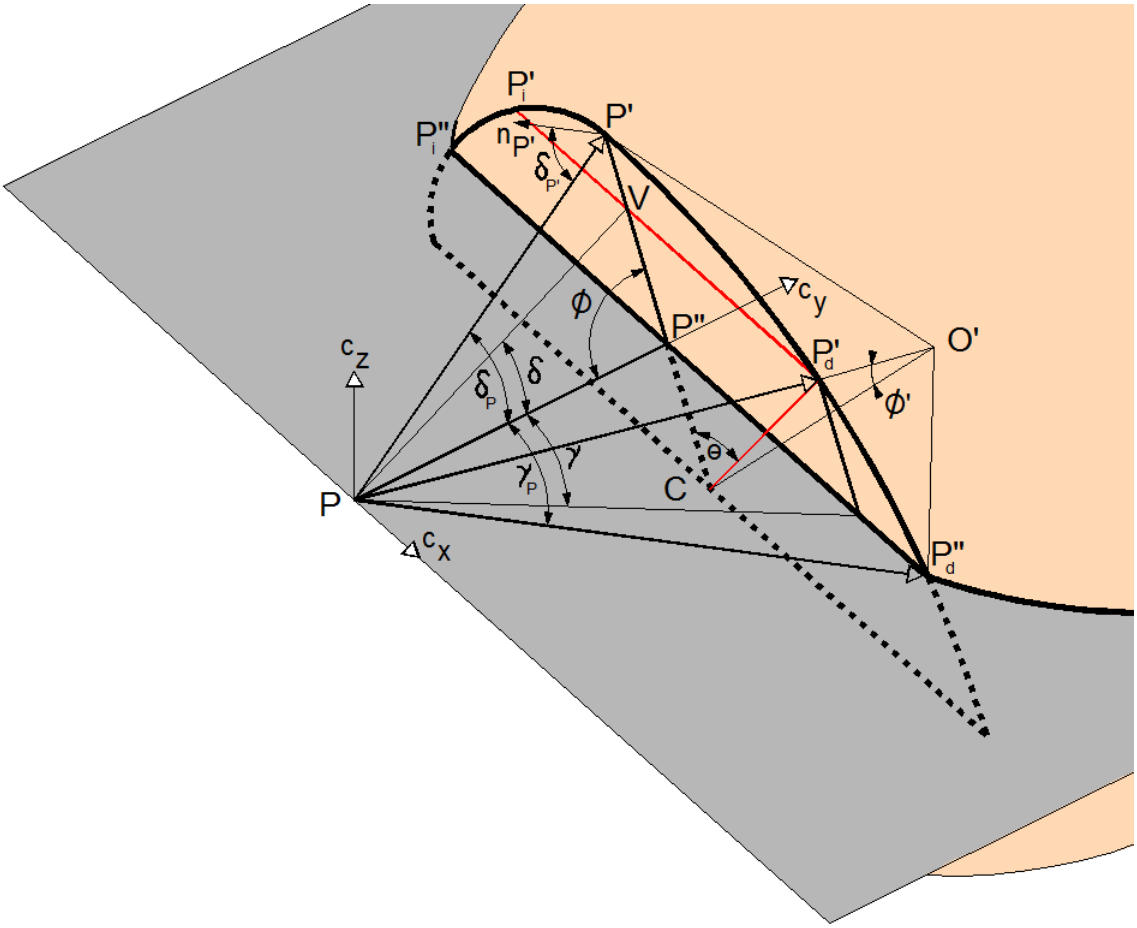

Figure A.12: The plane in gray is the tangent plane on point P that intersects the lower particle, in light yellow

A.2.2.2 forces on a particle due to second specular reflections

A.2.2.3 forces on a particle due to diffuse reflections

Diffuse reflection (controlled by the accommodation coefficient a) has a distribution function f^+ that coincides with the Maxwellian denoted by f^- (times the factor a) only to zeroth-order approximation (leading term). To first order (with the thermal contribution) f^+ is obtained by:

$$a\, n_i = n_D$$

$$a \int_{\mathbf{c}\cdot\mathbf{n}<0} f^-(\mathbf{c}\cdot\mathbf{n})\, \mathrm{d}^3\mathbf{c} = \int_{\mathbf{c}\cdot\mathbf{n}<0} f^+(\mathbf{c}\cdot\mathbf{n})\, \mathrm{d}^3\mathbf{c}$$

where f^+ can be written as $N_D \left(\frac{h}{\pi}\right)^{3/2} \exp\left(-h\,\mathbf{c}^2\right)$,

and, because the two parts of term $\left(\frac{m\,\mathbf{c}^2}{2\,k_B\,T} - \frac{5}{2}\right)$ cancel out by the integration,

we obtain finally:

$$f^+ = a\, N \left(\frac{h}{\pi}\right)^{3/2} \left(1 + \sqrt{\pi\, h}\, \boldsymbol{V}\cdot\mathbf{n}\right) \exp\left(-h\,\mathbf{c}^2\right)$$

Let's start ignoring the thermal contribution and making $f^+ = a\, f^-$. Now, to obtain the impinging rate on P' by diffuse reflection from P (see Figure A.13) the total incidence angle $\pi - \alpha_P$ on P, has to be considered. But P is a generic point on the upper particle, ranging from T to K, T and K being shown in Figure A.14.

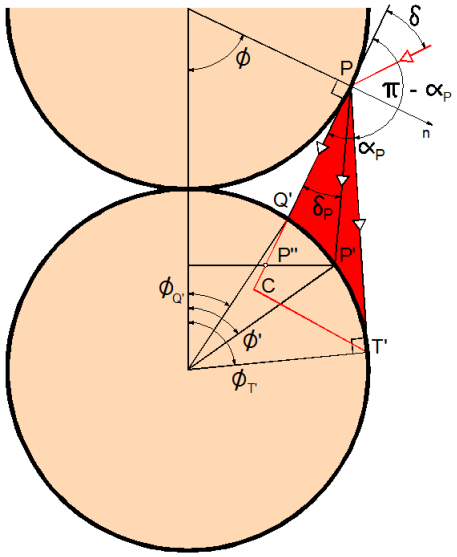

Figure A.13: Scattered rays from point P on the upper particle extend over a sector on the lower particle bounded by the tangent semi-cone in $C\,T'$ and the plane defined by $P\,Q'$.

The impinging rate per unit area (n_d) on the lower particle due to the first diffuse reflection from the upper particle consists in a summation at each point P from 0 to

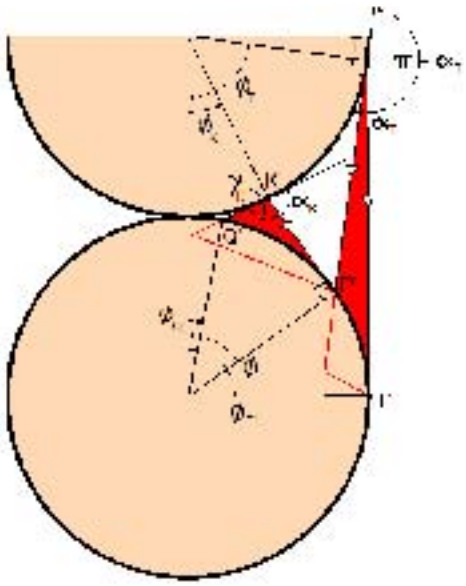

Figure A.14: Boundary points T and K on the upper particle that produce diffuse reflection on the point P'.

$\pi - \alpha_P$ of the corresponding region (defined by the tangent cone) in the lower particle, followed by a summation on P from T to K. That double summation can be particularized for any generic point P'. Later, change in latitude of point P is taken in account as in the specular reflection, through the arc of influence $P'\,P''$. Angles ϕ_T and ϕ_K are easily obtained:

$$\phi_T = \arcsin\left(\frac{\sin\,\phi' + 2\,\sqrt{4 - 8\,\cos\,\phi' + 5\,\cos^2\phi' - \cos^3\phi'}}{5 - 4\,\cos\,\phi'}\right)$$

$$\phi_K = \arccos\left(2\,\cos\phi' - 1\right) - \phi', \quad \text{for } \phi' > \pi/3$$

$$\phi_K = \arccos\left(2\,\cos\phi' - \cos 2\,\phi'\right) - \phi', \quad \text{for } \phi' < \pi/3$$

Next, the diffuse reflection rate per unit area (of each particle, the upper and the lower) is found as:

$$
\begin{aligned}
\alpha_P &= \pi - \phi - \phi_{T'} \\
\phi_{T'} &= \arcsin\left(\frac{\sin\,\phi + 2\,\sqrt{4 - 8\,\cos\,\phi + 5\,\cos^2\phi - \cos^3\phi}}{5 - 4\,\cos\,\phi}\right) \\
\gamma_P &= \gamma_P(\delta_P) \\
n_{d_P} &= 2\int_0^{\pi-\alpha_P}\int_{\gamma_P}^{\pi}\int_0^{\infty} a\,N\,m\left(\frac{h}{\pi}\right)^{3/2}(\mathbf{c}\cdot\mathbf{n})\,e^{-h\,\mathbf{c}^2}\mathbf{c}^2\,\cos\alpha\,\mathrm{d}\alpha\,\mathrm{d}\gamma\,\mathrm{d}\mathbf{c}
\end{aligned}
$$

where γ_P is the angle subtended by the tangent cone in the plane containing the line $P\,C$.

This rate per double unit area (n_{d_P}) diffusively reflected from P spreads in a solid angle $2\pi(1-\cos\alpha_P)$. Thus, the impingement rate on P' due to diffuse reflection on P is $\dfrac{n_{d_P}}{2\pi(1-\cos\alpha_P)}$.

Now, we have to integrate the former rate for the area of the upper particle that produces diffuse reflections on the lower, namely, from angles ϕ_T to ϕ_K and along the arc of influence $P\,P''$ (that is equivalent again to a change in latitude of generic point P) in the same way that has been done for the specular reflection (see Figure A.12):

$$
n_d = 2\,r_p^2\int_{\phi_K}^{\phi_T}\int_0^{\theta_{P''_d}} n_{d_P}\,\sin\phi\,\mathrm{d}\phi\,\mathrm{d}\theta
$$

Once the impingement rate per unit area on a point of a particle due to the first diffuse reflection from a neighbor tangent one, $n_d^{(1)} = n_d$, is known, the rates for the subsequent reflections can be obtained through a recursive procedure (taken from an unpublished work by P. L. García-Ybarra and J. L. Castillo). That procedure is based in the flux balance of molecules at any point of a particle, that is, flux of diffusively reflected molecules from that point must equal 'a' times the flux of impinging molecules (by direct incidence and diffuse reflection from another particle respectively).

$$
\begin{aligned}
n_d^{(2)} &= a\left(n_d^{(1)} + n_i\right) \\
n_d^{(i)} &= a\left(n_d^{(i-1)} + n_i\right)
\end{aligned}
$$

A.3 Model

A.3.1 total force and torque on the agglomerate

The forces per unit area, $\mathbf{f}_i$, $\mathbf{f}_r$ and $\mathbf{f}_d$, on any point of a particle of the agglomerate may be obtained by integration same as the impingement rates n_i, n_r and n_d. After that, the resultant force per unit area on a generic point is integrated on the whole surface for finding the net force, $\mathbf{F}_p$, on a particle. Because of the presence of its neighbors, the surface of integration is reduced by means of the rule mentioned in §A.1.1.

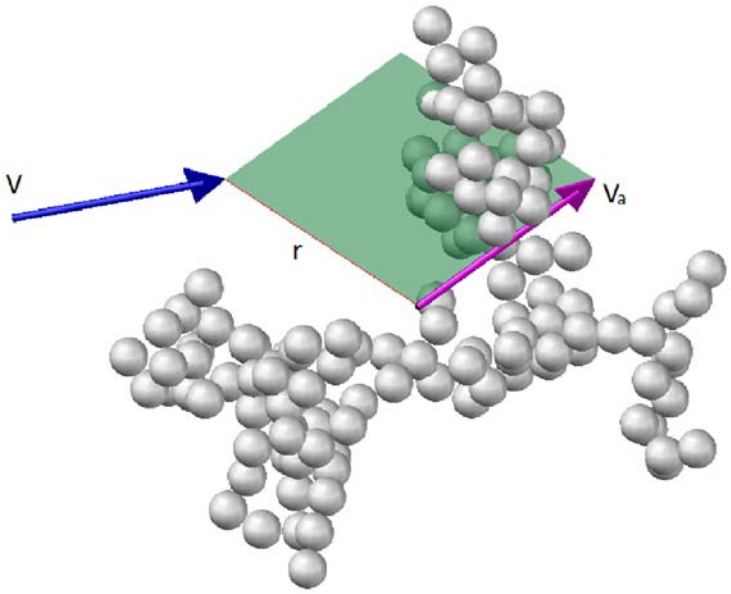

Figure A.15

Summing up the forces $\mathbf{F}_p$ from all the particles, the net force on the agglomerate is found. This net force can be transformed into momentum by multiplying by the time step Δt, and into velocity by dividing by $m_p\, N_p$. Let $\mathbf{V}_a$ be the preceding velocity of the center of mass of the agglomerate.

$$\mathbf{V} = \frac{\sum^{N_p} \mathbf{F}_p\, \Delta t}{m\, N_p}$$

$\mathbf{V}$ is neither contained in the plane defined by its position vector ($\mathbf{r}$) respecting to the center of mass of the agglomerate and the preceding velocity $\mathbf{V}_a$ nor pass through the agglomerate's center of mass. Because of this eccentricity the agglomerate will rotate and because of the resultant velocity the agglomerate will undergo a linear displacement (see Figure A.15). Both movements are assumed to be uniform, that is, torque and force shall

be balanced by the rotational and translational frictional resistance respectively, during the time step.

Bibliography

[1] G. K. Batchelor. *Introduction to fluid dynamics.* Cambridge Univ. Press., 1967.

[2] G. K. Batchelor. Brownian diffusion of particles with hydrodynamic interaction. *J. Fluid Mech.*, 74, 1975.

[3] R. E. Bellman and R. E. Kalaba. *Quasilinearization and nonlinear boundary-value problems.* American Elsevier Publishing Co., Inc., 1965.

[4] S. A. Benson, L. J. Michael, and J. N. Harb. *Fundamentals of coal combustion.* Elsevier (Edited by Smoot L. D.), 1993.

[5] D. Bichsel and P. Wittwer. Stationary flow past a semi-infinite flat plate. *Journal of Statistical Phys.*, 127, 2007.

[6] G. A. Bird. *Molecular gas dynamics and the direct simulation of gas flows.* Oxford Science Publications, 1994.

[7] J. M. Birkhoff and E. H. Zarantonello. *Jets, wakes and cavities.* Academic Press, Inc., 1957.

[8] G. F. Bolling and W. A. Tiller. Growth from the melt. III. Dendritic growth. *J. Applied Phys.*, 32, 1961.

[9] L. L. Bonilla, A. Carpio, Y. Farjoun, and J. C. Neu. Asymptotics and numerical studies of the Becker-Döring model for transient homogeneous nucleation. *Markov Process and Related Fields*, 12, 2006.

[10] J. W. Cahn. Theory of crystal growth and interface motion in crystalline materials. *Acta Matallurgica*, 8, 1960.

[11] J. W. Cahn, W. B. Hillig, and G. W. Sears. The molecular mechanism of solidification. *Acta Matallurgica*, 12, 1964.

[12] M. D. Camejo and L. L. Bonilla. Theory of homogeneous vapour condensation and surface deposition from boundary layers. *J. Fluid Mech.*, 706, 2012.

[13] F. Carbone, F. Beretta, and A. D'Anna. Nanoparticles formation during high temperature pulverized coal combustion. *Proceedings of the European Combustion Meeting*, 2009.

[14] G. F. Carrier and C. C. Lin. On the nature of the boundary layer near the leading edge of a flat plate. *Quart. Appl. Math.*, 6, 1947.

[15] J. L. Castillo and D. E. Rosner. A nonequilibrium theory of surface deposition from particle-laden, dilute condensible vapour-containing laminar boundary layers. *Int. J. Multiphase Flow*, 14, 1988.

[16] J. L. Castillo and D. E. Rosner. Theory of surface deposition from a unary dilute, vapour-containing steam, allowing for condensation within the laminar boundary layer. *Chem. Eng. Sci.*, 44, 1989.

[17] C. Cercignani. *The Boltzmann equation and its applications.* Springer-Verlag, 1988.

[18] S. Chandrasekhar. *Noise and stochastic processes.* Dover (Edited by Wax N.), 1954.

[19] M. C. O. Chang, J. C. Chow, J. G. Watson, P. K. Hopke, S. M. Yi, and G. C. England. Measurements of ultrafine particle size distributions from coal-, oil-, and gas-fired stationary combustion sources. *J. Air and Waste Managem. Assoc.*, 54, 2004.

[20] W. T. Coffey, Y. P. Kalmykov, and J. T. Waldron. *The Langevin equation.* World Scientific, 1996.

[21] E. J. Davis. Transport phenomena with single aerosol particles. *Aerosol Sci. Technol.*, 2, 1983.

[22] C. F. Delale and D. G. Crighton. Prandtl-Meyer flows with homogeneous condensation. Part 1. Subcritical flows. *J. Fluid Mech.*, 359, 1998.

[23] J. L. Doob. *Noise and stochastic processes.* Dover (Edited by Wax N.), 1954.

[24] L. Dufour and R. Defay. *Thermodynamics of clouds.* Academic Press, 1963.

[25] D. L. Ermak and H. Buckholz. Numerical integration of the Langevin equation: Monte Carlo simulations. *J. Comp. Phys.*, 35, 1980.

[26] D. L. Ermak and J. A. McCammon. Brownian dynamics with hydrodynamic interactions. *J. Chem. Phys.*, 72, 1978.

[27] T. Fan and O. B. Toon. Modeling sea-salt aerosols in a coupled climate and sectional microphysical model. *Atmos. Chem. Phys.*, 11, 2011.

[28] B. U. Felderhof. Frictional properties of dilute polymer solutions. III. Translational friction coefficient. *Physica*, 80A, 1975.

[29] B. U. Felderhof and J. M. Deutch. Frictional properties of dilute polymer solutions. I. Rotational friction coefficient. *J. Chem. Phys.*, 62, 1975.

[30] A. V. Filippov. Drag and torque on clusters of N arbitrary spheres at low Reynolds number. *J. Colloid Interface Sci.*, 229, 2000.

[31] A. V. Filippov. Simultaneous particle and vapour deposition in a laminar boundary layer. *J. Colloid Interface Sci.*, 257, 2003.

[32] A. V. Filippov, M. Zurita, and D. E. Rosner. Fractal-like aggregates: Relation between morphology and physical properties. *J. Colloid Interface Sci.*, 229, 2000.

[33] S. K. Friedlander. *Smoke, dust and haze. Fundamentals of aerosol dynamics, 2nd edition.* Oxford, 2000.

[34] S. K. Friedlander, W. Koch, and H. H. Main. The fate of sodium during pulverized coal combustion. *J. Aerosol Sci.*, 22, 1991.

[35] P. L. García Ybarra and J. L. Castillo. Mass transfer dominated by thermal diffusion in laminar boundary layers. *J. Fluid Mech.*, 336, 1997.

[36] P. L. García Ybarra, J. L. Castillo, and D. E. Rosner. Drag on a large spherical aggregate with self-similar structure: An asymptotic analysis. *J. Aerosol Sci.*, 37, 2006.

[37] P. L. García Ybarra and D. E. Rosner. Thermophoretic properties os nonspherical particles and large molecules. *AIChE Journal*, 35, 1989.

[38] S. A. Gökoglu and D. E. Rosner. Thermophoretically augmented mass transfer rates to solid walls across, laminar boundary layers. *AIAA J.*, 24, 1986.

[39] S. Goldstein. *Lectures on fluid mechanics.* Interscience Publishers, 1957.

[40] J. Hallet. Experimental studies of the crystallization of supercooled water. *J. Atmos. Sci.*, 21, 1964.

[41] G. M. Hidy. *Aerosols: an industrial and environmental science.* Academic Press, 1984.

[42] H. B. Hillig and D. Turnbull. Theory of crystal growth in undercooled pure liquids. *J. Chem. Phys.*, 24, 1956.

[43] E. J. Hinch. Application of the Langevin equation to fluid suspensions. *J. Fluid Mech.*, 72, 1975.

[44] J. D. Hoffman. Thermodynamic driving force in nucleation and growth processes. *J. Chem. Phys.*, 29, 1958.

[45] D. F. Hopkins and J. M. Robertson. Two-dimensional incompressible fluid jet penetration. *J. Fluid Mech.*, 29, 1967.

[46] M. Horsch, J. Vrabec, and H. Hasse. Modification of the classical nucleation theory based on molecular simulation data for surface tension, critical nucleus size and nucleation rate. *Phys. Rev. E*, 78, 2008.

[47] J. Huang and L. S. Bartell. Kinetics of homogenous nucleation in the freezing of large water clusters. *J. Phys. Chem.*, 99, 1995.

[48] R. H. Hurt, G. P. Crawford, and H. S. Shim. Equilibrium nanostructure of primary soot particles. *Proc. Comb. Inst.*, 28, 2000.

[49] M. Hütter and M. Kröger. Phoretic forces on convex particles from kinetic theory and nonequilibrium thermodynamics. *J. Chem. Phys.*, 125, 2006.

[50] M. Z. Jacobson. Develpment and application of a new air pollution modeling system-Part i. *Atmospheric Environment*, 30, 1996.

[51] R. Jansen, N. Gimelshein, S. Gimelshein, and I. Wysong. A Lagrangian-Eulerian approach to modeling homogeneous condensation in high density gas expansions. *J. Chem. Phys.*, 134, 2011.

[52] S. Kaplun. The role of coordinate systems in Boundary-Layer Theory. *Journal Appl. Math. and Phys.*, 5, 1954.

[53] H. B. Keller. Numerical methods in boundary-layer theory. *Ann. Rev. Fluid Mech.*, 10, 1978.

[54] M. Kröger and M. Hutter. Symbolic computation of the phoretic acceleration of convex particles suspended in a non-uniform gas. *Comp. Phys. Comm.*, 175, 2006.

[55] M. Kröger and M. Hütter. Unifying kinetic approach to phoretic forces and torques onto moving and rotating convex particles. *J. Chem. Phys.*, 124, 2006.

[56] P. A. Lagerstrom. *Laminar Flow Theory, from theory of laminar flows.* University Press, Princeton, 1964.

[57] H. Lamb. *Hydrodynamics.* Cambridge Univ. Press (6th Edition), 1932.

[58] K. H. Lau, R. H. Lamoreaux, and D. L. Hildenbrand. Decomposition of alkali sulfates. *J. Electrochem. Soc.*, 132, 1985.

[59] W. P. Linak, C. A. Miller, and J. O. L. Wendt. Fine particle emissions from residual fuel oil combustion: characterization and mechanism of formation. *Pro. Comb. Inst.*, 28, 2000.

[60] E. Lipsky, C. O. Stanier, S. N. Pandis, and A. L. Robinson. Effects of sampling conditions on the size distribution of fine particulate matter emitted from a pilot-scale pulverized-coal combustor. *Energy and Fuels*, 16, 2002.

[61] S. I. Lopatin and S. M. Shugurov. The thermodynamic properties of gaseous salts formed by some 3d metal oxides. *Russian J. Gen. Chem.*, 80, 2006.

[62] S. I. Lopatin and S. M. Shugurov. Thermochemical study of gaseous salts of oxygen-containing acids: XXII. Tin molybdates. *Russian J. Gen. Chem.*, 78, 2008.

[63] X. S. Luo, G. Lamanna, Holten, A. P. C., and M. E. H. van Dongen. Effects of homogeneous condensation in compressible flows: Ludwieg-tube experiments and simulations. *J. Fluid Mech.*, 572, 2007.

[64] W. C. Macklin and G. S. Payne. A theoretical study of the ice accretion process. *Quart. J. Roy. Meteor.*, 93, 1967.

[65] W. C. Macklin and G. S. Payne. Some aspects of the accretion process. *Quart. J. Roy. Meteor.*, 94, 1968.

[66] W. C. Macklin and B. F. Ryan. Growth velocities of ice in supercooled water and aqueous sucrose solutions. *Philos. Mag.*, 17, 1968.

[67] D. W. Mackowski. Monte Carlo simulation of hydrodynamic drag and thermophoresis of fractal aggregates of spheres in the free-molecule flow regime. *J. Aerosol. Sci.*, 37, 2006.

[68] P. C. Malte. *Pulverized-coal combustion and gasification.* Plenum Press (Edited by Smoot L. D. and Pratt D. T.), 1979.

[69] M. M. Maricq. Coagulation dynamics of fractal-like soot aggregates. *J. Aerosol Sci.*, 38, 2007.

[70] T. Matsoukas and S. K. Friedlander. Dynamics of aerosol agglomerate formation. *J. Colloid and Interface Sci.*, 146, 1991.

[71] P. H. McMurry and S. K. Friedlander. New particle formation in the presence of an aerosol. *Atmos. Environ.*, 13, 1979.

[72] P. Meakin. Effects of cluster trajectories on cluster-cluster aggregation. *Phys. Rev. A*, 29, 1984.

[73] L. M. Milne-Thomson. *Theoretical hydrodynamics.* Dover Publications, Inc., 5th Edn., 1968.

[74] G. W. Morgan, L. Zhou, M. R. Zachariah, W. R. Heinson, A. Chakrabarti, and C. Sorensen. Numerical simulations of soot aggregation in premixed laminar flames. *Proc. Comb. Inst.*, 31, 2007.

[75] R. D. Mountain, G. W. Mulholland, and H. Baum. Simulation of aerosol agglomeration in the free molecular and continuum flow regimes. *J. Colloid and Interface Sci.*, 114, 1986.

[76] N. Mulholland, M. Kraft, M. Balthasar, D. Wong, M. Frenklach, and P. Mitchell. Light scattering shape diagnostics for nano-agglomerates. *Aerosol Sci. and Technol.*, 47, 2013.

[77] K. H. Naumann. COSIMA-a computer program simulating the dynamics of fractal aerosols. *J. Aerosol Sci.*, 34, 2003.

[78] J. C. Neu, L. L. Bonilla, and A. Carpio. Igniting homogeneous nucleation. *Physical Rev. E*, 71, 2005.

[79] J. C. Neu, L. L. Bonilla, and A. Carpio. Theory of surface deposition from boundary layers containing condensable vapour and particles. *J. Fluid Mech.*, 626, 2009.

[80] M. Neville and A. F. Sarofim. The fate of sodium pulverized coal combustion. *Fuel*, 64, 1985.

[81] B. Nowakowski and E. Ruckenstein. A kinetic approach to the theory of nucleation in gases. *J. Chem. Phys.*, 94, 1991.

[82] C. Oh and C. M. Sorensen. Light scattering study of fractal aggregation near the free molecular regime. *J. Aerosol Sci.*, 28, 1997.

[83] R. Paoli, J. Helie, and T. Poinsot. Contrail formation in aircraft wakes. *J. Fluid Mech.*, 502, 2004.

[84] R. I. A. Patterson and M. Kraft. Model for the aggregate structure of soot particles. *Combustion and Flame*, 151, 2007.

[85] P. Peeters, C.C.M. Luijten, and M.E.H. van Dongen. Transport phenomena with single aerosol particles. *Int. J. Heat Mass Transfer*, 44, 2001.

[86] H. R. Pruppacher. Some relations between the structure of the ice-solution interface and the free growth rate of ice crystals in supercooled aqueous solutions. *J. Colloid Interface Sci.*, 25, 1967.

[87] H. R. Pruppacher and J. D. Klett. *Microphysics of clouds and precipitation.* Kluwer Academic, 1997.

[88] J. Pyykönen and J. Jokiniemi. Modelling alkali chloride superheater deposition and its implications. *Fuel Processing Technol.*, 80, 2003.

[89] Wood G. R. and Walton A. G. Homogeneous nucleation kinetics of ice from water. *J. Appl. Phys.*, 41, 1969.

[90] J. Riseman and J. G. Kirkwood. *Rheology.* Academic Press (Edited by Eirich F. R.), 1956.

[91] J. M. Robertson. *Hydrodynamics in theory and application.* Prentice-Hall, Inc., 1965.

[92] D. E. Rosner. *Transport processes in chemically reacting flow systems.* Dover, 2000.

[93] D. E. Rosner and S. Yu. MC simulation of aerosol aggregation and simultaneous spheroidization. *AIChE Journal*, 47, 2001.

[94] R. J. Samson, G.W. Mulholland, and J. W. Gentry. Structural analysis of soot agglomerates. *Langmuir*, 3, 1987.

[95] H. Schlichting and K. Gersten. *Boundary Layer Theory.* Springer, 8th Edn, 2000.

[96] S. Sinha, B. E. Wyslouzil, and G. Wilemski. Modeling of H_2O/D_2O condensation in supersonic nozzles. *Aerosol Sci. Technol.*, 43, 2009.

[97] C. M. Sorensen. The optics of single particle and fractal aggregates. *J. Aerosol Sci.*, 31, 2000.

[98] C. M. Sorensen and G. C. Roberts. The prefactor of fractal aggregates. *J. Colloid. and Interface Sci.*, 186, 1997.

[99] A. Tamir. *Impinging-stream reactors.* Elsevier, 1994.

[100] P. Tandom and D. E. Rosner. Translational Brownian diffusion coefficient of large (multiparticle) suspended aggregates. *Ind. Eng. Chem. Res.*, 34, 1995.

[101] P. Tandom and D. E. Rosner. Sintering kinetics and transport property evolution of large multi-particle aggregates. *Chem. Eng. Comm.*, 151, 1996.

[102] P. Tandom and D. E. Rosner. Monte Carlo simulation of particle aggregation and simultaneous reestructuring. *J. Colloid Interface Sci.*, 213, 1999.

[103] P. Tandon and M. Murtagh. Particle-vapour interaction in deposition systems: influence on deposit morphology. *Chem. Eng. Sci.*, 60, 2005.

[104] L. Ting. On the mixing of two parallel streams. *J. Math. Phys.*, 38, 1959.

[105] G. D. Ulrich. Theory of particle formation and growth in oxide synthesis flames. *Comb. Sci. Techn.*, 4, 1971.

[106] A. I. van de Vooren and D. Dijkstra. The Navier-Stokes solution for laminar flow past a semi-infinite flat plate. *Journal of Eng. Math.*, 4, 1970.

[107] A. I. van de Vooren and A. E. P. Veldman. Incompressible viscous flow near the leading edge of a flat plate admitting slip. *Journal of Eng. Math.*, 9, 1975.

[108] Von L. Waldmann. Über die Kraft eines inhomogenen Gases auf kleine suspendierte Kugeln. *Z. Naturforsch*, 14a, 1959.

[109] G. M. Wang and C. M. Sorensen. Diffusive mobility of fractal aggregates over the entire Knudsen number range. *Phys. Rev. E*, 60, 1999.

[110] D. A. Weitz, D. J. Pine, P. N. Pusey, and Tough R. J. A. Nondiffusive Brownian motion studied by diffusing-wave spectroscopy. *Phys. Rev. Lett.*, 63, 1989.

[111] J. O. L. Wendt. Pollutant formation in furnaces: NO_x and fine particulates. *IFRF Combustion Journal*, Article No 200301, 2003.

[112] L. J. Wibberley and T. F. Wall. Alkali-ash reactions and deposit formation in pulverized-coal-fired boilers. *Fuel*, 61, 1982.

[113] A. Williams, M. Pourkashanian, and J. M. Jones. *Combustion and gasification of coal.* Taylor and Francis, 2000.

[114] M. M. R. Williams and S. K. Loyalka. *Aerosol science. Theory and practice.* Pergamon Press, 1991.

[115] D. T. Wu. Nucleation theory. *Solid State Phys.*, 50, 1997.

[116] H. Yamakawa. *Modern theory of polymer solutions.* Harper and Row, Publishers Inc., 1971.

[117] J. I. Yoo, Y. C. Seo, and Shinagawa T. Particle size distributions and heavy metal partitioning in emission gas from different coal-fired power plants. *Environm. Eng. Sci.*, 22, 2005.

[118] A. L. Yule. Two-dimensional self-preserving turbulent mixing layers at different free stream velocity ratios. Technical report, Ministry of Defence. London: Her Majesty's Stationery Office. Internal Report No. 3683, 1972.

[119] F. Zheng. Thermophoresis of spherical and non-spherical particles: a review of theories and experiments. *Adv. Colloid Interface Sci.*, 97, 2002.

[120] R. M. Ziff, E. D. McGrady, and P. Meakin. On the validity of Smoluchowski's equation for cluster-cluster aggregation kinetics. *J. Chem. Phys.*, 82, 1985.